ELECTROMAGNETIC FORCES IN FLEXIBLE SYSTEMS

Thesis Submitted For The Degree Of Doctor of Philosophy

by

<u>JIA SHENG HONG</u>

Department of Engineering Science

University of Oxford

St.Peter's College

Hilary 1994

To My Family

ELECTROMAGNETIC FORCES IN FLEXIBLE SYSTEMS

JIA SHENG HONG

St.Peter's College, Oxford, UK

Thesis submitted for the degree of Doctor of Philosophy in

The Department of Engineering Science

The University of Oxford, Hilary 1994

ABSTRACT

Some problems in electrodynamics have been studied in the light of electromagnetic field theory and computational techniques.

One is that of the retrograde motion of the electric arc — an old and intriguing problem of physics. A more complete model based on electrodynamics has been proposed for study of this problem. In this model, the plasma column is treated as a flexible conductor. The associated 3-dimensional boundary-value problem was solved by the boundary element method (BEM). It has been shown that the retrograde motion can indeed be understood in terms of electrodynamics and a number of the reported features of this phenomenon have been explained by the proposed model.

The others are concerned with a recent controversy in electrodynamics. It has been discussed in the thesis that Lorentz and Ampère force laws are equivalent in the sense of magnetostatics provided that the latter is appropriately used. The interactions of electromagnetic forces on the systems of the electromagnetic jet propulsion and the electromagnetic impulse pendulum have been examined. It turns out that the observations are consistent with the laws of electromagnetic energy and momentum. Two aspects of the water-arc explosion problem have been studied. One is the electromagnetic (EM) aspect which is calculated by the method of separation of the variables. the other is the magnetohydrodynamic (MHD) aspect which is solved by the finite-difference method (FDM). The numerical results of the two aspects show that neither the pure EM model nor the MHD model for the incompressible fluid could explain the explosive phenomenon; this strongly suggests that the shock wave produced by the under-water arc must account for the phenomenon. On the wire fragmentation, a preliminary study has shown that this phenomenon could be caused by the electromagnetically driven stress waves and a theoretical model has been proposed for further investigation. This is described in an Appendix to the thesis.

Acknowledgements

I wish to express my thanks and appreciation to Dr J E Allen, my supervisor, for the help and guidance given me throughout this work.

The financial support of a K C Wong Scholarship granted by the University of Oxford is gratefully acknowledged. A Graduate Award from St.Peter's College and an ORS award are also acknowledged.

Finally I would like to acknowledge Dr P Neal Graneau and Dr G Hassall for their helping hands and minds when needed.

Contents

List of Principal Symbols†

(† unless otherwise specified)

$\mathbf{A}$	magnetic vector potential
$\mathbf{B}$	magnetic flux density / magnetic induction
$\mathbf{H}$	magnetic field strength
$\mathbf{E}$	electric field strength
$\mathbf{D}$	electric flux density
$\mathbf{j}$	current density
$\mathbf{f}$	force density
$\overleftrightarrow{\mathbf{T}}$	Maxwell stress tensor
V	electric potential / scalar potential
I	electric current
ρ	charge density
ρ_m	mass density
σ	conductivity
ϵ_0	permittivity of vacuum
ϵ	permittivity
μ_0	permeability of vacuum
μ	permeability
c	speed of light
$\mathbf{P}$	Poynting vector
$\mathbf{g}$	field momentum density
$\mathbf{v}$	velocity
t	time
T	temperature
p	pressure
τ	volume
s	area / surface
Γ	boundary surface
$\mathbf{n}$	unit vector normal to a surface

$\mathbf{r}$	field position vector
$\mathbf{r}'$	source position vector
x, y, z	Cartesian coordinates
ρ, ϕ, z	cylindrical coordinates
r, θ, ϕ	spherical coordinates
$\mathbf{a}_x$, $\mathbf{a}_y$, $\mathbf{a}_z$	unit vectors in Cartesian coordinates
$\mathbf{a}_\rho$, $\mathbf{a}_\phi$, $\mathbf{a}_z$	unit vectors in cylindrical coordinates
$\mathbf{a}_r$, $\mathbf{a}_\theta$, $\mathbf{a}_\phi$	unit vectors in spherical coordinates
η	viscosity
ψ	stream function
$\mathcal{J}$	Bessel function
$G(\mathbf{r}, \mathbf{r}')$	Green function
∇	gradient
$\nabla\cdot$	divergence
$\nabla\times$	curl
∇^2	Laplacian

Introduction

There is an old mystery of physics known as *the retrograde motion of the electric arc* that is under certain conditions (such as the gas pressure, the applied magnetic field etc.) the cathode spot of a direct current electric arc maintained between two metal electrodes seems to be moving in an opposite direction to that expected from the Lorentz force law [1]–[5]. Although the phenomenon has been known for ninety years since its discovery by Stark [6] and has stimulated numerous investigations which result in many models giving explanation from different points of view, there is still no theory that can account both qualitatively and quantitatively for all the observations.

On the other hand there is a recently increasing controversy in electrodynamics. Some newly reported experimental phenomena, which, according to the reporters, seem to be unexplained by classical relativistic electrodynamics, has put Lorentz force law into a position challenged by the obsolete Ampère force law. Among these phenomena one is that of *electromagnetic jet propulsion*, which shows a copper "submarine" driven along the longitudinal axis of a mercury trough when current was forced to flow [118]. The second one is that of *an electromagnetic impulse pendulum*, which was devised to demonstrate that for momentum conservation the electromagnetic field energy required would have been 1000 to 2000 times as large as the energy that was actually available from the source [126, 127]. The third one is that of *water-arc explosions*, which purports to show that electric arc current through salt water produces explosions by so-called longitudinal Ampère forces [132].

Obviously, to understand these phenomena or to clarify these matters are real problems in both science and engineering. That is the purpose of this thesis

The first part of this thesis, dealing with the retrograde motion of the electric arc, begins with a more comprehensive introduction of the phenomenon and its historical background (Chapter 1). The previous and proposed electrodynamic models for explanation of the retrograde motion are described in Chapter 2. The theoretical formulation of the proposed model is given in Chapter 3 which includes a useful treatment of the boundary conditions at interface between conductors of widely differing conductivity. Chapter 4 discusses in detail the computation of electrodynamic forces on the arc cathode spot using the boundary element method. This continues in Chapter 5 by describing the computer programme and the numerical results. Chapter 6 concludes the first part of this thesis by explaining the phenomenon with the aid of the numerical results obtained, which includes an extended electrodynamic model for explanation of the retrograde motion of multi–spots.

The second part of this thesis, considering some recent issues in electrodynamics, begins with a discussion of electrodynamic force laws (Chapter 7) which includes the proof of equivalence of the Lorentz and Ampère force laws as well as the correct application of the latter. The controversial issues on the electromagnetic jet propulsion and the electromagnetic impulse pendulum are clarified in Chapter 8 and Chapter 9 respectively, which involve discussions on the concepts of action and reaction, electromagnetic field momentum and energy. Chapter 10, the last chapter of this thesis, studies the phenomenon of water-arc explosion from two aspects, namely the electromagnetic (EM) aspect and the magnetohydrodynamic (MHD) aspect with the application of the method of separation of the variables and the finite-difference method.

Finally, the salient results described in this thesis are summarized as conclusions of this thesis.

Part I

Retrograde Motion of Electric Arcs

Chapter 1

Historical Background

Suppose that a direct current electric arc is maintained between metal electrodes, and a transverse magnetic field applied to it as shown in Fig.1.1.

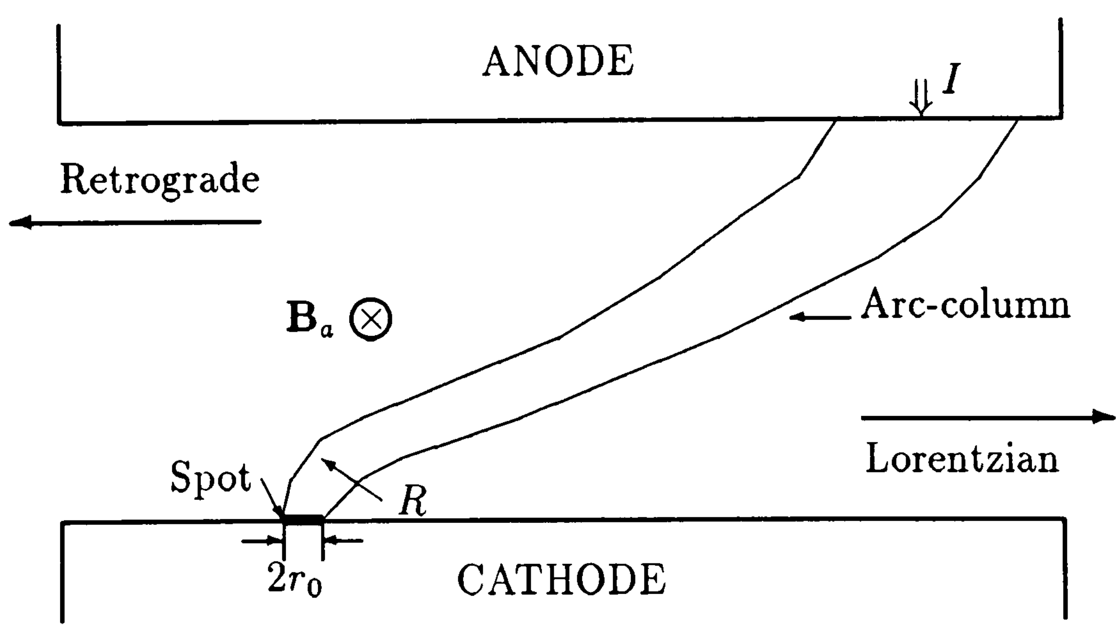

Figure 1.1: The electric arc in a transverse magnetic field

The positive column is always deflected in the same direction as a solid conductor. Under certain conditions, however, the arc cathode spot moves the "wrong" way, that is, in a direction opposite to that in which the Lorentz force resulting from the interaction of the current and the applied magnetic field would move it, dragging the deflected column with it. This is the so-called retrograde motion and is one of the more intriguing phenomena of the electric arc [1]- [5].

The retrograde motion has been observed to be dependent on the background gas pressure, the applied magnetic field, the arc current, the cathode temperature and the material, and the separation of the cathode and the anode. The phenomenon has been known for nearly ninety years since its discovery by Stark [6] in 1903 and has stimulated numerous investigations [7]–[43] not only because it has a fundamental interest in both theory and application, but also because it is probably one of the most challenging problems in arc physics. Many suggestions have been put forward to account for the retrograde motion.

Tanberg [8] assumed that the neutral gas flow from the cathode results in an ion displacement in the reverse direction which causes the retrograde motion. Rothstein [16] tried to explain the retrograde motion by introducing the hypotheses of hole conductivity in high compressed metal vapour clouds near the cathode. Longini [15] related the retrograde motion to displacement of the positive space charge as a result of the positive ions and the electrons being deflected by different amounts in the applied magnetic field. St.John and Winans [18] assume that the ions which are deflected in the Lorentzian direction interact with a negative space charge near the cathode, fly on due to their inertia and hit the cathode side opposite to the centre of primary electron emission so as to cause new emission centres.

Robson and von Engel [20, 21, 23] suggested that the retrograde motion could be understood by electrodynamics for two reasons. Firstly, the cathode spot is a microscopic region whose transverse dimensions are no greater than $10^{-3}\,cm$ so that in the spot the self magnetic field arrising from the arc current could exceed the applied magnetic field. Secondly, The density of cathode vapour[1] in the spot is $\sim 10^{20}\,cm^{-3}$

[1]The cathode vapour pressure in the spot is well above the atm pressure.

and the cathode fall region is $\sim 5 \times 10^{-5}\,cm$. It is hard to imagine how the addition of gas to a pressure of a few Torr,[2] or the variation of the position of the anode several millimetres away can affect conditions in the spot, yet both these effects can bring about reversal of the direction of motion. The second effect implies that the cause of the retrograde motion does not lie in the cathode spot alone, but also involves the arc column which can have a direct influence on the self magnetic field in the spot.

Ecker and Müller [24] base their approach on the assumption that the electron and ion motions are radially coupled by a space charge effect. The ions moving towards the cathode form a potential hose which limits the electrons in their radial motion. The applied magnetic field deflected this ion motion in the correct Lorentzian direction. The electrons, travelling from the cathode, however, due to the hose effect, are forced to move into the anti-Lorentzian direction and their collisions consequently produce the new plasma on the retrograde side of the original spot onset.

Guile and Secker [25] suggest that the retrograde motion occurs because the inherent self magnetic field of the arc current loop itself may exceed the external magnetic field applied. Hull [26] attributes the effect to the drift of slow "residual" electrons in the Lorentzian direction, parallel to the cathode surface, thus weakening the electric field drawing the positive ions to the surface, so that the positive ion current on the retrograde side predominates. Fursei [28] advanced an explanation based on the assumption that the ion motion is influenced by explosions on microroughness dots on the cathode. Sena [29] suggested an explanation of the retrograde motion by considering the distortion of the path of radially emitted ions by the magnetic field.

Pimley [32] tried to predict the retrograde motion by means of the variational (energy) method, in which the electric arc was modelled by a flexible wire loop and the motion of the moving part of the loop was predicted according to a maximum energy principle. Fang [34] connects the retrograde motion of vacuum arcs in transverse magnetic fields with an outflow of positive ions from the cathode spot. In transverse magnetic fields the high speed ion jets from the cathode to the anode are deflected in the retrograde direction and thereby the positive space charge shifts to the same

[2] $1\,Torr = 1\,mmHg = 1/760\,atm$.

direction. This leads to a displacement of the microscopic electric field between the positive space charge and the cathode surface, and in turn to a displacement of the active field emission sites in this direction and finally to the retrograde motion.

Drouet [37] attributes the retrograde motion to the asymmetrical confinement of the cathode-spot plasma which results from the asymmetrical combination of the self and applied magnetic fields. The confinement of the cathodic vapour on the retrograde side of microspot enhances the electron emission on that side, and thus favours the observed retrograde motion. Schrade [39, 40] attempted to explain the retrograde motion by a unique stability theory based on an analysis of the statics and dynamics of a current carrying plasma channel under the influence of an applied magnetic field and under general flow conditions.

Moizhes and Nemchinsky [43] developed an explanation of the retrograde motion based on the leading role of the Hall electric field. In a transverse magnetic field the electrons flowing from the cathode spot towards the anode are deflected by the Lorentz force. The surplus electric charges accumulate at the plasma-electrode boundary (positive at the retrograde side of the spot and negative at the opposite side), thus forming a Hall electric field, which leads to an asymmetrical cathode voltage drop and to the retrograde motion.

There are other theories which might be catalogued in addition the above mentioned models. No attempt is made at this stage to estimate the validity of these previous theories one by one because most of them rely on either assumptions or parameters which cannot be tested. Two important reviews covering most of these theories have been written by Kesaev [2] and Rakhovskii [81]. Nevertheless, at the present time, there is still no theory that can account both qualitatively and quantitatively for all the observations.

It can be seen that most of the explanations of the retrograde motion involve the study of cathode processes to give the preferential formation of new cathode spots along the retrograde direction [8, 15, 18, 24, 26, 29, 34, 37]. One line of explanation, which is rather different from the others and seems to be more ingenious, is based on electrodynamics [20, 32]. This approach treates the retrograde motion as an electrodynamic event and will be futher discussed in the next chapter.

Chapter 2

The Electrodynamic Models

2.1 On Robson and von Engels' Model

According to Robson and von Engel [20, 21, 23] the magnetic field acting upon the cathode spot is the sum of the applied field B_a and a self-field $-\mu_o I/R$, where I is the arc current and R an effective radius of curvature of the arc column where it joins the spot (refer to Fig.2.1). The direction of motion is then determined by the direction of the field B, given by

$$B = B_a - \mu_o I/R \tag{2.1}$$

Retrograde motion occurs if the self-field exceeds the applied field.

Smith [12] has criticised this model on the following grounds. For his purpose, he divided the arc path into three parts, α, β and γ as Fig.2.1 shows, then he might carry out his calculations based on two formulas

$$B = \frac{\mu_0 I}{2\pi r_0} \tag{2.2}$$

for the magnetic induction on surface of an infinite conductor bar of radius r_0 carrying a current I; and

$$p = \frac{B^2}{2\mu_0} \tag{2.3}$$

for the associated magnetic pressure.[1] If we note that 1 $Tesla$ = 10^4 $Gauss$ and

[1]Refer to page 62 of the book by Shercliff [136].

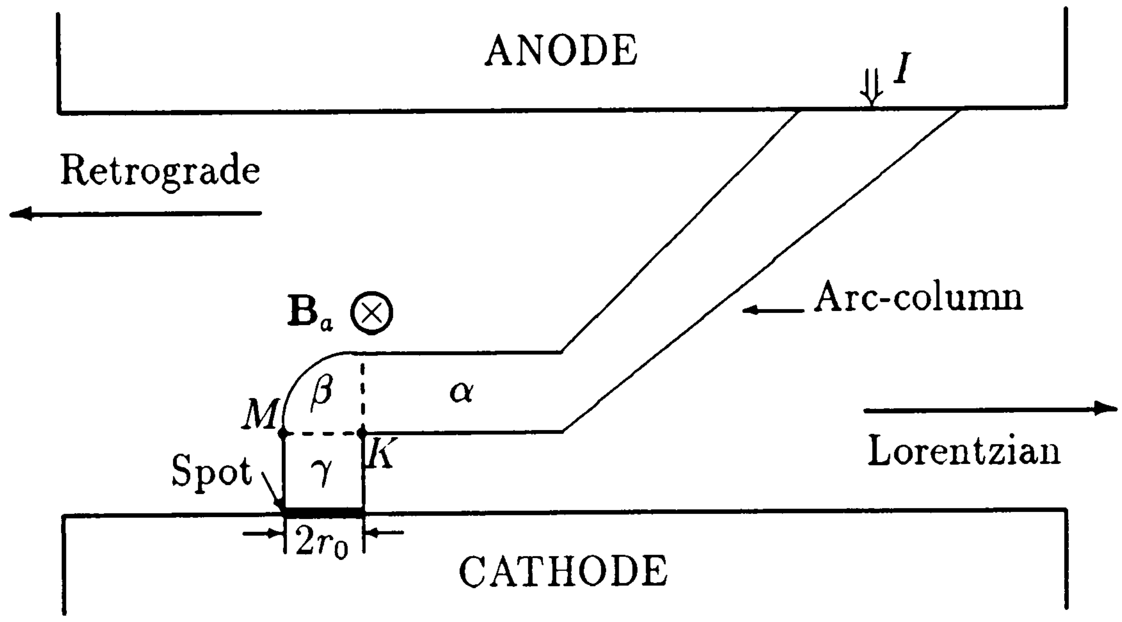

Figure 2.1: Smith's arc model for evaluating magnetic forces

1 $Newton = 10^5$ $Dynes$ we can transform Eqns.(2.2,2.3) into

$$B = \frac{I(A)}{5r_0(cm)} \quad (gauss) \tag{2.4}$$

$$p = \frac{B^2(gauss)}{8\pi} \quad \frac{dynes}{sq\ cm} \tag{2.5}$$

which were actually used by Smith. According to Smith, $B' = (I/10r_0)$ is the field at K (see Fig.2.1) due to a semi-infinite bar of radius r_0, the region α; the field due to γ is also $(I/10r_0)$ and the field due to region β is $(2I/15r_0)$. Adding the fields of α, β and γ, he obtained $B_K = (I/3r_0)$ gauss. By defining p_R = force per unit area directed in the retrograde sense and p_L = force per unit area directed in the Lorentz sense, Smith arrived at

$$p_R = \frac{(B_K - B_a)^2}{8\pi} \quad \frac{dynes}{sq\ cm} \tag{2.6}$$

$$p_L = \frac{(B_M + B_a)^2}{8\pi} \quad \frac{dynes}{sq\ cm} \tag{2.7}$$

where B_a is the applied field inward, $\perp$ to the paper, B_M is a field due to the arc current on the convex side of the arc path. At this stage, Smith stated that B_M is less than B_K and in the same sense as B_a, and to yield a resultant force per unit area in the retrograde direction, $B_K - B_a$ must be greater than $B_M + B_a$, hence, $B_K > 2B_a$. Letting $I = 3\,A$; and $r_0 = 0.001\,cm$ he found $B_K = 1000\,gauss$ by assuming a current density of 10^6 amperes per sq cm. He then argued that B_K is hardly able to exceed $2B_a$ ranged upward to values near 10000 gauss in the experiments so that he concluded that the resultant force is preponderantly in the Lorentzian direction and the theory of Robson and von Engel is not sustained.

However, Guile and Seeker [25] pointed out that the magnetic field values deduced by Smith are open to doubt inasmuch as the current density in a discharge varies considerably over the cross section so that the calculation of the forces is even more complicated and the fields cannot be determined in the simple way employed by Smith.

2.2 On Pimley's Model

Pimley's work [32] was aimed at reexamining the Robson–von Engel theory and to see if it has any similarity to a certain problem involving a simple circuit of wires with a moveable contact. The latter one was motived by another interesting electrodynamic problem [45] and based on a variational (or energy) method in electromagnetism, i.e.,

$$magnetic\ force = \frac{1}{2} I^2 \frac{\partial L}{\partial x} \tag{2.8}$$

where L is the self inductance of the (arc) circuit, I is the constant circuit current and x denotes a coordinate position in the circuit. Eqn.(2.8) implies a maximum energy principle that is the magnetic forces in a conducting circuit tend to increase the circuit inductance, thus the energy $(I^2L/2)$ of the current circuit so that at equilibrium the energy is a maximum for the constant current case [46].

In order to apply Eqn.(2.8) to the problem of the retrograde motion, Pimley assumed a shape of arc column as sketched in Fig.2.2 and proposed a criterion for the occurence of retrograde motion

$$F_c > F_\epsilon + F_a \tag{2.9}$$

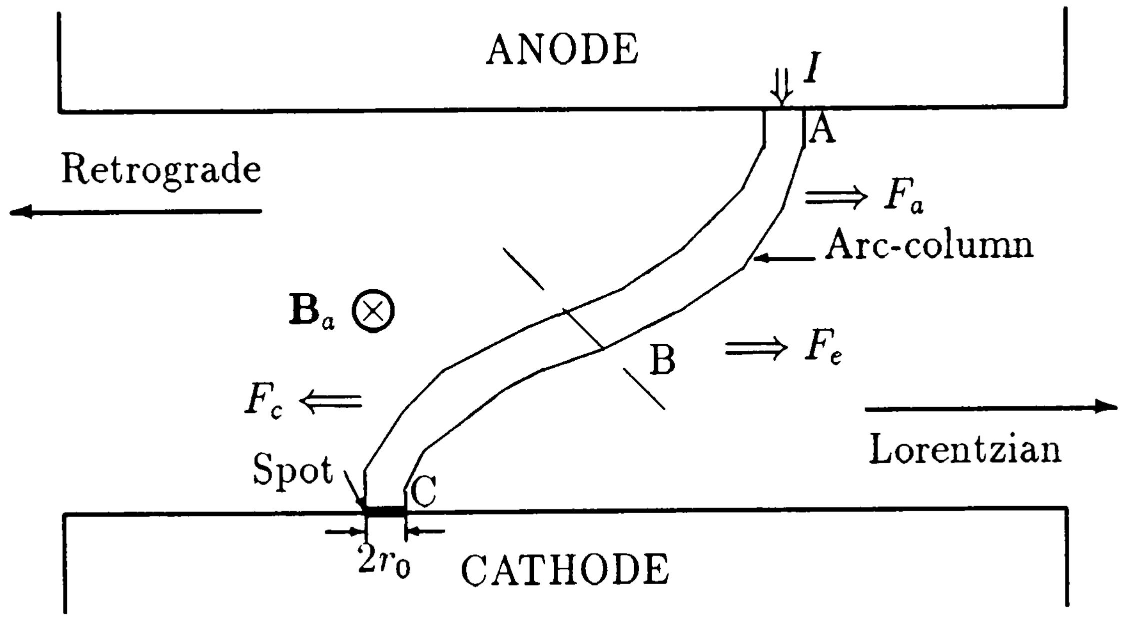

Figure 2.2: Pimley's arc model for explanation of retrograde motion

in which F_e indicates the external force resulting from the interaction of the column current and the applied magnetic field on the whole arc column, and was assumed to have a value of $(B_a I\, d)$ in the Lorentzian direction, where d is the distance between the anode and the cathode; F_c denotes the resolved cathode local force on the curved region BC in the retrograde direction while F_a the resolved anode local force on the curved region AB in the Lorentzian direction. Note both of F_c and F_a result from the interaction of current elements in the circuit. Based on Eqn.(2.8), Pimley derived the expressions for F_c and F_a for a special geometry of arc column and from Eqn.(2.9) arrived at an equivalent criterion in terms of the applied and the self magnetic fields.

The criticism of Pimley's model stems from the fact that the arc column is not a rigid body so that the motion of any part of the column is not necessarily the same as the other parts but merely dependent on the local forces exerted on it. Therefore the criterion of Eqn.(2.9) is called into question.

Although the method of looking at electromagnetic phenomena from the standpoint of energy has much to recommend it because of the three advantages in general which are first that the conceptual framework of the subject is simplified, second that particularly simple methods of calculation can be devised from energy considerations, and third that these methods of calculation are directly related to measurement techniques [46], it seems that such advantages are not so important in dealing with the problem of retrograde motion if one has to find force distributions (densities) locally.

2.3 The New Model

We also believe as Robson and von Engel, that the retrograde motion can be understood in terms of electrodynamics, but we do not agree with their criterion for occurrence of the retrograde motion because the cathode spot in reality is not just a point and over it the fields change from point to point, so do the forces. Therefore the retrograde motion cannot be judged by the field given by Eqn.(2.1). Pimley's model is also not suitable for the reason given in the last section. Hence we have to seek a new electrodynamic model.

For our purpose, let us first consider a cylindrical conducting wire with a radius of r_0 and a finite length of z_0 as Fig.2.3 shows. In terms of line current elements, the Biot-Savart law for a closed current circuit is given by[2]

$$\mathbf{B}(\mathbf{r}) = \frac{\mu_0}{4\pi} I \oint \frac{dl \times \mathbf{r}_{12}}{r_{12}^3} \tag{2.10}$$

where $\mathbf{r}_{12} = \mathbf{r} - \mathbf{r}'$ is the position vector from the source to the field. In our case, $dl = dz\,\mathbf{a}_z$, $\mathbf{r} = \rho\,\mathbf{a}_\rho$, $\mathbf{r}' = z\,\mathbf{a}_z$ and $r_{12} = \sqrt{z^2 + \rho^2}$. By substitution we get

$$B(\rho)\,\mathbf{a}_\phi = \frac{\mu_0}{4\pi} I \int_0^{z_0} \frac{\sin\theta dz}{(z^2 + \rho^2)^2}\,\mathbf{a}_\phi \tag{2.11}$$

where θ is the angle between the two vectors $dz\,\mathbf{a}_z$ and $\mathbf{r}_{12}$, thus $\sin\theta = \rho/\sqrt{z^2 + \rho^2}$ and the azimuthal magnetic induction on the radial axis is given by

$$B(\rho) = \frac{\mu_0 I}{4\pi} \int_0^{z_0} \frac{\rho}{(z^2 + \rho^2)^{3/2}} dz \qquad \rho \geq r_0 \tag{2.12}$$

Let $z = \rho \tan\psi$ so that

$$\psi = \tan^{-1}(\frac{z}{\rho}), \quad dz = \rho \sec^2\psi d\psi, \quad (z^2 + \rho^2)^{3/2} = \rho^3 \sec^3\psi \tag{2.13}$$

[2]Refer to page 125 in the book by Panofsky and Phillips [50].

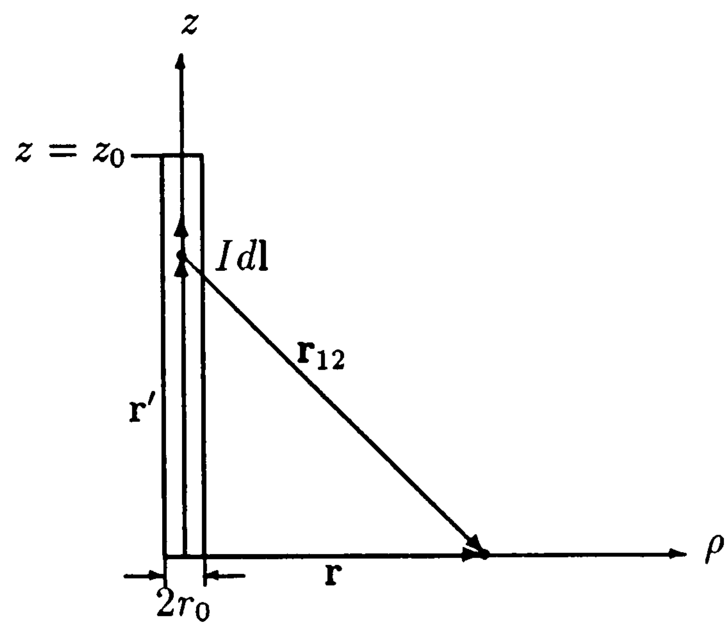

Figure 2.3: A section of a cylindrical conducting wire

and

$$\begin{aligned} B(\rho) &= \frac{\mu_0 I}{4\pi}\frac{1}{\rho}\int_0^{\tan^{-1}(z_0/\rho)} \frac{d\psi}{\sec\psi} \\ &= \frac{\mu_0 I}{4\pi}\frac{1}{\rho}\sin(\tan^{-1}\frac{z_0}{\rho}) \quad \rho \geq r_0 \end{aligned} \tag{2.14}$$

If $z_0 \to \infty$, $B(\rho) \to B_\infty(\rho) = \mu_0 I/(4\pi\rho)$ which is the result expected for the semi-infinite conducting wire. As shown in Table 2.1, even with a ratio z_0/ρ of 4, the resultant magnetic induction is 97% of that arising from the semi-infinite wire.

Now let us look at a simple arc model in Fig.2.4. According to Eqn.(2.14), the magnetic induction on the cathode spot resulting from wire section $\overline{AB}$ can be estimated by

$$B_{\overline{AB}}(d) < \frac{\mu_0}{4\pi}\frac{I}{d} \tag{2.15}$$

where $d = \overline{BD}$ is the distance between the anode and the cathode. According to Robson's experiment [21], for $d = 0.5\,mm$ and $I = 3\,A$ the retrograde motion occurs when the applied magnetic induction $B_a > 0.3\,tesla$ below which the motion reverses to

Table 2.1: Relative magnetic induction vs ratio of z_0/ρ

z_0/ρ	$\sin(\tan^{-1} z_0/\rho)$	$B(\rho)/B_\infty(\rho)$
2	0.894	89.4%
4	0.970	97.0%
6	0.986	98.6%
10	0.995	99.5%

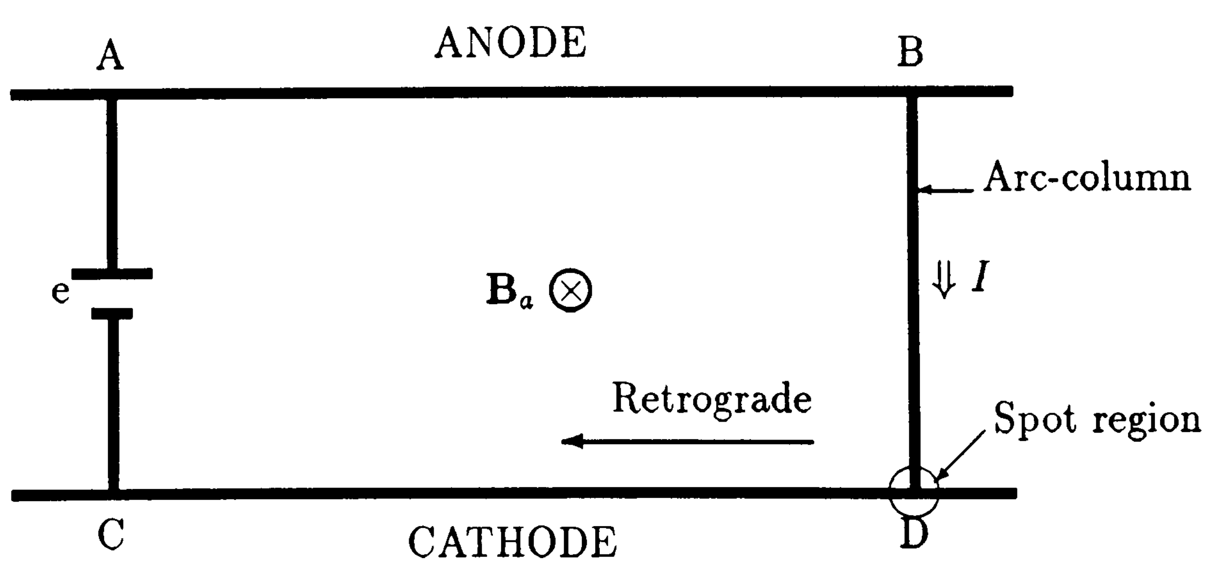

Figure 2.4: A simple electric arc model

the Lorentzian direction. From Eqn.(2.15) we find $B_{\overline{AB}}(0.5mm) < 6\times10^{-4}\,tesla \ll B_a$. It is, therefore, hard to imagine that the current in the anode has an influence on the directed motion of the cathode spot. To confirm this, let us look at another example. According to Carter and Murphree [31], for $d = 16.5\,mm$, $I = 540\,A$ and $B_a = 0.7\,tesla$, the cathode spot moves in the retrograde direction. Substituting the experimental data into Eqn.(2.15), we again find $B_{\overline{AB}}(16.5mm) < 3.276\times10^{-3}\,tesla \ll B_a$. Thus, if the retrograde motion can be attributed to electrodynamic forces, the self magnetic field must exceed the applied magnetic field somewhere in the spot region so that the contribution from the anode current to the self magnetic field on the spot is too small to be taken into account.

Letting $\rho = r_0$ in Eqn.(2.14), we can immediately see from Table 2.1 that the self magnetic field on the cathode spot is mainly due to the parts of the conducting wire sections $\overline{BD}$ and $\overline{CD}$ near the spot. Thus, we can just consider the contribution to the self magnetic field from nearby currents and ignore that from currents in the remainder of the circuit.

On the basis of the foregoing discussions together with the following facts (i) that the radius of cathode spot, which is no greater than $10^{-3}cm$ [47, 48, 49], is much smaller than the dimensions of the cathode; (ii) that the distance from the anode to the cathode is much larger than the radius of the cathode spot and (iii) that the arc column is deflected in the Lorentzian direction [12, 20, 27, 31], we propose a new three dimensional (3D) arc model for studying retrograde motion as shown in Fig.2.5 and suggest that the direction of motion is determined by

$$F_R + F_L = \int_{spot} \mathbf{f}(\mathbf{r})\cdot \mathbf{a}_\perp \, d\Gamma \qquad (2.16)$$

where $\mathbf{f}(\mathbf{r})$ is the electrodynamic force density arising from interactions of the spot current with the self as well as the applied magnetic fields; $\mathbf{a}_\perp$ is the unit vector parallel to the spot surface but perpendicular to the applied magnetic field; F_R and F_L represent the resultant forces per unit length exerted on the spot in the retrograde and the Lorentzian directions respectively. If $|F_R| > |F_L|$, the retrograde motion occurs.

Thus to determine the electrodynamic force distribution on the spot plays a decisive role in this model. Unfortunately at the present time it is impossible to measure this

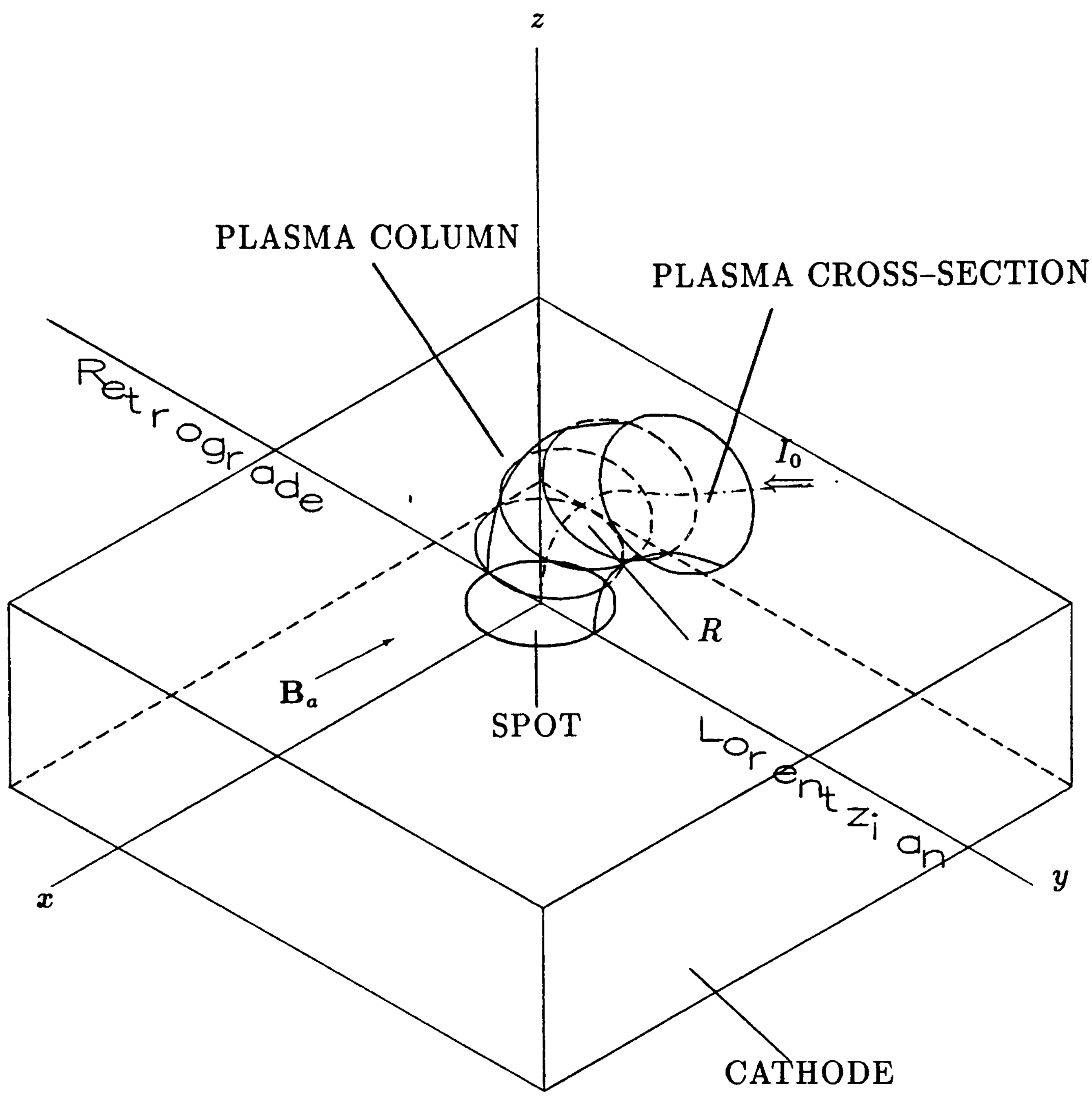

Figure 2.5: 3D physical model of an electric arc

distribution due to the tiny size of the spot. Theoretical prediction is obviously difficult and to best of our knowledge no attempt has yet been made. Hence it is purpose of the next chapter to present a theoretical approach to predict the electrodynamic force distribution on the arc cathode spot.

Chapter 3

Theoretical Formulation

3.1 Governing Equations

The governing equations for our proposed steady-state model are

$$\nabla \times \mathbf{E}(\mathbf{r}) = 0 \tag{3.1}$$

$$\nabla \cdot \mathbf{j}(\mathbf{r}) = 0 \tag{3.2}$$

$$\mathbf{j}(\mathbf{r}) = \sigma \mathbf{E}(\mathbf{r}) \tag{3.3}$$

$$\nabla \times \mathbf{B}(\mathbf{r}) = \mu_o \mathbf{j}(\mathbf{r}) \tag{3.4}$$

$$\nabla \cdot \mathbf{B}(\mathbf{r}) = 0 \tag{3.5}$$

$$\mathbf{f}(\mathbf{r}) = \mathbf{j}(\mathbf{r}) \times (\mathbf{B}(\mathbf{r}) + \mathbf{B}_a) \tag{3.6}$$

where $\mathbf{B}_a$ is the known constant magnetic induction applied. It should be remarked that we do not attempt to go in detail into plasma physics so the plasma column is just treated as an electric conductor and Ohm's law[1] of Eqn.(3.3) is employed in our theory.

By introducing a scalar potential $V(\mathbf{r})$ and a vector potential $\mathbf{A}(\mathbf{r})$ so that

$$\mathbf{E}(\mathbf{r}) = -\nabla V(\mathbf{r}) \tag{3.7}$$

$$\mathbf{B}(\mathbf{r}) = \nabla \times \mathbf{A}(\mathbf{r}) \tag{3.8}$$

[1]Strictly speaking, the Ohm's law in plasma is generally more complex [52]. Nevertheless, to a first approximation, Eqn.(3.3) is applicable.

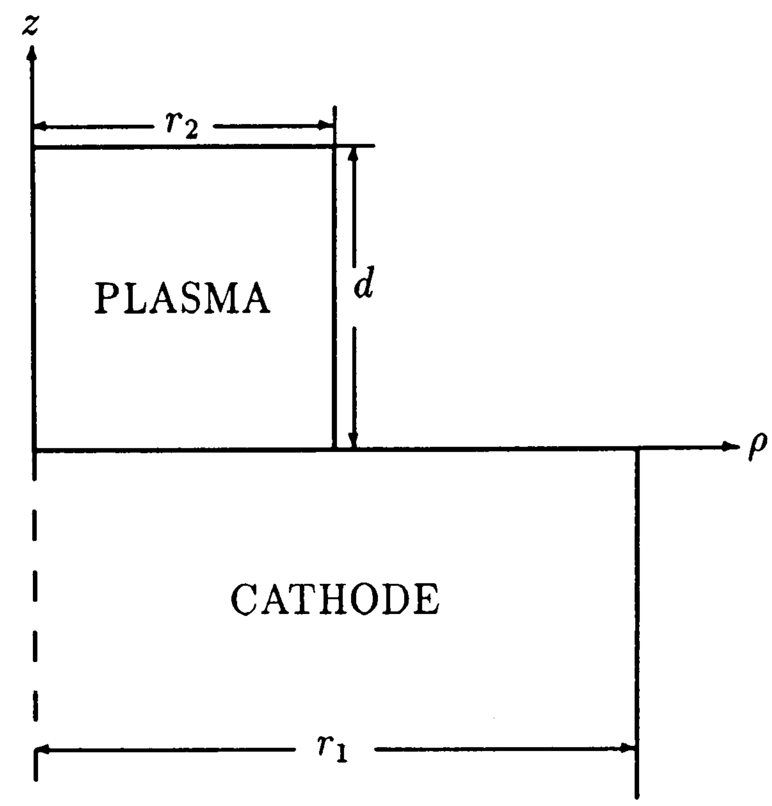

Figure 3.1: A simplified 2D model of electric arc

we have

$$\nabla^2 V(\mathbf{r}) = 0 \tag{3.9}$$

$$\mathbf{A}(\mathbf{r}) = \frac{\mu_o}{4\pi}\int_\tau \frac{\mathbf{j}(\mathbf{r}')}{|\mathbf{r}-\mathbf{r}'|}\,d\tau \tag{3.10}$$

where $\mathbf{r}'$ is the source position vector and τ indicates the whole current region. Equation (3.9) is the familar Laplace's equation. It is obvious that if the scalar potential is known the other field quantities of interest can be determined.

3.2 Boundary Conditions

In general the unique solution of Laplace's equation can only be determined when the associated boundary conditions are applied. For our purpose we have to solve a 3D boundary value problem. Apart from the irregular boundary of the plasma column, the coupled boundary between the plasma and the cathode makes the problem even more difficult. Therefore we first look for the possibility of decoupling the problem. To do so, let us consider a simplified 2D model in Fig.3.1, where $r_{1,2}$ are the radii of the cathode and the plasma column, respectively, and the cathode is assumed to extend a long way from the interface.

A general solution of Laplace's equation in cylindrical coordinates can be derived analytically and given by[2]

$$V(\rho,\phi,z) = V_{00} + \sum_{n\neq 0} \mathcal{R}_n(\rho)\Phi(n\phi)\mathcal{Z}(z) + \sum_{k\neq 0}\sum_{n} \mathcal{R}_n(k\rho)\Phi(n\phi)\mathcal{Z}(kz) \tag{3.11}$$

with

$$\begin{aligned}
V_{00} &= (A_0' + B_0' \ln \rho)(A_0 z + B_0)(C_0\phi + D_0) && (3.12)\\
\mathcal{Z}(z) &= A_0 z + B_0 && (3.13)\\
\mathcal{Z}(kz) &= A_k e^{kz} + B_k e^{-kz} && (3.14)\\
\Phi(n\phi) &= C_n e^{jn\phi} + D_n e^{-jn\phi} && (3.15)\\
\mathcal{R}_n(\rho) &= A_0'\rho^n + B_0'\rho^{-n} && (3.16)\\
\mathcal{R}_n(k\rho) &= A_k'\mathcal{J}_n(k\rho) + B_k'\mathcal{Y}_n(k\rho) && (3.17)
\end{aligned}$$

where $\mathcal{J}_n$ is called a Bessel function of the nth order of the first kind and $\mathcal{Y}_n$ a Bessel function of the nth order of the second kind.[3]

In our case because of the symmetric structure V should be independent of ϕ, this leads to $n = 0$ and $C_0 = 0$. Furthermore, V should be finite at the symmetric axis of $\rho = 0$, this requires $B_0' = 0$ and $B_k' = 0$ since $\mathcal{Y}_n(0)$ is infinite. Considering all of these, Eqn.(3.11) degenerates to

$$V(\rho, z) = V_0 + A_0 z + \sum_{k\neq 0} \left(A_k e^{kz} + B_k e^{-kz}\right) \mathcal{J}_0(k\rho) \tag{3.18}$$

in which V_0 is a constant. We note from Eqns.(3.3,3.7) that

$$\mathbf{j} = -\sigma \nabla V \tag{3.19}$$

so that a general solution for the current density is

$$\begin{aligned}
j_z(\rho,z) &= -\sigma\frac{\partial V(\rho,z)}{\partial z} = -\sigma\left\{A_0 + \sum_{k\neq 0} k\left(A_k e^{kz} - B_k e^{-kz}\right)\mathcal{J}_0(k\rho)\right\} && (3.20)\\
j_\rho(\rho,z) &= -\sigma\frac{\partial V(\rho,z)}{\partial \rho} = -\sigma\left\{\sum_{k\neq 0} k\left(A_k e^{kz} + B_k e^{-kz}\right)\mathcal{J}_1(k\rho)\right\} && (3.21)\\
j_\phi(\rho,z) &= -\frac{\sigma}{\rho}\frac{\partial V(\rho,z)}{\partial \phi} = 0 && (3.22)
\end{aligned}$$

---

[2]See page 169 of the book by Smythe [53].

[3]$\mathcal{Y}_n$ is also referred to as Neumann's function.

Since j_ρ must vanish at the boundaries of $\rho = r_{1,2}$ we get

$$\mathcal{J}_1(kr_{1,2}) = 0 \tag{3.23}$$

it follows

$$k = k_m^{1,2} = \frac{\alpha_m}{r_{1,2}} \quad \text{for } m = 1, 2, 3, \cdots \tag{3.24}$$

with α_m the mth non-zero root of the Bessel function of the first kind of the first order.[4] Thus Eqn.(3.18) becomes

$$V^{(1,2)}(\rho, z) = V_0^{(1,2)} + A_0^{(1,2)} z + \sum_{m=1}^{\infty} \left(A_m^{(1,2)} e^{k_m^{(1,2)} z} + B_m^{(1,2)} e^{-k_m^{(1,2)} z} \right) \mathcal{J}_0(k_m^{(1,2)} \rho) \tag{3.25}$$

where superscripts 1, 2 inside the brackets indicate the quantities for the cathode and the plasma regions respectively.

Further consideration is that the length of the cathode is much larger than the spot radius which enables us to assume that the cathode extends to infinity so that $B_m^{(1)} = 0$ because the current is finite in the cathode as $z \to -\infty$. Finally, we arrive at

$$\begin{aligned} V^{(1)}(\rho, z) &= V_0^{(1)} + A_0^{(1)} z + \sum_{m=1}^{\infty} A_m^{(1)} \mathcal{J}_0(k_m^{(1)} \rho) e^{k_m^{(1)} z} & (3.26) \\ V^{(2)}(\rho, z) &= V_0^{(2)} + A_0^{(2)} z + \sum_{n=1}^{\infty} \left(A_n^{(2)} e^{k_n^{(2)} z} + B_n^{(2)} e^{-k_n^{(2)} z} \right) \mathcal{J}_0(k_n^{(2)} \rho) & (3.27) \end{aligned}$$

for the general solutions of potential in the cathode and the plasma column, and

$$\begin{aligned} j_z^{(1)}(\rho, z) &= -\sigma^{(1)} \left\{ A_0^{(1)} + \sum_{m=1}^{\infty} A_m^{(1)} k_m^{(1)} \mathcal{J}_0(k_m^{(1)} \rho) e^{k_m^{(1)} z} \right\} & (3.28) \\ j_z^{(2)}(\rho, z) &= -\sigma^{(2)} \left\{ A_0^{(2)} + \sum_{n=1}^{\infty} \left(A_n^{(2)} e^{k_n^{(2)} z} - B_n^{(2)} e^{-k_n^{(2)} z} \right) k_n^{(2)} \mathcal{J}_0(k_n^{(2)} \rho) \right\} & (3.29) \end{aligned}$$

for the associated axial current density. For our purpose, we use the subscript n indicating the harmonics in the plasma region.

If we assume that $j_z^{(1)}$ is uniform and equal to a value of $-I_0/(\pi r_1^2)$ as $z \to -\infty$, where minus sign indicates the current flowing oppositely to the z direction, we get immediately

$$A_0^{(1)} = \frac{I_0}{\sigma^{(1)} \pi r_1^2} \tag{3.30}$$

---

[4]The solution of α_m is given in Appendix 3.1.

from Eqn.(3.28). The other unknown coefficients are to be determined from the boundary conditions for this particular problem

$$j_z^{(1)}(\rho,0) = \begin{cases} j_z^{(2)}(\rho,0) & \text{for } 0 \le \rho \le r_2 \\ 0 & \text{for } r_2 < \rho \le r_1 \end{cases} \tag{3.31}$$

$$V^{(2)}(\rho,0) = V^{(1)}(\rho,0) \quad \text{for } \rho \le r_2 \tag{3.32}$$

$$V^{(2)}(\rho,d) = V_p \quad \text{for } \rho \le r_2 \tag{3.33}$$

where the distant plasma cross-section is supposed to be an equipotential surface. Notice that Eqn. (3.32) is equivalent to the boundary condition $E_t^{(2)} = E_t^{(1)}$ on the interface, where the subscript t indicates the transverse component.

Substituting Eqns. (3.26,3.27,3.28,3.29) into the above boundary conditions gives

$$\sigma^{(1)}\left[A_0^{(1)} + \sum_{m=1}^{\infty} A_m^{(1)} k_m^{(1)} \mathcal{J}_0(k_m^{(1)}\rho)\right] = \begin{cases} \sigma^{(2)}\left[A_0^{(2)} + \sum_{n=1}^{\infty}(A_n^{(2)} - B_n^{(2)})k_n^{(2)}\mathcal{J}_0(k_n^{(2)}\rho)\right] & \text{for } 0 \le \rho \le r_2 \\ 0 & \text{for } r_2 < \rho \le r_1 \end{cases} \tag{3.34}$$

$$V_{(0)}^{(2)} + \sum_{n=1}^{\infty}(A_n^{(2)} + B_n^{(2)})\mathcal{J}_0(k_n^{(2)}\rho) = V_0^{(1)} + \sum_{m=1}^{\infty} A_m^{(1)}\mathcal{J}_0(k_m^{(1)}\rho) \quad \text{for } 0 \le \rho \le r_2 \tag{3.35}$$

$$V_{(0)}^{(2)} + A_0^{(2)}d + \sum_{n=1}^{\infty}(A_n^{(2)}e^{k_n^{(2)}d} + B_n^{(2)}e^{-k_n^{(2)}d})\mathcal{J}_0(k_n^{(2)}\rho) = V_p \quad \text{for } 0 \le \rho \le r_2 \tag{3.36}$$

In order to make Eqns.(3.34,3.35,3.36) solvable, we need to use one of the orthogonal properties of the Bessel function,[5] that is

$$\int_0^R \rho\mathcal{J}_0(\lambda'\rho)\mathcal{J}_0(\lambda\rho)d\rho = \begin{cases} \frac{R^2}{2}[\mathcal{J}_0(\lambda R)]^2 & \text{for } \lambda = \lambda' \\ 0 & \text{for } \lambda \ne \lambda' \end{cases} \tag{3.37}$$

if λR and $\lambda' R$ are the roots of $\mathcal{J}_0'(x) = -\mathcal{J}_1(x) = 0$. It might be noted that the choice of λR or $\lambda' R$ to be the root of $\mathcal{J}_1(x) = 0$ instead of $\mathcal{J}_0(x) = 0$ is for applying the result in Eqn.(3.23).

Multiplying the both sides on Eqn. (3.34) by $\rho\mathcal{J}_0(k_{m'}^{(1)}\rho)$ for $m' = 0, 1, 2, ...$ and integrating them from $\rho = 0$ to $\rho = r_1$, we obtain[6]

$$\sigma^{(1)}A_0^{(1)}\int_0^{r_1} \rho d\rho = \sigma^{(2)}A_0^{(2)}\int_0^{r_2} \rho d\rho \quad \text{for } m' = 0 \tag{3.38}$$

[5] Refer to Gray and Mathews [54], pp.14–16 and 91.

[6] Note $k_0^{(1)} = k_0^{(2)} = 0$ and $\mathcal{J}_0(0) = 1$.

which gives

$$A_0^{(2)} = I_0/\sigma^{(2)}\pi r_2^2 \tag{3.39}$$

and

$$\begin{aligned}\sigma^{(1)}A_m^{(1)}k_m^{(1)}[\mathcal{J}_0(k_m^{(1)}r_1)]^2 r_1^2/2 &= \sigma^{(2)}A_0^{(2)}\int_0^{r_2}\rho\mathcal{J}_0(k_m^{(1)}\rho)d\rho \\ &+\sum_{n=1}^{\infty}\sigma^{(2)}k_n^{(2)}(A_n^{(2)}-B_n^{(2)})\int_0^{r_2}\rho\mathcal{J}_0(k_m^{(1)}\rho)\mathcal{J}_0(k_n^{(2)}\rho)d\rho \\ &\text{for } m=m'=1,2,... \end{aligned}\tag{3.40}$$

according to the orthogonal property of the Bessel functions. In a similar way, multiplying each side of Eqns. (3.35,3.36) by $\rho\mathcal{J}_0(k_{n'}^{(2)}\rho)$ for $n' = 0,1,2,...$ and integrating them from $\rho = 0$ to $\rho = r_2$, we get

$$(A_n^{(2)} + B_n^{(2)})[\mathcal{J}_0(k_n^{(2)}r_2)]^2 r_2^2/2 = \sum_{m=1}^{\infty} A_m^{(1)}\int_0^{r_2}\rho\mathcal{J}_0(k_n^{(2)}\rho)\mathcal{J}_0(k_m^{(1)}\rho)d\rho \quad \text{for } n=n'=1,2,... \tag{3.41}$$

$$(A_n^{(2)}e^{k_n^{(2)}d} + B_n^{(2)}e^{-k_n^{(2)}d})[\mathcal{J}_0(k_n^{(2)}r_2)]^2 r_2^2/2 = 0 \quad \text{for } n=n'=1,2,... \tag{3.42}$$

$$V_0^{(1)} - V_0^{(2)} = -(r_2^2/2)^{-1}\sum_{m=1}^{\infty} A_m^{(1)}\int_0^{r_2}\rho\mathcal{J}_0(k_m^{(1)}\rho)d\rho \quad \text{for } n'=0 \tag{3.43}$$

$$A_0^{(2)}d + V_0^{(2)} = V_p \quad \text{for } n'=0 \tag{3.44}$$

Equations (3.40)–(3.42) can further be written into the matrix forms

$$[A^{(1)}] = [C] + [M_{12}]([A^{(2)}] - [B^{(2)}]) \tag{3.45}$$

$$[A^{(2)}] + [B^{(2)}] = [M_{21}][A^{(1)}] \tag{3.46}$$

$$[A^{(2)}] = -[D][B^{(2)}] \tag{3.47}$$

where $[A^{(1)}] = [A_1^{(1)}, A_2^{(1)}, ...]^T$, $[A^{(2)}] = [A_1^{(2)}, A_2^{(2)}, ...]^T$ and $[B^{(2)}] = [B_1^{(2)}, B_2^{(2)}, ...]^T$ are the unknowns with the superscript T denoting the matrix transpose; the remaining matrices are known with the elements given by

$$C(m,1) = 2\frac{\sigma^{(2)}A_0^{(2)}}{\sigma^{(1)}k_m^{(1)}}\frac{\int_0^{r_2}\rho\mathcal{J}_0(k_m^{(1)}\rho)d\rho}{r_1^2[\mathcal{J}_0(k_m^{(1)}r_1)]^2} \tag{3.48}$$

$$M_{12}(m,n) = 2\frac{\sigma^{(2)}k_n^{(2)}}{\sigma^{(1)}k_m^{(1)}}\frac{\int_0^{r_2}\rho\mathcal{J}_0(k_m^{(1)}\rho)\mathcal{J}_0(k_n^{(2)}\rho)d\rho}{r_1^2[\mathcal{J}_0(k_m^{(1)}r_1)]^2} \tag{3.49}$$

$$M_{21}(n,m) \;=\; 2\frac{\int_0^{r_2} \rho \mathcal{J}_0(k_n^{(2)}\rho)\mathcal{J}_0(k_m^{(1)}\rho)d\rho}{r_2^2[\mathcal{J}_0(k_n^{(2)}r_2)]^2} \tag{3.50}$$

$$D(n,n) \;=\; diagonal\, e^{-2k_n^{(2)}d} \tag{3.51}$$

Substituting Eqn. (3.47) into Eqns. (3.45,3.46) yields a system of linear equations

$$\begin{pmatrix} [I] & [M_{12}]([I]+[D]) \\ -[M_{21}]([I]-[D])^{-1} & [I] \end{pmatrix} \begin{pmatrix} [A^{(1)}] \\ [B^{(2)}] \end{pmatrix} = \begin{pmatrix} [C] \\ [0] \end{pmatrix} \tag{3.52}$$

where $[I]$ represents the unit matrix and $[0]$ the null matrix. Equation (3.52) can be solved for $[A^{(1)}]$ and $[B^{(2)}]$ by any standard algorithm,[7] and then $[A^{(2)}]$ is determined from Eqn. (3.47).

Now let us look at Eqns.(3.43,3.44). Since the potential is relative we have freedom to choose a reference potential. If V_p is given, then

$$V_0^{(2)} \;=\; V_p - A_0^{(2)}d \tag{3.53}$$

$$V_0^{(1)} \;=\; V_0^{(2)} - (r_2^2/2)^{-1}\sum_{m=1}^{\infty} A_m^{(1)} \int_0^{r_2} \rho\mathcal{J}_0(k_m^{(1)}\rho)d\rho \tag{3.54}$$

If instead we put the term $V_0^{(2)} = 0$, we have

$$V_p \;=\; A_0^{(2)}d \tag{3.55}$$

$$V_0^{(1)} \;=\; -(r_2^2/2)^{-1}\sum_{m=1}^{\infty} A_m^{(1)} \int_0^{r_2} \rho\mathcal{J}_0(k_m^{(1)}\rho)d\rho \tag{3.56}$$

Either set of the solutions together with the solved unknown coefficients will give a particular solution of the problem. For our purpose, we chose the second set of the solutions because this leads to more favourable boundary conditions for numerical computations later on.

We note that the dimension of the linear equation system of Eqn. (3.52) is infinite because the number of the harmonics expanded is theoretically infinite. For computations the number must be truncated, say the first M expansions in the cathode region and the first N in the plasma region. However the truncated numerical results suffer

[7]We used a routine based on the least squares solution [55].

from the so-called relative convergence problem, that is a stable solution depends on a ratio of N/M for a certain value of M. Some investigations have been carried out and finally $M = 150$ and $N = 30$ were chosen to obtain a stable numerical solution with a smaller computation.

For our purpose we fixed $\sigma^{(1)} = 10^7 (1/\Omega \cdot m)$, the order of the conductivity of copper, and let $\sigma^{(2)}/\sigma^{(1)} = 10^{-1}, 10^{-2}, 10^{-3}$ and 10^{-4} respectively. It was found that the current densities $j_z^{(1,2)}(\rho, 0)$ and $j_\rho^{(1)}(\rho, 0)$ were almost unchanged but $j_\rho^{(2)}(\rho, 0)$ decreased linearly with a decrease in the ratio of $\sigma^{(2)}/\sigma^{(1)}$. For clarity only the results for $\sigma^{(2)}/\sigma^{(1)} = 10^{-1}$ are shown in Fig.3.2, where the current densities are normalized by the average spot current density $j_a = I_0/\pi r_2^2$, and the associated current flow pattern is illustrated in Fig.3.3. Considering $E_\rho^{(2)} = E_\rho^{(1)}$ or $j_\rho^{(2)}/\sigma^{(2)} = j_\rho^{(1)}/\sigma^{(1)}$ and the magnitude of $j_\rho^{(1)}$ is the order of that of $j_z^{(1,2)}$ at the interface, we have $j_\rho^{(2)}(\rho, 0) \propto j_z^{(2)}(\rho, 0)\sigma^{(2)}/\sigma^{(1)}$ for $\rho < r_2$. This implies that for the small ratio of $\sigma^{(2)}/\sigma^{(1)}$ the transverse current density on the plasma side of the interface could be ignored as compared with the normal current density. Hence we could approximate the boundary condition $E_t^{(2)} = 0$ or $V^{(2)} = 0$ on the plasma side of the interface and solve the boundary value problem independently for the plasma column itself, and then take the normal current density determined on the plasma side of the interface as the known boundary condition on the cathode side to solve the boundary problem for the cathode separately. To demonstrate this approach, we apply it to the 2D problem.

Firstly, imposing the boundary conditions

$$V^{(2)}(\rho, 0) = 0 \quad \text{for } \rho \le r_2 \tag{3.57}$$

$$V^{(2)}(\rho, d) = V_p \quad \text{for } \rho \le r_2 \tag{3.58}$$

upon Eqn.(3.27), we get

$$V_0^{(2)} + \sum_{n=1}^{\infty} \left(A_n^{(2)} + B_n^{(2)}\right) \mathcal{J}_0(k_n^{(2)}\rho) = 0 \tag{3.59}$$

$$V_0^{(2)} + A_0^{(2)} d + \sum_{n=1}^{\infty} \left(A_n^{(2)} e^{k_n^{(2)} d} + B_n^{(2)} e^{-k_n^{(2)} d}\right) \mathcal{J}_0(k_n^{(2)}\rho) = V_p \tag{3.60}$$

Multiplying $\rho \mathcal{J}_0(k_{n'}^{(2)}\rho)$ for $n' = 0, 1, 2, ...$ and taking integrations over $0 \le \rho \le r_2$ with respect to ρ gives

$$\frac{r_2^2}{2}V_0^{(2)} = 0 \tag{3.61}$$

$$V_0^{(2)} + A_0^{(2)}d = V_p \tag{3.62}$$

for $n' = 0$, and

$$\frac{r_2^2}{2}[\mathcal{J}_0(k_n^{(2)}r_2)]^2\left(A_n^{(2)} + B_n^{(2)}\right) = 0 \tag{3.63}$$

$$\frac{r_2^2}{2}[\mathcal{J}_0(k_n^{(2)}r_2)]^2\left(A_n^{(2)}e^{k_n^{(2)}d} + B_n^{(2)}e^{-k_n^{(2)}d}\right) = 0 \tag{3.64}$$

for $n' = 1, 2, ...$, according to the orthogonal property of the Bessel function. Obviously, the solution is

$$\begin{aligned} V_0^{(2)} &= 0 \\ V_p &= A_0^{(2)}d \\ A_n^{(2)} &= B_n^{(2)} = 0 \quad \text{for } n = 1, 2, ... \end{aligned} \tag{3.65}$$

thus

$$V^{(2)}(\rho, z) = A_0^{(2)}z \tag{3.66}$$

$$j_z^{(2)}(\rho, z) = -\sigma^{(2)}A_0^{(2)} \tag{3.67}$$

which means $j_z^{(2)}$ is a constant so that for a given current I_0,

$$j_z^{(2)}(\rho, z) = -\frac{I_0}{\pi r_2^2} \tag{3.68}$$

$$A_0^{(2)} = \frac{I_0}{\sigma^{(2)}\pi r_2^2} \tag{3.69}$$

Secondly, applying the boundary condition

$$j_z^{(1)}(\rho, 0) = \begin{cases} j_z^{(2)}(\rho, 0) & \text{for } 0 \le \rho \le r_2 \\ 0 & \text{for } r_2 < \rho \le r_1 \end{cases} \tag{3.70}$$

to Eqn.(3.28), we obtain

$$\sigma^{(1)}\left[A_0^{(1)} + \sum_{m=1}^{\infty} A_m^{(1)}k_m^{(1)}\mathcal{J}_0(k_m^{(1)}\rho)\right] = \begin{cases} \sigma^{(2)}A_0^{(2)} & \text{for } 0 \le \rho \le r_2 \\ 0 & \text{for } r_2 < \rho \le r_1 \end{cases} \tag{3.71}$$

Similarly, multiplying $\rho\mathcal{J}_0(k_{m'}^{(1)}\rho)$ for $m' = 0, 1, 2, ...$ and taking integrations over $0 \le \rho \le r_1$ with respect to ρ yield

$$\sigma^{(1)}A_0^{(1)}\frac{r_1^2}{2} = \sigma^{(2)}A_0^{(2)}\frac{r_2^2}{2} \tag{3.72}$$

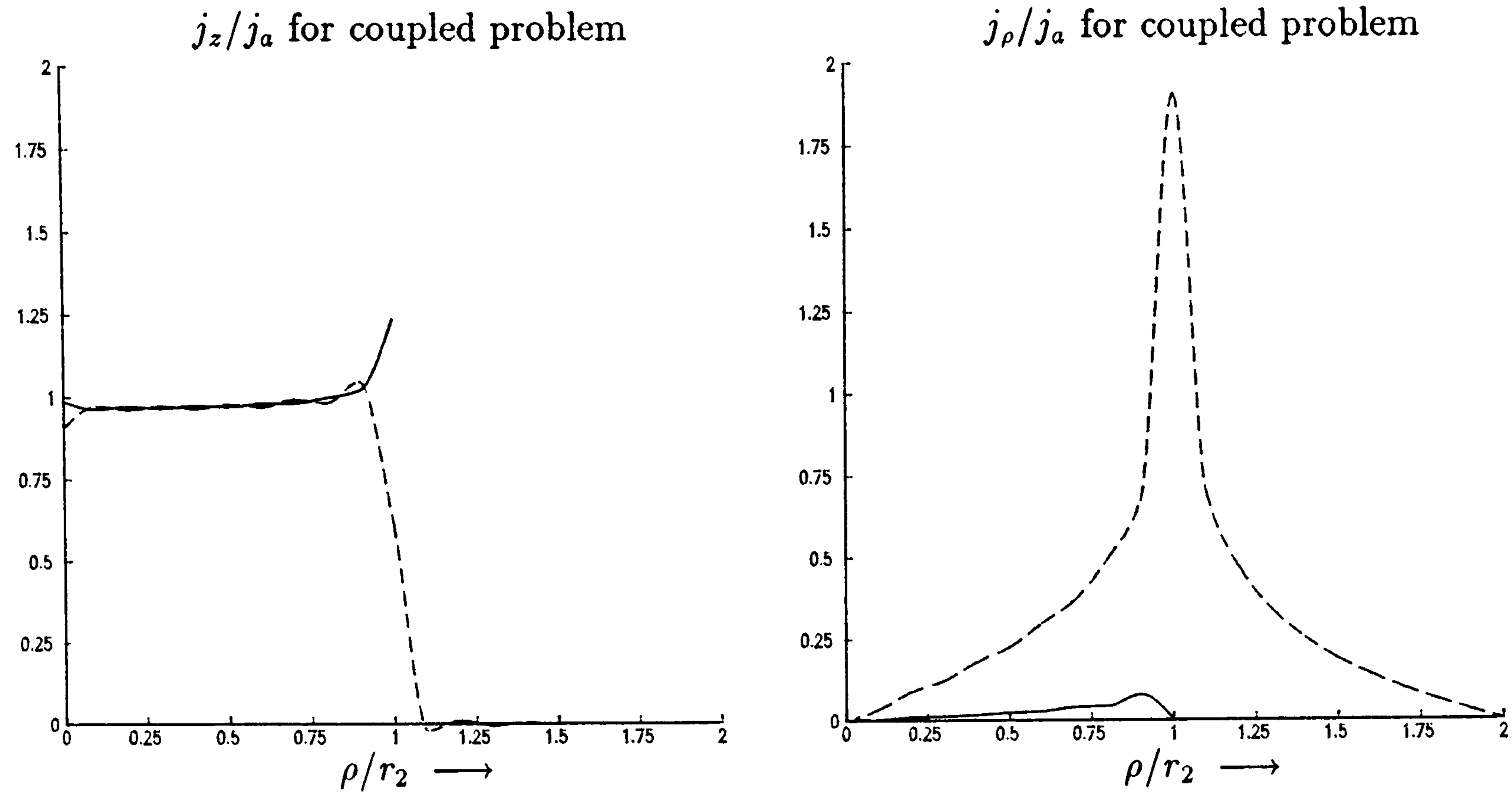

Figure 3.2: Current densities on the interface for the coupled problem
Real lines : current densities on the plasma side
Broken lines : current densities on the cathode side

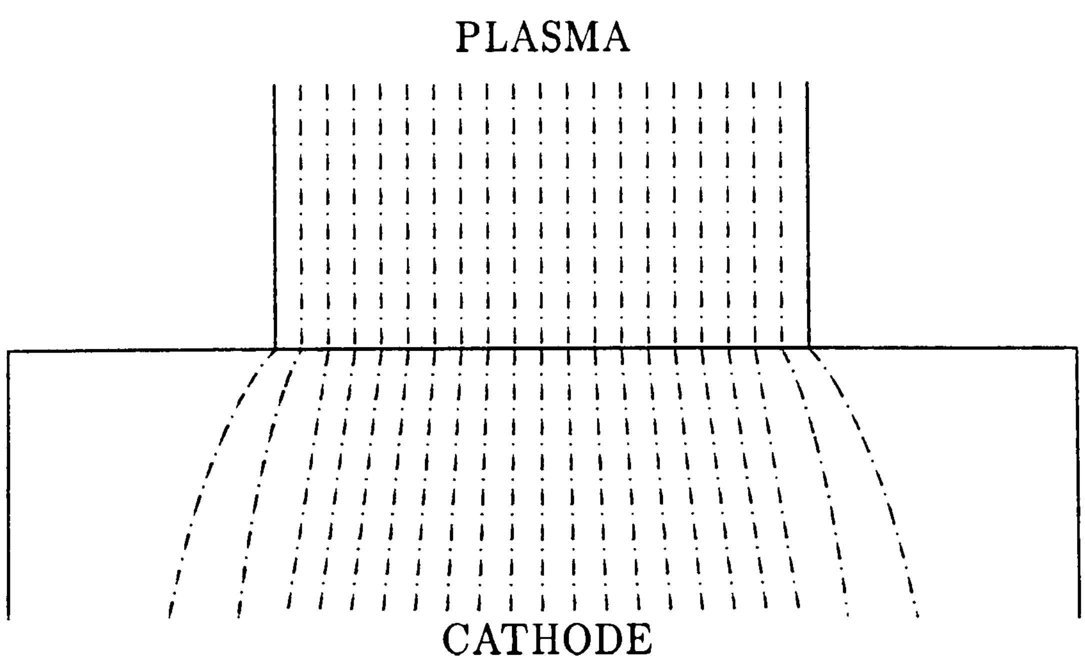

Figure 3.3: Current flow pattern (not to scale)

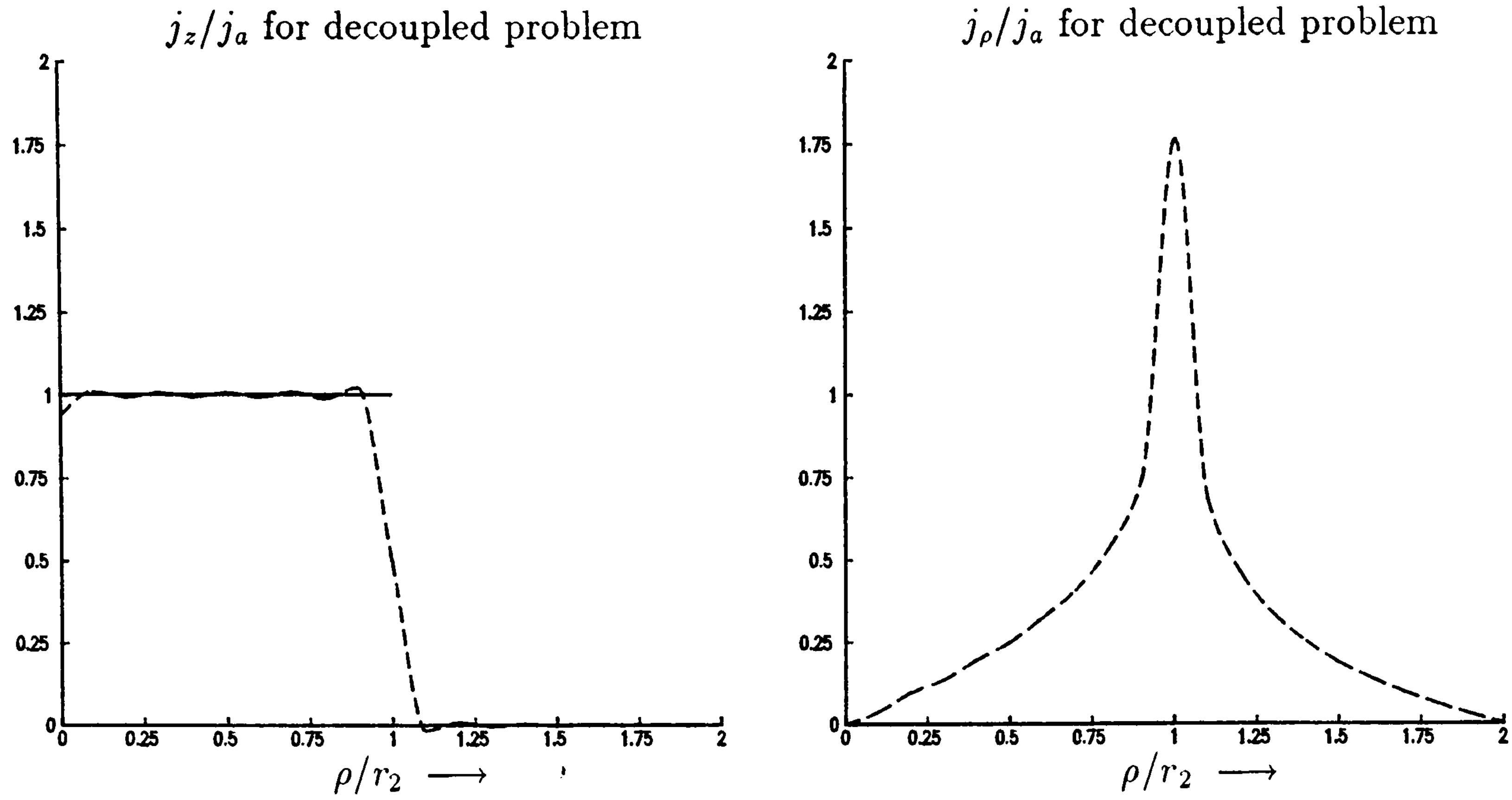

Figure 3.4: Current densities on the interface for the decoupled problem
Real lines : current densities on the plasma side
Broken lines : current densities on the cathode side

$$\sigma^{(1)} A_m^{(1)} k_m^{(1)} \frac{r_1^2}{2} [\mathcal{J}_0(k_m^{(1)} r_1)]^2 = \sigma^{(2)} A_0^{(2)} \int_0^{r_2} \rho \mathcal{J}_0(k_m^{(1)} \rho) d\rho \tag{3.73}$$

which result in

$$A_0^{(1)} = \frac{I_0}{\sigma^{(1)} \pi r_1^2} \tag{3.74}$$

$$A_m^{(1)} = \frac{2\sigma^{(2)} A_0^{(2)}}{\sigma^{(1)} r_1^2 [\mathcal{J}_0(k_m^{(1)} r_1)]^2 k_m^{(1)}} \int_0^{r_2} \rho \mathcal{J}_0(k_m^{(1)} \rho) d\rho \quad \text{for } m = 1, 2, ... \tag{3.75}$$

thus we solved the boundary problem of the cathode itself.

The computed results based on the decoupling approach are shown in Fig.3.4 where one can see clearly as compared with Fig.3.2 that the results obtained by this approch are almost the same as those determined from the coupled problem. Therefore the decoupling approach is valid as it would be expected and we can deal with two separate

3D boundary value problems, namely, for the plasma column :

$$\begin{aligned}
\nabla^2 V(\mathbf{r}) &= 0 \qquad \text{in the plasma column} \\
V(\mathbf{r}) &= \begin{cases} 0 & \text{on the spot interface} \\ V_p & \text{at a distant plasma cross-section} \end{cases} \\
\frac{\partial V(\mathbf{r})}{\partial n} &= 0 \qquad \text{on the column boundary}
\end{aligned} \tag{3.76}$$

and for the cathode :

$$\begin{aligned}
\nabla^2 V(\mathbf{r}) &= 0 \qquad \text{in the cathode} \\
\frac{\partial V(\mathbf{r})}{\partial n} &= Q(\mathbf{r}) \quad \text{on the closing boundary}
\end{aligned} \tag{3.77}$$

where Q, the directional derivative of the potential on the boundary, is supposed to be known. The problem of (3.76) is the mixed boundary value problem while the problem of (3.77) is the second boundary value problem (Neumann problem). We note that the problem of (3.77) still has infinitely many solutions. That is, Eqn. (3.77) involves the derivatives only, so that $V(\mathbf{r})$ can be altered by an additive constant. To make the solution unique, a reference potential must be fixed.

3.3 Integral Equations

Even with the decoupled boundary conditions an analytical solution of our problem is still difficult to be obtained mainly because of the irregular plasma boundaries.

The solution of field problems by conformal mapping is an analytical approach which has been extensively used. It is based on the properties of analytical complex functions and thus can only be applied to problems which can be reduced to Laplace's equation in a two-dimensional region. Clearly, this approach is not adoptable to solve our 3D boundary value problem.

The so-called method of separation of variables, which leads to series solutions, can be considered as being more general than the other analytical methods. But it suffers from severe restrictions essentially related to the treatment of the boundary and interface conditions. In practice, its use requires the existence of a suitable coordinate system, which must fulfil two conditions: (i) every boundary or interface surface must coincide with an equi-coordinate surface; (ii) the coordinate system must allow the separation of variables. Both these conditions are rarely satisfied in our plasma problem.

Another approach is that of the integral equation. Most differential equations together with their boundary conditions may be reformulated to give a single integral equation. If the latter can be solved, the mathematical difficulties are not appreciably greater even when the number of independent variables is increased, while differential equations, such as Laplace's, are considerably more complex in three dimensions than in two. Therefore we express our problem in terms of the integral equation [58]

$$cV(\mathbf{r}) = \int_{\Gamma} \left(G(\mathbf{r},\mathbf{r}')\frac{\partial V}{\partial n} - V\frac{\partial G(\mathbf{r},\mathbf{r}')}{\partial n} \right) d\Gamma \tag{3.78}$$

where Γ is a surface enclosing a homogeneous region τ and

$$c = \begin{cases} 1 & \text{if } \mathbf{r} \text{ is inside } \tau \\ 0 & \text{if } \mathbf{r} \text{ is outside } \tau \\ \frac{1}{2} & \text{if } \mathbf{r} \text{ is on } \Gamma \text{ (smooth)} \end{cases}$$

$G(\mathbf{r},\mathbf{r}')$ is the Green function which, in general, is the solution of Poisson's equation

$$\nabla^2 G(\mathbf{r},\mathbf{r}') = -\delta(\mathbf{r}-\mathbf{r}') \tag{3.79}$$

subject to boundary conditions, where δ indicates the Dirac delta function [56]. In free (unbounded) space the Green function is given by

$$G(\mathbf{r},\mathbf{r}') = \frac{1}{4\pi\,|\mathbf{r}-\mathbf{r}'|} \tag{3.80}$$

Notice that in Eqns.(3.78) the directional derivative $\partial/\partial n$ is along the direction of the outward normal $\mathbf{n}$ of Γ and with respect to $\mathbf{r}'$. Obviously, if $\partial V/\partial n$ and V are known over the whole boundary, the solution of the potential inside the region can be found with the free Green function of (3.80).

For the plasma column, however, neither $\partial V/\partial n$ nor V are known everywhere on Γ and it is also not easy (may be impossible) to find a particular Green function which vanishes on both the spot interface and the distant plasma cross-section as well as whose normal derivative vanishes on the flexible column boundary so as to get an exact analytical solution. Hence we have to find the remaining unknown boundary values of the plasma column through another approach, which will be discussed in the next chapter.

For the cathode, to solve the problem of Eqn. (3.77) by the integral equation we must eliminate the surface integral involving V on the R.H.S. of Eqn. (3.78). This can be done by requiring that $\partial G/\partial n$ be constant over Γ and by imposing

$$\int_\Gamma V\, d\Gamma = 0 \tag{3.81}$$

instead of a fixed reference potential for the unique solution [57]. Thus, Eqn. (3.78) reduces to

$$cV(\mathbf{r}) = \int_\Gamma G(\mathbf{r},\mathbf{r}')\frac{\partial V}{\partial n}\, d\Gamma \tag{3.82}$$

where the Green function is the solution of

$$\begin{aligned} \nabla^2 G(\mathbf{r},\mathbf{r}') &= -\delta(\mathbf{r}-\mathbf{r}') \quad \text{in } \tau \\ \frac{\partial G}{\partial n} &= \text{const.} \qquad\quad \text{on } \Gamma \end{aligned} \tag{3.83}$$

Since the spot radius ($r_0 \leq 10^{-3}cm$ [21]) is much smaller than the cathode dimensions, the cathode boundary planes except for the $z = 0$ plane seem to be located at infinity in comparison with the spot dimension. Furthermore, we are only interested in the fields around the spot. Thus the problem of (3.83) can be approximated by

$$\begin{aligned} \nabla^2 G(\mathbf{r},\mathbf{r}') &= -\delta(\mathbf{r}-\mathbf{r}') \quad \text{in half space } z < 0 \\ \frac{\partial G}{\partial n} &= \text{const.} \qquad\quad \text{on } z = 0 \text{ plane} \end{aligned} \tag{3.84}$$

and the solution is

$$G(\mathbf{r},\mathbf{r}') = \frac{1}{4\pi}\left(\frac{1}{|\mathbf{r}-\mathbf{r}'|} + \frac{1}{|\mathbf{r}-\mathbf{r}'_*|}\right) \tag{3.85}$$

where $\mathbf{r}'_* = \mathbf{r}' - 2(\mathbf{r}'\cdot\mathbf{a}_z)\mathbf{a}_z$, the image of $\mathbf{r}'$ with respect to $z = 0$ plane. For our formulation, from now on we denote the cathode potential by $V^\dagger$ to distinguish it from the plasma potential V. Then the potential of the cathode is finally given by

$$cV^\dagger(\mathbf{r}) = \frac{1}{4\pi}\int_{spot}\left(\frac{1}{|\mathbf{r}-\mathbf{r}'|} + \frac{1}{|\mathbf{r}-\mathbf{r}'_*|}\right)\frac{\partial V^\dagger}{\partial n}\, d\Gamma \tag{3.86}$$

because $\partial V^\dagger/\partial n = 0$ on $z = 0$ plane everywhere except for the spot, on which

$$\frac{\partial V^\dagger}{\partial n} = \frac{\sigma_p}{\sigma_c}\frac{\partial V}{\partial n} \tag{3.87}$$

where σ_p and σ_c represent the conductivities of the plasma and the cathode, respectively. Evidently once $\partial V/\partial n$ on the spot is found through the plasma problem, $V^{\dagger}(\mathbf{r})$ of the cathode is fixed. We shall solve the plasma problem by the boundary element method (BEM).

Appendix 3.1

McMahon's method[8] of calculating the zeros of $\mathcal{J}_n(\alpha)$ and $\mathcal{J}_n'(\alpha)$:

(i) The general formula for the mth root of $\mathcal{J}_n(\alpha) = 0$ is

$$\begin{aligned} \alpha_m^{(n)} &= a - \frac{c-1}{8a} - \frac{4(c-1)(7c-31)}{3(8a)^3} \\ &\quad - \frac{32(c-1)(83c^2-982c+3779)}{15(8a)^5} + \cdots \end{aligned} \tag{3.88}$$

where $c = 4n^2$ and $a = \dfrac{1}{4}\pi(2n-1+4m)$.

(ii) The general formula for the mth root of $\mathcal{J}_n'(\alpha) = 0$ is

$$\begin{aligned} \alpha_m^{(n)} &= b - \frac{c+3}{8b} - \frac{4(7c^2+82c-9)}{3(8b)^3} \\ &\quad - \frac{32(83c^3+2075c^2-3039m+3537)}{15(8b)^5} + \cdots \end{aligned} \tag{3.89}$$

where $c = 4n^2$ and $b = \dfrac{1}{4}\pi(2n+1+4m)$.

[8] From page 79 of the book by Gray and Mathews [54]

Chapter 4

Boundary Element Method Formulation

4.1 General Approach

Discretizing the boundary Γ into M boundary elements denoted by Γ_m $(m = 1, 2, \cdots, M)$, Eqn.(3.78) becomes

$$cV(\mathbf{r}) = \sum_{m=1}^{M} \int_{\Gamma_m} \left(G(\mathbf{r}, \mathbf{r}')\frac{\partial V}{\partial n} - V\frac{\partial G(\mathbf{r}, \mathbf{r}')}{\partial n} \right) d\Gamma_m \tag{4.1}$$

where the Green function is given by Eqn. (3.80). Arranging N sampled points (nodes) over the boundary, located by $\mathbf{r}_i$ $(i = 1, 2, \cdots, N)$; indicating the boundary values associated by V_i $(i = 1, 2, \cdots, N)$ and $Q_i = \partial V_i/\partial n$ $(i = 1, 2, \cdots, N)$; representing the boundary values over each boundary element by the interpolation according to the node boundary values within it; letting $V(\mathbf{r})$ on the L.H.S of Eqn.(4.1) take the values at these sampled points, namely $V(\mathbf{r}_i) = V_i$ $(i = 1, 2, \cdots, N)$; a system of linear equations can be arrived at

$$\begin{pmatrix} H_{11} & H_{12} & \cdots & H_{1N} \\ H_{21} & H_{22} & \cdots & H_{2N} \\ \vdots & \vdots & \vdots & \vdots \\ H_{N1} & H_{N2} & \cdots & H_{NN} \end{pmatrix} \begin{pmatrix} V_1 \\ V_2 \\ \vdots \\ V_N \end{pmatrix} = \begin{pmatrix} K_{11} & K_{12} & \cdots & K_{1N} \\ K_{21} & K_{22} & \cdots & K_{2N} \\ \vdots & \vdots & \vdots & \vdots \\ K_{N1} & K_{N2} & \cdots & K_{NN} \end{pmatrix} \begin{pmatrix} Q_1 \\ Q_2 \\ \vdots \\ Q_N \end{pmatrix} \tag{4.2}$$

The determination of the matrix elements H_{ij}, K_{ij} is discussed later on and here we suppose that they all are known. Because our boundary value problem is the mixed type, i.e., the boundary values of the potential are only known over one part of Γ while the boundary values of its normal derivative are only known on the remainder part, Eqn.(4.2) is so rearranged

$$\begin{pmatrix} -[K]_{11} & [H]_{12} \\ -[K]_{21} & [H]_{22} \end{pmatrix} \begin{pmatrix} [Q]_1 \\ [V]_2 \end{pmatrix} = \begin{pmatrix} [K]_{12}[Q]_2 - [H]_{11}[V]_1 \\ [K]_{22}[Q]_2 - [H]_{21}[V]_1 \end{pmatrix} \tag{4.3}$$

where $[V]_1 = [V_1, V_2, \cdots, V_{N'}]^T$ and $[Q]_2 = [Q_{N'+1}, Q_{N'+2}, \cdots, Q_N]^T$ are known, whereas $[V]_2 = [V_{N'+1}, V_{N'+2}, \cdots, V_N]^T$ and $[Q]_1 = [Q_1, Q_2, \cdots, Q_{N'}]^T$ are the unknowns. $[K]_{i'j'}$ and $[H]_{i'j'}$ for $i', j' = 1, 2$ are the associated submatrices. Eqn.(4.3) can be written into a standard form

$$[A][X] = [C] \tag{4.4}$$

and solved by any standard algorithm.

4.2 $[H]$ and $[K]$ Matrices

For our purpose each boundary element Γ_m is chosen to be triangular and flat. The function V is supposed to be constant over elements on both the spot interface and the distant plasma cross-section, and has a linear variation over elements on the column boundary while the function $\partial V/\partial n$ is taken to be constant over all elements. This has advantages of (i) being more consistent with the prescribed boundary conditions and (ii) avoiding special treatment on the corner nodes (the common nodes of the adjacent elements between the column boundary and the spot interface or the distant plasma cross-section) where the $\partial V/\partial n$ is not unique.

The element on both the spot interface and the distant plasma cross-section has its node inside as Fig.4.1(a) shows and both of V and $\partial V/\partial n$ take their nodal values over the element, hence we have

$$\int_{\Gamma_m} V \frac{\partial G(\mathbf{r}_i, \mathbf{r}')}{\partial n} d\Gamma = V_m h_{i,m} \tag{4.5}$$

with

$$h_{i,m} = \int_{\Gamma_m} \frac{\partial G(\mathbf{r}_i, \mathbf{r}')}{\partial n} d\Gamma \tag{4.6}$$

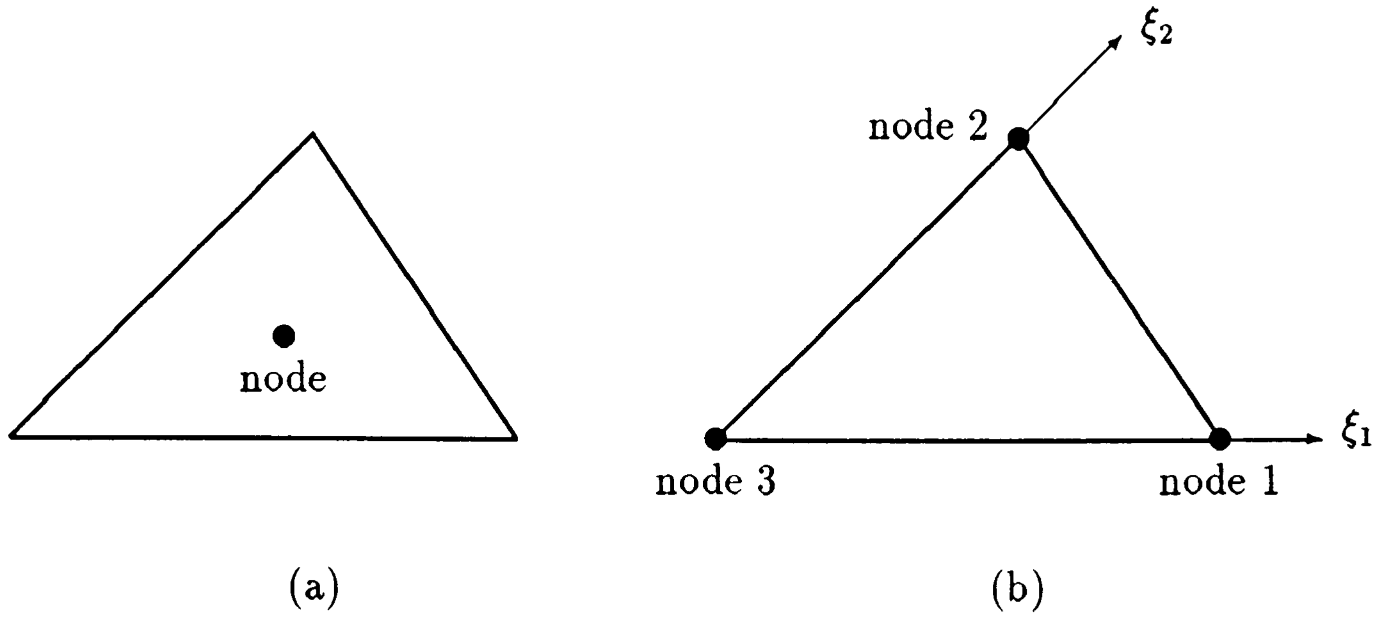

Figure 4.1: Triangular boundary elements
(a) Constant element; (b) Linear element

and

$$\int_{\Gamma_m} G(\mathbf{r}_i, \mathbf{r}') \frac{\partial V}{\partial n} d\Gamma = Q_m k_{i,m} \tag{4.7}$$

with

$$k_{i,m} = \int_{\Gamma_m} G(\mathbf{r}_i, \mathbf{r}') d\Gamma \tag{4.8}$$

where $h_{i,m}$ and $k_{i,m}$ are influence coefficients defining the interaction between the field point i interested and the node on an element m.

For the element on the column boundary, each has three nodes on its vertices as Fig.4.1(b) shown and the potential at any point on the element is defined as

$$V(\xi_1, \xi_2) = \sum_{p=1}^{3} N^p(\xi_1, \xi_2) V_m^p \tag{4.9}$$

in which V_m^p indicates the nodal potential at a local node p of an element m and $N^p(\xi_1, \xi_2)$ are the interpolation functions given by

$$\begin{aligned} N^1 &= \xi_1 \\ N^2 &= \xi_2 \\ N^3 &= 1 - \xi_1 - \xi_2 \end{aligned} \tag{4.10}$$

where ξ_1 and ξ_2 are area coordinates which have values ranging from 0 to 1. Thus the surface integrals over the linear element can be written as

$$
\begin{aligned}
\int_{\Gamma_m} V\frac{\partial G(\mathbf{r}_i,\mathbf{r}')}{\partial n}d\Gamma &= \int_{\Gamma_m}\left[N^1\,N^2\,N^3\right]\frac{\partial G(\mathbf{r}_i,\mathbf{r}')}{\partial n}d\Gamma\begin{bmatrix} V_m^1 \\ V_m^2 \\ V_m^3 \end{bmatrix} \\
&= \left[h_{i,m}^1\,h_{i,m}^2\,h_{i,m}^3\right]\begin{bmatrix} V_m^1 \\ V_m^2 \\ V_m^3 \end{bmatrix} \qquad (4.11)
\end{aligned}
$$

where

$$
h_{i,m}^p = \int_{\Gamma_m} N^p\frac{\partial G(\mathbf{r}_i,\mathbf{r}')}{\partial n}d\Gamma \qquad \text{for } p = 1,2,3 \qquad (4.12)
$$

represent influence coefficients defining the interaction of the field point i under consideration with a local node p on an element m.

Denote the elements on both the spot interface and the distant plasma cross-section by $m = 1,2,\cdots,M'$ and the corresponding nodes by $i = 1,2,\cdots,N'$. Similarly, denote the elements on the column boundary by $m = M'+1, M'+2,\cdots,M$ and the nodes by $i = N'+1, N'+2,\cdots,N$. Thus for a particular field point i, Eqn. (4.1) can be written as

$$
\begin{aligned}
& c_iV_i + h_{i,1}V_1 + h_{i,2}V_2 + \cdots + h_{i,N'}V_{N'} \\
& \quad + h_{i,M'+1}^1V_{M'+1}^1 + h_{i,M'+1}^2V_{M'+1}^2 + h_{i,M'+1}^3V_{M'+1}^3 \\
& \quad + \cdots\cdots\cdots \\
& \quad + h_{i,M}^1V_M^1 + h_{i,M}^2V_M^2 + h_{i,M}^3V_M^3 \\
& \quad = k_{i,1}Q_1 + k_{i,2}Q_2 + \cdots + k_{i,N'}Q_{N'} \qquad (4.13)
\end{aligned}
$$

Note that any node on the column boundary may be a common node for two or more adjoining elements, we need to add the contribution from these elements into one term, i.e.,

$$
h_{i,j} = \sum_m\sum_p h_{i,m}^p \qquad (4.14)
$$

for those of m $(M'+1 \le m \le M)$ and p $(1 \le p \le 3)$ such that the local nodal potential V_m^p is identified with the global nodal potential V_j $(N'+1 \le j \le N)$, then Eqn.(4.13) becomes

$$\begin{aligned} c_i V_i &+ h_{i,1}V_1 + h_{i,2}V_2 + \cdots + h_{i,N'}V_{N'} \\ &+ h_{i,N'+1}V_{N'+1} + \cdots + h_{i,N}V_N \\ &= k_{i,1}Q_1 + k_{i,2}Q_2 + \cdots + k_{i,N'}Q_{N'} \end{aligned} \tag{4.15}$$

Letting $i = 1, 2, \cdots N$ in Eqn.(4.15) yields a system of equations which can be arranged into the matrix form of Eqn.(4.2) with the identities

$$H_{ij} = \begin{cases} h_{i,j} & \text{if } i \neq j \\ c_i + h_{i,j} & \text{if } i = j \end{cases} \tag{4.16}$$

$$K_{i,j} = k_{ij} \qquad \text{if } j \leq N' \tag{4.17}$$

We need not to calculate K_{ij} for $j > N'$ because $Q_j = 0$ for $j > N'$.

It has been pointed out[1] that if the surface is not smooth at the point i the $c_i = 1/2$ is no longer valid, but one can calculate the diagonal elements of $[H]$ without determining c_i by using the fact that when a uniform potential is applied on the whole body the normal derivatives must be zero. Under this condition Eqn.(4.2) becomes

$$\begin{pmatrix} H_{11} & H_{12} & \cdots & H_{1N} \\ H_{21} & H_{22} & \cdots & H_{2N} \\ \vdots & \vdots & \vdots & \vdots \\ H_{N1} & H_{N2} & \cdots & H_{NN} \end{pmatrix} \begin{pmatrix} V_1 \\ V_2 \\ \vdots \\ V_N \end{pmatrix} = \begin{pmatrix} 0 \\ 0 \\ \vdots \\ 0 \end{pmatrix} \tag{4.18}$$

where $V_1 = V_2 = \cdots = V_N$ are not zero in general. Thus the sum of all the elements of $[H]$ in a row ought to be zero, i.e.,

$$\sum_{j=1}^{N} H_{ij} = 0 \qquad \text{for } i = 1, 2, \cdots N \tag{4.19}$$

it follows

$$H_{ii} = -\sum_{j=1; j\neq i}^{N} H_{ij} \qquad \text{for } i = 1, 2, \cdots N \tag{4.20}$$

which also implies that

$$det\,[H] = 0 \tag{4.21}$$

[1]Refer to Brebbia, Telles and Wrobel [64], page 111.

because

$$det\,[H] = det \begin{pmatrix} \sum\limits_{j=1} H_{1j} & H_{12} & \cdots & H_{1N} \\ \sum\limits_{j=1} H_{2j} & H_{22} & \cdots & H_{2N} \\ \vdots & \vdots & \vdots & \vdots \\ \sum\limits_{j=1} H_{Nj} & H_{N2} & \cdots & H_{NN} \end{pmatrix} \tag{4.22}$$

Hence the diagonal elements of $[H]$ for any closed domain are always determined once the off-diagonal elements of $[H]$ are calculated according to Eqn.(4.20). The calculations of H_{ij} $(i \neq j)$ and K_{ij} $(j \leq N')$ are discussed next.

4.3 Surface Integrals

In the BEM one has to evaluate many surface integrals such as Eqns.(4.6,4.8,4.12). It is convenient to evaluate these integrals based on the local area coordinates (ξ_1, ξ_2). The global coordinates within the element are interpolated linearly by

$$\begin{aligned} x'(\xi_1,\xi_2) &= \sum_{p=1}^{3} N^p(\xi_1,\xi_2)x_m^p \\ y'(\xi_1,\xi_2) &= \sum_{p=1}^{3} N^p(\xi_1,\xi_2)y_m^p \\ z'(\xi_1,\xi_2) &= \sum_{p=1}^{3} N^p(\xi_1,\xi_2)z_m^p \end{aligned} \tag{4.23}$$

in which, see Fig.4.2, (x', y', z') represent the global coordinates of the source; (x_m^p, y_m^p, z_m^p) denote the global coordinates at the point of the vertex p on the element m which are known once the surface mesh is defined; and the interpolation functions N^p are the same as those given in Eqn. (4.10). As we know from vector algebra that the magnitude of vector cross product is equal to a value of an area associated, it follows

$$d\Gamma = |\mathbf{n}| d\xi_1 d\xi_2 \tag{4.24}$$

with the outward normal of the triangular surface

$$\mathbf{n} \;=\; \frac{\partial \mathbf{r}'}{\partial \xi_1} \times \frac{\partial \mathbf{r}'}{\partial \xi_2}$$

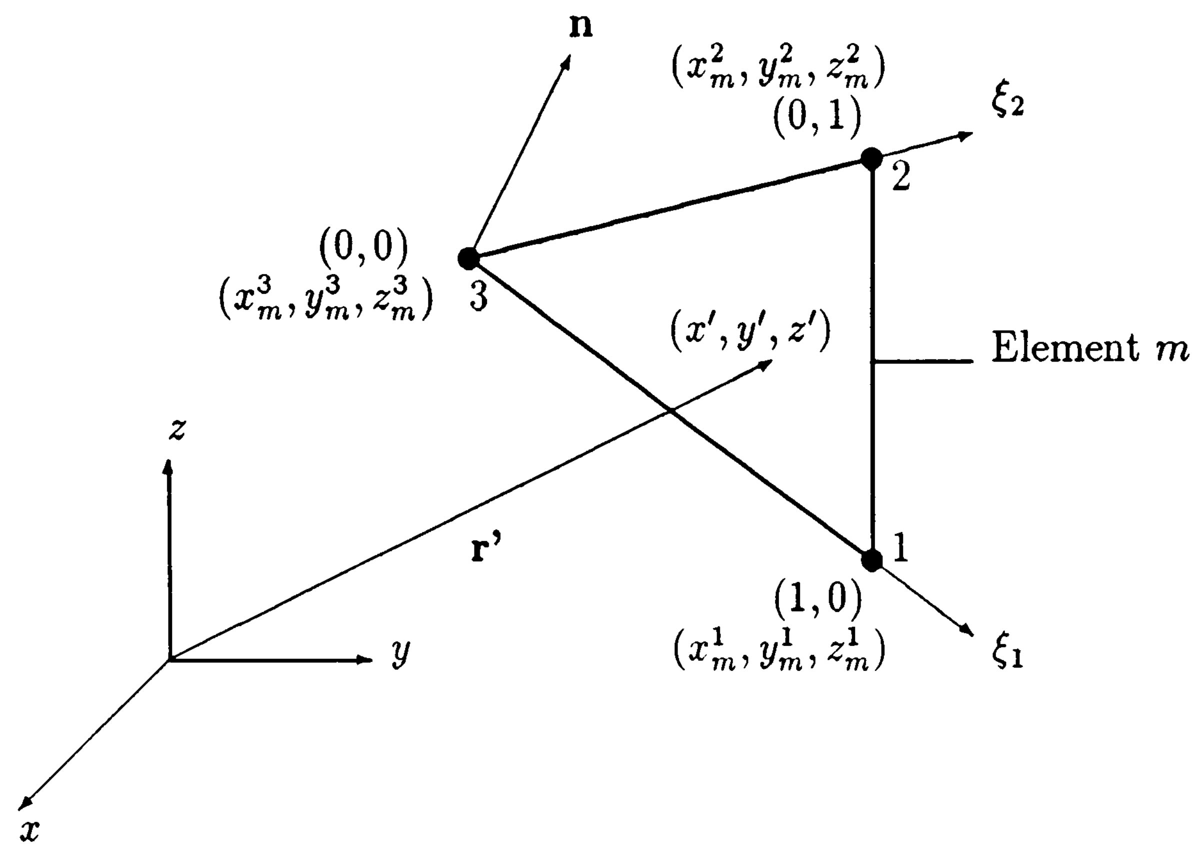

Figure 4.2: The local area coordinates of a triangular element

$$
\begin{aligned}
&= \begin{bmatrix} \mathbf{a}_x & \mathbf{a}_y & \mathbf{a}_z \\ \dfrac{\partial x'}{\partial \xi_1} & \dfrac{\partial y'}{\partial \xi_1} & \dfrac{\partial z'}{\partial \xi_1} \\ \dfrac{\partial x'}{\partial \xi_2} & \dfrac{\partial y'}{\partial \xi_2} & \dfrac{\partial z'}{\partial \xi_2} \end{bmatrix} \\
&= n_x \mathbf{a}_x + n_y \mathbf{a}_y + n_z \mathbf{a}_z
\end{aligned} \tag{4.25}
$$

Substituting Eqn.(4.23) into Eqn. (4.25) gives

$$
\begin{aligned}
n_x &= (y_m^1 - y_m^3)(z_m^2 - z_m^3) - (z_m^1 - z_m^3)(y_m^2 - y_m^3) \\
n_y &= (z_m^1 - z_m^3)(x_m^2 - x_m^3) - (x_m^1 - x_m^3)(z_m^2 - z_m^3) \\
n_z &= (x_m^1 - x_m^3)(y_m^2 - y_m^3) - (y_m^1 - y_m^3)(x_m^2 - x_m^3)
\end{aligned} \tag{4.26}
$$

so that

$$
|\mathbf{n}| = \sqrt{n_x^2 + n_y^2 + n_z^2} \tag{4.27}
$$

which is equal to the twice of the area Γ_m.

We also need to express the variables of integration of the free Green function and its normal derivative in terms of the local area coordinates, that is for a given field point i

$$G(\mathbf{r}_i,\mathbf{r}') = \frac{1}{4\pi\left\{[x_i - x'(\xi_1,\xi_2)]^2 + [y_i - y'(\xi_1,\xi_2)]^2 + [z_i - z'(\xi_1,\xi_2)]^2\right\}^{1/2}} \tag{4.28}$$

$$\begin{aligned}\frac{\partial G(\mathbf{r}_i,\mathbf{r}')}{\partial n} &= \nabla' G(\mathbf{r}_i,\mathbf{r}')\cdot\mathbf{n}_0 \\ &= \frac{[x_i - x'(\xi_1,\xi_2)]n_x + [y_i - y'(\xi_1,\xi_2)]n_y + [z_i - z'(\xi_1,\xi_2)]n_z}{4\pi|\mathbf{n}|\left\{[x_i - x'(\xi_1,\xi_2)]^2 + [y_i - y'(\xi_1,\xi_2)]^2 + [z_i - z'(\xi_1,\xi_2)]^2\right\}^{3/2}}\end{aligned} \tag{4.29}$$

where $\mathbf{n}_0$ denotes the unit normal.

So far we have transformed the surface integrals in Eqns.(4.6,4.8,4.12) into the form

$$I = \int_{\Gamma_m} \mathcal{F}(\xi_1,\xi_2)|\mathbf{n}|d\xi_1 d\xi_2$$

over a triangle of area Γ_m. This type of integral is usually evaluated using Hammer's numerical formula [59], that is

$$\int_{\Gamma_m} \mathcal{F}(\xi_1,\xi_2)|\mathbf{n}|d\xi_1 d\xi_2 = \frac{|\mathbf{n}|}{2}\sum_{s=1}^{N} w^s \mathcal{F}(\xi_1^s,\xi_2^s) \tag{4.30}$$

where ξ_1^s, ξ_2^s are the area coordinates of the s-th sampling point and w^s is the weight associated with the s-th sampling point. Values of the constants w^s, ξ_1^s, ξ_2^s for the various N are given in Appendix 4.1. The Hammer's formula is thought to be the best from the point of view of both numerical efficiency and aesthetics because its sampling points are fully symmetric with respect to the three vertices of the triangle [60].

In the BEM we not only deal with the regular integrals but have to encounter the singular or nearly singular integrals when the distance between the field and the source tends to zero. Our experience indicates that the scheme on the R.H.S. of Eqn.(4.30) is adequate for the regular integrals but not accurate enough for the singular or nearly singular integrals because only up to 13-point schemes are available. In this case, one can use the Gaussian quadrature,[2] which has much higher order schemes. Thus the L.H.S. of Eqn.(4.30) can be expressed as

$$\int_{\Gamma_m} \mathcal{F}(\xi_1,\xi_2)|\mathbf{n}|d\xi_1 d\xi_2 \;=\; |\mathbf{n}|\int_0^1\int_0^{1-\xi_1} \mathcal{F}(\xi_1,\xi_2)d\xi_1 d\xi_2$$

[2]The standard 2D Gaussian quadrature is given in Appendix 4.2.

$$= \frac{|\mathbf{n}|}{2} \sum_{s=1}^{N_s} \frac{w^s(1-\xi_1^s)}{2} \sum_{t=1}^{N_t} w^t \mathcal{F}(\xi_1^s, \xi_2^t) \tag{4.31}$$

where

$$\xi_1^s = \frac{1}{2}(1+\eta^s)$$
$$\xi_2^t = \frac{(1-\xi_1^s)}{2}(1+\eta^t)$$

where η^i $(i = s, t)$ denotes the value of the i-th Gaussian sampling point and w^i $(i = s, t)$ is the weight associated with the i-th sampling point, which are listed in Appendix 4.2.

Another way to deal with the singular or nearly singular integrals is to seek some coordinate transformations to cancel or to reduce the singular behaviour [61, 62, 63]. Suppose the field point is located at a vertex, say vertex 3, of a linear element and set up two auxiliary local coordinate systems with their origins at this vertex as Fig.4.3 shows. We deduced a coordinate transformation[3]

$$\begin{aligned} \xi_1 &= \frac{L_{23}\rho}{D}(\sin\phi_3 \cos\phi - \cos\phi_3 \sin\phi) \\ \xi_2 &= \frac{L_{31}\rho}{D} \sin\phi \end{aligned} \tag{4.32}$$

with

$$\begin{aligned} D &= L_{31} L_{23} \sin\phi_3 \\ \phi_3 &= \cos^{-1}\left(\frac{L_{23}^2 + L_{31}^2 - L_{12}^2}{2L_{23}L_{31}}\right) \end{aligned}$$

so that

$$\int_{\Gamma_m} \mathcal{F}(\xi_1, \xi_2)|\mathbf{n}| d\xi_1 d\xi_2 = \int_0^{\phi_3} \int_0^{\rho_2(\phi)} \mathcal{F}(\rho, \phi) \rho d\rho d\phi \tag{4.33}$$

where

$$\rho_2(\phi) = \frac{L_{31} \sin\phi_1}{\sin(\phi + \phi_1)}$$

[3]See Appendix 4.3 for details.

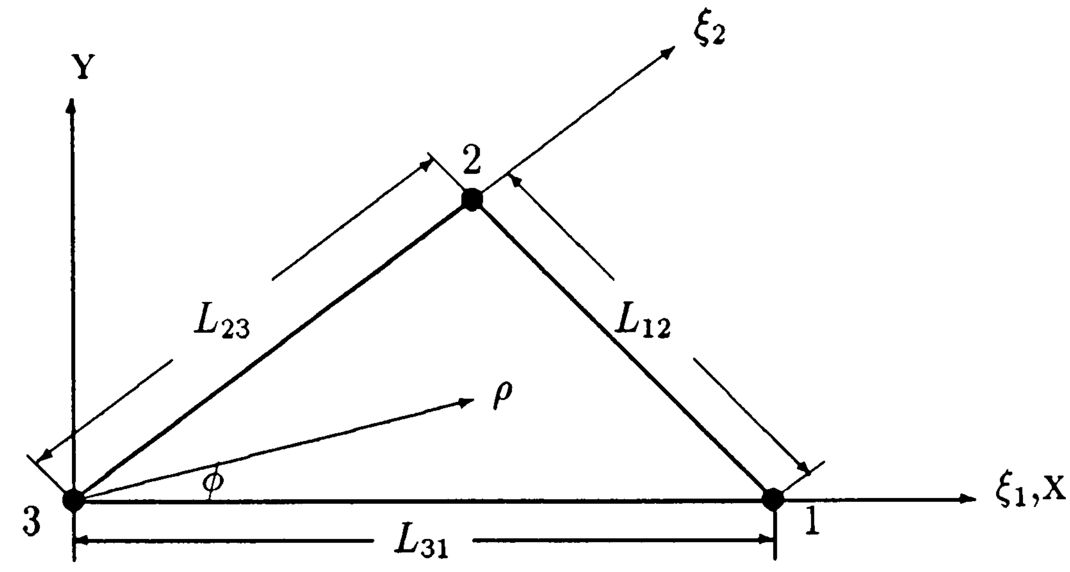

Figure 4.3: Linear element for transformation between the area and the polar coordinates

$$\phi_1 = \cos^{-1}\left(\frac{L_{31}^2 + L_{12}^2 - L_{23}^2}{2L_{31}L_{12}}\right)$$

In evidence, if $\mathcal{F}(\rho,\phi)$ is type of $1/\rho$ or $1/\rho^2$, the R.H.S. of Eqn.(4.33) will cancel or reduce the singular behaviour, which can further be evaluated using the Gaussian quadrature

$$\int_0^{\phi_3}\int_0^{\rho_2(\phi)} \mathcal{F}(\rho,\phi)\rho d\rho d\phi = \frac{\phi_3}{2}\sum_{s=1}^{N_s}\frac{w^s\rho_2(\phi^s)}{2}\sum_{t=1}^{N_t} w^t\mathcal{F}(\rho^t,\phi^s)\rho^t \tag{4.34}$$

where

$$\phi^s = \frac{\phi_3}{2}(1+\eta^s)$$

$$\rho^t = \frac{\rho_2(\phi^s)}{2}(1+\eta^t)$$

We note that in Eqns.(4.31,4.34) the number N_t of the sampling points of ξ_2 or ρ and the number N_s of the sampling points of ξ_1 or ϕ can be chosen from a wide range and they are not necessarily the same. $N = N_t \times N_s$ gives the total sampling points on the surface element over which the integration is taken. For example, $N_t = N_s = 10$ gives a 100-point scheme which is much more accurate than Hammer's 13-point scheme. Generally, the higher the sampling number, the more accurate is the numerical integration, but at the cost of the computation time. It was found worthwhile to monitor the distance from the field point to the source element (the element over which the integration is taken) and to use this information to select an appropriate integration scheme so as to ensure the accuracy and to save the CPU time as well. The distance was estimated by comparing the area of source element with the sum of areas of three triangles which are obtained by connecting three vertices of the element to the field point. Letting r_{i1}, r_{i2} and r_{i3} denote the distances from the field to the three vertices of the element while L_{12}, L_{23} and L_{31} denote the distances between the adjoining vertices, we define a ratio

$$R_A = \frac{A_\sum}{A_e} \tag{4.35}$$

where

$$\begin{aligned}
A_e &= \sqrt{a_0(a_0 - L_{12})(a_0 - L_{23})(a_0 - L_{31})} \\
A_\sum &= \sqrt{a_1(a_1 - r_{i1})(a_1 - r_{i2})(a_1 - L_{12})} \\
&+ \sqrt{a_2(a_2 - r_{i2})(a_2 - r_{i3})(a_2 - L_{23})} \\
&+ \sqrt{a_3(a_3 - r_{i3})(a_3 - r_{i1})(a_3 - L_{31})}
\end{aligned}$$

with

$$a_0 = (L_{12} + L_{23} + L_{31})/2, \quad a_1 = (r_{i1} + r_{i2} + L_{12})/2$$
$$a_2 = (r_{i2} + r_{i3} + L_{23})/2, \quad a_3 = (r_{i3} + r_{i1} + L_{31})/2$$

Thus if $R_A = 1$, the field point is inside the source element and the integral is of the singular type; if $R_A \approx 1$, the integral is of the nearly singular type; if $R_A \gg 1$, the field is far away from the element and the integral is regular. Our experience (some test examples are shown in Table.4.1 and Table.4.2) indicates that when $R_A < 1.1$ for the integrand of type $1/|\mathbf{r} - \mathbf{r}'|$ and $R_A < 1.5$ for the integrand of type $1/|\mathbf{r} - \mathbf{r}'|^2$, the higher order integration schemes should be called upon.

All the surface integrals we encountered are then evaluated numerically except for the $k_{i,i}$ in Eqn.(4.8) which contain integrable singularities and can be evaluated

Table 4.1: Test for numerical integrations‡ (Integrand = $1/4\pi|\mathbf{r}-\mathbf{r}'|$)

Scheme		$R_A = 1.0$	$R_A = 1.03$	$R_A = 1.14$
Hammer's Eqn.(4.30)	4-point	0.0220	0.0220	0.0218
	7-point	0.0234	0.0234	0.0231
	9-point	0.0233	0.0233	0.0230
	12-point	0.0240	0.0239	0.0235
Gaussian Eqn.(4.31)	2 × 2-point	0.0221	0.0221	0.0219
	3 × 3-point	0.0234	0.0233	0.0231
	4 × 4-point	0.0239	0.0239	0.0235
	5 × 5-point	0.0242	0.0241	0.0236
	10 × 10-point	0.0246	0.0245	0.0236
	15 × 15-point	0.0247	0.0245	0.0236
Gaussian Eqn.(4.34)	2 × 2-point	0.0248	0.0247	0.0244
	3 × 3-point	0.0248	0.0247	0.0241
	4 × 4-point	0.0248	0.0247	0.0239
	5 × 5-point	0.0248	0.0247	0.0237
	10 × 10-point	0.0248	0.0245	0.0236
	15 × 15-point	0.0248	0.0245	0.0236
Analytical: Eqn.(4.36)		0.0248		

‡ : The source element is fixed at vertices

(0.25,0.25,0.0), (0.0,0.5,0.0) and (0.0,0.0,0.0),

the field point has coordinates for $x = 0.0$, $y = 0.0$ and variable z.

Table 4.2: Test for numerical integrations‡ (Integrand = $1/4\pi|\mathbf{r}-\mathbf{r}'|^2$)

Scheme		$R_A = 1.0$	$R_A = 1.07$	$R_A = 1.35$
Hammer's Eqn.(4.30)	4-point	0.115	0.114	0.105
	7-point	0.157	0.156	0.127
	9-point	0.156	0.154	0.126
	12-ponit	0.189	0.184	0.132
Gaussian Eqn.(4.31)	2 × 2-point	0.117	0.117	0.107
	3 × 3-point	0.155	0.154	0.127
	4 × 4-point	0.185	0.181	0.131
	5 × 5-point	0.209	0.201	0.131
	10 × 10-point	0.289	0.232	0.130
	15 × 15-point	0.337	0.230	0.130
	20 × 20-point	0.372	0.230	0.130
Gaussian Eqn.(4.34)	2 × 2-point	0.188	0.185	0.147
	3 × 3-point	0.229	0.221	0.139
	4 × 4-point	0.260	0.241	0.131
	5 × 5-point	0.285	0.248	0.129
	10 × 10-point	0.366	0.230	0.130
	15 × 15-point	0.415	0.229	0.130
	20 × 20-point	0.450	0.230	0.130

‡ : The source element is fixed at vertices

(0.25,0.25,0.0), (0.0,0.5,0.0) and (0.0,0.0,0.0),

the field point has coordinates for $x = 0.0$, $y = 0.0$ and variable z.

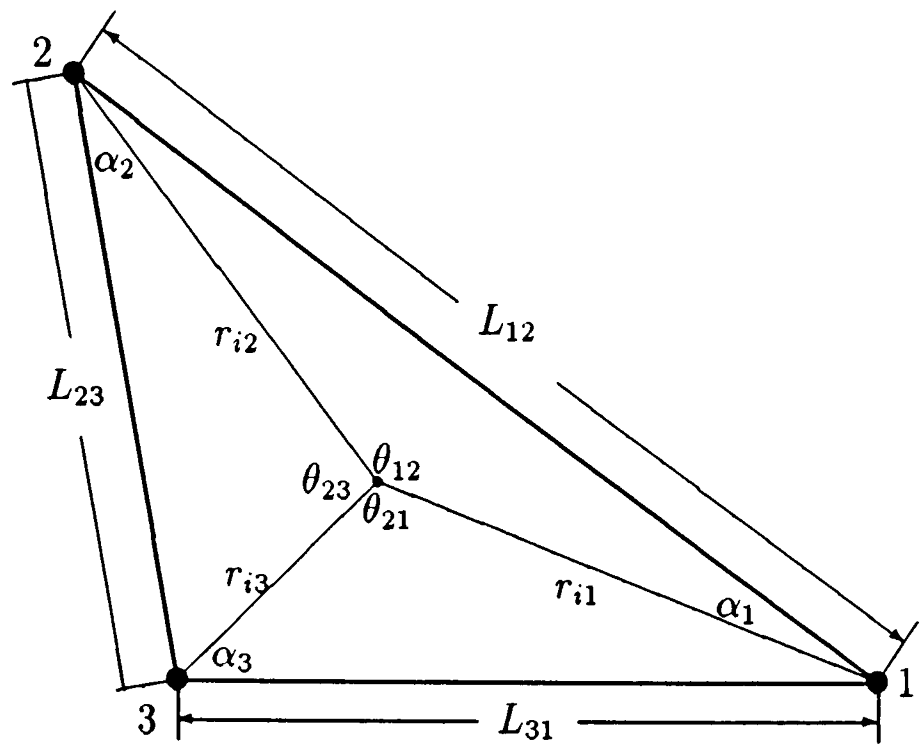

Figure 4.4: Constant element with node i inside for analytical integration

analytically [64], i.e.,

$$
\begin{aligned}
k_{i,i} &= \int_{\Gamma_i} \frac{1}{4\pi|\mathbf{r}_i - \mathbf{r}'|} d\Gamma \\
&= \frac{1}{4\pi}\left\{ r_{i1}\sin\alpha_1 \ln\left[\frac{\tan(\theta_{12}+\alpha_1)/2}{\tan\alpha_1/2}\right] + r_{i2}\sin\alpha_2 \ln\left[\frac{\tan(\theta_{23}+\alpha_2)/2}{\tan\alpha_2/2}\right] \right. \\
&\quad \left. + r_{i3}\sin\alpha_3 \ln\left[\frac{\tan(\theta_{31}+\alpha_3)/2}{\tan\alpha_3/2}\right]\right\} \qquad (4.36)
\end{aligned}
$$

where (refer to Fig.4.4)

$$
\begin{aligned}
\alpha_1 &= \cos^{-1}\left(\frac{r_{i1}^2 + L_{12}^2 - r_{i2}^2}{2r_{i1}L_{12}}\right) \\
\alpha_2 &= \cos^{-1}\left(\frac{r_{i2}^2 + L_{23}^2 - r_{i3}^2}{2r_{i2}L_{23}}\right) \\
\alpha_3 &= \cos^{-1}\left(\frac{r_{i3}^2 + L_{31}^2 - r_{i1}^2}{2r_{i3}L_{31}}\right) \\
\theta_{12} &= \cos^{-1}\left(\frac{r_{i2}^2 + r_{i1}^2 - L_{12}^2}{2r_{i2}r_{i1}}\right)
\end{aligned}
$$

$$
\begin{aligned}
\theta_{23} &= \cos^{-1}\left(\frac{r_{i2}^2 + r_{i3}^2 - L_{23}^2}{2r_{i2}r_{i3}}\right) \\
\theta_{31} &= \cos^{-1}\left(\frac{r_{i3}^2 + r_{i1}^2 - L_{31}^2}{2r_{i3}r_{i1}}\right)
\end{aligned}
$$

4.4 Surface Mesh Generation

It is obvious that without the mesh information such as the global coordinates of the vertices of surface element, the nodal coordinates and so on, the numerical analysis of our boundary-value problem cannot be carried out. Hence the mesh generation which generates all information required plays an important role in the BEM and will be presented in this section.

First we need a quantitative description of the boundary surface. This is not so straightforward because the plasma column may take many different irregular shapes. For our purpose, we assume that any cross-section along the centre axis of the plasma column is a circular area defined by four parameters, i.e., the radius $R(s)$, the inclined angle $\alpha(s)$, the centre coordinates $y_o(s)$ and $z_o(s)$ as Fig.4.5 shows. The degree of bending and deforming of the plasma column can then be defined through a set of these four parameters for $s = 1, 2, \cdots, S$. The boundary coordinates $x(s), y(s), z(s)$ around the cross-section are given by

$$
\left.
\begin{aligned}
x(s) &= R(s)\sin(\theta) \\
y(s) &= y_o(s) - R(s)\cos\alpha(s)\cos\theta \\
z(s) &= z_o(s) + R(s)\sin\alpha(s)\cos\theta
\end{aligned}
\right\} \text{ for } 0 \leq \theta \geq 2\pi \tag{4.37}
$$

The boundary coordinates between any two adjacent cross-sections can also be found from Eq. (4.37) by automatically interpolating one or more sets of medial cross-section parameters.

Next we generate our surface mesh based on the way suggested by Zienkiewicz and his co-workers [68], that is,

1. Divide the surface into several four-side (quadrilateral) zones, over each of which

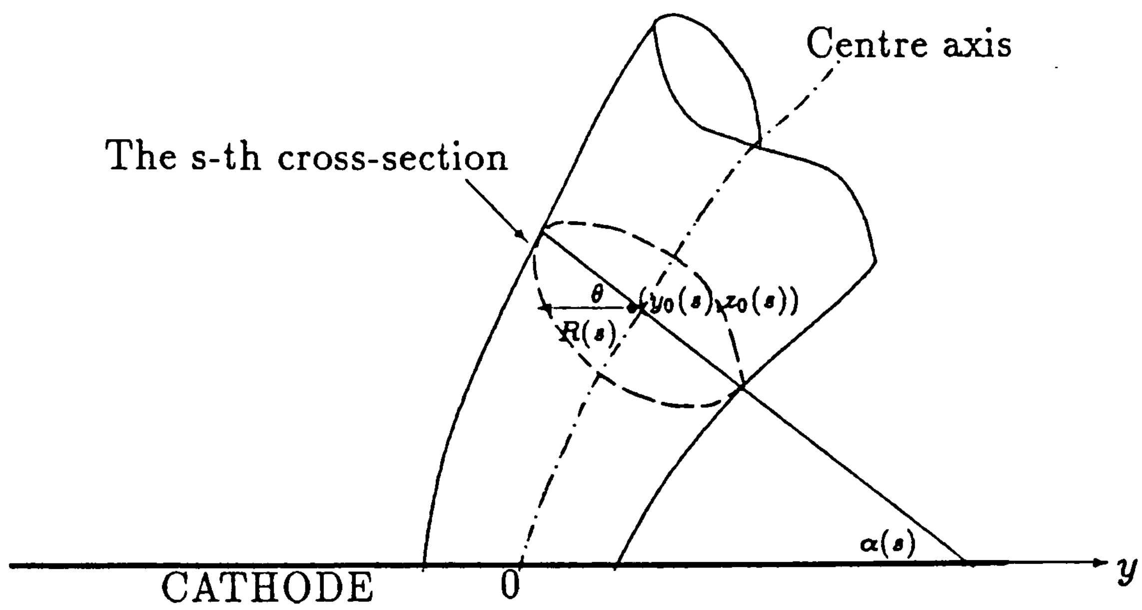

Figure 4.5: Geometry for description of the plasma column boundary

the global coordinates are interpolated according to

$$
\begin{aligned}
x &= \sum_{i=1}^{8} N_i x_i \\
y &= \sum_{i=1}^{8} N_i y_i \\
z &= \sum_{i=1}^{8} N_i z_i
\end{aligned}
\tag{4.38}
$$

in which N_i is a shape function associated with each node and defined in terms of a curve-linear coordinate system η_1 and η_2 which have values ranging from 1 to -1 on opposite sides as Fig.4.6 shows,

$$
\begin{aligned}
N_1 &= (\eta_1 - 1)(1 - \eta_2)(1 + \eta_1 + \eta_2)/4 \\
N_2 &= (1 - \eta_1^2)(1 - \eta_2)/2 \\
N_3 &= (1 + \eta_1)(1 - \eta_2)(\eta_1 - \eta_2 - 1)/4 \\
N_4 &= (1 - \eta_2^2)(1 + \eta_1)/2 \\
N_5 &= (1 + \eta_1)(1 + \eta_2)(\eta_1 + \eta_2 - 1)/4 \\
N_6 &= (1 - \eta_1^2)(1 + \eta_2)/2 \\
N_7 &= (1 - \eta_1)(1 + \eta_2)(\eta_2 - \eta_1 - 1)/4 \\
N_8 &= (1 - \eta_2^2)(1 - \eta_1)/2
\end{aligned}
\tag{4.39}
$$

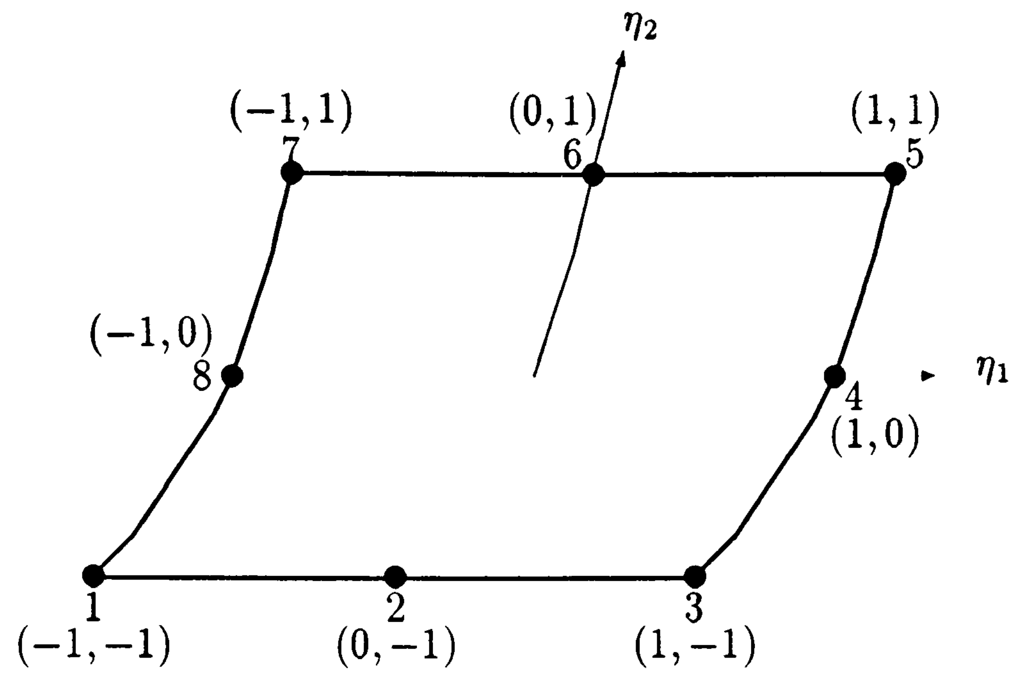

Figure 4.6: A quadrilateral zone

2. A mesh of any refinement is automatically generated inside each zone by specifying the number of required subdivisions in η_1 and η_2 directions.

3. The triangular elements are obtained by connecting two diagonal nodes in each elementary quadrilaterals.

4.5 Numerical Formulation of j and B

Once the all boundary values are found, the current density at any internal point $\mathbf{r}$ of the plasma column is computed by

$$\mathbf{j}(\mathbf{r}) = -\sigma_p \sum_{m=1}^{M} \int_{\Gamma_m} (\frac{\partial V}{\partial n} \nabla G(\mathbf{r},\mathbf{r}') - V \nabla \frac{\partial G(\mathbf{r},\mathbf{r}')}{\partial n}) \, d\Gamma_m \tag{4.40}$$

according to Eqns. (3.3,3.7,3.78), where the operation ∇ is with respect to $\mathbf{r}$ so that

$$\begin{aligned} \nabla G(\mathbf{r},\mathbf{r}') &= \frac{1}{4\pi}\nabla\frac{1}{|\mathbf{r}-\mathbf{r}'|} \\ &= -\frac{[x - x'(\xi_1,\xi_2)]\mathbf{a}_x + [y - y'(\xi_1,\xi_2)]\mathbf{a}_y + (z - z'(\xi_1,\xi_2)]\mathbf{a}_z}{4\pi|\mathbf{r}-\mathbf{r}'|^3} \end{aligned} \tag{4.41}$$

$$\begin{aligned} \nabla\frac{\partial G(\mathbf{r},\mathbf{r}')}{\partial n} &= \frac{1}{4\pi|\mathbf{n}|}\nabla\frac{(\mathbf{r}-\mathbf{r}')\cdot\mathbf{n}}{|\mathbf{r}-\mathbf{r}'|^3} \\ &= \frac{1}{4\pi}\left\{\frac{n_x}{|\mathbf{r}-\mathbf{r}'|^3} - 3\frac{(\mathbf{r}-\mathbf{r}')\cdot\mathbf{n}[x - x'(\xi_1,\xi_2)]}{|\mathbf{r}-\mathbf{r}'|^5}\right\}\mathbf{a}_x \\ &\quad + \frac{1}{4\pi}\left\{\frac{n_y}{|\mathbf{r}-\mathbf{r}'|^3} - 3\frac{(\mathbf{r}-\mathbf{r}')\cdot\mathbf{n}[y - y'(\xi_1,\xi_2)]}{|\mathbf{r}-\mathbf{r}'|^5}\right\}\mathbf{a}_y \\ &\quad + \frac{1}{4\pi}\left\{\frac{n_z}{|\mathbf{r}-\mathbf{r}'|^3} - 3\frac{(\mathbf{r}-\mathbf{r}')\cdot\mathbf{n}[z - z'(\xi_1,\xi_2)]}{|\mathbf{r}-\mathbf{r}'|^5}\right\}\mathbf{a}_z \end{aligned} \tag{4.42}$$

where $\mathbf{n}$ is the outward normal of surface element defined by Eqn. (4.25) and its components n_x, n_y and n_z are constant on each surface element given in Eqn. (4.26); and

$$|\mathbf{r}-\mathbf{r}'| = \sqrt{[x - x'(\xi_1,\xi_2)]^2 + [y - y'(\xi_1,\xi_2)]^2 + [z - z'(\xi_1,\xi_2)]^2} \tag{4.43}$$

For the constant elements (on both the spot interface and the distant plasma cross-section) $\partial V/\partial n$ and V at any point on each element are taken to equal their nodal values respectively while for the linear elements (on the column boundary) V at any point on each element is interpolated by Eqn. (4.9), therefore for a given field point (x, y, z) the integrands involving in Eqn.(4.40) are functions of ξ_1 and ξ_2 and the associated surface integrals over each element are numerically evaluated using Gaussian quadrature in the way described in the previous section so as to determine $\mathbf{j}(\mathbf{r})$.

Similarly, the current density inside the cathode is obtained by

$$\mathbf{j}(\mathbf{r}) = -\sigma_c \sum_{m=1}^{M^\dagger} \int_{\Gamma_m} \frac{\sigma_p}{\sigma_c}\frac{\partial V}{\partial n}\nabla G(\mathbf{r},\mathbf{r}') \, d\Gamma_m \tag{4.44}$$

where $M^\dagger$ denotes the number of the surface elements within the spot region and the sum is taken on these elements only according to Eqns (3.86,3.87) and

$$\begin{aligned}\nabla G(\mathbf{r},\mathbf{r}') &= -\frac{1}{4\pi}\left\{\frac{[x-x'(\xi_1,\xi_2)]}{|\mathbf{r}-\mathbf{r}'|^3}+\frac{[x-x'(\xi_1,\xi_2)]}{|\mathbf{r}-\mathbf{r}'_*|^3}\right\}\mathbf{a}_x \\ &-\frac{1}{4\pi}\left\{\frac{[y-y'(\xi_1,\xi_2)]}{|\mathbf{r}-\mathbf{r}'|^3}+\frac{[y-y'(\xi_1,\xi_2)]}{|\mathbf{r}-\mathbf{r}'_*|^3}\right\}\mathbf{a}_y \\ &-\frac{1}{4\pi}\left\{\frac{[z-z'(\xi_1,\xi_2)]}{|\mathbf{r}-\mathbf{r}'|^3}+\frac{[z+z'(\xi_1,\xi_2)]}{|\mathbf{r}-\mathbf{r}'_*|^3}\right\}\mathbf{a}_z \end{aligned} \tag{4.45}$$

in which

$$|\mathbf{r}-\mathbf{r}'_*| = \sqrt{[x-x'(\xi_1,\xi_2)]^2+[y-y'(\xi_1,\xi_2)]^2+[z+z'(\xi_1,\xi_2)]^2} \tag{4.46}$$

according to Eqn.(3.86). Actually, we do not need to determine the cathode potential.

The magnetic induction arising from the current is computed by

$$\mathbf{B}(\mathbf{r}) = \frac{\mu_o}{4\pi}\int_\tau \nabla\times\frac{\mathbf{j}(\mathbf{r}')}{|\mathbf{r}-\mathbf{r}'|}\,d\tau \tag{4.47}$$

according to Eqns. (3.8,3.10). It is convenient to divide τ into some volume elements over which the volume integrals are evaluated numerically, that is

$$\mathbf{B}(\mathbf{r}) = \frac{\mu_o}{4\pi}\sum_{e=1}^{N_B}\int_{\tau_e}\mathcal{F}(x',y',z')\,d\tau \tag{4.48}$$

which should sum up the contributions of the plasma column and the cathode and where

$$\begin{aligned}\mathcal{F}(x',y',z') &= \nabla\times\frac{\mathbf{j}(\mathbf{r}')}{|\mathbf{r}-\mathbf{r}'|} \\ &= \left(j_y\frac{z-z'}{|\mathbf{r}-\mathbf{r}'|^3}-j_z\frac{y-y'}{|\mathbf{r}-\mathbf{r}'|^3}\right)\mathbf{a}_x \\ &+\left(j_z\frac{x-x'}{|\mathbf{r}-\mathbf{r}'|^3}-j_x\frac{z-z'}{|\mathbf{r}-\mathbf{r}'|^3}\right)\mathbf{a}_y \\ &+\left(j_x\frac{y-y'}{|\mathbf{r}-\mathbf{r}'|^3}-j_y\frac{x-x'}{|\mathbf{r}-\mathbf{r}'|^3}\right)\mathbf{a}_z \end{aligned} \tag{4.49}$$

in which j_x, j_y and j_z are the components of $\mathbf{j}(\mathbf{r}')$.

4.6 Volume integrals

We employ Hammer's five-point numerical integration scheme to evaluate the volume integral [59]

$$\int_{\tau_e} \mathcal{F}(x', y', z')\, d\tau = det(J) \sum_{s=1}^{5} w^s \mathcal{F}(\xi_1^s, \xi_2^s, \xi_3^s) \tag{4.50}$$

where τ_e is a tetrahedral region as Fig.4.7 shows; ($\xi_1^s, \xi_2^s, \xi_3^s$) are the volume coordinates of the s-th sampling point and w^s is the associated weight which are listed in Table 4.3.

Table 4.3: Sampling points and weights after Hammer

s	ξ_1^s	ξ_2^s	ξ_3^s	w^s
1	1/6	1/6	1/6	9/120
2	3/6	1/6	1/6	9/120
3	1/6	3/6	1/6	9/120
4	1/6	1/6	3/6	9/120
5	1/4	1/4	1/4	-16/120

The $det(J)$ is the Jacobian determinant in association with the coordinate transformation

$$\begin{aligned} x'(\xi_1, \xi_2, \xi_3) &= \sum_{p=1}^{4} N^p(\xi_1, \xi_2, \xi_3) x_e^p \\ y'(\xi_1, \xi_2, \xi_3) &= \sum_{p=1}^{4} N^p(\xi_1, \xi_2, \xi_3) y_e^p \\ z'(\xi_1, \xi_2, \xi_3) &= \sum_{p=1}^{4} N^p(\xi_1, \xi_2, \xi_3) z_e^p \end{aligned} \tag{4.51}$$

where (x_e^p, y_e^p, z_e^p) for $p = 1, 2, 3, 4$ are the global coordinates of the four vertices of the tetrahedral element e; and

$$\begin{aligned} N^1 &= \xi_1 \\ N^2 &= \xi_2 \\ N^3 &= \xi_3 \\ N^4 &= 1 - \xi_1 - \xi_2 - \xi_3 \end{aligned} \tag{4.52}$$

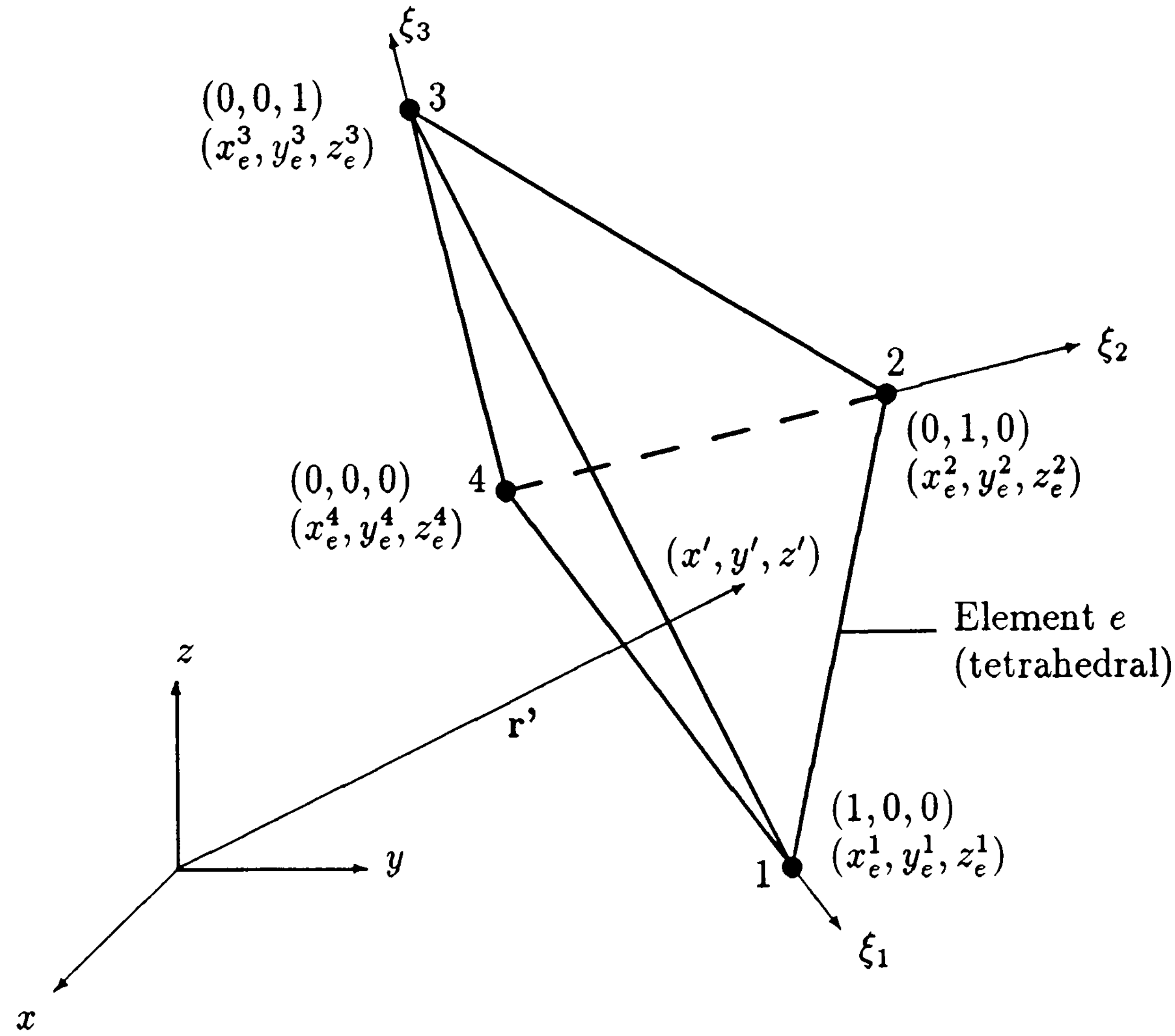

Figure 4.7: The local 3D volume coordinates of a tetrahedral element

so that

$$det(J) = det\begin{pmatrix} \frac{\partial x'}{\partial \xi_1} & \frac{\partial y'}{\partial \xi_1} & \frac{\partial z'}{\partial \xi_1} \\ \frac{\partial x'}{\partial \xi_2} & \frac{\partial y'}{\partial \xi_2} & \frac{\partial z'}{\partial \xi_2} \\ \frac{\partial x'}{\partial \xi_3} & \frac{\partial y'}{\partial \xi_3} & \frac{\partial z'}{\partial \xi_3} \end{pmatrix} \tag{4.53}$$

$$= det\begin{pmatrix} (x_e^1 - x_e^4) & (y_e^1 - y_e^4) & (z_e^1 - z_e^4) \\ (x_e^2 - x_e^4) & (y_e^2 - y_e^4) & (z_e^2 - z_e^4) \\ (x_e^3 - x_e^4) & (y_e^3 - y_e^4) & (z_e^3 - z_e^4) \end{pmatrix} \tag{4.54}$$

which is equal to a value of $6\tau_e$.

For each volume element, the global coordinates of the five sampling points are obtained by substituting the cooresponding volume coordinates of Table 4.3 into Eqn. (4.51) and then these five sets of the global coordinates become the five points at which the current densities need to be determined first so that $\mathcal{F}(x', y', z')$ of Eqn.(4.49) is ready to be transformed to $\mathcal{F}(\xi_1^s, \xi_2^s, \xi_3^s)$ in Eqn.(4.50) by means of Eqn.(4.51) and the volume

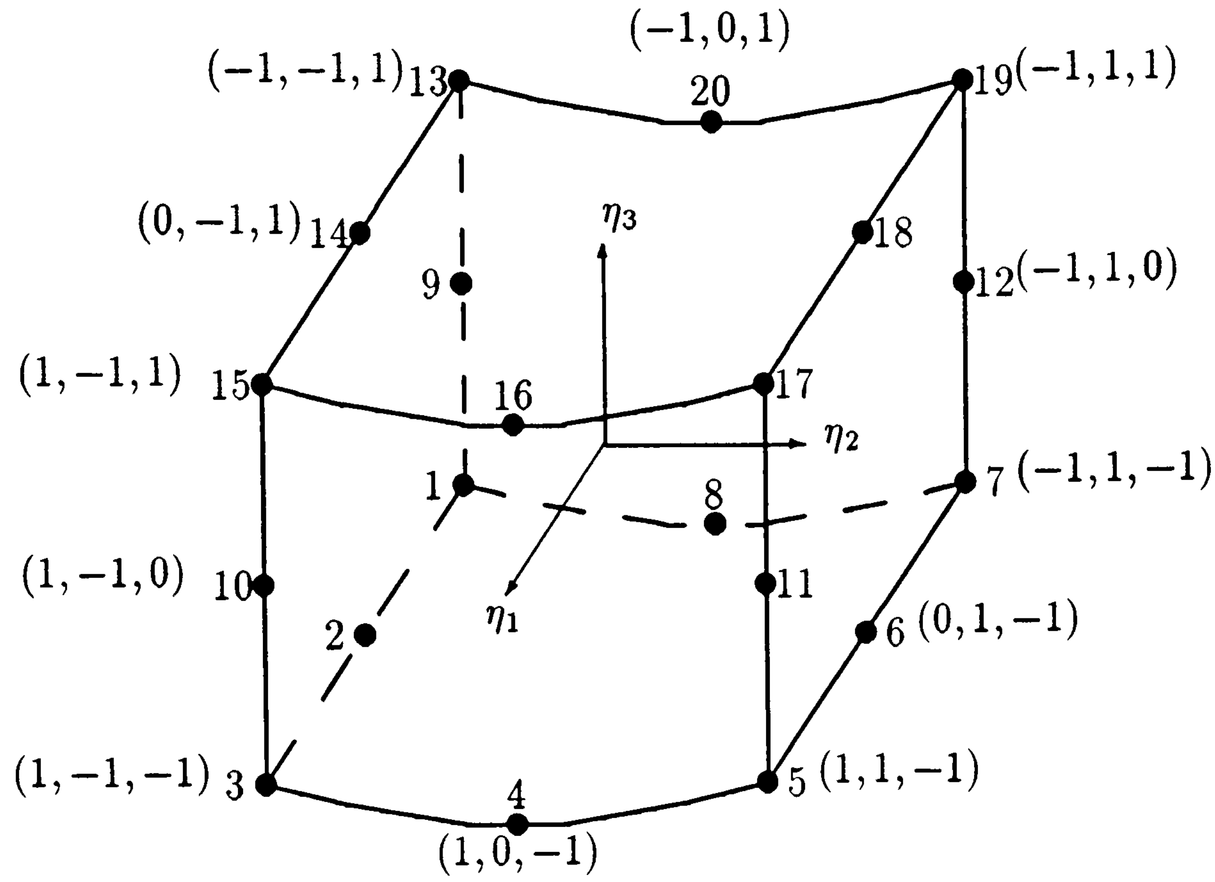

Figure 4.8: A hexahedral zone

integral is numerically evaluated.

4.7 Volume mesh generation

Similar to the surface mesh generation, the volume mesh generation brings about all the information required for the numerical volume integrations and is realized based on three steps :

1. Division of the 3D-region into hexahedrons, one of which is shown in Fig.4.8 where the global coordinates are interpolated by

$$
\begin{aligned}
x &= \sum_{i=1}^{20} N_i x_i \\
y &= \sum_{i=1}^{20} N_i y_i \\
z &= \sum_{i=1}^{20} N_i z_i
\end{aligned}
\tag{4.55}
$$

Table 4.4: The coefficients for the shape functions of a hexahedron

i	1	2	3	4	5	6	7	8	9	10
a	−1		1	1	1		−1	−1	−1	1
b	−1	−1	−1		1	1	1		−1	−1
c	−1	−1	−1	−1	−1	−1	−1	−1		
i	11	12	13	14	15	16	17	18	19	20
a	1	−1	−1		1	1	1		−1	−1
b	1	1	−1	−1	−1		1	1	1	
c			1	1	1	1	1	1	1	1

with

$$N_i = \begin{cases} (1-\eta_1^2)(1+b\eta_2)(1+c\eta_3)/4 & \text{for } i = 2,6,14,18 \\ (1-\eta_2^2)(1+a\eta_1)(1+c\eta_3)/4 & \text{for } i = 4,8,16,20 \\ (1-\eta_3^2)(1+a\eta_1)(1+b\eta_2)/4 & \text{for } i = 9,10,11,12 \\ (1+a\eta_1)(1+b\eta_2)(1+c\eta_3)(a\eta_1+b\eta_2+c\eta_3-2)/8 & \text{for } i = \text{else} \end{cases} \tag{4.56}$$

where (η_1, η_2, η_3) are the curve-linear coordinates ranging from 1 to -1 respectively and coefficients a, b, c are listed in Table 4.4.

2. Division of a hexahedron into sub-cuboids by specifying the number of required subdivisions in η_1, η_2 and η_3 directions.

3. Division of a cuboids into five tetrahedra; in each of which the vertices should be numbered as Fig.4.9 indicates so as to ensure ξ_1, ξ_2 and ξ_3 obey a 'right-hand' rule obvious from Fig.4.7, that is the first three vertices are numbered in an anti-clockwise manner when the last one is viewed from their triangular plane, so $det(J) = 6\tau_e > 0$.

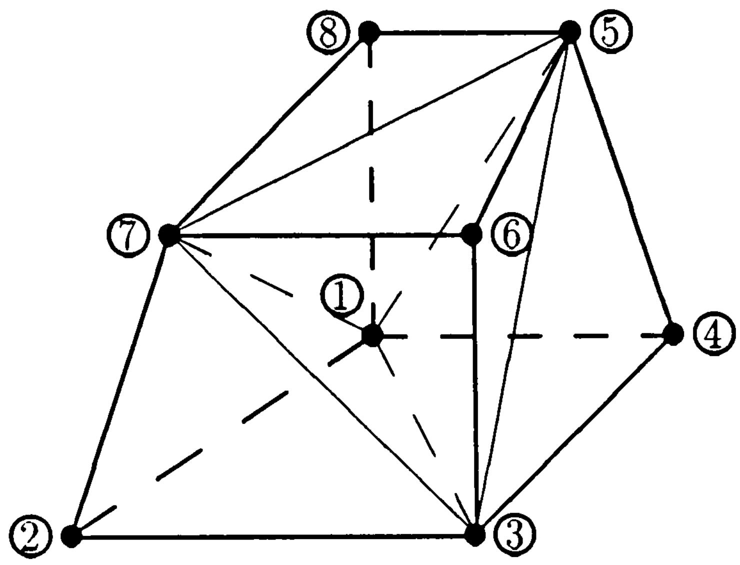

Element \ Vertex	1	2	3	4
1	③	②	①	⑦
2	①	④	③	⑤
3	⑥	⑤	⑦	③
4	⑧	⑦	⑤	①
5	⑤	⑦	③	①

Figure 4.9: Division of a cuboid into five tetrahedral elements

4.8 Normalization

For the numerical analysis it is very useful to define nondimensional quantities. By introducing r_0 (the spot radius) and V_p (the potential on the distant plasma cross-section) as two references, we define

$$\begin{array}{lll} \tilde{V} = \frac{V}{V_p} & \tilde{\Gamma} = \frac{\Gamma}{r_0^2} & \tilde{\tau} = \frac{\tau}{r_0^3} \\ \tilde{\mathbf{r}} = \frac{\mathbf{r}}{r_0} & \tilde{\mathbf{r}}' = \frac{\mathbf{r}'}{r_0} & \tilde{\mathbf{n}} = \frac{\mathbf{n}}{r_0} \end{array} \tag{4.57}$$

are nondimensional variables. The spot radius r_0 can be chosen as an input parameter but the potential on the distant plasma cross-section V_p cannot be arbitrary in our case because we have already defined $V = 0$ on the spot interface. For a given arc current I_0, the following equation must be fulfilled at any cross-section of the plasma column

$$\int_{\Gamma_{cross-section}} -\sigma_p \frac{\partial V}{\partial n} d\Gamma = I_0 \tag{4.58}$$

where $\partial V/\partial n$ is the directional derivative of the potential on that cross-section. Subsititution of Eqn.(4.57) into Eqn.(4.58) yields

$$-\sigma_p V_p r_0 \int_{\tilde{\Gamma}_{cross-section}} \frac{\partial \tilde{V}}{\partial \tilde{n}} d\tilde{\Gamma} = I_0 \tag{4.59}$$

which leads to

$$V_p = \frac{I_0}{-\sigma_p r_0 \int_{\tilde{s}pot} \frac{\partial \tilde{V}}{\partial \tilde{n}} d\tilde{\Gamma}} \tag{4.60}$$

where we let $\tilde{s}pot = \tilde{\Gamma}_{cross-section}$ for simplicity though $\Gamma_{cross-section}$ could be any one of the column cross-sections.

By substituting Eqn.(4.57) into Eqn.(4.40), we can obtain

$$\mathbf{j}(\tilde{\mathbf{r}}) = -\frac{\sigma_p V_p}{r_0} \sum_{m=1}^{M} \int_{\tilde{\Gamma}_m} \left(\frac{\partial \tilde{V}}{\partial \tilde{n}} \nabla G(\tilde{\mathbf{r}}, \tilde{\mathbf{r}}') - \tilde{V}\, \nabla \frac{\partial G(\tilde{\mathbf{r}}, \tilde{\mathbf{r}}')}{\partial \tilde{n}}\right) d\tilde{\Gamma}_m \tag{4.61}$$

which, by further replacing V_p with Eqn.(4.60), becomes

$$\mathbf{j}(\tilde{\mathbf{r}}) = j_a \left(- \frac{\pi \sum_{m=1}^{M} \int_{\tilde{\Gamma}_m} \left(\frac{\partial \tilde{V}}{\partial \tilde{n}} \nabla G(\tilde{\mathbf{r}}, \tilde{\mathbf{r}}') - \tilde{V}\, \nabla \frac{\partial G(\tilde{\mathbf{r}}, \tilde{\mathbf{r}}')}{\partial \tilde{n}}\right) d\tilde{\Gamma}_m}{\tilde{V}_s} \right) \tag{4.62}$$

where $j_a = I_0/(\pi r_0^2)$ is the average current density of the cathode spot and

$$\tilde{V}_s = \int_{\tilde{s}pot} -\frac{\partial \tilde{V}}{\partial \tilde{n}} d\tilde{\Gamma} \tag{4.63}$$

In the same manner, for the current density in the cathode Eqn.(4.44) can be written as

$$\mathbf{j}(\tilde{\mathbf{r}}) = j_a \left(\frac{\sum_{m=1}^{M^\dagger} \int_{\tilde{\Gamma}_m} \frac{\partial \tilde{V}}{\partial \tilde{n}} \nabla G(\tilde{\mathbf{r}}, \tilde{\mathbf{r}}')\, d\tilde{\Gamma}_m}{\tilde{V}_s} \right) \tag{4.64}$$

It can clearly be seen that the quantities inside the big parentheses on the R.H.S. of Eqns.(4.62,4.64) are nondimensional, hence we can define the normalized current density

$$\tilde{\mathbf{j}}(\tilde{\mathbf{r}}) = \frac{\mathbf{j}(\tilde{\mathbf{r}})}{j_a} \tag{4.65}$$

which is only the function of the normalized geometrical shape of physical mode.

The magnetic induction can also be normalized as follows. From Eqns.(4.48,4.49) and Eqns.(4.57,4.65), we have

$$\mathbf{B}(\tilde{\mathbf{r}}) = \mu_o \sqrt{I_0 j_a} \left(\frac{1}{4\pi^{3/2}} \sum_{e=1}^{N_B} \int_{\tilde{\tau}_e} \tilde{\mathcal{F}}(\tilde{x}', \tilde{y}', \tilde{z}')\, d\tilde{\tau} \right) \tag{4.66}$$

where $\tilde{\mathcal{F}}(\tilde{x}', \tilde{y}', \tilde{z}')$ is obtained by replacing all variables on the R.H.S.of Eqn.(4.49) with the corresponding nondimensional ones, so that the normalized magnetic induction is defined by

$$\tilde{\mathbf{B}}(\tilde{\mathbf{r}}) = \frac{\mathbf{B}(\tilde{\mathbf{r}})}{\mu_o\sqrt{I_0 j_a}} \tag{4.67}$$

Thus the normalized electrodynamic force density is defined by

$$\tilde{\mathbf{f}}(\tilde{\mathbf{r}}) = \tilde{\mathbf{j}}(\tilde{\mathbf{r}}) \times \left(\tilde{\mathbf{B}}(\tilde{\mathbf{r}}) + \frac{\mathbf{B}_a}{\mu_o\sqrt{I_0 j_a}}\right) \tag{4.68}$$

and the electrodynamic forces per unit length on the cathode spot is finally computed by

$$F_R + F_L = (r_0^2 j_a \mu_0 \sqrt{I_0 j_a}) \int_{\tilde{s}pot} \tilde{\mathbf{f}}(\tilde{\mathbf{r}}) \cdot \mathbf{a}_\perp d\tilde{\Gamma} \tag{4.69}$$

Appendix 4.1

Values of the sampling points and the weights in Eqn.(4.30) for the numerical integration over a triangular area after Cowper [60] :

Hammer's 3-point scheme			
sampling point (s)	weight (w^s)	ξ_1^s	ξ_2^s
1	1/3	2/3	1/6
2	1/3	1/6	2/3
3	1/3	1/6	1/6

Hammer's 4-point scheme			
sampling point (s)	weight (w^s)	ξ_1^s	ξ_2^s
1	25/48	3/5	1/5
2	25/48	1/5	3/5
3	25/48	1/5	1/5
4	−27/48	1/3	1/3

Hammer's 6-point scheme			
sampling point (s)	weight (w^s)	ξ_1^s	ξ_2^s
1	wa	a	b
2	wa	b	a
3	wa	b	b
4	wa'	a'	b'
5	wa'	b'	a'
6	wa'	b'	b'
wa = 0.10995 17436 55322		wa' = 0.22338 15896 78011	
a = 0.81684 75729 80459		b = 0.09157 62135 09771	
a' = 0.10810 30181 68070		b' = 0.44594 84909 15965	

Hammer's 7-point scheme			
sampling point (s)	weight (w^s)	ξ_1^s	ξ_2^s
1	wa	a	b
2	wa	b	a
3	wa	b	b
4	wa'	a'	b'
5	wa'	b'	a'
6	wa'	b'	b'
7	9/40	1/3	1/3
wa = 0.12593 91805 44827		wa' = 0.13239 41527 88506	
a = 0.79742 69853 53087		b = 0.10128 65073 23456	
a' = 0.47014 20641 05115		b' = 0.47014 20641 05115	

Hammer's 9-point scheme			
sampling point (s)	weight (w^s)	ξ_1^s	ξ_2^s
1	wa	a	b
2	wa	b	a
3	wa	b	b
4	wb	c	d
5	wb	c	e
6	wb	d	c
7	wb	d	e
8	wb	e	c
9	wb	e	d
wa = 0.20595 05047 60887		wb = 0.06369 14142 86223	
a = 0.12494 95032 33232		b = 0.43752 52483 83384	
c = 0.79711 26518 60071		d = 0.16540 99273 89841	
e = 0.03747 74207 50088			

Hammer's 12-point scheme			
sampling point (s)	weight (w^s)	ξ_1^s	ξ_2^s
1	wa	a	b
2	wa	b	a
3	wa	b	b
4	wa'	a'	b'
5	wa'	b'	a'
6	wa'	b'	b'
7	wb	c	d
8	wb	c	e
9	wb	d	c
10	wb	d	e
11	wb	e	c
12	wb	e	d
wa = 0.05084 49063 70207		wa' = 0.11678 62757 26379	
wb = 0.08285 10756 18374			
a = 0.87382 19710 16996		b = 0.06308 90144 91502	
a' = 0.50142 65096 58179		b' = 0.24928 67451 70910	
c = 0.63650 24991 21399		d = 0.31035 24510 33785	
e = 0.05314 50498 44816			

Hammer's 13-point scheme			
sampling point (s)	weight (w^s)	ξ_1^s	ξ_2^s
1	wa	a	b
2	wa	b	a
3	wa	b	b
4	wa'	a'	b'
5	wa'	b'	a'
6	wa'	b'	b'
7	wb	c	d
8	wb	c	e
9	wb	d	c
10	wb	d	e
11	wb	e	c
12	wb	e	d
13	wb'	1/3	1/3
wa = 0.17561 52574 33204		wa' = 0.05334 72356 08839	
wb = 0.07711 37608 90257		wb' = −0.14957 00444 67670	
a = 0.47930 80678 41923		b = 0.26034 59660 79038	
a' = 0.86973 97941 95568		b' = 0.06513 01029 02216	
c = 0.63844 41885 69809		d = 0.31286 54960 04875	
e = 0.04869 03154 25316			

Appendix 4.2

The standard 2D Gaussian quadrature :

$$\int_a^b \int_{g_1(x)}^{g_2(x)} f(x,y)dxdy = \frac{b-a}{2}\sum_{s=1}^{N_s} w^s \frac{b_1-a_1}{2}\sum_{t=1}^{N_t} w^t f(x^s,y^t) \tag{4.70}$$

with

$$\begin{aligned} x^s &= \frac{b+a}{2}+\frac{b-a}{2}\eta^s \\ y^t &= \frac{b_1+a_1}{2}+\frac{b_1-a_1}{2}\eta^t \end{aligned}$$

$$a_1 = g_1(x^s)$$
$$b_1 = g_2(x^s)$$

where η^i $(i = s, t)$ is the value of the i-th sampling point and w^i $(i = s, t)$ is the weight associated, which are listed below for various schemes [65, 66] we may need.

Gaussian 2-point scheme		
sampling point (i)	weight (w^i)	η^i
1	1.00000 00000 00000	0.57735 02691 89626
2	1.00000 00000 00000	−0.57735 02691 89626

Gaussian 3-point scheme		
sampling point (i)	weight (w^i)	η^i
1	0.55555 55555 55556	0.77459 66692 41483
2	0.88888 88888 88889	0.00000 00000 00000
$w^3 = w^1$ and $\eta^3 = -\eta^1$		

Gaussian 4-point scheme		
sampling point (i)	weight (w^i)	η^i
1	0.34785 48451 37454	0.86113 63115 94053
2	0.65214 51548 62546	0.33998 10435 84856
for $i = 3$ to 4, $w^i = w^{i-2}$ and $\eta^i = -\eta^{i-2}$		

Gaussian 5-point scheme		
sampling point (i)	weight (w^i)	η^i
1	0.23692 68850 56189	0.90617 98459 38664
2	0.47862 86704 99366	0.53846 93101 05683
3	0.56800 00000 00000	0.00000 00000 00000
for $i = 4$ to 5, $w^i = w^{i-3}$ and $\eta^i = -\eta^{i-3}$		

Gaussian 10-point scheme		
sampling point (i)	weight (w^i)	η^i
1	0.06667 13443 08688	0.97390 65285 17172
2	0.14945 13491 50581	0.86506 33666 88985
3	0.21908 63625 15982	0.67940 95682 99024
4	0.26926 67193 09996	0.43339 53941 29247
5	0.29552 42247 14753	0.14887 43389 81631
for $i = 6$ to 10, $w^i = w^{i-5}$ and $\eta^i = -\eta^{i-5}$		

Appendix 4.3

The coordinate transformation for surface integrations :

Let

$$\begin{aligned} \xi_1 &= a_1 X + b_1 Y + c_1 \\ \xi_2 &= a_2 X + b_2 Y + c_2 \end{aligned} \tag{4.71}$$

Substituting the area coordinates (ξ_1, ξ_2) and the auxiliary coordinates (X,Y) at three vertices respectively into Eqn.(4.71) yields a system of linear equations

$$\begin{aligned} a_1 X_3 + b_1 Y_3 + c_1 &= 0 \\ a_2 X_3 + b_2 Y_3 + c_2 &= 0 \\ a_1 X_2 + b_1 Y_2 + c_1 &= 0 \\ a_2 X_2 + b_2 Y_2 + c_2 &= 1 \\ a_1 X_1 + b_1 Y_1 + c_1 &= 1 \\ a_2 X_1 + b_2 Y_1 + c_2 &= 0 \end{aligned} \tag{4.72}$$

whose solution is

$$\begin{aligned} a_1 = (Y_2 - Y_3)/D, \quad b_1 = (X_3 - X_2)/D, \quad c_1 = (X_2 Y_3 - X_3 Y_2)/D \\ a_2 = (Y_3 - Y_1)/D, \quad b_2 = (X_1 - X_3)/D, \quad c_2 = (X_3 Y_1 - X_1 Y_3)/D \end{aligned} \tag{4.73}$$

with

$$D = (X_2 Y_3 - X_3 Y_2) + (X_3 Y_1 - X_1 Y_3) + (X_1 Y_2 - X_2 Y_1)$$

We note (refer to Fig.4.3)

$$\begin{aligned} \mathrm{X} &= \rho\cos\phi \\ \mathrm{Y} &= \rho\sin\phi \end{aligned} \tag{4.74}$$

so that

$$\begin{aligned} &\mathrm{X}_1 = L_{31}, \quad \mathrm{X}_2 = L_{23}\cos\phi_3, \quad \mathrm{X}_3 = 0 \\ &\mathrm{Y}_1 = 0, \qquad \mathrm{Y}_2 = L_{23}\sin\phi_3, \quad \mathrm{Y}_3 = 0 \end{aligned} \tag{4.75}$$

where ϕ_3 is the apical angle of vertex 3. By substituting we obtain

$$\begin{aligned} &a_1 = L_{23}\sin\phi_3/D, \quad b_1 = -L_{23}\cos\phi_3/D, \quad c_1 = 0 \\ &a_2 = 0, \qquad\qquad\qquad b_2 = L_{31}/D, \qquad\qquad c_2 = 0 \end{aligned} \tag{4.76}$$

with

$$D = \mathrm{X}_1\mathrm{Y}_2 = L_{31}L_{23}\sin\phi_3$$

Substituting Eqns.(4.74,4.76) into Eqn.(4.71) we arrive at Eqn.(4.32). The transformations with the field point located at vertex 1 or 2 can be deduced in the similar way.

Chapter 5

Numerical Computation

5.1 Programme Description

A computer programme using FORTRAN language has been developed based on the above formulations. Its structure is depicted in Fig.5.1 and briefly described as follows.

The INPUT reads two quite simple data files named as ARCINPUT in Table 5.1, where the parameters (refer to Fig.4.5) have been defined in Section 4.4, and CATINPUT in Table 5.2, where x_c, y_c and z_c are the three dimensions of the cathode. Note all geometrical dimensions have been normalized by the spot radius.

The PRE-MESH automatically divides the surface or the volume into several quadrilateral or hexahedral zones, which results in sets of global coordinates of the nodes required by Eqns.(4.38,4.55).

Table 5.1: ARCINPUT data file

s	$R(s)$	$\alpha(s)_{Rad}$	$y_o(s)$	$z_o(s)$
1	1.00	0.00	0.00	0.00
2	1.10	0.17	0.17	0.98
3	1.20	0.35	0.68	1.88
4	1.40	0.52	1.50	2.60
5	1.60	0.70	2.57	3.06

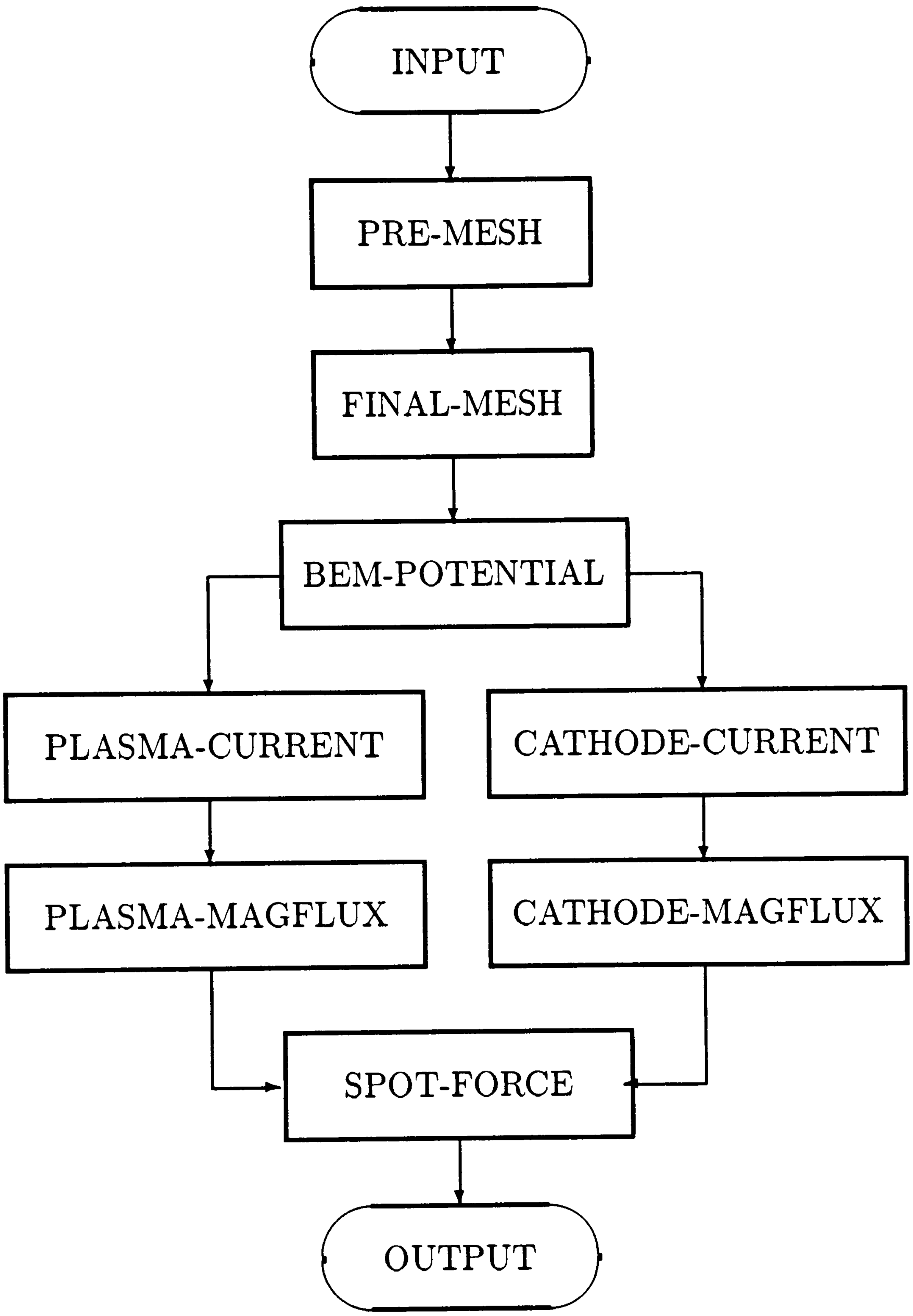

Figure 5.1: Programme structure

Table 5.2: CATINPUT data file

x_c	y_c	z_c
6.0	6.0	3.0

The FINAL-MESH generates all the mesh information required for further computations, namely the global coordinates of the vertices of each surface or volume element; the global coordinates of the nodes and the global numbering in association with the local numbering of the nodes. Care should be taken that numbering vertices of each triangular surface element must ensure the surface normal is outwards as Fig.4.2 shows. A generated surface mesh is shown in Fig.5.2 while a generated volume mesh is partially shown in Fig.5.3 for clearness. The 3D illustration of the mesh is realized by projecting the 3D coordinates to a plane, on which the coordinates are given by

$$\left.\begin{aligned} x' &= (y-x)\cos(\pi/6) \\ y' &= z-(x+y)\sin(\pi/6) \end{aligned}\right\} \tag{5.1}$$

The BEM-POTENTIAL carries out the computations of $[H]$ and $[K]$ matrices as well as the associated linear equations as described in the last chapter so as to give the solution of the mixed boundary value problem of the plasma column.

The PLASMA-CURRENT and the CATHODE-CURRENT compute Eqn.(4.65) associated with Eqn.(4.62) and Eqn.(4.64) respectively at the sampling points in the plasma column and the cathode, which are needed for calculation of the magnetic induction. The numerical scheme for the surface integration encountered is chosen in the manner as same as one used by the BEM-POTENTIAL.

The PLASMA-MAGFLUX and the CATHODE-MAGFLUX evaluate the contributions of the plasma current and the cathode current respectively on the normalized magnetic induction (flux) over the cathode spot according to Eqn.(4.67) associated with Eqn.(4.66).

The SPOT-FORCE calculates Eqn.(4.68) and Eqn.(4.69), where the normalized

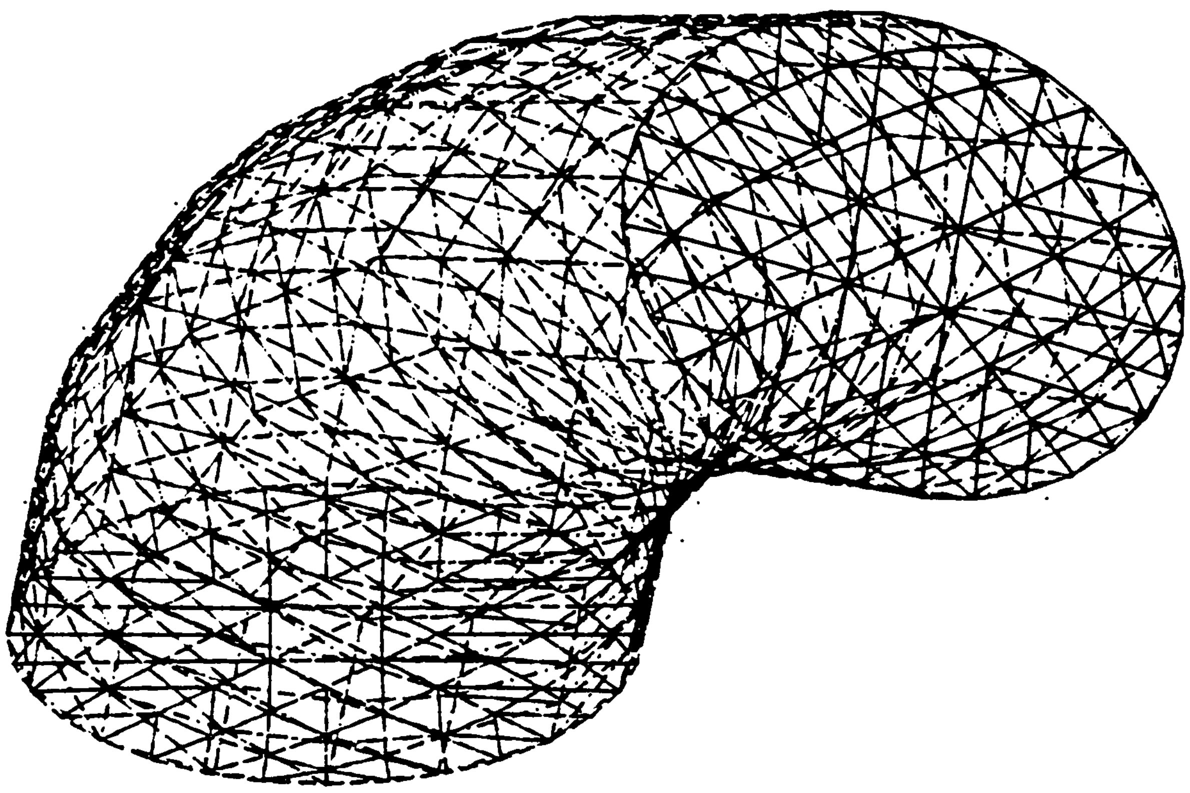

Figure 5.2: Surface mesh illustration

current density on the spot is directly given by

$$\tilde{\mathbf{j}}_{spot} = -\frac{\pi}{\tilde{V}_s}\frac{\partial \tilde{V}}{\partial \tilde{n}}\mathbf{a}_z \tag{5.2}$$

The programme was run on Convex at Oxford University Computing Centre. For a complete run, the CPU time was about 120 minutes depending on the size of mesh. It was found that the computation of current density cost most of the CPU time because a lot of the surface integrations were performed.

5.2 Numerical results

In order to check the accuracy for numerically computing Eqn.(2.16), firstly, the numerical results for the straight arc are compared with the analytical results which are obtained as follows.

Since the normal current density j_z is uniform over the cathode spot for the straight

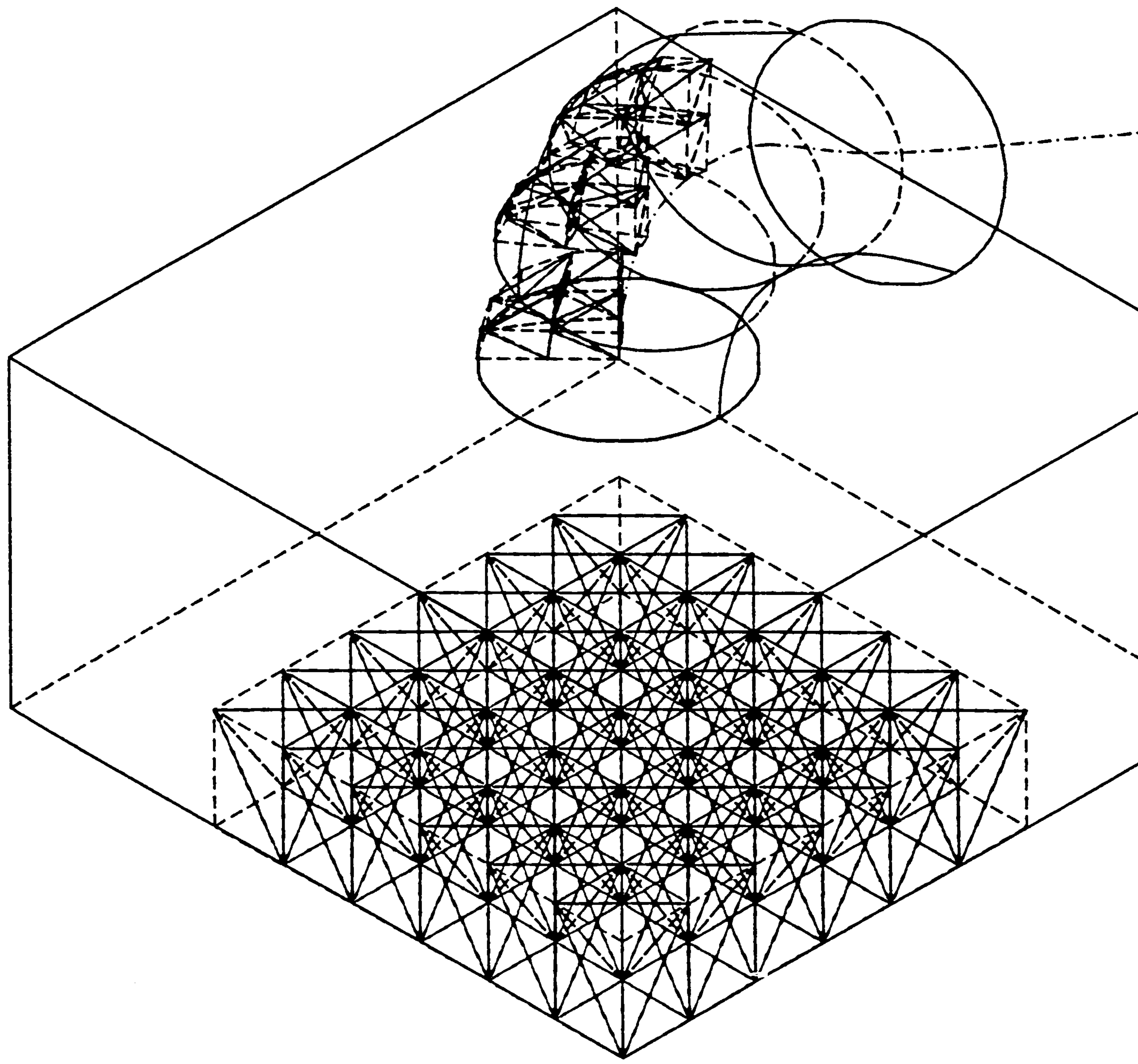

Figure 5.3: Volume mesh illustration

arc, the azimuthal magnetic induction is given by

$$B_\phi = \frac{\mu_0 j_z \rho}{2} \qquad \text{for } \rho \leq r_0 \tag{5.3}$$

according to Ampère's circuital law. In our coordinates (refer to Fig.2.5)

$$B_x = B_\phi sin\phi - B_a \tag{5.4}$$

$$\mathbf{f}(\mathbf{r}) \cdot \mathbf{a}_\perp = -j_z B_x \tag{5.5}$$

thus, we have

$$F_R + F_L = \int_0^\pi \int_0^{r_0} (-j_z B_x)\rho d\rho d\phi + \int_\pi^{2\pi} \int_0^{r_0} (-j_z B_x)\rho d\rho d\phi \tag{5.6}$$

where r_0 is the radius of the cathode spot. The first integral on the R.H.S. can be solved analytically and results in

$$F_1 = j_z B_a \pi r_0^2/2 - \mu_0 j_z^2 r_0^3/3 \tag{5.7}$$

Similarly, the result of the second integral is given by

$$F_2 = j_z B_a \pi r_0^2/2 + \mu_0 j_z^2 r_0^3/3 \tag{5.8}$$

Obviously,

$$\begin{aligned} &F_R = F_1, \quad and \quad F_L = F_2 \qquad\quad if\, F_1 < 0 \\ &F_R = 0, \quad and \quad F_L = F_1 + F_2 \quad if\, F_1 \geq 0 \end{aligned}$$

Let j_a represent the average current density of the cathode spot and $I_0 = j_a \pi r_0^2$ the arc current. Considering $j_z = j_a$ for the straight arc, we finally obtain

$$\frac{F_R}{r_0^2} = \begin{cases} \pi j_a B_a/2 - \mu_0 j_a \sqrt{j_a I_0}/3\sqrt{\pi} & \text{if } F_1 < 0 \\ 0 & \text{otherwise} \end{cases} \tag{5.9}$$

$$\frac{F_L}{r_0^2} = \begin{cases} \pi j_a B_a/2 + \mu_0 j_a \sqrt{j_a I_0}/3\sqrt{\pi} & \text{if } F_1 < 0 \\ \pi j_a B_a & \text{otherwise} \end{cases} \tag{5.10}$$

The comparison of the analytical and the numerical results is listed in Table 5.3, where one can see that the relative errors are within 10 percent.

Table 5.3: Comparison of the analytical and the numerical results

(straight arc)

j_a (A/cm^2)	I_0 (A)	B_a $(Tesla)$	$\lvert F_L\rvert/r_o^2(N/m^3)$ analytical	numerical	$\lvert F_R\rvert/r_o^2(N/m^3)$ analytical	numerical
10^6	1.00	0.06	1.88×10^9	1.89×10^9	0.00	0.00
10^8	1.00	0.06	3.30×10^{11}	3.58×10^{11}	1.42×10^{11}	1.55×10^{11}
10^6	50.0	0.30	9.42×10^9	9.49×10^9	0.00	0.00
10^8	50.0	0.30	2.14×10^{12}	2.30×10^{12}	1.20×10^{12}	1.25×10^{12}
10^6	100	0.50	1.57×10^{10}	1.58×10^{10}	0.00	0.00
10^8	100	0.50	3.15×10^{12}	3.39×10^{12}	1.58×10^{12}	1.67×10^{12}

Using the straight arc model, we can also investigate the convergent property of numerical results as a function of arc length, which is described in Fig.5.4. This figure shows that the numerical calculations approximate to a reasonable accuracy when the acr length truncated is only 4 to 5 times the spot radius. This is a consequence of the fact that the Biot-Savart law[1] (the law we used to calculate the self magnetic induction) varies as the inverse square of distance. This is also in agreement with the previous discussion in Section 2.3. Thus the contribution of the arc column beyond $5r_0$ from the cathode spot on the force calculations has little physical meaning and the truncated calculation is plausible. This conclusion is applicable to the cathode truncated computation as well.

Secondly, numerical computations were carried out for the deflected arc bending step by step away from the straight arc as displayed in Fig.5.5. The applied magnetic field is not taken into account at this stage. The results for F_R and F_L versus arc bending are presented in Fig.5.6, where the letter (a,b,...k) inserted on the curves indicates the result arising from the arc with the same identified letter in Fig.5.5. It can be observed from Fig.5.6 that as the arc is getting bent more and more, the numerical

[1]The law is obtained by substituting Eqn.(3.10) to Eqn.(3.8).

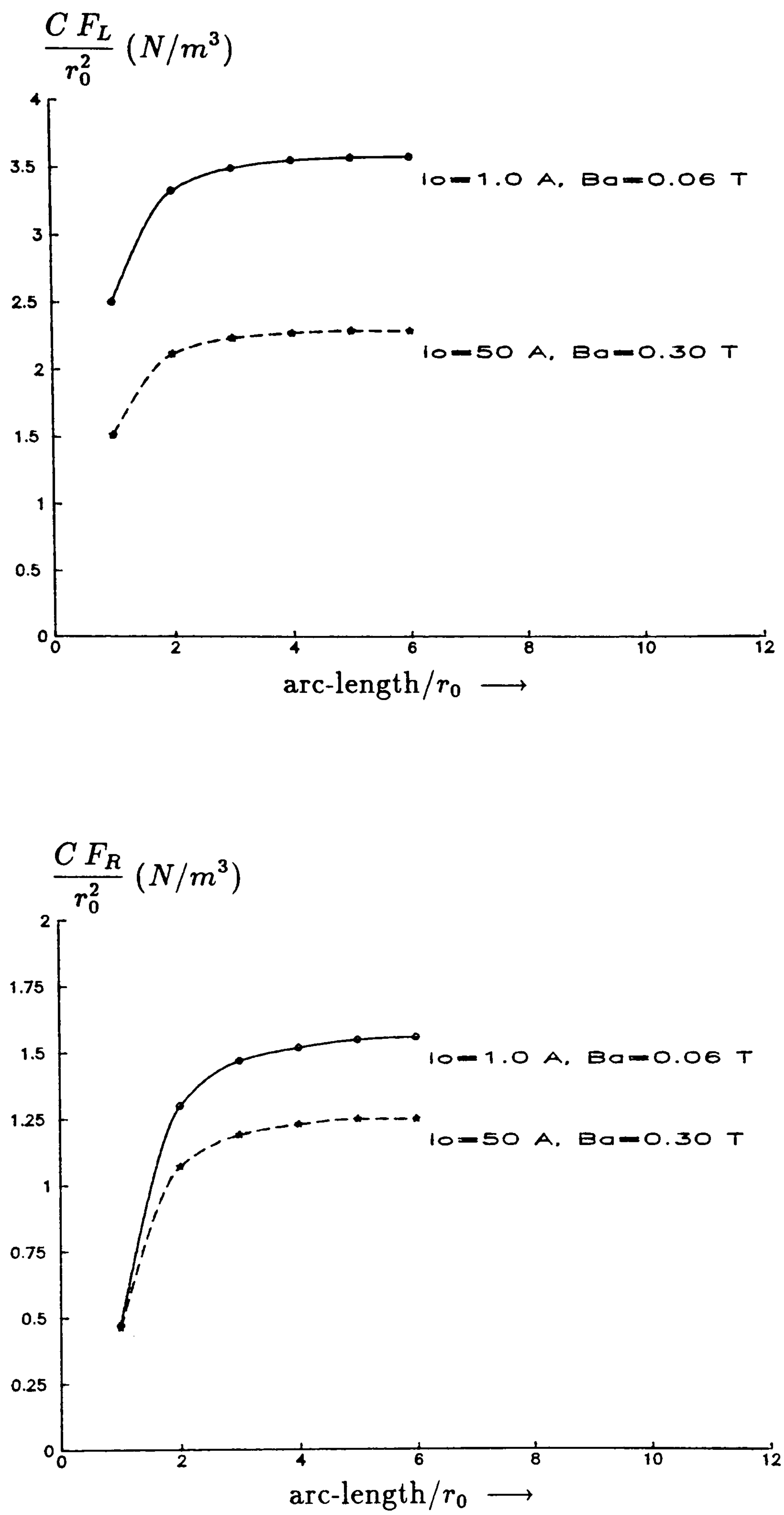

Figure 5.4: Convergence of numerical results vs arc length
Real lines: $C = 10^{11}$; broken lines: $C = 10^{12}$
$(j_a = 10^8\,A/cm^2)$

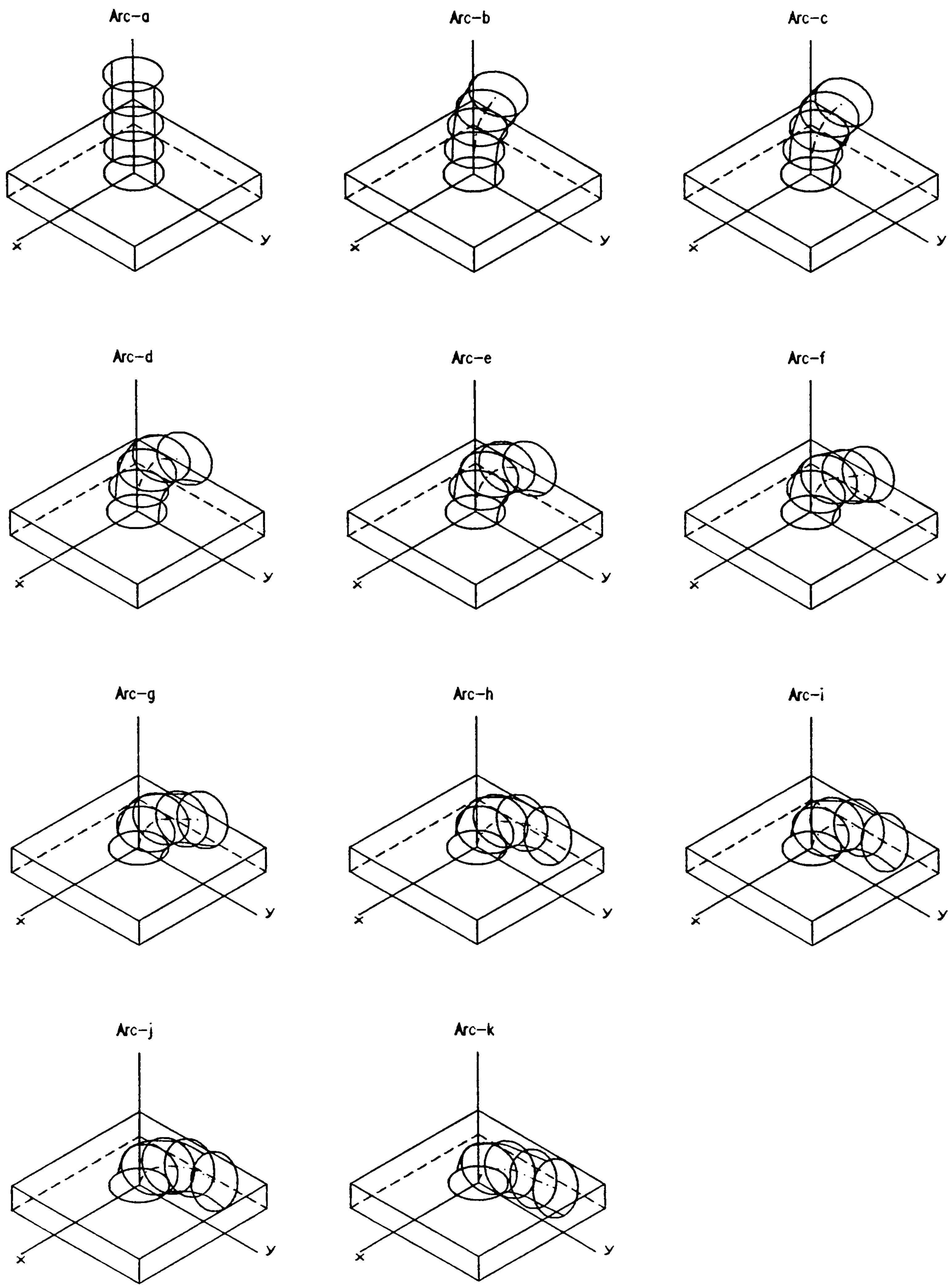

Figure 5.5: Deformation of arcs

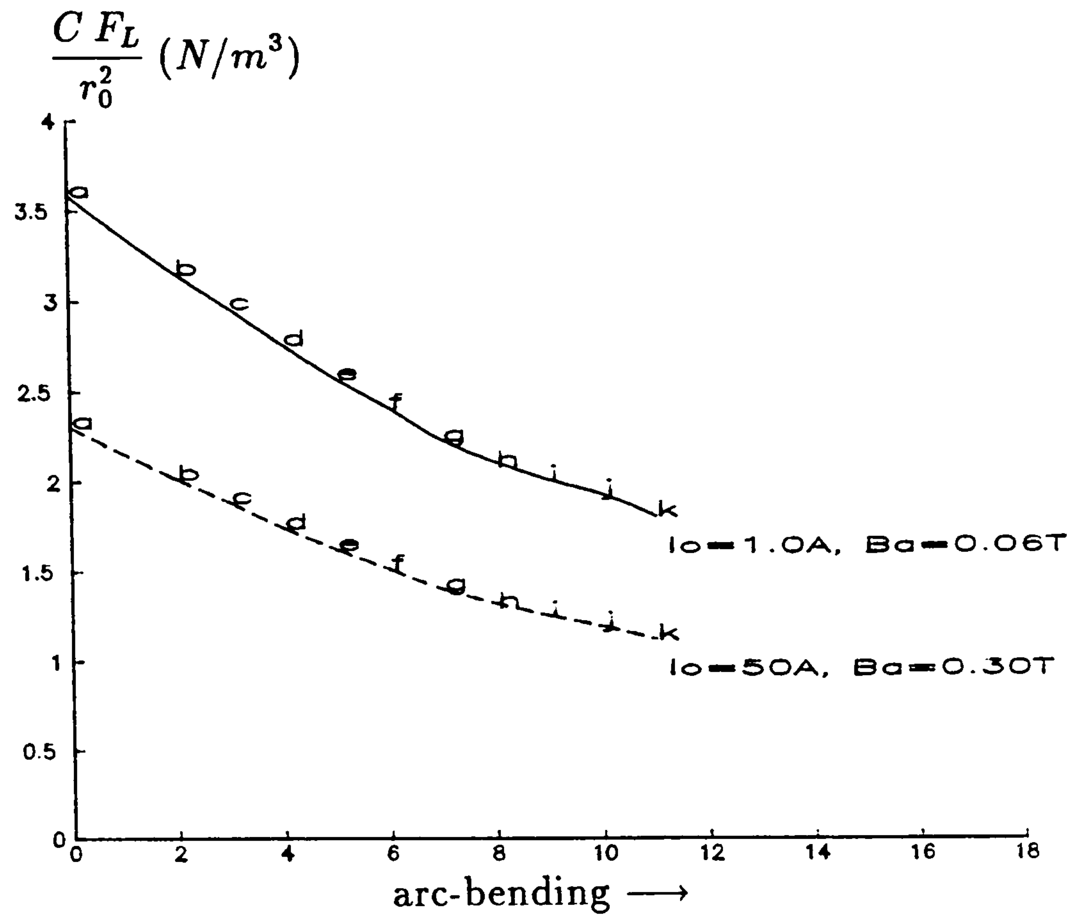

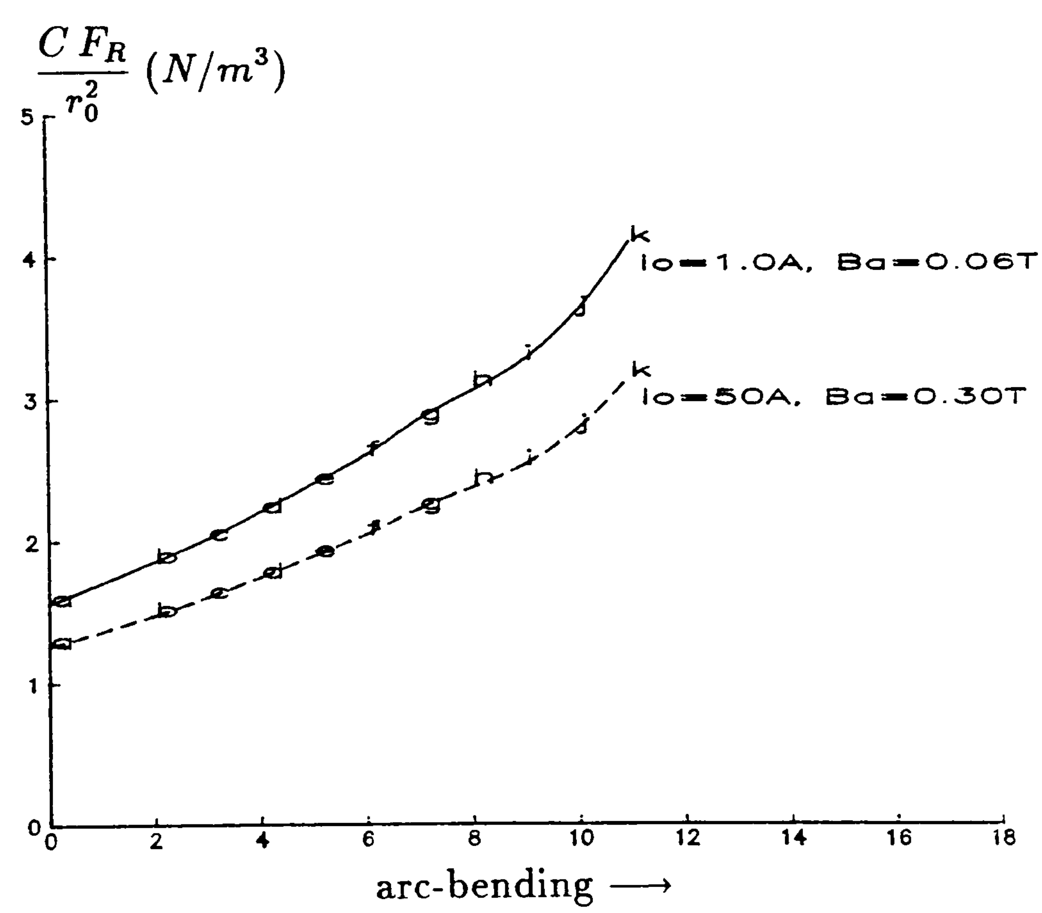

Figure 5.6: Electrodynamic forces vs arc bending
Real lines: $C = 10^{11}$; broken lines: $C = 10^{12}$
$(j_a = 10^8\ A/cm^2)$

results for F_L and F_R change smoothly away from those of the straight arc, which is expected physically. Therefore, the reliability of the numerical results is guaranteed.

The field components in which we are interested are computed and plotted in Fig.5.7, where the normalized current density is given by j_z/j_a; the normalized magnetic induction is defined by $B_x/\mu_o\sqrt{I_o j_a}$ and the normalized force density results from the multiplication of the normalized current density and the normalized magnetic induction. It should be remembered that the applied magnetic field is not involved in Fig.5.7.

One can see from Fig.5.7 that the numerical results for the straight arc are in good agreement with the analytical one denoted by the dotted lines. As the plasma column becomes more bent, the numerical results for the bent arcs change smoothly in the direction indicated by the arrows. It turns out that as the plasma column is bent in the Lorentzian direction due to the applied magnetic field, the current density over the cathode spot is no longer uniform and becomes stronger on the Lorentzian side while weaker on the retrograde side. This feature is very important, but was overlooked by the previous investigators. A similar tendency for changes in the distributions of the self magnetic induction and the force density due to the self-field is obtained. However, the change in the self magnetic induction is less sensible because the magnetic induction results from integration of the current distribution. These distributions for a typical bent arc can be clearer seen in Fig.5.8 (for comparison, the distributions for the straight arc are drawn on the left side).

It is obvious that in the absence of the applied magnetic field, the cathode spot of the bent arc would always move in the retrograde direction. However, it should be kept in mind that the bending of the plasma column is attributed to the applied field which is in favour of the motion in the Lorentzian direction. Figure 5.9 shows a resultant magnetic field obtained by superposing the applied field upon the self field for different experimental parameters under which the retrograde motion was observed. We can see that the resultant field changes sign within the spot in all cases and the component which is in favour of the Lorentzian motion can become dominant. Hence, if the current density on the cathode spot were uniform, the resultant magnetic field

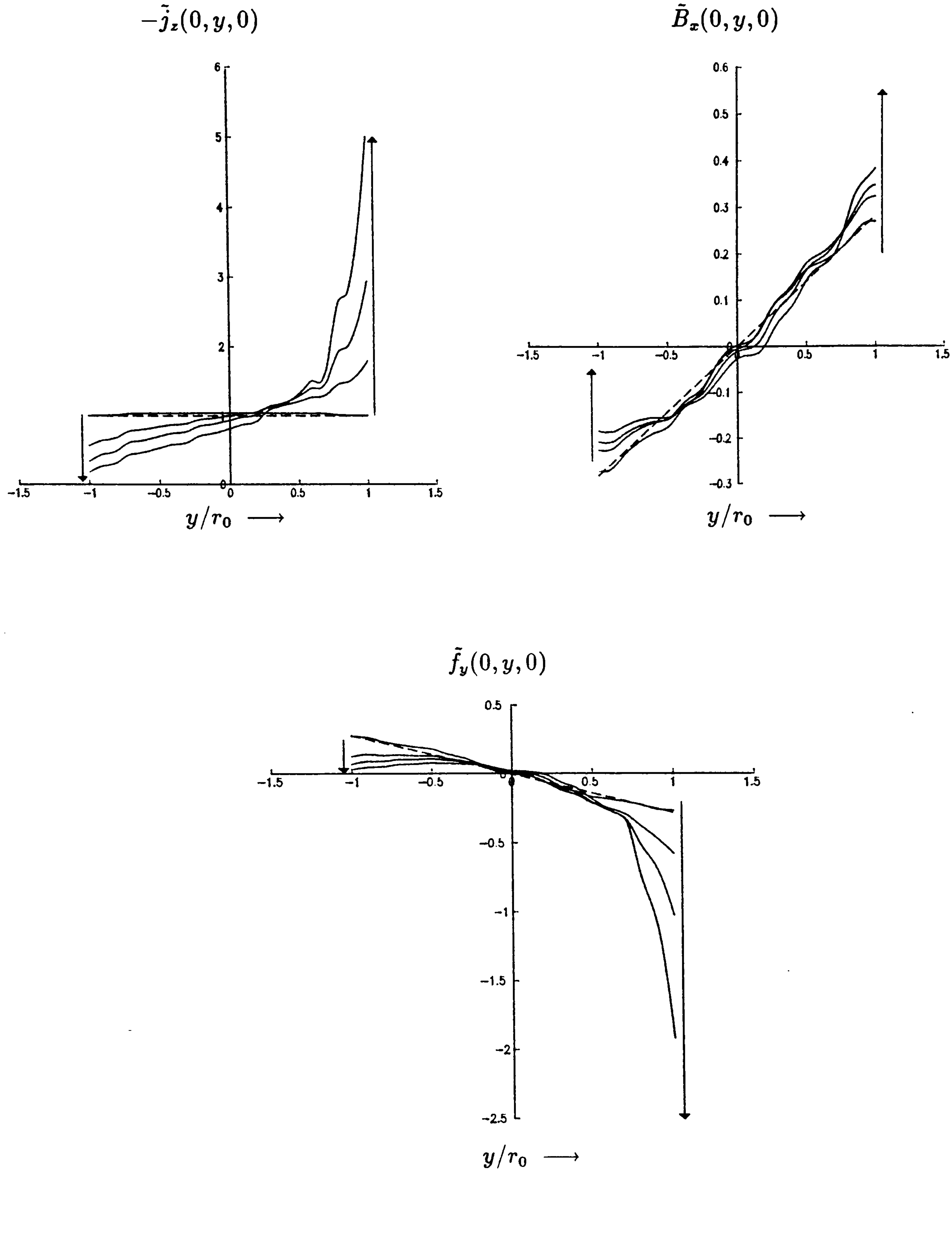

Figure 5.7: Field components on arc cathode spot
(dotted lines : analytical; real lines: numerical)

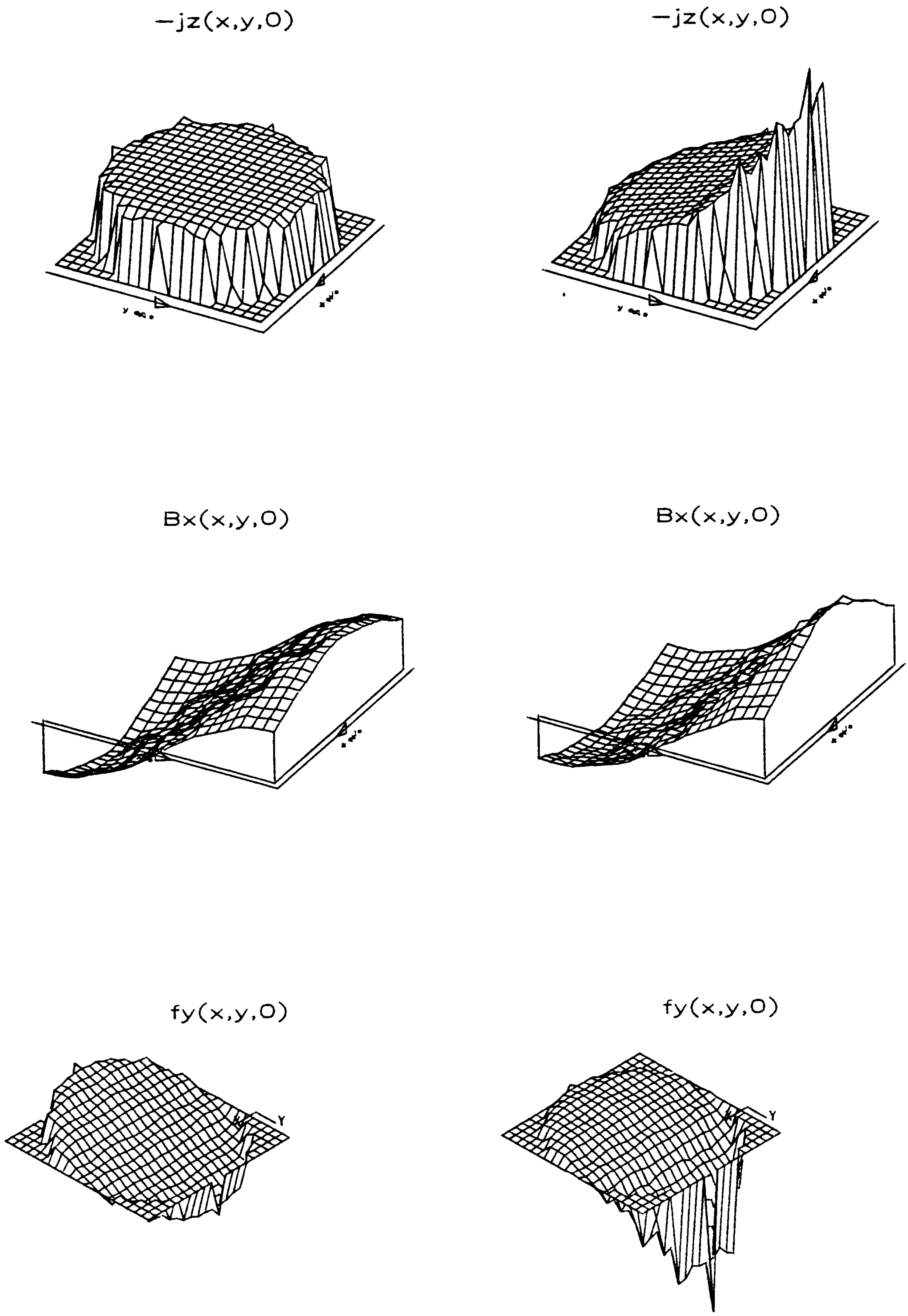

Figure 5.8: Field distributions on arc cathode spot
Left side: the straight arc (Arc-a); right side: the bent arc (Arc-g)

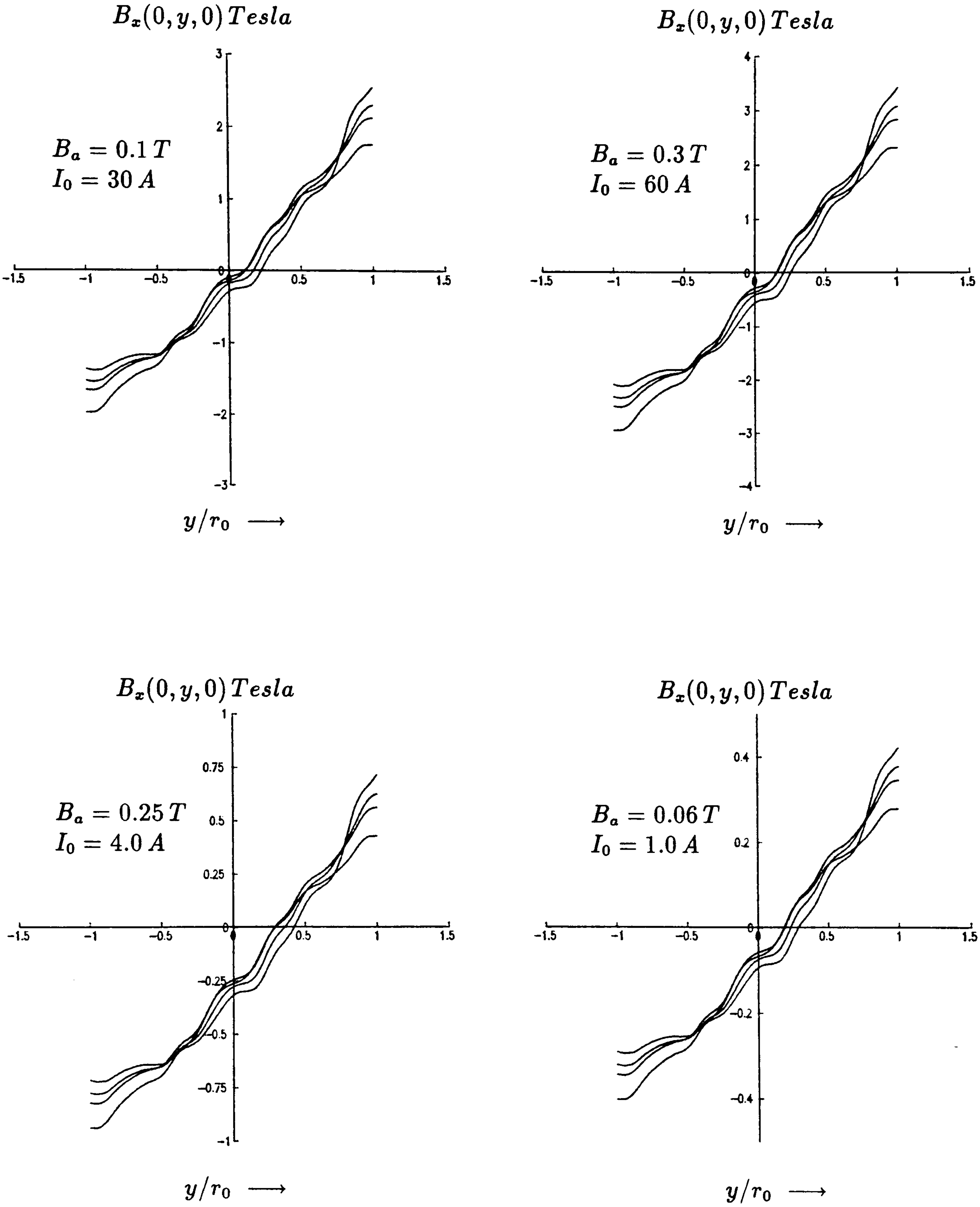

Figure 5.9: Resultant magnetic field on arc cathode spot
($j_a = 10^8\,A/cm^2$)

itself would not cause the retrograde motion in all cases. In other words, to make the spot move in the retrograde direction the condition that the self magnetic field exceeds the applied magnetic field is merely a necessary condition. So as a matter of fact, only the combination of the nonuniform current distribution on the spot together with this condition could serve for a complete cause of the retrograde motion.

According to our model, therefore, there exist two opposite motion tendencies within the cathode spot region and the spot will move as a whole in the direction in which the force is dominant. To demonstrate our model, we chose a set of experimental data from different sources and inserted them into our theory. The results are tabulated in Table 5.4. One can first see that the retrograde motion can indeed be predicted by our model if the average current density j_a is of the order of $10^8 A/cm^2$, which is in agreement with the values suggested by recent studies of spot current density [47, 49, 70]. Further explanation of the retrograde motion will be given in the next chapter.

Table 5.4: Numerical results of electrodynamic forces for different current densities and arc columns

(a) $I_0 = 1.0\,A$, $B_a = 0.06\,Tesla$, copper cathode, motion observed: retrograde, ref.[25]

$j_a(A/cm^2)$	arc-	$\|F_L\|/r_o^2(N/m^3)$	$\|F_R\|/r_o^2(N/m^3)$	$\|F_R/F_L\|$	motion predicted
10^6	e	1.70×10^9	0.00	0.00	Lorentzian
	g	1.62×10^9	0.00	0.00	Lorentzian
	k	1.56×10^9	6.98×10^5	4.47×10^{-4}	Lorentzian
10^7	e	1.60×10^{10}	2.63×10^9	0.165	Lorentzian
	g	1.43×10^{10}	3.50×10^9	0.244	Lorentzian
	k	1.21×10^{10}	5.79×10^9	0.477	Lorentzian
10^8	e	2.57×10^{11}	2.40×10^{11}	0.94	Lorentzian
	g	2.23×10^{11}	2.85×10^{11}	1.28	retrograde
	k	1.81×10^{11}	4.10×10^{11}	2.26	retrograde
5×10^8	e	2.30×10^{12}	3.27×10^{12}	1.42	retrograde
	g	1.96×10^{12}	3.82×10^{12}	1.94	retrograde
	k	1.56×10^{12}	5.35×10^{12}	3.43	retrograde

(b) $I_0 = 60\,A$, $B_a = 0.3\,Tesla$, copper cathode, motion observed: retrograde, ref.[27]

$j_a(A/cm^2)$	arc-	$\lvert F_L\rvert/r_o^2(N/m^3)$	$\lvert F_R\rvert/r_o^2(N/m^3)$	$\lvert F_R/F_L\rvert$	motion predicted
10^6	e	8.04×10^9	9.61×10^5	1.20×10^{-4}	Lorentzian
	g	7.44×10^9	1.15×10^7	1.54×10^{-3}	Lorentzian
	k	6.70×10^9	7.60×10^7	1.13×10^{-2}	Lorentzian
10^7	e	8.99×10^{10}	3.81×10^{10}	0.424	Lorentzian
	g	7.96×10^{10}	4.71×10^{10}	0.592	Lorentzian
	k	6.63×10^{10}	7.17×10^{11}	1.08	retrograde
10^8	e	1.73×10^{12}	2.12×10^{12}	1.22	retrograde
	g	1.49×10^{12}	2.48×10^{12}	1.67	retrograde
	k	1.19×10^{12}	3.51×10^{12}	2.95	retrograde
5×10^8	e	1.66×10^{13}	2.67×10^{13}	1.61	retrograde
	g	1.41×10^{13}	3.11×10^{13}	2.20	retrograde
	k	1.11×10^{13}	4.32×10^{13}	3.89	retrograde

(c) $I_0 = 540\,A$, $B_a = 0.7\,Tesla$, copper cathode, motion observed: retrograde, ref.[31]

$j_a(A/cm^2)$	arc-	$\lvert F_L\rvert/r_o^2(N/m^3)$	$\lvert F_R\rvert/r_o^2(N/m^3)$	$\lvert F_R/F_L\rvert$	motion predicted
10^6	e	1.83×10^{10}	3.75×10^8	2.06×10^{-2}	Lorentzian
	g	1.67×10^{10}	6.79×10^8	4.04×10^{-2}	Lorentzian
	k	1.46×10^{10}	1.30×10^9	8.90×10^{-2}	Lorentzian
10^7	e	2.33×10^{11}	1.40×10^{11}	0.601	Lorentzian
	g	2.05×10^{11}	1.70×10^{11}	0.829	Lorentzian
	k	1.69×10^{11}	2.51×10^{11}	1.49	retrograde
10^8	e	4.88×10^{12}	6.67×10^{12}	1.37	retrograde
	g	4.18×10^{12}	7.80×10^{12}	1.86	retrograde
	k	3.33×10^{12}	1.09×10^{13}	3.29	retrograde
5×10^8	e	4.84×10^{13}	8.19×10^{13}	1.69	retrograde
	g	4.11×10^{13}	9.50×10^{13}	2.31	retrograde
	k	3.22×10^{13}	1.32×10^{14}	4.10	retrograde

(d) $I_0 = 10\,A,\ B_a = 0.5\,Tesla$, copper cathode, motion observed: retrograde, ref.[23]

$j_a(A/cm^2)$	arc-	$\lvert F_L\rvert/r_o^2(N/m^3)$	$\lvert F_R\rvert/r_o^2(N/m^3)$	$\lvert F_R/F_L\rvert$	motion predicted
10^6	e	1.51×10^{10}	0.00	0.00	Lorentzian
	g	1.48×10^{10}	0.00	0.00	Lorentzian
	k	1.52×10^{10}	7.57×10^6	4.97×10^{-4}	Lorentzian
10^7	e	1.39×10^{11}	0.00	0.00	Lorentzian
	g	1.31×10^{11}	0.00	0.00	Lorentzian
	k	1.23×10^{11}	5.26×10^7	4.27×10^{-4}	Lorentzian
10^8	e	1.38×10^{12}	3.61×10^{11}	0.26	Lorentzian
	g	1.24×10^{12}	4.64×10^{11}	0.38	Lorentzian
	k	1.04×10^{12}	7.34×10^{11}	0.71	Lorentzian
5×10^8	e	9.71×10^{12}	7.95×10^{12}	0.82	Lorentzian
	g	8.42×10^{12}	9.49×10^{12}	1.12	retrograde
	k	6.92×10^{12}	1.38×10^{13}	1.99	retrograde

(e) $I_0 = 30\,A,\ B_a = 0.1\,Tesla$, copper cathode, motion observed: retrograde, ref.[34]

$j_a(A/cm^2)$	arc-	$\lvert F_L\rvert/r_o^2(N/m^3)$	$\lvert F_R\rvert/r_o^2(N/m^3)$	$\lvert F_R/F_L\rvert$	motion predicted
10^6	e	2.68×10^9	4.92×10^8	1.84×10^{-1}	Lorentzian
	g	2.40×10^9	6.48×10^8	2.70×10^{-1}	Lorentzian
	k	2.03×10^9	1.06×10^9	5.22×10^{-1}	Lorentzian
10^7	e	4.38×10^{10}	4.22×10^{10}	0.96	Lorentzian
	g	3.81×10^{10}	5.01×10^{10}	1.32	retrograde
	k	3.09×10^{10}	7.19×10^{10}	2.33	retrograde
10^8	e	1.06×10^{12}	1.68×10^{12}	1.59	retrograde
	g	9.01×10^{11}	1.95×10^{12}	2.17	retrograde
	k	7.08×10^{11}	2.72×10^{12}	3.84	retrograde
5×10^8	e	1.10×10^{13}	1.99×10^{13}	1.81	retrograde
	g	9.29×10^{12}	2.30×10^{13}	2.48	retrograde
	k	7.22×10^{12}	3.18×10^{13}	4.40	retrograde

(f) $I_0 = 6\,A$, $B_a = 0.2\,Tesla$, mercury cathode, motion observed: retrograde, ref.[12]

$j_a(A/cm^2)$	arc-	$\lvert F_L\rvert/r_o^2(N/m^3)$	$\lvert F_R\rvert/r_o^2(N/m^3)$	$\lvert F_R/F_L\rvert$	motion predicted
	e	5.83×10^9	0.00	0.00	Lorentzian
10^6	g	5.63×10^9	0.00	0.00	Lorentzian
	k	5.58×10^9	2.63×10^6	4.71×10^{-4}	Lorentzian
	e	5.19×10^{10}	2.72×10^9	5.24×10^{-2}	Lorentzian
10^7	g	4.72×10^{10}	4.15×10^9	8.79×10^{-2}	Lorentzian
	k	4.08×10^{10}	7.62×10^9	0.187	Lorentzian
	e	7.18×10^{11}	5.12×10^{11}	0.71	Lorentzian
10^8	g	6.29×10^{11}	6.16×10^{11}	0.98	Lorentzian
	k	5.16×10^{11}	9.02×10^{11}	1.75	retrograde
	e	6.02×10^{12}	7.58×10^{12}	1.26	retrograde
5×10^8	g	5.17×10^{12}	8.89×10^{12}	1.72	retrograde
	k	4.13×10^{12}	1.25×10^{13}	3.03	retrograde

(g) $I_0 = 4\,A$, $B_a = 0.25\,Tesla$, mercury cathode, motion observed: retrograde, ref.[14]

$j_a(A/cm^2)$	arc-	$\lvert F_L\rvert/r_o^2(N/m^3)$	$\lvert F_R\rvert/r_o^2(N/m^3)$	$\lvert F_R/F_L\rvert$	motion predicted
	e	7.46×10^9	0.00	0.00	Lorentzian
10^6	g	7.30×10^9	0.00	0.00	Lorentzian
	k	7.43×10^9	3.67×10^6	4.90×10^{-4}	Lorentzian
	e	6.72×10^{10}	2.61×10^5	3.89×10^{-6}	Lorentzian
10^7	g	6.23×10^{10}	5.34×10^7	8.57×10^{-4}	Lorentzian
	k	5.63×10^{10}	4.56×10^8	8.11×10^{-3}	Lorentzian
	e	7.43×10^{11}	3.05×10^{11}	0.41	Lorentzian
10^8	g	6.59×10^{11}	3.78×10^{11}	0.57	Lorentzian
	k	5.49×10^{11}	5.77×10^{11}	1.05	retrograde
	e	5.59×10^{12}	5.51×10^{12}	0.97	Lorentzian
5×10^8	g	4.86×10^{12}	6.53×10^{12}	1.35	retrograde
	k	3.93×10^{12}	9.36×10^{13}	2.38	retrograde

Chapter 6

The Electrodynamic Explanation

6.1 The role of the electrodynamic force

It is instructive for us to judge the decisive role of the electrodynamic force in the retrograde motion. Following Mitterauer [72], the vapour pressure p of the cathode material evaporating from the cathode spot surface can be approximated by the relation

$$p = 10^{A'-B'/T}\ (\mathrm{Pa}) \tag{6.1}$$

where the constants for copper and for $T > 2826\,K$ are $A' = 10.7$ and $B' = 1.63\times10^4\,K$. If the spot surface temperature $T = 4\times10^3\,K$ [73], Eqn. (6.1) yields a surface vapour pressure of $42\,atm$ ($1\,atm \approx 10^5\mathrm{Pa}$). This vapour pressure may appear high, but there is experimental justification. According to Robertson [74], the force on the cathode of a copper arc was measured by a pendulum and for the ambient gases of hydrogen and nitrogen at $20 \sim 500\,mmHg$ pressure and at $10A$ arc current, the force was found to lie in the range $2 \sim 14\times10^{-5}\,N$. If this force is mainly due to the reaction of the metal vapour jet erupting from an active crater, whose size would be larger than the real spot or current carrying area [73], and the radius of the crater is estimated by $r_c = r^*\exp(I_0/I^*)$ where $r^* = 1.7\,um$ and $I^* = 83\,A$ for copper [47], the corresponding pressure is found to be $16 \sim 111\,atm$. It is therefore not surprising to have the high vapour pressure from the empirical formula of Eqn. (6.1). Thus the average thermal velocity v_T related to the spot vapour pressure can be found to be the order of $10^3\,m/s$ by assuming $v_T = (3\kappa T/m_a)^{1/2}$ [75], where $\kappa = 1.38\times10^{-23}\,J/K$ is Boltzmann's constant and m_a the atomic mass. Now looking at Table 5.4(d) where we have similar experimental conditions [23], namely, at $30\,mmHg$ ambient pressure of a mixture of air and argon and at $10\,A$ arc current for the copper arc, we can find that the density $f_a = |F_R - F_L|/(\pi r_0^2)$ of the average net electrodynamic force for the retrograde motion predicted by our theory is the order of $10^{12}\,N/m^3$ for $j_a = 5 \times 10^8\,A/cm^2$. Multiplying this force density by $2r_0$ the diameter of the spot, we obtain $2r_0 f_a = 1.6 \times 10^6\,N/m^2$ which is equivalent to an electrodynamic pressure of the order of $16\,atm$. It turns out that the electrodynamic pressure is comparable to the vapour pressure so that the electrodynamic force predicted by our theory can be responsible for the retrograde motion with the velocity less than $10^3\,m/s$ as observed.

The important role of the electrodynamic force in the spot directed motion could be estimated from another point of view. It is obvious that the electrodynamic force resulting from our model only has a direct effect on the current carriers of the spot current. Although the electrons are major current carriers, the magnetic force on the electrons can be transferred to the ions through the Hall field [76]. Furthermore the spot plasma is highly ionized [47, 75], and the ionic mass m_i is much larger than the electronic mass m_e ($m_i/m_e \approx 10^5$). Thus the swarm motion of the spot is mainly due to the motion of the ions subject to the electrodynamic force so that we simply employ the mobility theory of ions [77] and suppose

$$v_d = \frac{F_a}{m_i}\tau \tag{6.2}$$

where v_d represents the average directed velocity of the spot; F_a denotes the average electrodynamic force on the ion and τ is the average free time between two collisions. Since $F_a = f_a/n_i$ and $\tau = (n_a \sigma_i v_i)^{-1}$, where f_a is the density of the average net electrodynamic force on the spot; n_i the ion density; n_a the neutral particle density; σ_i the ionic collision cross-section and v_i the mean ion thermal velocity, Eqn. (6.2) becomes

$$v_d = \frac{f_a}{n_i n_a \sigma_i v_i m_i} \tag{6.3}$$

The experimental data are available for $n_i = 10^{20} cm^{-3}$ [47], $v_i = 10^5 cm/s$ [47], and $\sigma_i = 10^{-15} cm^2$ [79, 80]. However, to the best of our knowledge, there is no reliable experimental datum for the neutral particle density in the spot region. The reported data for n_a vary over a wide range, from 10^{16} to $10^{22}\,cm^{-3}$ depending on the experimental conditions and diagnostic methods used [81]. Considering the spot plasma is highly ionized [47, 75], we assume $n_a = 10^{19}\,cm^{-3}$. The ionic mass $m_i = M_i m_0$ amounts to $10^{-25}\,kg$, where M_i is the atomic mass number and $m_0 = 1.66 \times 10^{-27}\,kg$. Referring to Table 5.4 we can find that for the retrograde motion predicted by our theory, f_a is the order of $10^{11} \sim 10^{13}\,N/m^3$. Substituting these data into Eqn. (6.3) yields $v_d = 10^1 \sim 10^3\,m/s$ which is among the retrograde velocities observed.

Although the above estimation is rather rough and the determination of the relation between the electrodynamic force and the retrograde velocity needs more sophisticated considerations, it at least lets us see the important role of the electrodynamic force in the retrograde motion of the cathode spot.

6.2 Retrograde motion of a single spot

A number of the reported features of the retrograde motion of the single spot can be explained by our model as below.

- *The retrograde motion is temperature dependent. With increasing cathode temperature, the retrograde velocity decreases [35]; and the retrograde motion can be reversed if the temperature is sufficiently high [11].* As the cathode temperature is increased, the spot current density is observed to decrease [35]. In our model the ratio of $|F_R/F_L|$ decreases with decreasing spot current density as shown in Fig.6.1; thus the retrograde velocity decreases with increasing cathode temperature. If the cathode is heated to a sufficiently high temperature, which can vary with the cathode material, the spot current density can be so low that $|F_R/F_L| < 1$ and the motion is reversed.

- *Lower background gas pressures favour retrograde motion and the motion can be reversed if the gas pressure rises above a critical value [14, 27, 31].* The bending of the arc also depends on the background gas pressure. The lower the pressure, the more bent is the arc column. As a result, the ratio of $|F_R/F_L|$ increases and

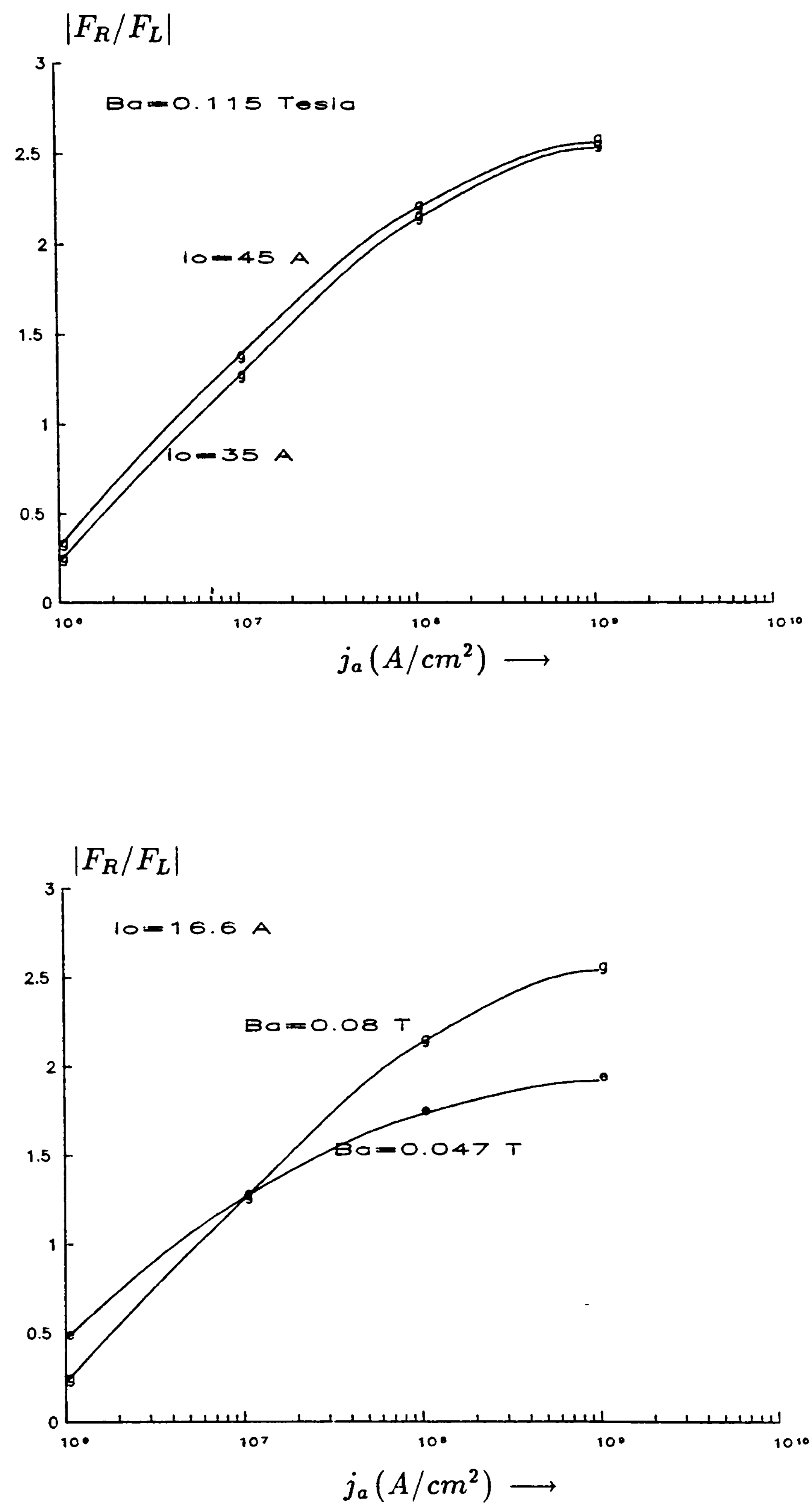

Figure 6.1: $|F_R/F_L|$ vs cathode spot average current density
The current density is in logarithmic scale
The experimental parameters refer to Fang [34]

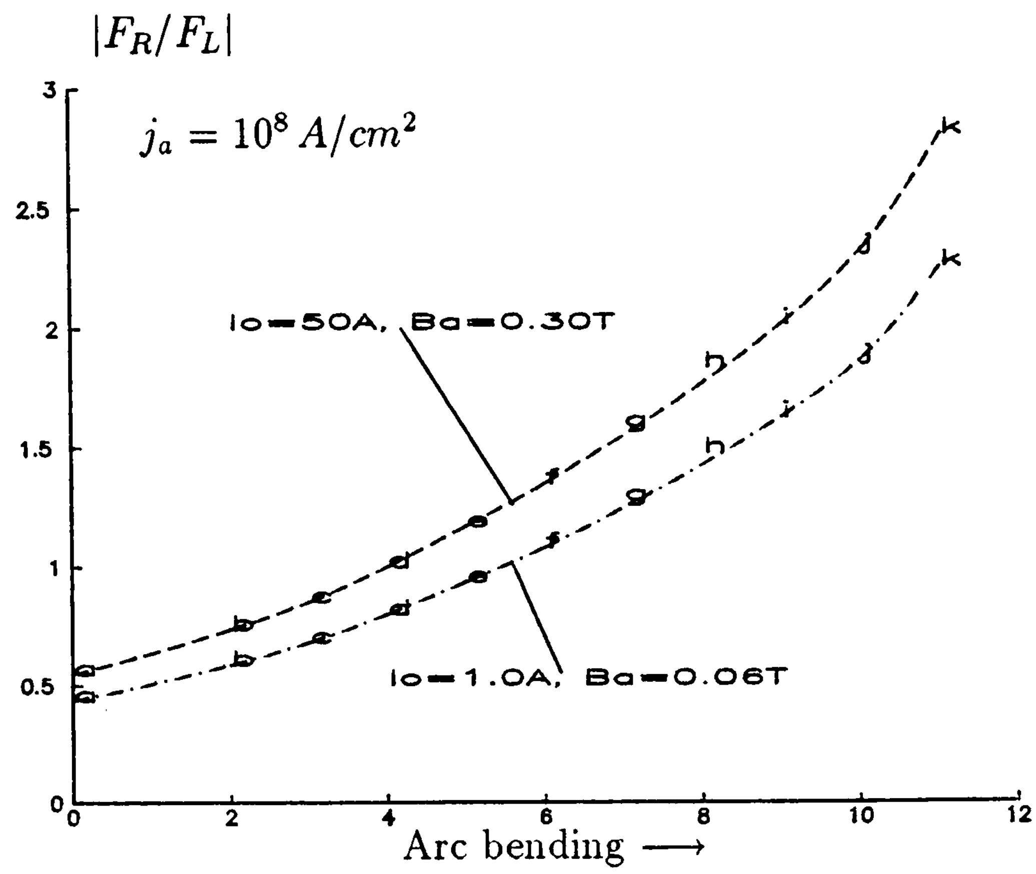

Figure 6.2: $|F_R/F_L|$ as a function of arc bending
Experimental parameters refer to Roman [27] and Gallagher [14]

so does the retrograde velocity. On the other hand, if the pressure is increased, the arc column becomes straight and the ratio of $|F_R/F_L|$ decreases and can be smaller than unity above a certain pressure so that the direction of motion changes to the Lorentzian direction. Figure 6.2 illustrates $|F_R/F_L|$ against arc bending.

- *The retrograde velocity is generally found to increase with an increase in the magnitude of the applied magnetic field [27, 34, 41]. However, reversal of the motion occurs with a very strong field [23].* The model proposed clearly shows the two simultaneous effects of the applied magnetic field, namely (a) bending the arc column in the Lorentzian direction; (b) enhancing the force component F_L. Because the first effect is in favour of the retrograde motion and is opposite to the second one, the resultant effect of increasing the applied magnetic field will depend on the dominant one of the two effects. As the applied magnetic field is

Table 6.1: Computation of forces for a strong magnetic field

$I_0 = 10\,A$, $B_a = 1.2\,Tesla$, copper cathode, motion observed: Lorentzian, ref.[23]

$j_a(A/cm^2)$	arc-	$\lvert F_L\rvert/r_o^2(N/m^3)$	$\lvert F_R\rvert/r_o^2(N/m^3)$	$\lvert F_R/F_L\rvert$	motion predicted
10^8	e	3.21×10^{12}	9.88×10^8	3.08×10^{-4}	Lorentzian
	g	2.96×10^{12}	8.35×10^9	2.82×10^{-3}	Lorentzian
	k	2.66×10^{12}	4.07×10^{10}	1.53×10^{-2}	Lorentzian
5×10^8	e	1.63×10^{13}	3.62×10^{12}	0.22	Lorentzian
	g	1.46×10^{13}	4.70×10^{12}	0.32	Lorentzian
	k	1.23×10^{13}	7.54×10^{12}	0.61	Lorentzian
10^9	e	3.62×10^{13}	1.59×10^{13}	0.44	Lorentzian
	g	3.21×10^{13}	1.96×10^{13}	0.61	Lorentzian
	k	2.67×10^{13}	2.97×10^{13}	1.11	retrograde
5×10^9	e	2.75×10^{14}	2.79×10^{14}	1.01	retrograde
	g	2.39×10^{14}	3.31×10^{14}	1.38	retrograde
	k	1.93×10^{14}	4.73×10^{14}	2.45	retrograde

increased from a lower level, the arc column is expected to be bent at first rapidly and then less so due to a limit of the bending. Hence, the first effect is dominant and the retrograde velocity increases before this limit is reached. Then, the second effect becomes dominant and the motion will be reversed when $|F_L| > |F_R|$. The dependence of the average net force density, i.e, $f_a = (|F_R| - |F_L|)/(\pi r_0^2)$ on the applied magnetic field is shown in Fig.6.3, where we take the Arc-k as the most bent arc. The prediction of the motion in the Lorentzian direction with a strong field can also be seen in Table 6.1. It should be noted that our model also predicts an upper limit of j_a with an order of $5 \times 10^9 A/cm^2$.

- *The critical pressure increases with an increase of the applied magnetic field [17].* As previously stated an increase in the applied magnetic field will cause the arc

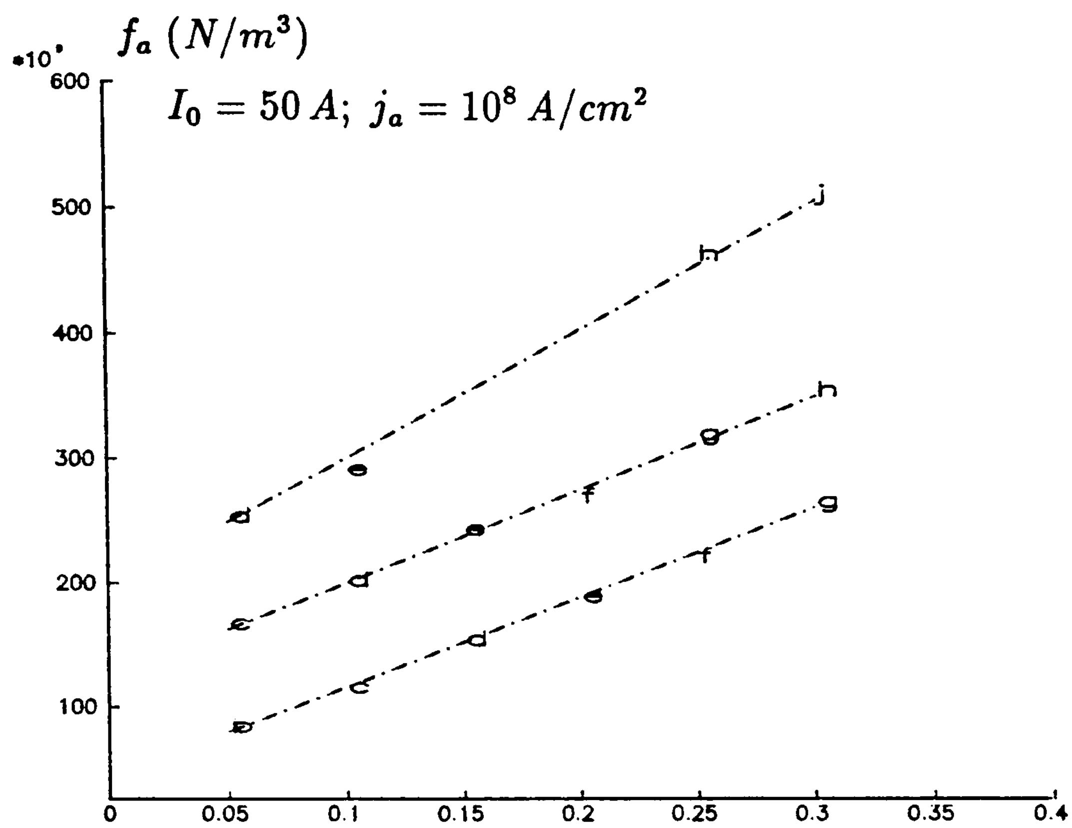

(a) $B_a\ (Tesla) \longrightarrow$

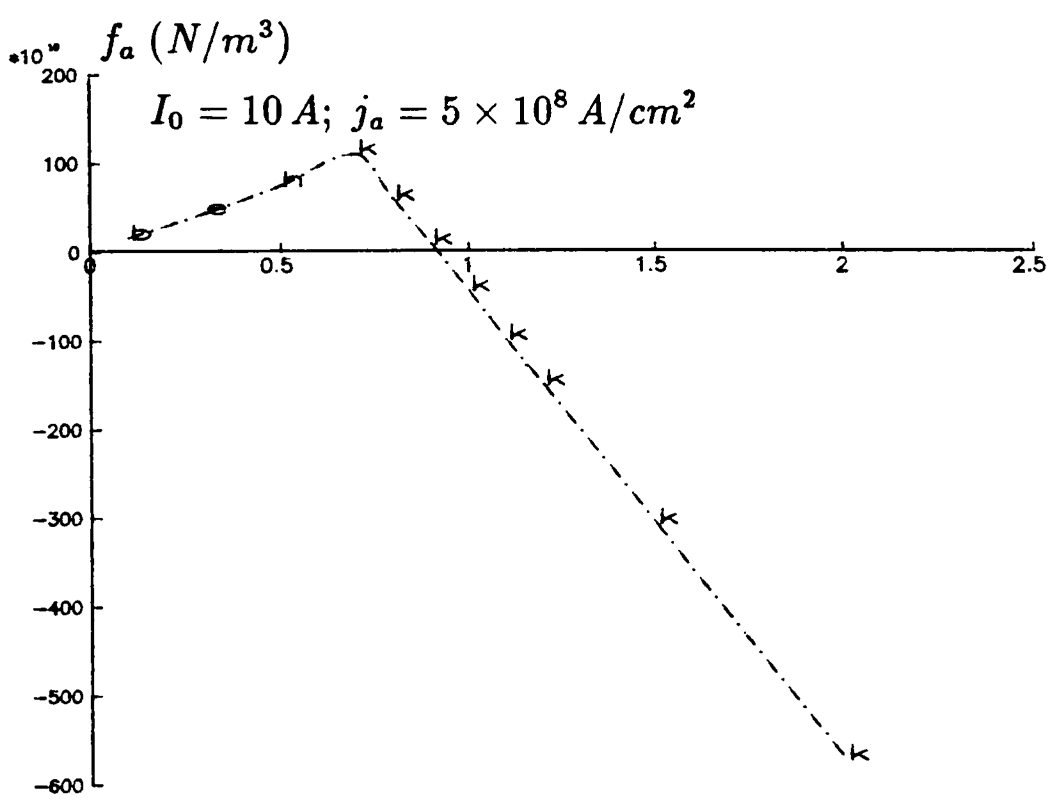

(b) $B_a\ (Tesla) \longrightarrow$

Figure 6.3: Average net force density vs the applied magnetic field
(a) Experimental parameters refer to Roman [27]
(b) Experimental parameters refer to Robson [23]

column to bend before reaching a limit. On the other hand, an increase in the background gas pressure makes the arc column straighter. At a reversal position of the arc column, the effects of the increase in the two quantities can cancel each other out which directly leads to the observed result.

- *In vacuum or low pressure the retrograde velocity was found to increase with an increase in arc current [14, 34, 41].* According to the proposed model it can be shown as Fig.6.4 that the average net force density increases with an increase in arc current, so does the retrograde velocity.

- *The retrograde motion depends on the material and surface condition of the cathode [25, 30].* The connection of the present model to this feature is twofold. Firstly, the cathode current density is found to be material-sensitive, so is the force predicted by the model. Secondly, the spot is a plasma source of dense metal vapour evaporated from the cathode material so that the plasma mass density of the spot will also affect the spot motion.

- *The critical pressure increases with decreasing separation of the electrodes [9, 38, 71] and very short ($\sim 0.5mm$) arcs have been driven in the retrograde direction in atmospheric air [21].* If decreasing the electrode separation presses the bent arc on to the cathode and makes it even more bent; the resultant effect is opposite to that due to an increase in the background pressure so that the retrograde motion persists to higher pressures the shorter the electrode separation. For the same reason a very short separation can encourage retrograde motion in a pressure as high as atmospheric, as is observed.

- *If the applied magnetic field is inclined with respect to the cathode surface, the moving cathode spot has an extra velocity component in the direction of the acute angle between the field and the cathode surface [10, 22].* The transverse component of the applied magnetic field gives rise to a bending of the arc column. As a consequence there is a component of the arc current flowing parallel to the cathode surface and in the retrograde direction. This component of the arc current interacts with the normal component of the applied magnetic field, which gives

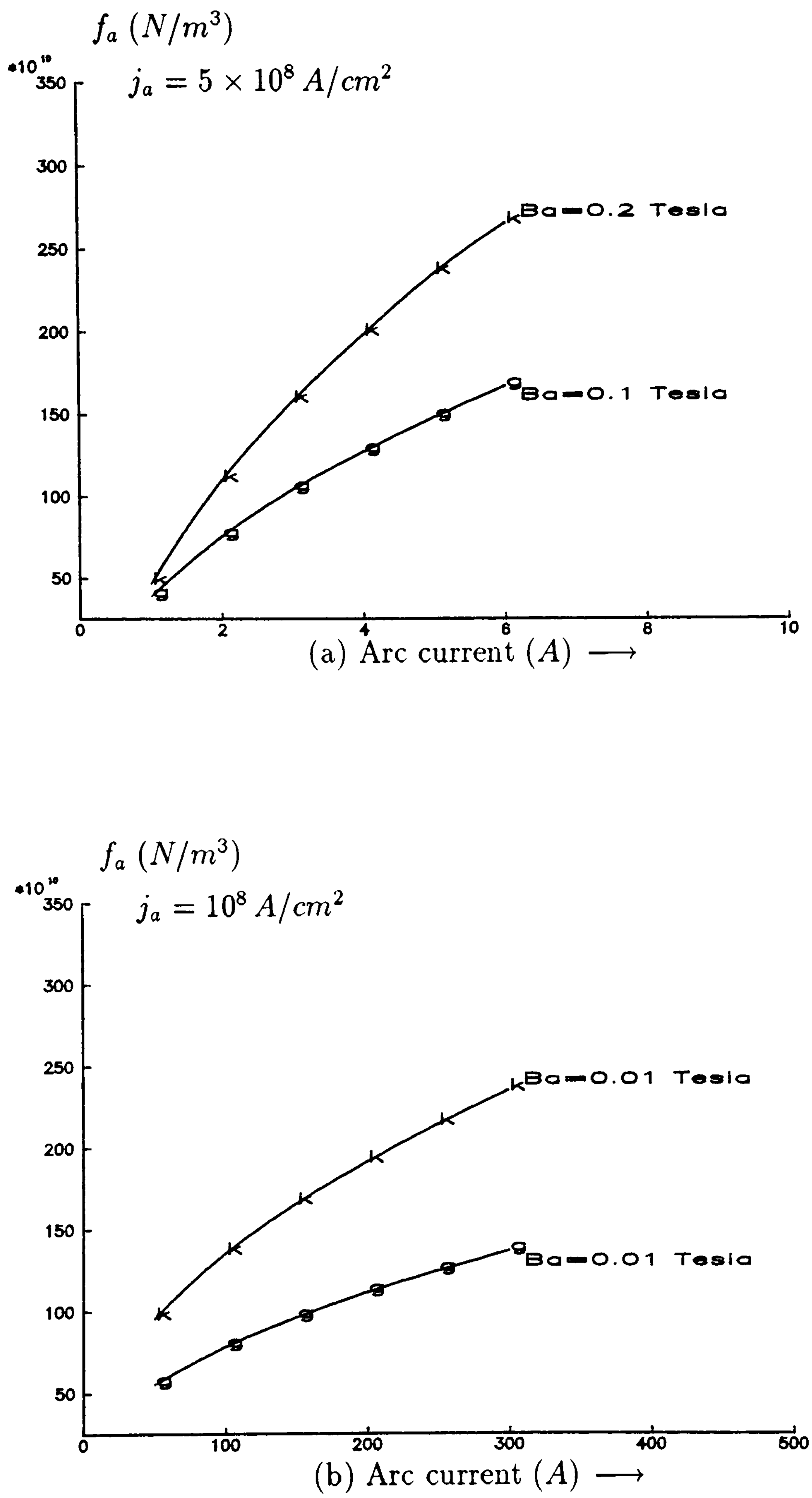

Figure 6.4: Average net force density vs arc current
(a) Experimental parameters refer to Gallagher [14]
(b) Experimental parameters refer to Swift [41]

rise to an extra force component on the cathode spot region in the direction of the observed drift. This extra force component is therefore responsible for the sideways drift.

6.3 Retrograde motion of multi-spots

The retrograde motion of multi-spots on the cathode in vacuum arcs under the influence of the self-generated magnetic field has also been reported [82, 83, 84, 85]. The arc currents for these experiments are sufficiently high (up to $10kA$) that the cathode region consists of many independent cathode spots which are observed to be moving radially outwards on the cathode in a basically ring-shaped pattern. A model of multispot formation after Djakov and Holmes [82] is sketched in Fig.6.5. The previous investigators attributed such a kind of motion to the retrograde motion because they thought that each spot could be considered as moving in an equivalent applied transverse magnetic field $\mathbf{B}_a(R)$, which corresponded to the inherent (azimuthal) magnetic field of the remaining spots distributed around the ring of a radius R, the spot would have been driven moving inwards to the ring centre by the $\mathbf{I}_s \times \mathbf{B}_a(R)$ force, where $\mathbf{I}_s$ denoted the spot current flowing into the cathode. In the earlier studies [82] the inherent (azimuthal) magnetic field was simply calculated by $\mu_0 I_0/4\pi R$ with I_0 the total arc current from an assumed discharge current distribution whereas in the latter experiments [84, 85] the field was measured directly with a magnetic probe positioned about $2 \sim 3\,mm$ from the cathode surface.

It is essential to point out that the previous investigators ignored the fact that each spot in reality is not a rigid point and in the region occupied by that spot the magnetic field generated by the spot current itself can play an important role in determining the motion of that spot. To demonstrate this, let us assume that each spot carries a linear current $I_s = I_0/N$, where N is the number of spots. The azimuthal magnetic induction

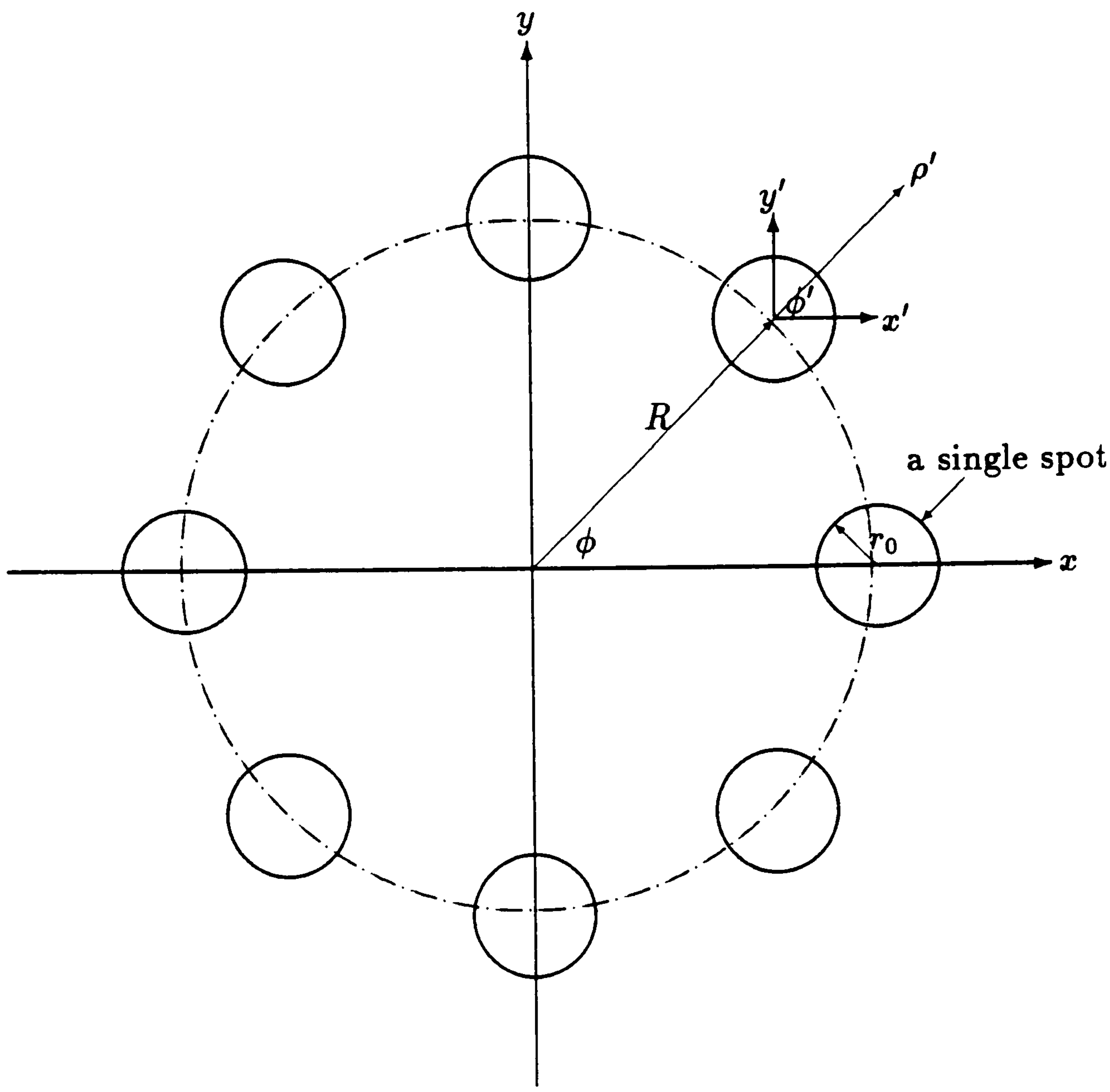

Figure 6.5: Model of multi-spot formation on cathode surface

generated by each spot in the local coordinates (ρ', ϕ') as shown in Fig.6.5 is given by

$$B_{\phi'}(\rho') = \begin{cases} -\dfrac{\mu_0 I_s}{2\pi\rho'} & \text{if } \rho' \geq r_0 \\ \\ -\dfrac{\mu_0 I_s}{2\pi\rho'}\left(\dfrac{\rho'}{r_0}\right)^2 & \text{if } \rho' \leq r_0 \end{cases} \tag{6.4}$$

which can further be decomposed into two components in the global coordinates (x, y)

$$\begin{aligned} B_x(x,y) &= -B_{\phi'}(\rho')\sin\phi' \\ B_y(x,y) &= B_{\phi'}(\rho')\cos\phi' \end{aligned} \tag{6.5}$$

with

$$\begin{aligned} &\rho' = \sqrt{x'^2 + y'^2} \quad \text{and} \quad \phi' = \tan^{-1}(y'/x') \\ &x' = x - R\cos\phi \quad \text{and} \quad y' = y - R\sin\phi \end{aligned} \tag{6.6}$$

where R is the ring radius and ϕ is the azimuthal angle of the spot centre with respect to the origin of the global coordinates. Considering a single spot as indicated in Fig.6.5, we are merely interested in the field component B_y over the region occupied by that spot and the results computed for $N = 50, 100$ and the different ratios of R/r_0 are plotted in Fig.6.6, where $\tilde{B}_y$ is normalized by $B_y/\mu_0\sqrt{I_s j_a}$ with $j_a = I_s/\pi r_0^2$ the average spot current density. One can immediately see from Fig.6.6 that the resultant field of combination of the self-field of the single spot (denoted by the real line) and the equivalent applied field of the remaining spots (denoted by the dotted line) can change sign on the inward and the outward sides within the spot and the equivalent applied field decreases with an increase in the ratio of the ring radius to the spot radius. Taking the experimental parameters $j_a = 10^8\,A/cm^2$ and $I_s = 100\,A$ (for copper), which result in $r_0 = 5.6 \times 10^{-3}\,mm$ and assuming $R = 1\,mm$, we have already a ratio of R/r_0 as large as 178. In recent experiments [84, 85] the ring radii observed are supposed to be larger than $3\,mm$ because at the centre of the cathode face there is a $6\,mm$ diameter hole for a trigger assembly, which gives a minimum $R/r_0 = 534$ so that the equivalent applied field is even smaller and can be ignored.

Based on the above arguments we believe that the so-called retrograde motion of the multispot under the influence of the self-generated magnetic field can simply be understood by extending our single spot model, which is strongly supported by the experimental observations of the multispot vacuum arcs, namely (i) the arc appears to be constricted near the anode [86, 87, 88]; (ii) the arc current is more concentrated closer to the axis near the anode in comparison with the cathode [86, 87, 89]. The theoretical predictions of constrictions in both the arc current and the plasma flow from the spots can also be found elsewhere [90, 91]. The proposed physical model for the multispot arc is sketched in Fig.6.7, where the bending of each spot column near the cathode surface inwards to the centre axis of the arc is the direct result of the constrictions.

According to our single spot model, the current density is stronger on the inward side of each spot due to the inward bending so is the magnetic field induced by that spot current, which can exceed the equivalent applied magnetic field generated by the

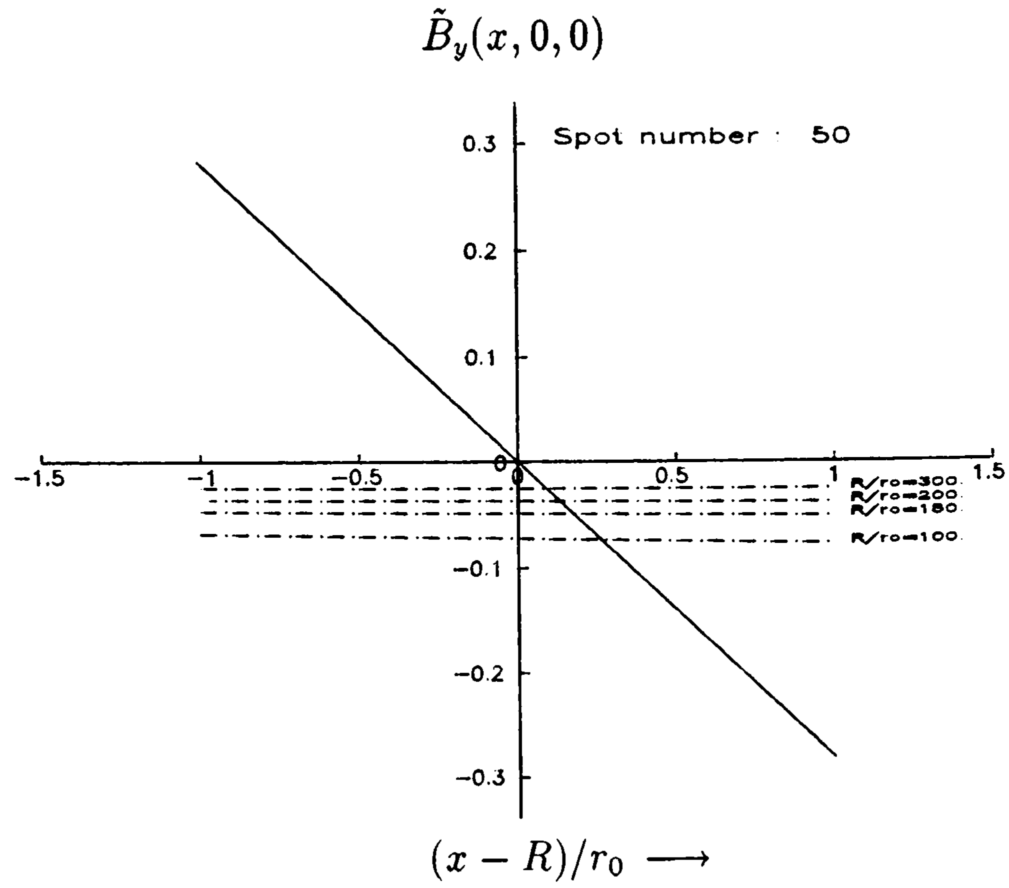

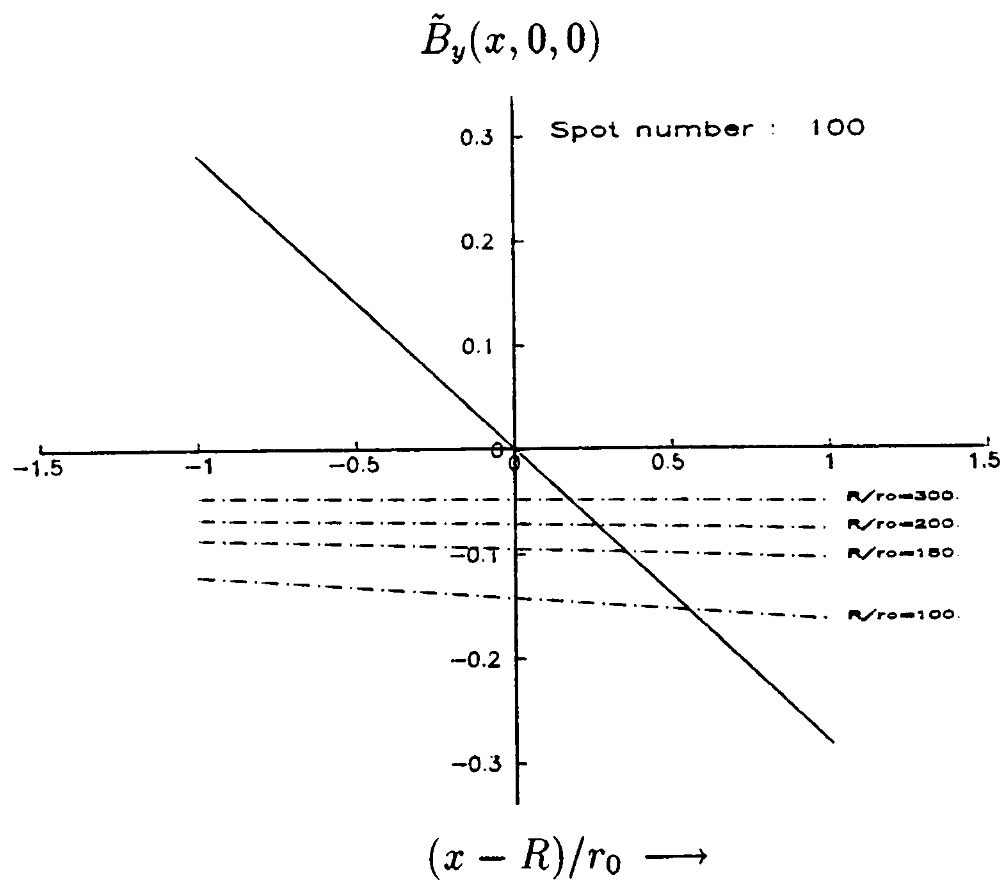

Figure 6.6: Magnetic field of multi-spots
Real lines: the field of the single spot
Dotted lines: the field of the remaining spots

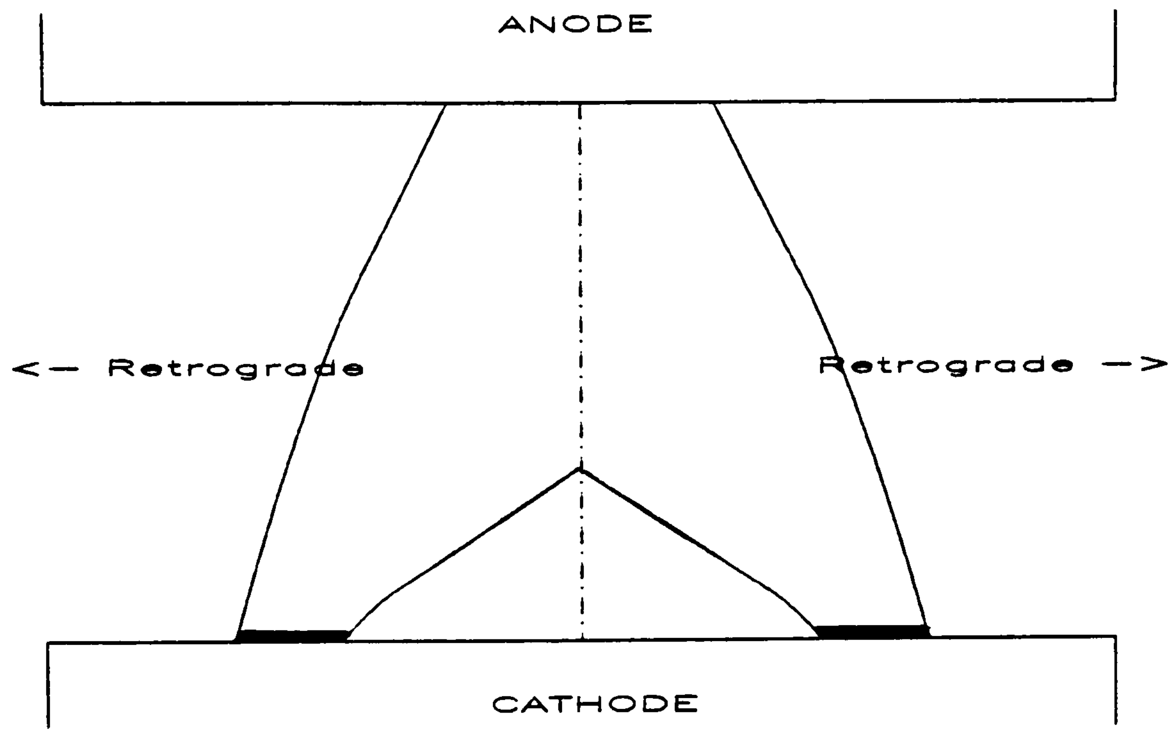

Figure 6.7: Model of the multispot arc

other spot currents in the opposite direction on the inward side of that spot as we have just demonstrated. Therefore, the resultant electrodynamic force on each spot is dominant in the outward direction and will drive each spot radially outwards which can certainly account for the retrograde motion observed. Similarly, some typical features of the retrograde motion of the multispot arc can be explained by our model.

- *The retrograde velocity is independent of arc current [84, 85].* In our single spot model the retrograde velocity is dependent on the arc current which is nothing else but the spot current. In the case of the multispot arc each spot carries approximately the same current which is independent of the total arc current [85]. Although the equivalent applied magnetic field is dependent on the arc current, it is not important in a single spot region as previously demonstrated. Therefore, as long as the spot current is invariable with respect to arc currents, our model, which relates to the spot current rather than the arc current, can also predict this feature.

- *Saturation of the retrograde velocity can be observed at high self-generated mag-*

netic fields measured against different ring radius R for a total arc current [84, 85]. As the self-generated magnetic field is increased (the smaller the expansion of the discharge) a limit to the bending is approached. According to our model the retrograde velocity increases as the spot columns become more bent so it is expected that the retrograde velocity will be increased slowly as the spot columns are reaching the bending limit, which directly leads to the observation.

- *The retrograde velocity decreases with increasing the applied axial magnetic field [85].* According to our model the more bent the spot columns, the higher is the retrograde velosity. If the applied axial magnetic field reduces the bending of the spot columns, which is at least supported by the experimental observation that the constrictions in both the plasma flow and the arc current are less pronounced when the axial magnetic field is applied [87], it turns out that the stronger the applied axial magnetic field, the less bent are the spot columns, and the smaller is the retrograde velocity.

Part II

Some Recent Issues in Electrodynamics

Chapter 7

On Ampère and Lorentz force laws

7.1 Development of the force laws

In recent years there has been a new controversy about the electrodynamic force laws, namely, the Ampère and Lorentz force laws [92] - [110]. A focus of the controversy lies on whether the two force laws are equivalent in conducting current systems. To help to clarify this matter, it is necessary to look back on the history of development of the two force laws, which has been overlooked in most of the previous discussions. Although a good account of the development of the Ampère and Lorentz force laws can be found in Maxwell's famous book "A Treatise on Electricity and Magnetism" [111] as well as Whittaker's one "A History of the Theories of Aether and Electricity" [112], for our purpose, let us review it briefly hereon before going any further.

On 21 July 1820, Hans Christian Oersted published his discovery that a wire connecting the ends of a voltaic battery affected a magnet in its vicinity. It appears therefore that in the space surrounding a wire transmitting an electric current a magnet is acted on by forces depending on the position of the wire and on the strength of the current. The space in which these forces act may therefore be considered as a magnetic field. However, Oersted did not determine the quantitative law of the action.

Having repeated and extended Oersted's experiments, Jean-Baptiste Biot and Félix Savart soon found the law

$$\mathbf{B}(\mathbf{r}) = \frac{\mu_0}{4\pi}\int_{\tau'} \frac{\mathbf{j}(\mathbf{r}')d\tau' \times (\mathbf{r}-\mathbf{r}')}{|\mathbf{r}-\mathbf{r}'|^3} \tag{7.1}$$

where $\mathbf{B}$ represents the magnetic induction; $\mathbf{j}$ denotes the current density; $\mathbf{r}$ and $\mathbf{r}'$ are the position vectors of the field and the source respectively and τ' indicates the whole source current region.

The next step came from André-Marie Ampère, who on 18 September 1820 showed that two parallel wires carrying currents attract each other if the currents are in the same direction, and repel each other if the currents are in opposite directions. During the next three years Ampère continued to prosecute the researches thus inaugurated, and in 1825 published his electrodynamic force law

$$d^2\mathbf{F}_A = \frac{\mu_0}{4\pi}\frac{\mathbf{R}}{R^3}\left[\frac{3}{R^2}(\mathbf{j}(\mathbf{r}')d\tau'\cdot\mathbf{R})(\mathbf{j}(\mathbf{r})d\tau\cdot\mathbf{R}) - 2(\mathbf{j}(\mathbf{r}')d\tau'\cdot\mathbf{j}(\mathbf{r})d\tau)\right] \tag{7.2}$$

where $d^2\mathbf{F}_A$ indicates the force on the current element $\mathbf{j}(\mathbf{r})d\tau$ exerted by the current element $\mathbf{j}(\mathbf{r}')d\tau'$ and $\mathbf{R} = (\mathbf{r}-\mathbf{r}')$. It should be remarked that the Ampère force law of mutual action of electric currents is founded on four experimental facts and one assumption.[1] With reference to these experiments, it may be observed that every electric current forms a closed circuit, so that the ultimate result of each experiment is the action of one or more closed current upon the whole or a part of a closed current. Hence, as Maxwell points out, "no statement about the mutual action of two elements of circuits can be said to rest on purely experimental grounds",[2] it is more precise to interpret Ampère force law as

$$d\mathbf{F}_A = \int_{\tau'} d^2\mathbf{F}_A \tag{7.3}$$

The other weakness of Eqn. (7.2) lies in the assumption that the force between two current elements acts along the line joining them. It is clear that one may, if one pleases, adopt another assumption and add to this expression any term which vanishes when integrated over τ'. One of such alternative formulae was given by Grassmann in 1845

$$d^2\mathbf{F}_L = \frac{\mu_0}{4\pi}\frac{1}{R^3}[(\mathbf{j}(\mathbf{r})d\tau\cdot\mathbf{R})\mathbf{j}(\mathbf{r}')d\tau' - (\mathbf{j}(\mathbf{r}')d\tau'\cdot\mathbf{j}(\mathbf{r})d\tau)\mathbf{R}]$$

---

[1] Refer to J.C.Maxwell [111], Chapter 2.

[2] Refer to J.C.Maxwell [111], page 151.

$$= \mathbf{j}(\mathbf{r})d\tau \times \frac{\mu_0}{4\pi}\left[\mathbf{j}(\mathbf{r}')d\tau' \times \frac{\mathbf{R}}{R^3}\right] \tag{7.4}$$

with the assumption that two current elements in the same straight line have no mutual action. Integrating Eqn. (7.4) over τ', we obtain

$$\begin{aligned} d\mathbf{F}_L &= \mathbf{j}(\mathbf{r})d\tau \times \frac{\mu_0}{4\pi}\int_{\tau'} \mathbf{j}(\mathbf{r}')d\tau' \times \frac{\mathbf{R}}{R^3} \\ &= \mathbf{j}(\mathbf{r})d\tau \times \mathbf{B} \end{aligned} \tag{7.5}$$

where the value of $\mathbf{B}$ is precisely the value defined by Biot-Savart law in Eqn. (7.1). Thus we may consider the mutual action of one electric circuit upon another, by determining the action on the first due to the magnetic field produced by the second.

In 1889 Oliver Heaviside, based on experiments, gave for the first time the formula for the ponderomotive force on an electric charge which is moving in a magnetic field

$$\mathbf{F} = q\mathbf{v} \times \mathbf{B} \tag{7.6}$$

where q is the charge and $\mathbf{v}$ is the moving velocity thus $q\mathbf{v}$ represents the convective current.

In 1892 Hendrik Antoon Lorentz published his electron theory, that is to say, all electrodynamic phenomena were ascribed to the agency of moving electric charges, which were supposed in a magnetic field to communicate these forces to the ponderable matter with which they might be associated. Lorentz supposed that the phenomena of conduction currents are due to the motion of electrons. If $\mathbf{v}$ represents the drift velocity of electrons of conduction currents and ρ denotes the charge density, $\mathbf{j} = \rho\mathbf{v}$ and $\mathbf{j}d\tau = q\mathbf{v}$ so that the Lorentz theory unifies the individual experimental findings of Eqn. (7.5) and Eqn. (7.6) which are now usually called the Lorentz force law.

7.2 Equivalence of the force laws

Two points should be declared to start this section (i) since Ampère force law was postulated for currents flowing in conductors we only discuss the equivalence of the two force laws in the range of conduction currents which satisfy $\nabla \cdot \mathbf{j} = 0$ everywhere in the current system interested; (ii) neither Eqn.(7.2) nor Eqn.(7.4) directly result from the experimental findings so that as far as the two force laws are concerned, we imply the laws given by Eqn.(7.3) and Eqn.(7.5) respectively.

It is agreed that for a complete current distribution $\mathbf{j}'$ which exerts a force on a volume current element or the whole of another current distribution $\mathbf{j}$, the two force laws predict the same forces. The argument is about the equivalence between the two force laws when they are used for a self-closed system, namely the volume current element $\mathbf{j}d\tau$ is a part of the complete current distribution $\mathbf{j}'$. Ternan [93] and Jolly [94] demonstrated individually how either law may be derived from the other, thus showing that two laws are equivalent. Christodoulides [100] used a quite different approach, which examines an expression for the difference of the forces predicted by the two laws, to prove the equivalence of them in a self-closed system. However, using almost the same approach, Cornille [108] found a contrary consequence. It is therefore necessary to clarify this matter first.

7.2.1 Proof for continuum electrodynamics

By defining the force distributions or densities

$$\mathbf{f}_A = \lim_{d\tau \to 0} \frac{d\mathbf{F}_A}{d\tau} \tag{7.7}$$

$$\mathbf{f}_L = \lim_{d\tau \to 0} \frac{d\mathbf{F}_L}{d\tau} \tag{7.8}$$

we start to examine the difference between them

$$\begin{aligned} d\mathbf{f} &= \mathbf{f}_A - \mathbf{f}_L \\ &= \frac{\mu_0}{4\pi}\int_{\tau'} \frac{1}{R^3}\left[\frac{3\mathbf{R}}{R^2}(\mathbf{j}(\mathbf{r}')\cdot\mathbf{R})(\mathbf{j}(\mathbf{r})\cdot\mathbf{R}) - \mathbf{j}(\mathbf{r}')(\mathbf{j}(\mathbf{r})\cdot\mathbf{R}) - \mathbf{R}(\mathbf{j}(\mathbf{r}')\cdot\mathbf{j}(\mathbf{r}))\right] d\tau' \end{aligned} \tag{7.9}$$

Let $\mathbf{N} = \mathbf{j}(\mathbf{r}')(\mathbf{j}(\mathbf{r}) \cdot \mathbf{R}/R^3)$, we can find (see Appendix 7.1)

$$\nabla' \cdot \mathbf{N} = \frac{3}{R^5}(\mathbf{j}(\mathbf{r}) \cdot \mathbf{R})(\mathbf{j}(\mathbf{r}') \cdot \mathbf{R}) - \frac{\mathbf{j}(\mathbf{r}) \cdot \mathbf{j}(\mathbf{r}')}{R^3} \tag{7.10}$$

subject to $\nabla' \cdot \mathbf{j}(\mathbf{r}') = 0$, where ∇' indicates the operation with respect to **r**'. Then Eqn. (7.9) becomes

$$d\mathbf{f} = \frac{\mu_0}{4\pi} \int_{\tau'} (\mathbf{R}\nabla' \cdot \mathbf{N} - \mathbf{N}) d\tau' \tag{7.11}$$

which can be converted to a surface integral

$$\begin{aligned} d\mathbf{f} &= \frac{\mu_0}{4\pi} \int_{s'} \mathbf{R}(\mathbf{N} \cdot d\mathbf{s}') \\ &= \frac{\mu_0}{4\pi} \int_{s'} \frac{\mathbf{R}}{R^3}(\mathbf{j}(\mathbf{r}) \cdot \mathbf{R})(\mathbf{j}(\mathbf{r}') \cdot d\mathbf{s}') \end{aligned} \tag{7.12}$$

where s' is the surface enclosing τ'. The conversion of Eqn. (7.11) to Eqn. (7.12) is given in Appendix 7.2. Now Eqn. (7.12) is identical with equation (20) in [100] and equation (10) in [108]. It can clearly be seen that as long as $\mathbf{j}(\mathbf{r})$ does not belong to the current system $\mathbf{j}(\mathbf{r}')$ or in the other words that $\mathbf{j}(\mathbf{r})$ is the current density of the other closed circuit, the vector **N** is continuous and differentiable everywhere in τ' and on s' so that the conversion from Eqn. (7.11) to Eqn. (7.12) is legitimate and $d\mathbf{f} = 0$ because $\mathbf{j}(\mathbf{r}') \cdot d\mathbf{s}' = 0$. Hence it confirms that the two force laws have the same effects on the target current which is outside the active current circuit. This is expected without argument. A difficulty arises in the application of Eqn. (7.12) to prove the equivalence of the two laws when $\mathbf{j}(\mathbf{r})$ and $\mathbf{j}(\mathbf{r}')$ are belong to the same self-closed current system. In this case, the position of the source may coincide with the position of the target, that is $R = 0$, thus the surface integral becomes singular and one cannot use it directly any more. However the difficulty may be overcome in the following way.

Surrounding the target by a spherical surface s_f with an origin of local coordinates at the terminal of **r** and a radius ε as Fig.7.1 shows, because the vector **N** is continuous and differentiable again in the region $\tau' - \tau$, where τ is the sphere surrounded by s_f, as well as on the surrounding boundary $s' + s_f$ (for clearness s' is omitted in the figure), we obtain

$$\int_{\tau'-\tau} (\mathbf{R}\nabla' \cdot \mathbf{N} - \mathbf{N}) d\tau' = \int_{s'+s_f} \mathbf{R}(\mathbf{N} \cdot d\mathbf{s}')$$

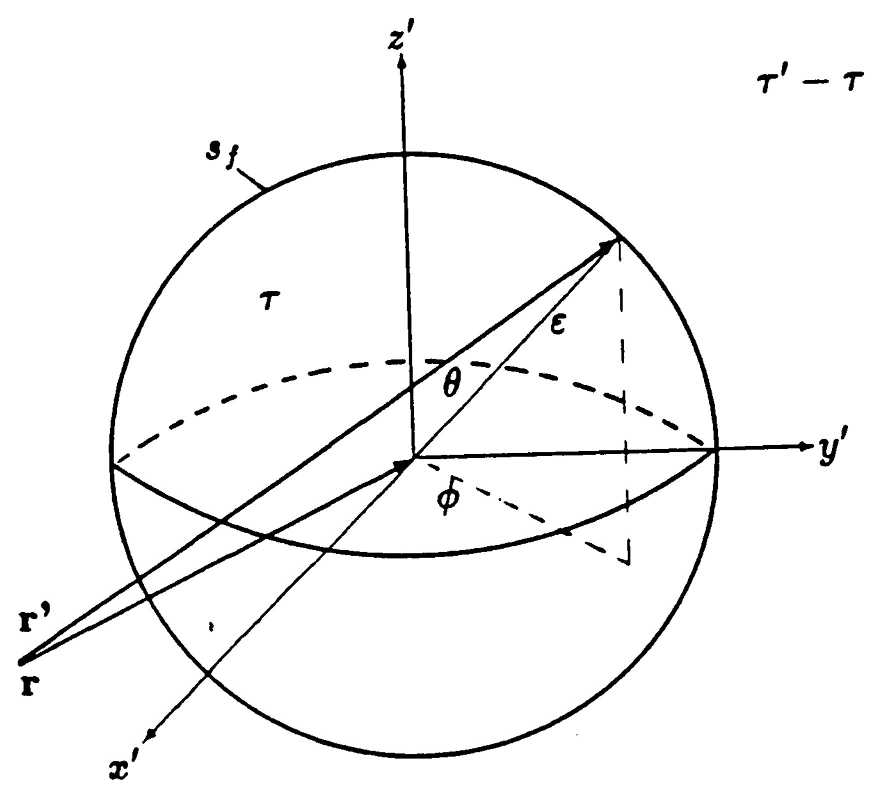

Figure 7.1 : The spherical surface enclosing the target

$$= \int_{s_f} \frac{\mathbf{R}}{R^3}(\mathbf{j}(\mathbf{r}) \cdot \mathbf{R})(\mathbf{j}(\mathbf{r}') \cdot \mathbf{ds}') \tag{7.13}$$

because $\mathbf{j}(\mathbf{r}') \cdot \mathbf{ds}' = 0$ on s'. We notice that $\mathbf{R} = \varepsilon\mathbf{n}$ on s_f, where $\mathbf{n}$ is the unit vector of the inwards normal of s_f, and $\mathbf{ds}' = \mathbf{n}\varepsilon^2 \sin\theta d\theta d\phi$. Hence we have

$$\begin{aligned} d\mathbf{f} &= \lim_{\tau\to 0} \frac{\mu_0}{4\pi} \int_{\tau'-\tau} (\mathbf{R}\nabla' \cdot \mathbf{N} - \mathbf{N}) d\tau' \\ &= \lim_{\varepsilon\to 0} \frac{\mu_0}{4\pi}\varepsilon \int_0^{2\pi}\int_0^{\pi} \mathbf{n}(\mathbf{j}(\mathbf{r}) \cdot \mathbf{n})(\mathbf{j}(\mathbf{r}') \cdot \mathbf{n}) \sin\theta d\theta d\phi \end{aligned} \tag{7.14}$$

Obviously, the integrand $\mathbf{n}(\mathbf{j}(\mathbf{r}) \cdot \mathbf{n})(\mathbf{j}(\mathbf{r}') \cdot \mathbf{n}) \sin\theta$ is finite so that as ε tends to zero $d\mathbf{f}$ definitely vanishes which proves that the two force laws are equivalent even when they are applied to a self-closed current system.

We have demonstrated that the foregoing mathematical proof is perfectly legitimate irrespective of the distribution of $\mathbf{j}(\mathbf{r}')$ on s_f. Therefore, Cornille's criticism of

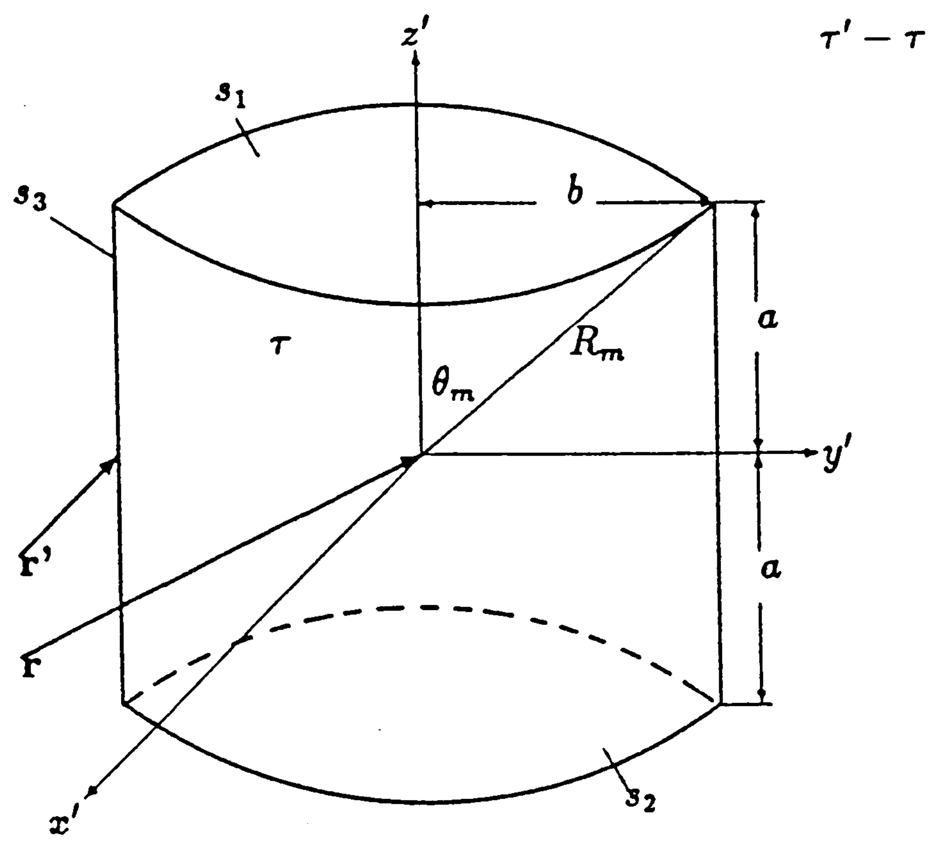

Figure 7.2 : The cylindrical box enclosing the target

Christodoulides's mistake [108] concerning the current distributions is not important. What surprises us is that Cornille used a cylindrical box instead of the spherical surface to enclose the target current element and found the opposite consquence. It can be expected that $d\mathbf{f}$ should vanish anyway as τ approaches zero regardless of its shape.

To support the foregoing proof and to verify our expectation let us consider a cylindrical box enclosing the target as depicted in Fig.7.2, where the dimensions of the enclosed cylindrical volume τ are sufficiently defined by the two parameters R_m and θ_m. Obviously, we have three ways to make τ vanish : (i) $R_m \to 0$, which makes τ shrink into a point; (ii) $\theta_m \to \pi/2$, which compresses τ into an infinitely thin disk and (iii) $\theta_m \to 0$, which compresses τ into a section of line. However, only the first way makes the 3-dimensions of τ vanish simultaneously so that it is more plausible to fix θ_m for $0 < \theta_m < \pi/2$ and let R_m tend to zero to perform our proof. Referring to Eqn.(7.13), we have

$$
\begin{aligned}
d\mathbf{f} &= \lim_{\tau\to 0}\frac{\mu_0}{4\pi}\int_{\tau'-\tau}(\mathbf{R}\nabla'\cdot\mathbf{N}-\mathbf{N})d\tau' \\
&= \lim_{R_m\to 0}\frac{\mu_0}{4\pi}\int_{s_c}\frac{\mathbf{R}}{R^3}(\mathbf{j}(\mathbf{r})\cdot\mathbf{R})(\mathbf{j}(\mathbf{r}')\cdot d\mathbf{s}')
\end{aligned}
\tag{7.15}
$$

where s_c is the closed surface of the cylindrical box which is composed of the top cover s_1, the bottom cover s_2 and the cylindrical surface s_3. From Fig.7.2 one can find the following relationships in terms of cylindrical coordinates (ρ, ϕ, z') and/or spherical coordinates (r, ϕ, θ):

$$
\rho = R\sin\theta,\quad R = \pm R_m\frac{\cos\theta_m}{\cos\theta},\quad ds' = \rho d\rho d\phi = \pm R^2\tan\theta d\theta d\phi \tag{7.16}
$$

on s_1 (positive sign) and s_2 (negative sign); and

$$
z' = R\cos\theta,\quad R = R_m\frac{\sin\theta_m}{\sin\theta},\quad ds' = R_m\sin\theta_m d\phi dz' = R^2 d\theta d\phi \tag{7.17}
$$

on s_3; where $d\rho, d\theta, d\phi$ and dz' are all positive. Thus the surface integral in Eqn. (7.15) becomes

$$
\begin{aligned}
d\mathbf{f} &= \lim_{R_m\to 0}\frac{\mu_0}{4\pi}R_m\int_0^{2\pi}\int_0^{\theta_m}\mathbf{R}_0(\mathbf{j}(\mathbf{r})\cdot\mathbf{R}_0)(\mathbf{j}(\mathbf{r}')\cdot\mathbf{n})\frac{\cos\theta_m}{\cos\theta}\tan\theta d\theta d\phi \\
&+ \lim_{R_m\to 0}\frac{\mu_0}{4\pi}R_m\int_0^{2\pi}\int_{\pi-\theta_m}^{\pi}\mathbf{R}_0(\mathbf{j}(\mathbf{r})\cdot\mathbf{R}_0)(\mathbf{j}(\mathbf{r}')\cdot\mathbf{n})\frac{\cos\theta_m}{\cos\theta}\tan\theta d\theta d\phi \\
&+ \lim_{R_m\to 0}\frac{\mu_0}{4\pi}R_m\int_0^{2\pi}\int_{\theta_m}^{\pi-\theta_m}\mathbf{R}_0(\mathbf{j}(\mathbf{r})\cdot\mathbf{R}_0)(\mathbf{j}(\mathbf{r}')\cdot\mathbf{n})\frac{\sin\theta_m}{\sin\theta}d\theta d\phi
\end{aligned}
\tag{7.18}
$$

where $\mathbf{n}$ is the unit vector of the inwards normal and $\mathbf{R}_0 = \mathbf{R}/R$. Now it can clearly be seen that since the integrand of each double integral on the R.H.S. of Eqn. (7.18) is finite, $d\mathbf{f}$ vanishes as R_m approaches zero. As a matter of fact, Cornille made a mistake in his proof which can be shown in Appendix 7.3.

7.2.2 On finite size of metallic current elements

Another main argument raised against the mathematical proof of the equivalence of the two force laws is that metallic current elements must have finite size [109]. Leaving aside the question of the structure of the conductor, it seems that the argument stems from the worry that the closed integration of the two force laws over a self-closed current system would lead to infinite forces because R^2 in the denominator of the laws goes to zero [109]. We are therefore going to show that such a worry is not necessary.

Having defined the Ampère force density, we have

$$\mathbf{f}_A = \frac{\mu_0}{4\pi}\int_{\tau'} \frac{\mathbf{Y}(\mathbf{r},\mathbf{r}')}{R^2} d\tau' \tag{7.19}$$

with

$$\mathbf{Y}(\mathbf{r},\mathbf{r}') = \mathbf{R}_0 \left[3(\mathbf{j}(\mathbf{r}')\cdot\mathbf{R}_0)(\mathbf{j}(\mathbf{r})\cdot\mathbf{R}_0) - 2(\mathbf{j}(\mathbf{r}')\cdot\mathbf{j}(\mathbf{r}))\right]$$

according to Eqns. (7.7), (7.3) and (7.2).

Let the point $Q(\mathbf{r})$ at which the force density to be determined be surrounded by a closed surface s of arbitrary shape, thus dividing the self-closed current system into two parts, i.e. a portion τ_1' representing the volume within s and a portion τ_2' external to s, we obtain

$$|\mathbf{f}_A| \le \frac{\mu_0}{4\pi}\int_{\tau_1'} \frac{|\mathbf{Y}(\mathbf{r},\mathbf{r}')|}{R^2} d\tau' + \frac{\mu_0}{4\pi}\int_{\tau_2'} \frac{|\mathbf{Y}(\mathbf{r},\mathbf{r}')|}{R^2} d\tau' \tag{7.20}$$

Obviously, the second integral of Eqn. (7.20) is bounded so as to contribute a finite amount to the resultant force density at $Q(\mathbf{r})$. The first integral is still improper (singular). However, the current densities $\mathbf{j}(\mathbf{r}')$ and $\mathbf{j}(\mathbf{r})$ are finite so that

$$|\mathbf{Y}(\mathbf{r},\mathbf{r}')| < C \tag{7.21}$$

where C is a finite constant. It follows that

$$\frac{\mu_0}{4\pi}\int_{\tau_1'} \frac{|\mathbf{Y}(\mathbf{r},\mathbf{r}')|}{R^2} d\tau' < C\frac{\mu_0}{4\pi}\int_{\tau_1'} \frac{1}{R^2} d\tau' \tag{7.22}$$

Now, because

$$\int_{\tau_1'} \frac{1}{R^2} d\tau' \le \int_{\tau_a'} \frac{1}{R^2} d\tau' \tag{7.23}$$

where τ_a is a sphere having radius a concentric with $Q(\mathbf{r})$ and circumscribing about τ_1, and

$$\int_{\tau_a'} \frac{1}{R^2} d\tau' = \int_0^a \int_0^{2\pi} \int_0^{\pi} \frac{1}{R^2} R^2 \sin\theta d\theta d\phi dR = 4\pi a \tag{7.24}$$

we have

$$\int_{\tau_1'} \frac{1}{R^2} d\tau' \leq 4\pi a \tag{7.25}$$

It is therefore proved that the singular integral of Eqn. (7.19) definitely converges for every interior point of a self-closed current system regardless of the current element size. Since the force density is everywhere bounded, the Ampère force on any portion τ_e of the current system

$$\mathbf{F}_A = \int_{\tau_e} \mathbf{f}_A d\tau \tag{7.26}$$

is, of course, unable to be infinite even though the current element size is treated as zero. A similar proof can be obtained for the Lorentz force law.

In fact, when the denominator of the two force laws vanishes as the square of distance, the current in the numerator vanishes as the cube of a linear dimension so that the two inverse square force laws do not cause any self-interaction regardless of whatever the current element size is supposed. Hence, in this aspect, it is not necessary to require that current elements must retain finite non-zero size and any infinite force arising from computations must cast doubts on the adopted numerical method itself.

We recall that the so-called current elements originate from the formulation of Eqns. (7.2) and (7.4), and at the very beginning we emphasized that these two formulae are not directly based on the pure experimental findings but resulted from a proposed analysis of the phenomena. Maxwell himself demonstrated how to reach these two formulae and said, "In the analysis of the phenomena, however, we may regard the action of a closed circuit on an element of itself or of another circuit as the resultant of a number of separate forces, depending on the separate parts into which the first circuit may be conceived, for mathematical purposes, to be divided. This is a merely mathematical analysis of the action, and is therefore perfectly legitimate, whether these forces can really act separately or not".[3] It seems therefore that the current elements

[3]Refer to J.C.Maxwell [111], page 151.

have more mathematical meaning than physical and their physical size can be ignored.

Yet it is true in nature that everything has a finite size. If the current elements exist in reality and have finite size, it is not surprising to find a difference between the two force laws, which can so easily be demonstrated by considering two summations :

$$I_1 = \sum_{x=0}^{\pi/2} \sin x \delta x \text{ and } I_2 = \sum_{x=0}^{\pi/2} \frac{8x}{\pi^2} \delta x \tag{7.27}$$

Only when $\delta x \to 0$ they become two integrals which are equal. The situation is analogous to comparison of the two force laws given by Eqns. (7.3) and (7.5) respectively. Given this situation, a question arises, i.e., is such a difference significant ? The answer to this question may be drawn from the the following two considerations (i) if the current elements have, for example, cylindrical shape and their size is so small (non-zero) that the current carried by each element can be considered to be uniform, we have already shown in Appendix 7.3 that the difference also vanishes; (ii) as a matter of fact, so far there has been no experimental evidence to tell the significant difference between the two force laws due only to the finite size of the current elements when the force laws have been correctly applied.

Given these facts, we can certainly say that whether the current elements have finite size or not is not important on the issue of equivalence of the two force laws. On the contrary, the way to apply the force laws is most important, and will be discussed in detail in the next section.

7.3 The way to use the force laws

In classical electrodynamics one looks at the force on a current element due to the magnetic field created by the whole current distribution, and this force is always perpendicular to the current flow (the transverse force) as it can clearly be seen in Eqn. (7.5). This feature should also be predicted by Ampère force law though it is not explicit in Eqn. (7.3). However, in recent publications [113, 114, 115, 116] some authors claim that when determining internal electrodynamic forces in a conductor due to its own current, the Ampère force law generally does not predict a purely perpendicular force on a current element, that is it can predict a longitudinal force (parallel to current flow). To support their claim, they from time to time cited the following demonstration. Start from Eqn. (7.2) and suppose two current elements lying on the same straight streamline, i.e., $\mathbf{j}(\mathbf{r}') \cdot \mathbf{j}(\mathbf{r}) = j'j$, $\mathbf{j}(\mathbf{r}') \cdot \mathbf{R} = j'R$ and $\mathbf{j}(\mathbf{r}) \cdot \mathbf{R} = jR$. For these two elements, Eqn. (7.2) reduces to

$$d^2\mathbf{F}_A = \frac{\mu_0}{4\pi}\mathbf{R}_0\frac{jj'd\tau d\tau'}{R^2} \tag{7.28}$$

where $\mathbf{R}_0$ reverses if the positions of the source and the target reverse. Thus it seems that collinear current elements repel each other due to the longitudinal forces. This, as the authors claimed, leads to tension in a straight conduction channel so as to explain several experimental phenomena.

Against this we have two points to argue. The first one is because Eqn. (7.2) is not directly obtained from the experiments based on two current elements, any conclusion drawn from this equation is in doubt. The second one is that even if Eqn. (7.2) were true for two current elements, to explain the experimental phenomena, one still needs to use Ampère force law given by Eqn. (7.3) because we are not just interested in the interaction between any two individual current elements. On the second point it can be seen by any means that Eqn. (7.3) gives the real electrodynamic force on the target element wherever it is located when the integration is taken over the whole current region (we call this way the complete calculation). In view of the above cited publications, one can find that the authors always make selective integration over part of the current system (we call this way the incomplete calculation) so as to obtain a fictitious longitudinal force to explain the experimental phenomena. To demonstrate this, let us consider a simple but instructive example, that is the calculation of the electrodynamic force distribution on a section of a straight wire in Fig.7.3(a) where sections A and C extend far away.

Assuming a uniform current distribution $\mathbf{j} = j_a\mathbf{a}_z$ along the wire and a ratio of $z_0/r_0 = 10$, we use the Ampère force law to predict the force distribution on section B in the two ways. In the way of the complete calculation, not only the interactions between any interior element (the element inside B) with any external element (the element of the remainder of the current system, i.e., A and C), but also the interactions of the interior elements themselves are taken into account. The computed result is shown in

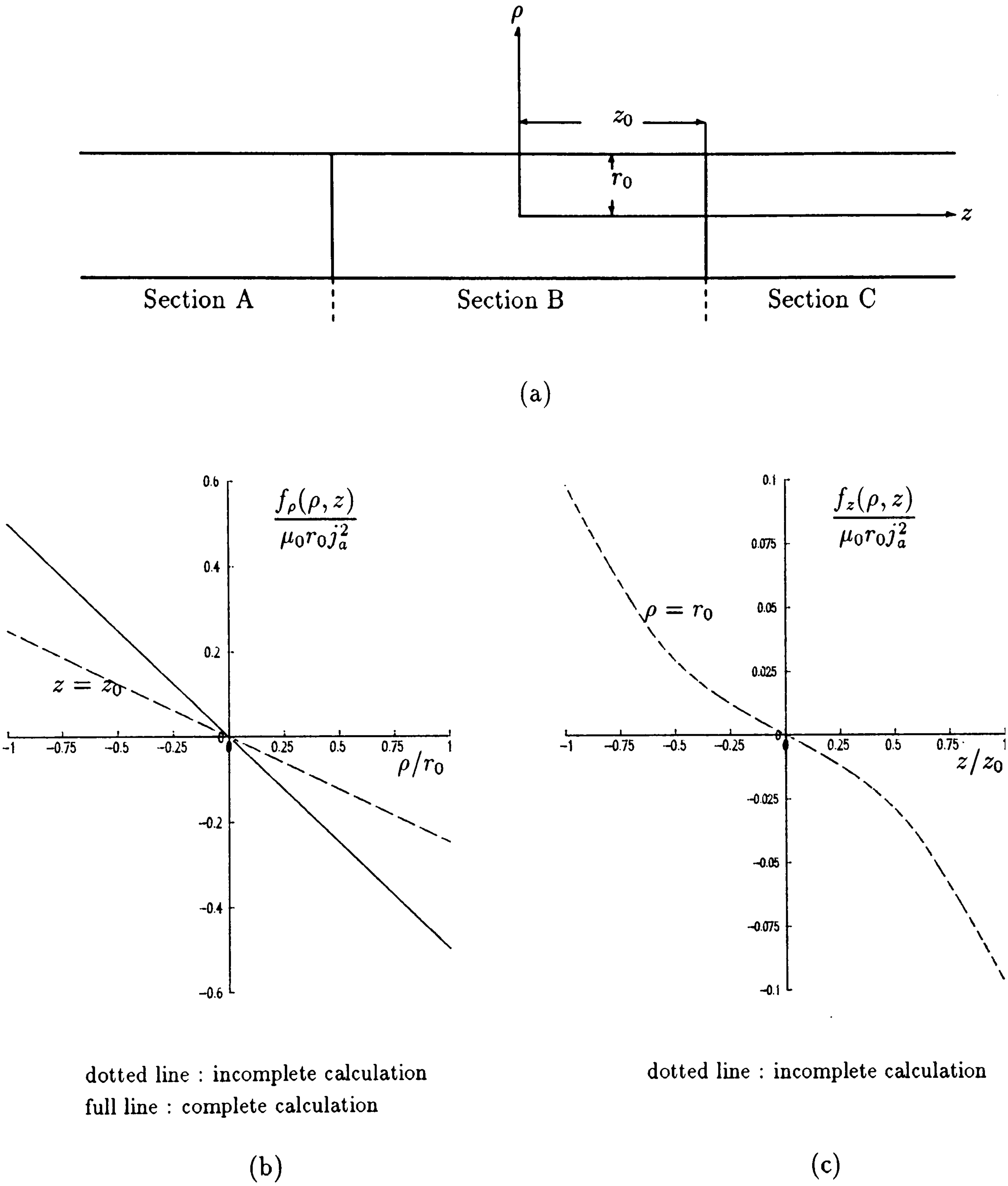

dotted line : incomplete calculation
full line : complete calculation

(b)

dotted line : incomplete calculation

(c)

Figure 7.3 : (a) a straight wire
(b) normalized transverse force density
(c) normalized longitudinal force density

Fig.7.3(b) by the full line and is in agreement with that predicted by Lorentz force law. In this way the resultant force distribution has only the transverse component which causes the well-known pinch effect on section B.

Next the incomplete calculation is carried out, in which only the interactions of the current elements of B with those of A and C are considered. The result is shown in Fig.7.3(b) and Fig.7.3(c) by the dotted lines. In this way the resultant force distribution on B has not only a transverse component which is not equal to that given by the Lorentz force law, but also a longitudinal component which causes an additional axial pressure on B. By the same way one can find the pressures on A and C as well. It has been interpreted as a tension by the authors and is called the Ampère tension and employed to explain some experiments [113, 117, 118].

It should be noticed that the net force obtained by integrating the resultant force distributions (densities) over B is the same, i.e. zero, in the two methods. Clearly, the difference of the two force laws in predicting electrodynamic force distribution stems from the method of the incomplete calculation. The users of the incomplete calculation defend their method by citing the philosophy[4] (or a very similar one) that no matter how hard you tug on your bootstraps you will not raise yourself an observable amount. However we say that the philosophy is only applicable to the case in which the net force on a body is concerned, and in this case we have noticed there is no difference between the two force laws despite in which way Ampère force law is used. But the situation is different if we look at the force distribution which, obviously, is independent of the cited philosophy.

To help to make a judgement on the way of using the Ampère force law, let us look at another example in which we use Coulomb's electrostatic force law instead of Ampère's force law because their formulations are quite similar. Fig.7.4(a) shows the problem under consideration, i.e., four charged balls fixed along a string with a separation d to any adjacent one. Supposing each ball has charge q and radius tending to zero, we will calculate tension on the string across planes p_1, p_2 and p_3.

First, by making a complete calculation, that is by determining Coulomb's force on

[4]Private communication.

each ball with interactions with all the others without considering the force effect (e.g. pulling the string in tension), we have

$$\mathbf{f}_1 = -kq^2(\frac{1}{d^2} + \frac{1}{4d^2} + \frac{1}{9d^2})\mathbf{a}_x \tag{7.29}$$

$$\mathbf{f}_2 = -k\frac{q^2}{4d^2}\mathbf{a}_x \tag{7.30}$$

$$\mathbf{f}_3 = -\mathbf{f}_2 \tag{7.31}$$

$$\mathbf{f}_4 = -\mathbf{f}_1 \tag{7.32}$$

where $k = 1/(4\pi\epsilon)$. The tensions T_i across p_i for $i = 1, 2, 3$ are then obtained by summing up the applied electrostatic forces on each side of p_i, i.e.,

$$T_1 = T_3 = kq^2(\frac{1}{d^2} + \frac{1}{4d^2} + \frac{1}{9d^2}) \tag{7.33}$$

$$T_2 = k\frac{q^2}{4d^2} + T_1 \tag{7.34}$$

which are illustrated in Fig.7.4(b).

If the incomplete calculation is carried out the same results for the tensions can be obtained, but the calculated electrostatic force on each ball is dependent on the reference plane across which the tension is concerned. For example, when T_2 is concerned, the incomplete calculation gives

$$\mathbf{f}_1 = -kq^2(\frac{1}{4d^2} + \frac{1}{9d^2})\mathbf{a}_x \tag{7.35}$$

$$\mathbf{f}_2 = -kq^2(\frac{1}{d^2} + \frac{1}{4d^2})\mathbf{a}_x \tag{7.36}$$

$$\mathbf{f}_3 = -\mathbf{f}_2 \tag{7.37}$$

$$\mathbf{f}_4 = -\mathbf{f}_1 \tag{7.38}$$

Obviously, only the complete calculation gives the real Coulomb's force (or the applied electrostatic force) on each charged ball.

Evidently the way of the complete calculation is always correct for applying Ampère's force law to determine both the net force and the force distribution on a current carrying conductor, but the way of the incomplete calculation is only correct in determining the net force. Therefore, the resultant effect of the electrodynamic force distribution obtained by the incomplete calculation cannot be produced as evidence against the equivalence of the two electrodynamic force laws or as an explanation of any experimental phenomenon.

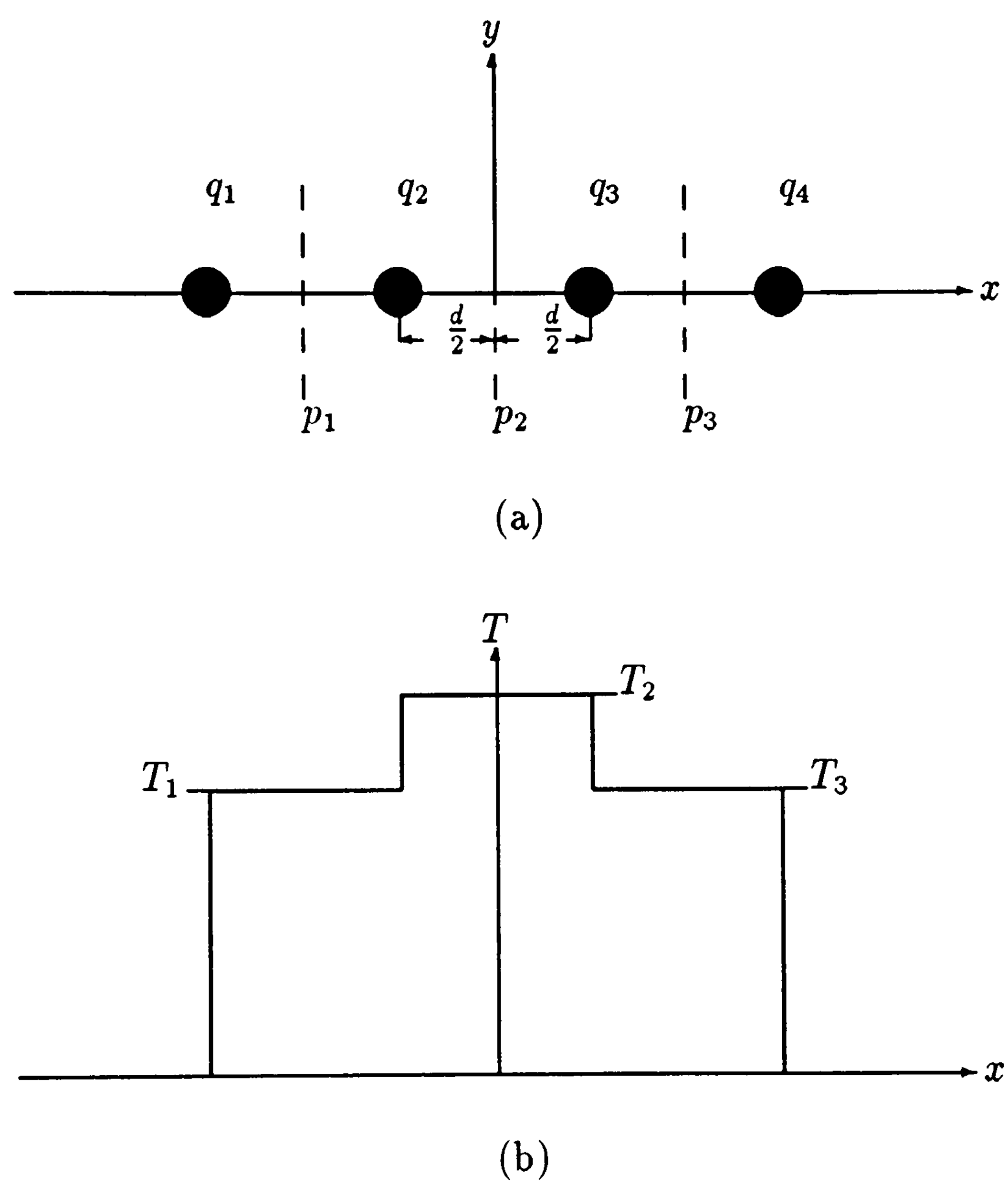

Figure 7.4 : (a) Four charged balls along a string;

(b) the resultant tension along the string (not to scale).

Appendix 7.1

Substituting $\mathbf{N} = \mathbf{j}(\mathbf{r}')(\mathbf{j}(\mathbf{r}) \cdot \mathbf{R}/R^3)$ into the L.H.S. on Eqn. (7.10) yields

$$\begin{aligned} \nabla' \cdot [\mathbf{j}(\mathbf{r}')(\mathbf{j}(\mathbf{r}) \cdot \mathbf{R}/R^3)] &= \mathbf{j}(\mathbf{r}') \cdot \nabla'(\mathbf{j}(\mathbf{r}) \cdot \mathbf{R}/R^3) + (\mathbf{j}(\mathbf{r}) \cdot \mathbf{R}/R^3)(\nabla' \cdot \mathbf{j}(\mathbf{r}')) \\ &= \mathbf{j}(\mathbf{r}') \cdot \nabla'(\mathbf{j}(\mathbf{r}) \cdot \mathbf{R}/R^3) \qquad (7.39) \end{aligned}$$

because $\nabla' \cdot \mathbf{j}(\mathbf{r}') = 0$. We note

$$\nabla'(\mathbf{j}(\mathbf{r}) \cdot \mathbf{R}/R^3) = (\mathbf{j}(\mathbf{r}) \cdot \mathbf{R})\nabla'(\frac{1}{R^3}) + \frac{1}{R^3}\nabla'(\mathbf{j}(\mathbf{r}) \cdot \mathbf{R}) \qquad (7.40)$$

in which

$$\begin{aligned} \nabla'(\frac{1}{R^3}) &= \nabla'[(x-x')^2 + (y-y')^2 + (z-z')^2]^{-3/2} \\ &= 3\frac{\mathbf{R}}{R^5} \qquad (7.41) \end{aligned}$$

and

$$\begin{aligned} \nabla'(\mathbf{j}(\mathbf{r}) \cdot \mathbf{R}) &= (\mathbf{R} \cdot \nabla')\mathbf{j}(\mathbf{r}) + (\mathbf{j}(\mathbf{r}) \cdot \nabla')\mathbf{R} + \mathbf{R} \times (\nabla' \times \mathbf{j}(\mathbf{r})) + \mathbf{j}(\mathbf{r}) \times (\nabla' \times \mathbf{R}) \\ &= (\mathbf{j}(\mathbf{r}) \cdot \nabla')\mathbf{R} \qquad (7.42) \end{aligned}$$

since the operation ∇' is only w.r.t. the variable $\mathbf{r}$' and $\nabla' \times \mathbf{R} = -\nabla' \times \mathbf{r}' = 0$. We can further find

$$\begin{aligned} (\mathbf{j}(\mathbf{r}) \cdot \nabla')\mathbf{R} &= -(j_x(\mathbf{r})\frac{\partial}{\partial x'} + j_y(\mathbf{r})\frac{\partial}{\partial y'} + j_z(\mathbf{r})\frac{\partial}{\partial z'})\mathbf{r}' \\ &= -\mathbf{j}(\mathbf{r}) \qquad (7.43) \end{aligned}$$

Substituting these results step by step back to Eqn. (7.39) directly leads to Eqn. (7.10).

Appendix 7.2

Let $\mathbf{a} = \mathbf{R}(\nabla' \cdot \mathbf{N}) - \mathbf{N}$, then

$$\begin{aligned} a_x &= (x-x')(\nabla' \cdot \mathbf{N}) + \mathbf{N} \cdot \nabla'(x-x') \\ &= \nabla' \cdot [(x-x')\mathbf{N}] \qquad (7.44) \end{aligned}$$

$$\begin{aligned} a_y &= (y-y')(\nabla'\cdot\mathbf{N}) + \mathbf{N}\cdot\nabla'(y-y') \\ &= \nabla'\cdot[(y-y')\mathbf{N}] \end{aligned} \tag{7.45}$$

$$\begin{aligned} a_z &= (z-z')(\nabla'\cdot\mathbf{N}) + \mathbf{N}\cdot\nabla'(z-z') \\ &= \nabla'\cdot[(z-z')\mathbf{N}] \end{aligned} \tag{7.46}$$

As long as **N** is continuous differentiable in τ' and on s', we have

$$\int_{\tau'} a_x d\tau' = \int_{s'} [(x-x')\mathbf{N}]\cdot d\mathbf{s}' \tag{7.47}$$

$$\int_{\tau'} a_y d\tau' = \int_{s'} [(y-y')\mathbf{N}]\cdot d\mathbf{s}' \tag{7.48}$$

$$\int_{\tau'} a_z d\tau' = \int_{s'} [(z-z')\mathbf{N}]\cdot d\mathbf{s}' \tag{7.49}$$

according to Gauss's theorem. In evidence thses integrals can be identified from

$$\int_{\tau'} (\mathbf{R}(\nabla'\cdot\mathbf{N}) - \mathbf{N})d\tau' = \int_{s'} \mathbf{R}(\mathbf{N}\cdot d\mathbf{s}') \tag{7.50}$$

Thus the conversion from Eqn. (7.11) to Eqn. (7.12) is proved.

Appendix 7.3

Following Cornille's assumption that in τ and over s_c the current uniformly directs in z direction only, we have further definitions in Eqn. (7.18)

$$\mathbf{j}(\mathbf{r}')\cdot\mathbf{n} = \begin{cases} -j' & \text{on } s_1 \\ j' & \text{on } s_2 \\ 0 & \text{on } s_3 \end{cases} \tag{7.51}$$

$$\left.\begin{aligned} &\mathbf{j}(\mathbf{r})\cdot\mathbf{R}_0 = -j\cos\theta \\ &\mathbf{R}_0 = -\sin\theta\mathbf{a}_r - \cos\theta\mathbf{a}_z \end{aligned}\right\} \text{on } s_1 \text{ and } s_2 \tag{7.52}$$

so that the last integral on the R.H.S. of Eqn. (7.18) equals zero because $\mathbf{j}(\mathbf{r}')\cdot\mathbf{n} = 0$ in the region of integration and the equation becomes

$$\begin{aligned} d\mathbf{f} &= \lim_{R_m\to 0} \frac{\mu_0}{4\pi} j j' R_m \cos\theta_m \\ &\left\{ [\sin\theta_m - \ln\tan(\frac{\pi}{4} + \frac{\theta_m}{2})] \int_0^{2\pi} \mathbf{a}_r d\phi + 2\pi(\cos\theta_m - 1)\mathbf{a}_z \right\} \end{aligned}$$

$$+ \lim_{R_m \to 0} \frac{\mu_0}{4\pi} j j' R_m \cos\theta_m$$
$$\left\{ [\sin\theta_m - \ln\tan(\frac{\pi}{4} + \frac{\theta_m}{2})] \int_0^{2\pi} \mathbf{a}_r d\phi - 2\pi(\cos\theta_m - 1)\mathbf{a}_z \right\} \quad (7.53)$$

If one notices that

$$\int_0^{2\pi} \mathbf{a}_r d\phi = \int_0^{2\pi} \cos\phi d\phi \mathbf{a}_x + \int_0^{2\pi} \sin\phi d\phi \mathbf{a}_y = 0 \quad (7.54)$$

one can find that $d\mathbf{f} = 0$ without requiring $R_m \to 0$. This implies that if the assumption of the uniform current distribution for each target current element is plausible on the ground that the physical size of the current element (if it exists) must be very small in comparison with the size of the whole current system, the proof of the equivalence of the two force laws is also valid for non-zero size current elements.

In Cornille's exercise, he let $\theta_m \to \pi/2$ to make τ vanish and argued that $d\mathbf{f}$ did not vanish because he found that as $\theta_m \to \pi/2$, the term $R_m \cos\theta_m \ln\tan(\pi/4 + \theta_m/2)$ in Eqn. (7.53) was infinity. However it is not true. Keeping $b = R_m \sin\theta_m$ in Fig.7.2 constant as θ_m tends to $\pi/2$, we find

$$\begin{aligned}
\lim_{\theta_m \to \pi/2} R_m \cos\theta_m \ln\tan(\frac{\pi}{4} + \frac{\theta_m}{2}) &= \lim_{\theta_m \to \pi/2} \frac{b}{\sin\theta_m} \frac{\ln\tan(\frac{\pi}{4} + \frac{\theta_m}{2})}{\frac{1}{\cos\theta_m}} \\
&= \frac{b}{2} \lim_{\theta_m \to \pi/2} \cos\theta_m \cdot \lim_{\theta_m \to \pi/2} \frac{\cos\theta_m}{\cos(\frac{\pi}{4} + \frac{\theta_m}{2})} \\
&= b \lim_{\theta_m \to \pi/2} \cos\theta_m \cdot \lim_{\theta_m \to \pi/2} \frac{\sin\theta_m}{\sin(\frac{\pi}{4} + \frac{\theta_m}{2})} \\
&= 0 \qquad (7.55)
\end{aligned}$$

according to L'Hospital rule.

Chapter 8

On Electromagnetic jet propulsion

8.1 Background

The recent controversy on electrodynamics might originate from a paper which bore the title "Electromagnetic jet-propulsion in the direction of current flow" by Graneau [118]. In this paper the author reported an experiment to demonstrate jet-propulsion in the direction of current flow between liquid and solid conductors. Figure 8.1 gives the details of this experiment. A copper "submarine" consisting of a short piece of straight wire, squared off at one end and pointed at the other, is placed on the surface of a straight-through mercury trough conductor. When current is forced to flow along the trough, the wire is submerged and driven along the centre of the trough until it strikes the solid copper bar. The wire travels with its blunt end forward. Its velocity is apparent from the bow wave on the liquid surface. The direction of travel does not depend on the direction of current flow and the experiment works equally well with 60-Hz alternating current.

Graneau claimed that the observed effects seemed to conform with Ampère force law, but no qualitative nor quantitative explanation had so far been found in terms of the Lorentz force. Hillas [119] made an opposite comment on this. He suggests an explanation that because of the high conductivity of copper, much of the current will be funnelled into the copper from a point, from where the lines of current flow will spread apart somewhat on moving towards the wider part of the copper, and in this

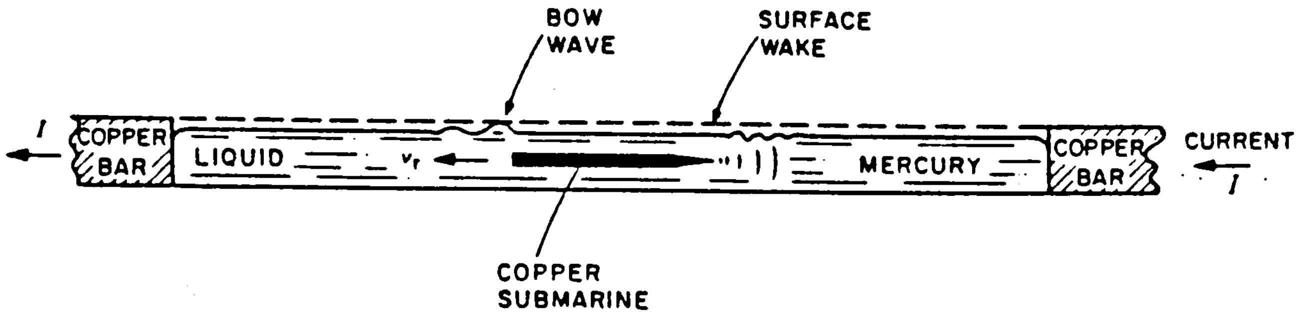

Figure 8.1: Copper submarine experiment after Graneau [118]
Mercury trough length=30 cm; cross-section 0.5 × 0.5 inch
Copper submarine; 5 cm long, 3 mm diameter, 1 cm long taper
Copper extension of troughs 30 cm long, 0.5 × 0.5 inch cross-section
$I = 400\ A$, $v_r = 15$ cm/s

cone section the Lorentz force has a component parallel to the axis, the magnetic field lines being circles around the axis. It is this axial component of the Lorentz force that drives the copper submarine moving in the axial direction. Graneau [120], however, objected to Hillas's suggestion by reasoning that the axial component of the Lorentz force which acted on the copper submarine had no corresponding equal and opposite reaction force in the liquid mercury or any other material medium. He termed such a force the self-force, giving rise to self-propulsion.

We believe as Hillas that the observation of jet-propulsion can be understood in terms of the Lorentz forces. Since we have discussed in the previous Chapter that both Lorentz and Ampère force laws yield identical results when the latter is appropriately used, it is the main purpose of this Chapter to demonstrate that Graneau's objection is groundless.

8.2 Action and reaction of the Lorentz forces

Let us consider, for the purpose of demonstration, a closed current system fed by a constant source. The system occupies a material volume τ bounded by a surface s. We further assume that both charge and current are zero in the whole space except τ. Since Newton's third law leads to the important law of conservation of momentum in classical mechanics, to discuss the interaction of the Lorentz forces, we therefore start with the momentum conservation law of electromagnetic fields [121]

$$\mathbf{f} + \frac{\partial \mathbf{g}}{\partial t} = \nabla \cdot \overleftrightarrow{\mathbf{T}} \tag{8.1}$$

in which

$$\begin{aligned} \mathbf{f} &= \rho \mathbf{E} + \mathbf{j} \times \mathbf{B} && (8.2) \\ \mathbf{g} &= \frac{\mathbf{E} \times \mathbf{H}}{c^2} && (8.3) \end{aligned}$$

are the Lorentz force density and the field momentum density respectively where ρ is charge density, c is the light speed in medium; and

$$\overleftrightarrow{\mathbf{T}} = \mathbf{DE} + \mathbf{BH} - \frac{1}{2} \overleftrightarrow{\mathbf{I}} (\mathbf{D} \cdot \mathbf{E} + \mathbf{B} \cdot \mathbf{H}) \tag{8.4}$$

is the Maxwell stress tensor[1] where

$$\overleftrightarrow{\mathbf{I}} = \mathbf{a}_1 \mathbf{a}_1 + \mathbf{a}_2 \mathbf{a}_2 + \mathbf{a}_3 \mathbf{a}_3 \tag{8.5}$$

is the unit tensor with $\mathbf{a}_i$ $(i = 1, 2, 3)$ the unit vectors of the coordinate axes. Applying Gauss's theorem to Eqn.(8.1) we obtain[2]

$$\int_{space-\tau} \frac{\partial \mathbf{g}}{\partial t} d\tau = - \oint_s \overleftrightarrow{\mathbf{T}} \cdot \mathbf{n} ds + \oint_{s_\infty} \overleftrightarrow{\mathbf{T}} \cdot d\mathbf{s} \tag{8.6}$$

when the integration is taken over the space excluding the volume τ, and

$$\int_\tau \mathbf{f} d\tau + \int_\tau \frac{\partial \mathbf{g}}{\partial t} d\tau = \oint_s \overleftrightarrow{\mathbf{T}} \cdot \mathbf{n} ds \tag{8.7}$$

when the integration is taken over the current system, where $\mathbf{n}$ is defined as the outward normal of the surface enclosing τ and s_∞ is the surface at an infinite remote distance. If fields are static, the fields die out within a finite distance because they vary in inverse proportion of the square of the distance. If fields are time-varying, one can imagine that the infinite remote surface s_∞ is so far that the fields, which are propagated with a finite velocity, have not yet arrived. Thus the Maxwell stress tensor over s_∞ is strictly zero, and by adding Eqn.(8.6) to Eqn.(8.7) we arrive at

$$\int_\tau \mathbf{f} d\tau + \int_{space} \frac{\partial \mathbf{g}}{\partial t} d\tau = 0 \tag{8.8}$$

[1]Acturally, this is a tensor of the second rank and then is also known as dyadic.

[2]Refer to Appendix 8.1.

Suppose the current system is divided into two parts, namely $\tau = \tau_1 + \tau_2$. Equation (8.8) can be rewritten as

$$\int_{\tau_2} \mathbf{f} d\tau = -\int_{\tau_1} \mathbf{f} d\tau - \int_{space} \frac{\partial \mathbf{g}}{\partial t} d\tau \tag{8.9}$$

or

$$\mathbf{F}_2 = -\left(\mathbf{F}_1 + \int_{space} \frac{\partial \mathbf{g}}{\partial t} d\tau\right) \tag{8.10}$$

where $\mathbf{F}_1$ and $\mathbf{F}_2$ represent the Lorentz forces on conductors 1,2 respectively.

Now if neither conductor 1 nor conductor 2 can move, $\partial \mathbf{g}/\partial t$ is strictly zero everywhere and Eqn.(8.10) reduces to

$$\mathbf{F}_2 = -\mathbf{F}_1 \tag{8.11}$$

which indicates that in a stationary current system fed by a DC source the Lorentz force acting on one part of the system finds its equal and opposite reaction force on the remaining part. Both of the parts are obviously the real material media.

Next let us consider the case of conductor 2 moving with a constant velocity $\mathbf{v} = v\mathbf{a}_x$. To see the moving effect, we consider two inertial frames of reference $\sum$ and $\sum'$. Suppose $\sum$ be our laboratory frame while $\sum'$ the moving frame with the velocity $\mathbf{v}$ relative to $\sum$. Although the source is steady, the fields in $\sum$ will in general vary with respect to time due to the relativistic effect, which can be demonstrated as follows. From the Lorentz transformations[3]

$$\begin{aligned} x' &= \gamma(x - vt) & x &= \gamma(x' + vt') \\ y' &= y & y &= y' \\ z' &= z & z &= z' \\ t' &= \gamma(t - vx/c^2) & t &= \gamma(t' + vx'/c^2) \end{aligned} \tag{8.12}$$

with

$$\gamma = (1 - v^2/c^2)^{-1/2}$$

we obtain[4]

$$\frac{\partial}{\partial t} = \gamma\left(\frac{\partial}{\partial t'} - v\frac{\partial}{\partial x'}\right) \tag{8.13}$$

---

[3]Refer to French [122], page 80.

[4]See Appendix 8.2.

$$\frac{\partial}{\partial x'} = \gamma\left(\frac{\partial}{\partial x}+\frac{v}{c^2}\frac{\partial}{\partial t}\right) \tag{8.14}$$

Substituting Eqn.(8.14) into Eqn.(8.13) and assuming the fields are time-independent as observed at $\sum'$, i.e. omitting $\partial/\partial t'$, yield

$$\frac{\partial}{\partial t} = -v\frac{\partial}{\partial x} \tag{8.15}$$

Since v is in the x direction, Eqn.(8.15) can be written as

$$\frac{\partial}{\partial t} = -(\mathbf{v}\cdot\nabla) \tag{8.16}$$

Applying this operation on the fields $\mathbf{E}$ and $\mathbf{H}$ at $\sum$, we have

$$\frac{\partial \mathbf{E}}{\partial t} = -(\mathbf{v}\cdot\nabla)\mathbf{E} \tag{8.17}$$

$$\frac{\partial \mathbf{H}}{\partial t} = -(\mathbf{v}\cdot\nabla)\mathbf{H} \tag{8.18}$$

Thus the time rate of change of the field momentum density is given by

$$\begin{aligned}\frac{\partial \mathbf{g}}{\partial t} &= \frac{1}{c^2}\left(\frac{\partial \mathbf{E}}{\partial t}\times\mathbf{H}+\mathbf{E}\times\frac{\partial \mathbf{H}}{\partial t}\right)\\ &= -\frac{(\mathbf{v}\cdot\nabla)\mathbf{E}\times\mathbf{H}+\mathbf{E}\times(\mathbf{v}\cdot\nabla)\mathbf{H}}{c^2}\end{aligned} \tag{8.19}$$

which does not vanish generally. Even though in this situation, one cannot say following Graneau that the Lorentz force on the moving conductor, which is taken as the copper submarine, is endowed with reaction in the field (vacuum) because it is not the case, as indicated by Eqn.(8.10), unless $\mathbf{F}_1 = 0$. Try to imagine that we have obtained the force relation of Eqn.(8.11) in the case of conductor 2 being at rest. How could this relation be totally changed just due to conductor 2 moving with a velocity only 15 cm/s ? As a matter of fact, the moving effect on the force measurements could be ignored if we note the general force transformations[5]

$$\begin{aligned}F'_x &= \frac{F_x-(v/c^2)dE/dt}{1-vu_x/c^2} & F_x &= \frac{F'_x+(v/c^2)dE'/dt'}{1+vu'_x/c^2}\\ F'_y &= \frac{F_y/\gamma}{1-vu_x/c^2} & F_y &= \frac{F'_y/\gamma}{1+vu'_x/c^2}\\ F'_z &= \frac{F_z/\gamma}{1-vu_x/c^2} & F_z &= \frac{F'_z/\gamma}{1+vu'_x/c^2}\end{aligned} \tag{8.20}$$

[5]Refer to French [122], page 221.

where v is the velocity of moving frame $\sum'$ in the x direction; F'_x, F'_y, F'_z, E' and u'_x represent the force components, the energy and the x-component of velocity of the object as measured in $\sum'$; while F_x, F_y, F_z, E and u_x represent the force components, the energy and the x-component of velocity of the object as measured in our laboratory frame $\sum$. As far as $v \ll c$, $u'_x \ll c$ and $u_x \ll c$, we obtain

$$\begin{aligned} F'_x &\approx F_x \\ F'_y &\approx F_y \\ F'_z &\approx F_z \end{aligned} \tag{8.21}$$

to a quite high degree of approximation. Hence one can expect that the Lorentz forces on the two parts of the current system do not vary significantly due to the relative motion between them as compared with those in the stationary case. Thus the relation of Eqn.(8.11) still holds good and the reaction of the Lorentz force on the moving conductor is carried by the remaining part of the system, which is the real material medium.

So far we have shown that the momentum conservation law of electromagnetic fields can predict the action and reaction of the electromagnetic jet propulsion as if they were predicted by Newton's third law. This is however by no means to say that the Newton's third law is *always* correct. The reason is because one of Newton's basic assertions about forces between bodies—that the action and reaction at a distance are instantaneous—is not the case in relativistic mechanics owing to the relativity of simultaneity. This means that if two interaction forces separated by a distance x occur at the same time, say $t = 0$ in one inertial frame $\sum$, they occur however at the different time with a time difference of $\gamma vx/c^2$ in another inertial frame $\sum'$, which may clearly be seen when we refer to the Lorentz transformations in Eqn.(8.12). Nevertheless, whenever the relativistic effects can be negligible, Newton's third law is still valid.

Even if the relation of action and reaction is satisfied, it still means nothing about the force transmission. We see that two bodies at a distance from each other exert a mutual influence of each other's motion. Does this mutual action depend on the existence of some third thing, some medium of communication, occupying the space between the bodies, or do the bodies act on each other immediately, without the intervention of anything else? Newton himself, as pointed out by great Maxwell [123], with that wise moderation which is characteristic of all his speculations, answered that he made no pretence of explaining the mechanism by which the heavenly bodies act on each other. To determine the mode in which their mutual action depends on their relative position was a great step in science, and this step Newton asserted that he had made. To explain the process by which this action is effected was a quite distinct step, and this step Newton, in his "Principia", does not attempt to make. In classical relativistic electrodynamics one might look at the interaction of the Lorentz forces through the electromagnetic fields, which is somehow furnished in the associated momentum conservation law but has not yet achieved the second step so closely as to explain how that force is transmitted in all cases [129]. Nevertheless, this does not mean that classical relativistic electrodynamics can be faulted in the way in which the forces are determined.

8.3 Submerging

We have discussed that the submarine propulsion can be understood in terms of the Lorentz forces. Nevertheless, as a whole it is worth to briefly discuss the mechanism of submerging before ending this Chapter.

Before the current is passed through, the equilibrium of forces on the copper submarine is given by

$$M_c g = \tau_c' \rho_m g \tag{8.22}$$

or

$$\tau_c' = \tau_c \frac{\rho_c}{\rho_m} \tag{8.23}$$

where M_c, ρ_c and τ_c represent the mass, mass density and volume of the copper submarine respectively; τ_c' is the immersion part of τ_c; ρ_m is the mass density of mercury; g is the gravitational acceleration. For pure materials $\rho_c = 8.96 \times 10^3\, kg/m^3$ and $\rho_m = 13.546 \times 10^3\, kg/m^3$ at $20\,^\circ C$ [124]. Hence $\tau_c' < \tau_c$ and the submarine is in a semi-floating state about the mercury surface.

As soon as current flows, the submarine experiences not only a net longitudinal force, but also a net transverse force because the magnetic field is stronger about the mercury surface and weaker towards the centre. Therefore the equilibrium condition in Eqn.(8.22) or Eqn.(8.23) is distorted and the transverse force submerges the submarine into the mercury until the following new force equilibrium is reached

$$\mathbf{a}_t \cdot \int_{\tau_c} \mathbf{j} \times \mathbf{B} d\tau = \tau_c g(\rho_m - \rho_c) \tag{8.24}$$

in which $\mathbf{a}_t$ indicates the transverse unit vector. Notice the force on the R.H.S. of Eqn.(8.24) is constant, but the Lorentz force on the L.H.S. depends on the submerging position. Since at the centre of mercury trough (the axisymmetrical position) the net transverse force disappears, the balance position in the transverse direction will be above the centre line. Then the transverse Lorentzian force will increase above the balance position whereas it will decrease below it so that any displacement will be drawn back, which implies that the dynamic equilibrium described by Eqn.(8.24) is stable.

Appendix 8.1

In Cartesian coordinates the Maxwell stress tensor can be expressed as

$$\overleftrightarrow{\mathbf{T}} = \mathbf{a}_x \mathbf{T_x} + \mathbf{a}_y \mathbf{T_y} + \mathbf{a}_z \mathbf{T_z} \tag{8.25}$$

with

$$\begin{aligned} \mathbf{T_x} &= T_{xx}\mathbf{a}_x + T_{xy}\mathbf{a}_y + T_{xz}\mathbf{a}_z & (8.26)\\ \mathbf{T_y} &= T_{yx}\mathbf{a}_x + T_{yy}\mathbf{a}_y + T_{yz}\mathbf{a}_z & (8.27)\\ \mathbf{T_x} &= T_{zx}\mathbf{a}_x + T_{zy}\mathbf{a}_y + T_{zz}\mathbf{a}_z & (8.28) \end{aligned}$$

Thus we have

$$\nabla \cdot \overleftrightarrow{\mathbf{T}} = \mathbf{a}_x(\nabla \cdot \mathbf{T_x}) + \mathbf{a}_y(\nabla \cdot \mathbf{T_y}) + \mathbf{a}_z(\nabla \cdot \mathbf{T_z}) \tag{8.29}$$

or

$$\int_\tau \nabla \cdot \overleftrightarrow{\mathbf{T}}\, d\tau = \mathbf{a}_x \int_\tau (\nabla \cdot \mathbf{T_x}) d\tau + \mathbf{a}_y \int_\tau (\nabla \cdot \mathbf{T_y}) d\tau + \mathbf{a}_z \int_\tau (\nabla \cdot \mathbf{T_z}) d\tau \tag{8.30}$$

where τ denotes an arbitrary volume enclosed by a surface s. Applying Gauss's theorem to each component on the R.H.S. of Eqn.(8.30) gives

$$\int_\tau \nabla\cdot \overleftrightarrow{\mathbf{T}}\, d\tau = \mathbf{a}_x \oint_s \mathbf{T_x}\cdot d\mathbf{s} + \mathbf{a}_y \oint_s \mathbf{T_y}\cdot d\mathbf{s} + \mathbf{a}_z \oint_s \mathbf{T_z}\cdot d\mathbf{s} \tag{8.31}$$

By referring to Eqn.(8.25) we can obviously rewrite Eqn.(8.31) as

$$\int_\tau \nabla\cdot \overleftrightarrow{\mathbf{T}}\, d\tau = \oint_s \overleftrightarrow{\mathbf{T}}\cdot d\mathbf{s} \tag{8.32}$$

This equation enable us to obtain Eqns.(8.6,8.7).

Appendix 8.2

The rule for changing partial differential coefficients with respect to one set of variables into partial differential coefficients with respect to another set of variables, can be obtained as follows [139]. Consider a function F, which is a function of x, y, z and t in $\sum$. The total differential of F is

$$dF = \frac{\partial F}{\partial x}dx + \frac{\partial F}{\partial y}dy + \frac{\partial F}{\partial z}dz + \frac{\partial F}{\partial t}dt \tag{8.33}$$

Now for a given event, x, y, z and t are all functions of x', y', z' and t' as given by the Lorentz transformations in Eqn.(8.12). The total differentials of x, y, z and t can be expressed as

$$\begin{aligned} dx &= \gamma(dx' + v dt') \\ dy &= dy' \\ dz &= dz' \\ dt &= \gamma(dt' + v dx'/c^2) \end{aligned} \tag{8.34}$$

Substituting those into Eqn.(8.33) gives

$$\begin{aligned} dF &= \frac{\partial F}{\partial x}\gamma(dx' + v dt') + \frac{\partial F}{\partial y}dy' + \frac{\partial F}{\partial z}dz' + \frac{\partial F}{\partial t}\gamma(dt' + v dx'/c^2) \\ &= \left(\gamma\frac{\partial F}{\partial x} + \gamma\frac{v}{c^2}\frac{\partial F}{\partial t}\right)dx' + \frac{\partial F}{\partial y}dy' + \frac{\partial F}{\partial z}dz' + \left(\gamma\frac{\partial F}{\partial t} + \gamma v\frac{\partial F}{\partial x}\right)dt' \end{aligned} \tag{8.35}$$

But, if F is a function of x', y', z' and t' the total differential of F can be written as

$$dF = \frac{\partial F}{\partial x'}dx' + \frac{\partial F}{\partial y'}dy' + \frac{\partial F}{\partial z'}dz' + \frac{\partial F}{\partial t'}dt' \tag{8.36}$$

Comparing the coefficients of dx', dy', dz' and dt' in Eqns.(8.35) and (8.36), we obtain

$$\frac{\partial}{\partial x'} = \gamma\left(\frac{\partial}{\partial x} + \frac{v}{c^2}\frac{\partial}{\partial t}\right) \tag{8.37}$$

$$\frac{\partial}{\partial y'} = \frac{\partial}{\partial y} \tag{8.38}$$

$$\frac{\partial}{\partial z'} = \frac{\partial}{\partial z} \tag{8.39}$$

$$\frac{\partial}{\partial t'} = \gamma\left(\frac{\partial}{\partial t} + v\frac{\partial}{\partial x}\right) \tag{8.40}$$

In the same way we can derive

$$\frac{\partial}{\partial x} = \gamma\left(\frac{\partial}{\partial x'} - \frac{v}{c^2}\frac{\partial}{\partial t'}\right) \tag{8.41}$$

$$\frac{\partial}{\partial y} = \frac{\partial}{\partial y'} \tag{8.42}$$

$$\frac{\partial}{\partial z} = \frac{\partial}{\partial z'} \tag{8.43}$$

$$\frac{\partial}{\partial t} = \gamma\left(\frac{\partial}{\partial t'} - v\frac{\partial}{\partial x'}\right) \tag{8.44}$$

Chapter 9

On the Electromagnetic Impulse Pendulum

9.1 Background

In 1983 Pappas [126] reported an invented electromagnetic impulse pendulum experiment which, according to the author, was aimed to indicate that the momentum imparted to the pendulum was not balanced by an equal and opposite momentum change of field energy. Two years later Graneau and Graneau [127] repeated Pappas's experiment at MIT using discharge currents from a capacitor bank which contained a known amount of stored energy. Figure 9.1 shows the experimental set-up of the electromagnetic impulse pendulum used at MIT. The hairpin pendulum was made of a copper strip 0.5 inch high and 0.05 inch thick. The strip formed two 1 m long sides and one 30 cm short side of an open rectangle. The pendulum conductor was mounted on a rigid frame (not shown in Fig.9.1) of insulating material. The assembly weighed 0.815 kg. The pendulum was suspended from the laboratory ceiling by four 2.56 m long cotton threads. The horizontal displacement of the pendulum was measured with the cardboard slide C resting on a flat table top. The pulse current was derived from an 8 μF high-voltage capacitor bank. The discharge was initiated by dropping the mechanical switch S. Two parallel copper rails F brought the current to the pendulum via two, 1 mm long, arc gaps in air. The rail were fixed on a rigid frame and two heavy

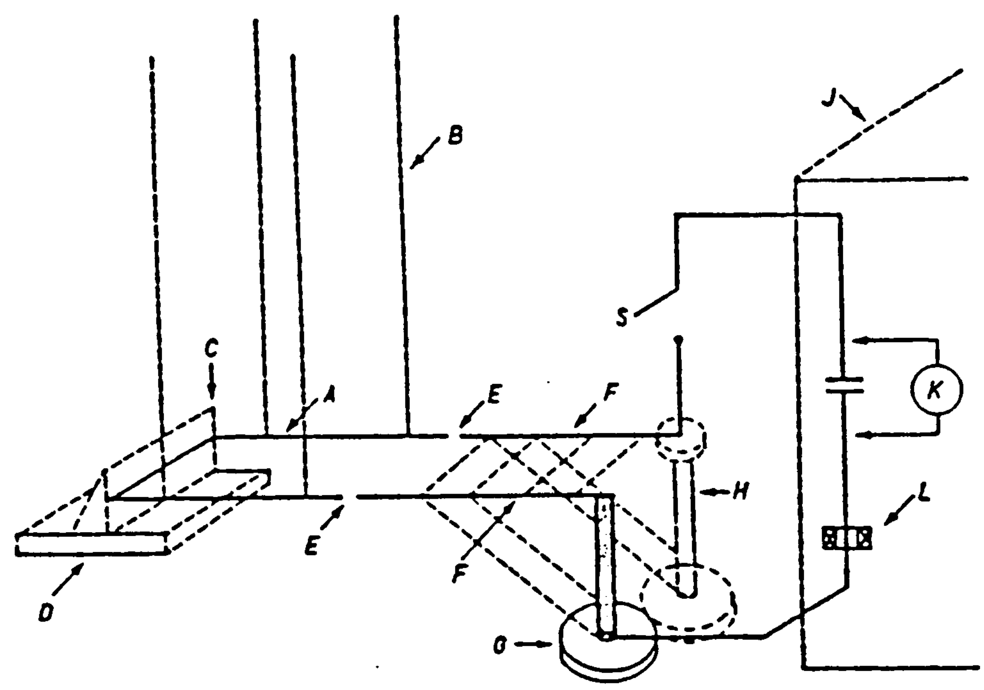

Figure 9.1: Electromagnetic impulse pendulum after Graneau and Graneau [127]
A) Hairpin pendulum, B) Pendulum suspension on cotton threads
C) Cardboard slide, D) Flat table top, E) Arc gaps in air
F) Current rails on dielectric frame G) Metal stand, H) Dielectric stand
S) Mechanical high-voltage switch, J) Capacitor bank (8 μF, 100 kV)
K) Charging set, L) Rogowski coil for pulse current measurement

stands.

To perform an experiment, the capacitor bank was charged to a voltage between 30 and 80 kV. The switch was then dropped, causing arcing across the short gaps between current rails and pendulum legs. The damped oscillatory current pulse was recorded with the aid of the Rogowski coil and an oscilloscope. The current pulse did cause the pendulum to swing away from the current rails and move the cardboard slide through a distance d. The duration of the current pulse was a fraction of a millisecond. Almost all the pendulum displacement occurred after the current had ceased to flow. Two typical sets of the experimental data are listed in Table 9.1, where T is the time constant of the equivalent RLC circuit for the experimental set-up and f is the corresponding ring frequency.

Based on the experimental results, Graueau and Graneau asserted that, for momentum conservation, the magnetic-field energy required would have been 1000 to 2000 times as large as the energy that was actually stored in the capacitors. This has caused some confusion. Therefore the remainder of this Chapter is aimed at clarifying

Table 9.1: Two typical sets of the experimental data†

$T = 0.27\,ms,\ \ f = 15.7\,kHz$	Symbol	Unit	40 kV	80 kV
maximum pulse current	I_0	A	28 500	60 000
pendulum displacement	d	cm	1.93	10.95
energy stored in capacitors	U_c	J	6 400	25 600
maximum pendulum momentum	mv	$kg \cdot m/s$	0.0308	0.1747

† After Graneau and Graneau [127]

the matter.

9.2 Previous analytical approach

For our purpose it is worth while reviewing the analytical approach [127] by which Pappas and his successors obtained their findings.

Starting from the field-momentum density

$$\mathbf{g} = \frac{\mathbf{E} \times \mathbf{H}}{c^2} \tag{9.1}$$

where c is the velocity of light, they defined a vacuum reaction force

$$\mathbf{F}_{vac} = \int \frac{d\mathbf{g}}{dt} d\tau = \frac{1}{c^2} \int \frac{d(\mathbf{E} \times \mathbf{H})}{dt} d\tau \tag{9.2}$$

and related this force to

$$\mathbf{F}_{vac} = \frac{d(m_e c)}{dt} \tag{9.3}$$

where m_e is the equivalent electromagnetic mass of the field energy.[1] The amount of field energy U_f that must at any time be associated with the vacuum reaction force was

$$U_f = m_e c^2 \tag{9.4}$$

according to the famous mass-energy relation of special relativity.

[1]This equation is not so well defined because one side is a vector while the other side is a scalar.

Next they stated that if $\mathbf{F}_{vac}$ was all times the simultaneous reaction force to the Lorentz force $\mathbf{F}_L$ when the latter accelerates a metallic conductor object of real mass m from zero velocity to the velocity v, then momentum conservation was expressed by

$$mv = m_e c \tag{9.5}$$

The field energy which had to be radiated or absorbed by the conductor body to comply with Eqn.(9.5) was

$$U_f = m_e c^2 = mvc \tag{9.6}$$

Taking $c = 3 \times 10^8\, m/s$ and replacing mv by the numerical values in Table 9.1, they found the field energy required by Eqn.(9.6) for the both sets of experiments were $9.24 \times 10^6\, J$ and $52.41 \times 10^6\, J$ respectively, which were far greater than the amount of energy available from the capacitors by factors of 1443 and 2047. It is these results which led Pappas, Graneau and Graneau to call electromagnetic field theory into question.

9.3 The field-theory prediction

In spite of the dispute on field concepts, as far as the field energy and momentum are concerned, we should base our prediction on the relevant laws of field theory, i.e.

$$\mathbf{E} \cdot \mathbf{j} + \frac{\partial w}{\partial t} = -\nabla \cdot \mathbf{P} \tag{9.7}$$

$$\mathbf{f} + \frac{\partial \mathbf{g}}{\partial t} = \nabla \cdot \overleftrightarrow{T} \tag{9.8}$$

Equation (9.7) states the energy conservation law where

$$\frac{\partial w}{\partial t} = \mathbf{E} \cdot \frac{\partial \mathbf{D}}{\partial t} + \mathbf{H} \cdot \frac{\partial \mathbf{B}}{\partial t} \tag{9.9}$$

$$\mathbf{P} = \mathbf{E} \times \mathbf{H} \tag{9.10}$$

are the time rate of change of the field energy density and the Poynting vector.[2] Equation (9.8) is the momentum conservation law we have encountered in the last Chapter.

Now let us consider the experimental set-up of electromagnetic impulse pendulum as a complete current system $\tau = \tau_1 + \tau_2$ bounded by a surface s, where τ_2 stands for

[2] Refer to Panofsky and Phillips [50], Chapter 10.

the hairpin pendulum while τ_1 the remainder of the system including the fixed current rails. Suppose the whole space except τ is free from charges and currents.[3]

The volume integrals of both sides of Eqn.(9.7) over the whole space yields

$$\int_{space}\left(\mathbf{E}\cdot\mathbf{j}+\frac{\partial w}{\partial t}\right)d\tau=\int_{space}-\nabla\cdot\mathbf{P}d\tau \tag{9.11}$$

Considering $\mathbf{j}=0$ in the space except τ and applying Gauss's theorem to the R.H.S. of Eqn.(9.11) we obtain

$$\int_{\tau}\mathbf{E}\cdot\mathbf{j}d\tau+\int_{space}\frac{\partial w}{\partial t}d\tau=\int_{s_\infty}-\mathbf{P}\cdot ds \tag{9.12}$$

where s_∞ indicates the surface enclosing infinite space. We note that the Poynting vector is strictly zero over s_∞ because the fields either die out within a finite distance (if static) or are far away to reach this surface (if propagated). Thus Eqn.(9.12) becomes

$$\int_{\tau}\mathbf{E}\cdot\mathbf{j}d\tau+\int_{space}\frac{\partial w}{\partial t}d\tau=0 \tag{9.13}$$

If we take the supply source into account, the extra term p_s representing the supply power should be added to the R.H.S. of Eqn.(9.13), namely

$$\int_{\tau}\mathbf{E}\cdot\mathbf{j}d\tau+\int_{space}\frac{\partial w}{\partial t}d\tau=p_s \tag{9.14}$$

For the flexible current system, part of which is mobile (such as the hairpin pendulum in this case), due to electromagnetic forces part of the electromagnetic energy must be transformed into the mechanical energy. It can be shown[4] that the first term on the L.H.S. of Eqn.(9.14) becomes

$$\int_{\tau}\mathbf{E}\cdot\mathbf{j}d\tau=\int_{\tau_1}\mathbf{E}\cdot\mathbf{j}d\tau+\int_{\tau_2}(\mathbf{E}+\mathbf{v}\times\mathbf{B})\cdot(\mathbf{j}-\rho\mathbf{v})d\tau+\int_{\tau_2}\mathbf{f}\cdot\mathbf{v}d\tau \tag{9.15}$$

where all quantities are observed at the laboratory frame. The first two terms on the R.H.S. of Eqn.(9.15) denotes the total dissipation power of the Joule heat while the last term is identifiable as work per unit time done by the electromagnetic forces on the moving conductor [128]. Substituting Eqn.(9.15) into Eqn.(9.14) and integrating each term with respect to time yield

$$U_j+U_m+U_f=U_s \tag{9.16}$$

[3]Such a space is so-called vacuum by Graneau and Graneau.

[4]See Appendix 9.1.

with

$$U_j = \int_0^t \left(\int_{\tau_1} \mathbf{E} \cdot \mathbf{j} d\tau + \int_{\tau_2} (\mathbf{E} + \mathbf{v} \times \mathbf{B}) \cdot (\mathbf{j} - \rho \mathbf{v}) d\tau \right) dt \tag{9.17}$$

$$U_m = \int_0^t \int_{\tau_2} \mathbf{f} \cdot \mathbf{v} d\tau dt \tag{9.18}$$

$$U_f = \int_0^t \int_{space} \frac{\partial w}{\partial t} d\tau dt \tag{9.19}$$

$$U_s = \int_0^t p_s dt \tag{9.20}$$

Equation (9.16) states that in a flexible current system, the supply energy U_s can be transformed into Joule heat energy U_j, mechanical energy U_m and field energy U_f, but the total transformed energy must be equal to the supply energy.

In a similar way used in the last Chapter one can derive from Eqn.(9.8) that

$$\mathbf{F}_2 = -\left(\mathbf{F}_1 + \int_{space} \frac{\partial \mathbf{g}}{\partial t} d\tau \right) \tag{9.21}$$

where $\mathbf{F}_2$ represents the Lorentz force on the hairpin pendulum while $\mathbf{F}_1$ the Lorentz force on the remainder of the current system. According to the experiment [127], the mechanical momentum of the pendulum was due to the impulse action of the Lorentz force. Suppose from $t = 0$ to $t = t_d$ the pendulum gains its all momentum subject to $\mathbf{F}_2$. It turns out

$$m\mathbf{v} = \int_0^{t_d} \mathbf{F}_2 dt \tag{9.22}$$

Since Eqn.(9.21) must hold at any instant in time, by integrating it with respect to time and then substituing into Eqn.(9.22), we have

$$m\mathbf{v} = -\int_0^{t_d} \left(\mathbf{F}_1 + \int_{space} \frac{\partial \mathbf{g}}{\partial t} d\tau \right) dt \tag{9.23}$$

In the experiment, the current is a pulse. Take t_d as the duration of the current pulse and let C_d be the distance between points on τ_1 and τ_2 respectively. If $C_d \gg ct_d$, where c is the speed of light, it is possible that when the current wave–front reaches τ_2, the current in τ_1 has ceased flowing and τ_1 experiences no Lorentz force in the period following t_d, then the first term on the R.H.S. of Eqn.(9.23) may be omitted. In this experiment, however, $t_d \sim T = 0.27\,ms$, which gives $ct_d \sim 0.81 \times 10^5\,m$, and C_d is no more than $5\,m$, thus $C_d \ll ct_d$ and there is no reason to take away the first term in this case.

Now let us estimate the field momentum. As we know, the momentum conservation can hold in any direction. Let G'_f be the total field momentum in the moving direction of pendulum, i.e.

$$G'_f = -\int_0^{t_d}\left(\int_{space}\frac{\partial \mathbf{g}}{\partial t}\cdot\frac{\mathbf{v}}{v}d\tau\right)dt \tag{9.24}$$

If the time-varying fields are propagated with the speed of light, G'_f may be expressed as

$$G'_f = m_e c \tag{9.25}$$

where m_e is the equivalent electromagnetic mass.[5] The field energy associated with this momentum component is

$$U'_f = m_e c^2 \tag{9.26}$$

according to the well-known mass-energy relation of special relativity. It is obvious that U'_f is smaller than the total field energy U_f in Eqn.(9.16) and then is impossible to exceed the initial stored energy U_s. It turns out

$$U'_f = m_e c^2 < U_s \tag{9.27}$$

or

$$G'_f = m_e c < U_s/c \tag{9.28}$$

On substitution of the maximum stored energy 25 600 J from Table 9.1 we obtain

$$G'_f = m_e c < 8.5\times10^{-5}\ (kg\cdot m/s) \tag{9.29}$$

which is a minuscule amount as compared with the minimum pendulum momentum $mv = 3.08\times10^{-2}\ kg\cdot m/s$ in Table 9.1. Therefore it is justifiable in this case to write down

$$m\mathbf{v} = -\int_0^{t_d}\mathbf{F}_1 dt \tag{9.30}$$

which in association with Eqn.(9.22) implies that the Lorentz force which accelerates the electromagnetic impulse pendulum to acquire a certain mechanical momentum finds its reaction on the stationary portion of the current system. This theoretical prediction is in accord with the experimental observation.

[5] The rest mass of the time-varying fields travelling with a speed c is zero so that the associated rest energy is also zero.

Turning to Pappas and his successors' approach, it is now clear that error made by them was to suppose that the momentum acquired by the pendulum was equal to that associated with the Poynting vector ($\mathbf{g} = \mathbf{P}/c^2$). This, as we have demonstrated, is not the case.

Yet there are some difficulties in a universal explanation of the force transmission in terms of classical relativistic electrodynamics. But this is by no means the same as saying that the field theory fails to determine the electrodynamic forces, or to explain the associated observations whenever the theory is valid. If it were so, how could Newtonian mechanics which does not tell us anything about the force transmission survive today? Hence one must not be confused by these two steps in science, namely one for force calculation and the other for force transmission as we have briefly discussed in the last Chapter. It is not more philosophical to admit the existence of a mechanism which could transmit the forces between two bodies such as the field momentum though it might be abstract, than to assert that a body can act at a place where it is not—the theory of action at a distance. Recently, an attempt to use the concept of field momentum to explain a similar experiment—the operation of railguns has been successfully made by Allen and Jones [129] at the University of Oxford.

Appendix 9.1

From the Lorentz force law

$$\mathbf{f} = \rho\mathbf{E} + \mathbf{j} \times \mathbf{B} \tag{9.31}$$

we have

$$\mathbf{f} \cdot \mathbf{v} = \rho\mathbf{E} \cdot \mathbf{v} + (\mathbf{j} \times \mathbf{B}) \cdot \mathbf{v} \tag{9.32}$$

and, with the help of vector identity $(\mathbf{a} \times \mathbf{b}) \cdot \mathbf{c} = (\mathbf{b} \times \mathbf{c}) \cdot \mathbf{a}$

$$0 = \mathbf{f} \cdot \mathbf{v} - \rho\mathbf{E} \cdot \mathbf{v} + (\mathbf{v} \times \mathbf{B}) \cdot \mathbf{j} \tag{9.33}$$

Then, adding to the R.H.S. of the last equation the term $-\rho\mathbf{v} \cdot (\mathbf{v} \times \mathbf{B})$ which is identically equal to zero, and to both sides of the same equation the term $\mathbf{E} \cdot \mathbf{j}$, yields

$$\mathbf{E} \cdot \mathbf{j} = \mathbf{f} \cdot \mathbf{v} + (\mathbf{E} + \mathbf{v} \times \mathbf{B}) \cdot (\mathbf{j} - \rho\mathbf{v}) \tag{9.34}$$

Substituting this result into the first term on the L.H.S. of Eqn.(9.14) and considering that τ_1 is at rest (with a zero velocity) in our laboratory lead to Eqn.(9.15).

Chapter 10

On the Water-Arc Explosions

10.1 Background

The enormous strength of water-arc explosions has been exploited for decades [130, 131]. It was commonly held that the high pressure was due to shock waves produced by underwater electric arcs until 1985 when a paper by Graneau and Graneau [132] reported experiments performed at MIT in 1984 with a salt-water cup and proposed another mechanism. In that paper, they claimed that the high pressure could be a direct result of electrodynamic forces and the explosive phenomenon could be explained with the aid of longitudinal Ampère forces but not with traditional Lorentz forces. Since then, some confusion has been caused and the phenomenon has been said to be anomalous [133, 134].

Figure 10.1 is a diagram of experiments carried out in the salt-water cup. An insulated copper rod, bare at the endface, projects through the bottom of a dielectric cup filled with a solution of common salt (NaCl) saturated water at room temperature. A bare copper ring electrode is immersed in the upper part of the cup and connected to an energy storage capacitor via an induction coil and switch. The other end of the capacitor is connected to the copper rod. The capacitor C is charged to the voltage V_0. When the switch S was closed, and depending on the values of C and V_0, the discharge through the salt water was either silent (no arc occured) and left the water undisturbed or it resulted in a luminuous underwater water arc in the vicinity of the

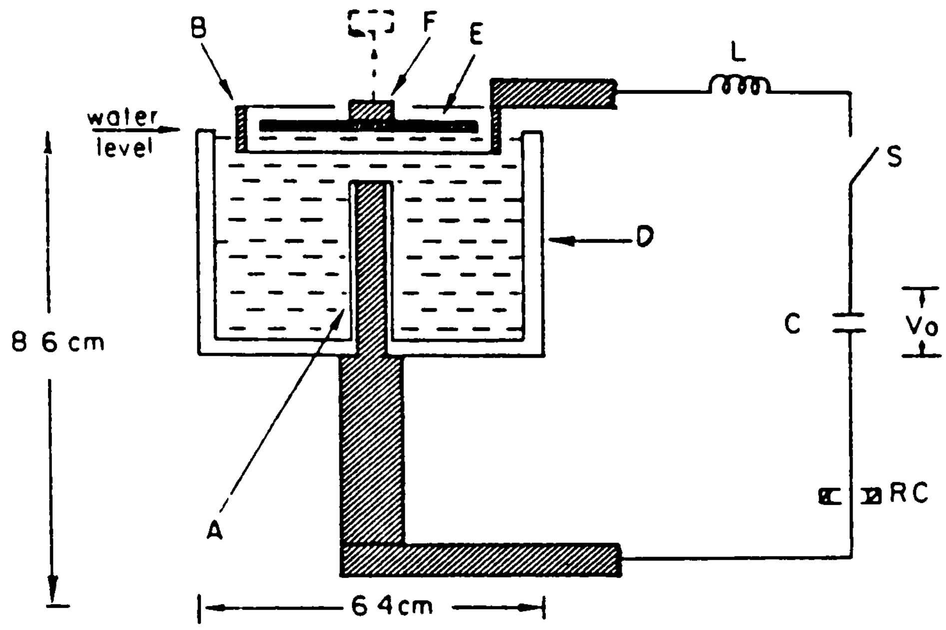

Figure 10.1 : Cross section of saltwater cup for experiments [132]
A–insulated copper rod with bare endface; B–bare copper ring electrode
D–dielectric cup containing salt water; E–wooden disc float
F-2.8 g metal weight; L–induction coil; S–switch in air
C–energy storage capacitor; RC–Rogowski coil

endface of the copper rod. Visible arcs were always accompanied by a snapping sound and a shock disturbance of the liquid. Two typical sets of experimental parameters are listed in Table 10.1. With the large arc discharge current, e.g. $I_0 = 104.7\,A$, a wood float on the water surface would fling a $2.8\,g$ metal weight originally resting on top of it upward by as much as $20\,cm$ without spilling any water. No followthrough push from expanding steam nor any vapour escape from the cup could be discerned.

Table 10.1: Typical experimental parameters

		No arc	Arc
Capacitance	C	$0.5\,\mu F$	$2.0\,\mu F$
Charging voltage	V_0	$6.0\,kV$	$3.0\,kV$
Stored energy	E_s	$9.0\,J$	$9.0\,J$
Undamped current amplitude	I_0	$78.8\,A$	$93.8\,A$

The authors argued that since in those two cases (referring to Table 10.1) approximately the same amount of energy was being dissipated over roughly the same current path and time, it seemed unlikely that the arc explosion was a thermal event. According to their estimation [132], the average force exerted on the metal weight by the explosion could come to $21.6\,N$. They said that this order of the force could be predicted by the Ampère's longitudinal forces but not by the traditional Lorentz forces. We have discussed in Chapter 7 that the so-called Ampère's longitudinal forces predicted by Graneau's approach do not exist. Thus, if the water-arc explosive phenomenon could be understood by electrodynamics, it should be explicable in terms of the Lorentz force law. Therefore it is the purpose of the next section to examine whether the up-thrust force of the water-arc explosion in this particular set up could be explained by an electromagnetic field model.

For our investigation, the structure in Fig.10.1 will be simplified to one as shown in Fig.10.2 through this Chapter because it is unlikely that such a simplification may affect the foundation on which the physical mechanism underlying the creation of water pressure is based.

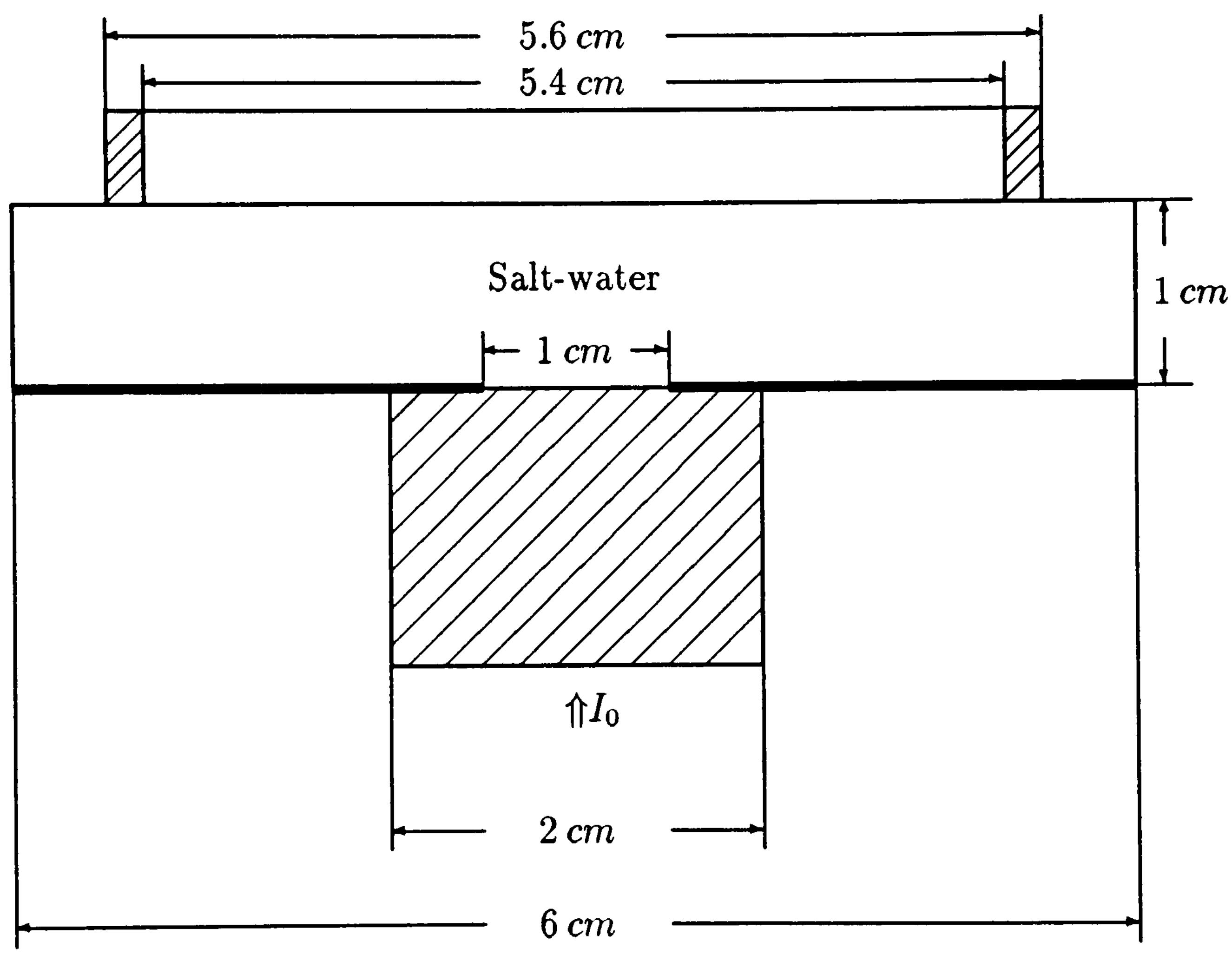

Figure 10.2 : The simplified model for theoretical study

10.2 Electromagnetic Model

10.2.1 Governing Equations

To examine if the water–arc explosive phenomenon could be understood by electrodynamics, in this section we do not consider any hydrodynamic effect and assume the governing equations are Maxwell's equations

$$\nabla \times \mathbf{E} = -\frac{\partial \mathbf{B}}{\partial t} \tag{10.1}$$

$$\nabla \times \mathbf{B} = \mu(\mathbf{j} + \epsilon\frac{\partial \mathbf{E}}{\partial t}) \tag{10.2}$$

$$\nabla \cdot \mathbf{B} = 0 \tag{10.3}$$

$$\nabla \cdot \mathbf{E} = 0 \quad \text{for charge-free region} \tag{10.4}$$

where μ and ϵ are the permeability and permittivity in the medium under consideration, together with the Ohm's and Lorentzian force laws

$$\mathbf{j} = \sigma\mathbf{E} \tag{10.5}$$

$$\mathbf{f} = \mathbf{j} \times \mathbf{B} \tag{10.6}$$

However it has been shown[1] that in general, the displacement current $\epsilon\partial\mathbf{E}/\partial t$ is negligible relative to the conduction current in metals. This may directly be seen by examining

$$|\epsilon\frac{\partial \mathbf{E}}{\partial t}| \ll |\mathbf{j}| \tag{10.7}$$

Consider a field that varies with an angular frequency w :

$$\mathbf{E}(\mathbf{r},t) = Re\left\{\mathbf{E}(\mathbf{r})e^{-iwt}\right\} \tag{10.8}$$

where the operation Re means "Real part of follows" and $\mathbf{E}(\mathbf{r})$ is called the phasor of electric field, whose modulus is the amplitude of $\mathbf{E}(\mathbf{r},t)$ and whose phase is the phase at $t = 0$. By substitution we have

$$\epsilon w|\mathbf{E}| \ll \sigma|\mathbf{E}| \tag{10.9}$$

[1]Refer to Panofsky and Phillips [50], Chapter 11.

Taking $\epsilon = \epsilon_0 = 8.854 \times 10^{-12}\,(F/m)$ and $\sigma \sim 1\,(\Omega m)^{-1}$ for the salt water, we find a relaxation time[2] $\epsilon/\sigma \sim 10^{-12}\,(s)$. On the other hand, according to the experiments [132], the angular frequency for AC discharges is order of $10^3\,(s)^{-1}$. It is clear that $(\epsilon/\sigma) \ll 1/w$ so that the relation in Eqn.(10.7) is true and the displacement current is negligible indeed.

Next we are going to show that $\partial\mathbf{B}/\partial t$ may also be neglected. By introducing a vector potential $\mathbf{A}$ that satisfies

$$\mathbf{B} = \nabla \times \mathbf{A} \tag{10.10}$$

and substituting it into Eqn.(10.1), we obtain

$$\nabla \times (\mathbf{E} + \frac{\partial \mathbf{A}}{\partial t}) = 0 \tag{10.11}$$

It is clear that we can let

$$\mathbf{E} + \frac{\partial \mathbf{A}}{\partial t} = -\nabla V \tag{10.12}$$

in which V is a scalar potential. This equation may be written as

$$\begin{aligned} \mathbf{E} &= -\nabla V - \frac{\partial \mathbf{A}}{\partial t} \\ &= \mathbf{E}_{con} + \mathbf{E}_{ind} \end{aligned} \tag{10.13}$$

where $\mathbf{E}_{con}$ denotes the conservative field whereas $\mathbf{E}_{ind}$ the induced field. Thus

$$\mathbf{j} = \sigma\mathbf{E}_{con} + \sigma\mathbf{E}_{ind} = \mathbf{j}_{con} + \mathbf{j}_{ind} \tag{10.14}$$

according to Ohm's law. In addition to Eqn.(10.8), we can define

$$\mathbf{B}(\mathbf{r},t) = Re\left\{\mathbf{B}(\mathbf{r})e^{-iwt}\right\} \tag{10.15}$$

$$\mathbf{j}(\mathbf{r},t) = Re\left\{\mathbf{j}(\mathbf{r})e^{-iwt}\right\} \tag{10.16}$$

so that

$$\nabla \times \mathbf{E} = \nabla \times \mathbf{E}_{ind} = iw\mathbf{B} \tag{10.17}$$

[2]The relaxation time is a characteristic time for a medium in that it gives an indication of the time in which essentially stationary condition will be reached after the initiation of a particular flow of charge.

because $\nabla \times \mathbf{E}_{con} = 0$. We can therefore say that

$$|\mathbf{E}_{ind}| \sim C_L w |\mathbf{B}| \tag{10.18}$$

where C_L is a length characteristic of the dimensions of the system. On the other hand, we have

$$\nabla \times \mathbf{B} = \mu \mathbf{j} \tag{10.19}$$

Let us consider salt water inside the cup as a long cylindrical conductor with a radius r_0 and a current

$$I_0 \sin wt = Re\left\{ I e^{-iwt} \right\} \tag{10.20}$$

passing through it. For symmetry, only the azimuthal magnetic induction exists and has a maximum complex amplitude

$$B_{max} = \frac{\mu I}{2\pi r_0} \tag{10.21}$$

which can be derived from Eqn.(10.19). Thus we can also say

$$|\mathbf{B}| \sim |B_{max}| = \frac{\mu I_0}{2\pi r_0} \tag{10.22}$$

Now we are able to estimate the value of induced field. For $\mu = \mu_0 = 4\pi \times 10^{-7}\,(H/m)$, $I_0 = 100\,A$, $r_0 \sim 10^{-2}\,m$, $C_L \sim 10^{-2}\,m$ and $w \sim 10^3\,(s)^{-1}$, we have $|\mathbf{B}| \sim 10^{-3}\,Tesla$ from Eqn.(10.22), and then $|\mathbf{E}_{ind}| \sim 10^{-2}\,(V/m)$ from Eqn.(10.18) that gives the value of induced current density with an order $|\mathbf{j}_{ind}| \sim 10^{-2}\,(A/m^2)$ according to Eqn.(10.14) if the conductivity of salt-water amounts to $1\,(\Omega m)^{-1}$. Thus the maximum contribution of induced current to the passing current could be estimated by

$$I_{ind} = \pi r_0^2 |\mathbf{j}_{ind}| \tag{10.23}$$

Substituting the associated values yields $I_{ind} \sim 10^{-6}\,A$ that is obviously a tiny amount of the total passing current and is negligible. Therefore $\partial \mathbf{B}/\partial t$ can be ignored in the salt-water region without any difficulty.[3] However, in the copper region where the conductivity is much higher, $\sigma_{copper} = 5.8 \times 10^7\,(\Omega m)^{-1}$, we can see by substitution

[3]It is interesting to find that the condition of $|\mathbf{E}_{ind}| \ll |\mathbf{E}_{con}|$ for ignoring $\partial \mathbf{B}/\partial t$ is equivalent to that of $1/\sqrt{\mu\sigma w}\,(skin\,depth) \gg r_0$ in this case if we let $|\mathbf{E}_{con}| \sim I_0/(\sigma\pi r_0^2)$.

that the induced field is the same order as that of the conservative field. Nevertheless, because we are more interested in the fields within the salt-water, to a first degree of approximation, we have ignored $\partial \mathbf{B}/\partial t$ in the copper region.

Based on the forgoing discussions, the governing equations of Eqns.(10.1,10.2) may reduced to

$$\nabla \times \mathbf{E} = 0 \tag{10.24}$$

$$\nabla \times \mathbf{B} = \mu \mathbf{j} \tag{10.25}$$

and Eqn.(10.12) becomes

$$\mathbf{E} = -\nabla V \tag{10.26}$$

By applying Eqn.(10.4), we obtain from Eqn.(10.26)

$$\nabla^2 V = 0 \tag{10.27}$$

which is the Laplace's equation. Thus in analogy to a steady-state case, the EM fields at time t can be determined by solely solving the scalar potential subject to the boundary conditions given at that time without coupling to the vector potential. Since electrodynamic forces do not change directions even in AC discharges, for our purpose we may study a DC discharge instead of an AC discharge. Hence the problem of the EM model is simplified to be a homogeneous elliptic boundary-value problem in a steady-state case, whose solution will be presented in the following.

10.2.2 Solution by the Separation of variables

It is felt that knowing current density distributions on such a particular current system is necessary before the associated electrodynamic forces can be correctly figured out in spite of which force law, the Lorentzian or the Ampère's one being used. According to Eqns.(10.5,10.26), we have

$$\mathbf{j} = -\sigma \nabla V \tag{10.28}$$

A general solution of V in cylindrical coordinates has been given in Section 3.2.

We note that on the liquid and the copper rod interface there is an overlapped step discontinuity where the current density distribution is expected to be very non-uniform. In order to be able to employ the method of separation of variables to solve this boundary value problem, we insert an auxiliary conductor section with its length $\delta \longrightarrow 0$ into the interface as shown in Fig.10.3, where only a half of the axisymmetric structure is plotted. Then the potential in terms of harmonics in each region is expanded as

$$V^{(u)}(\rho,z) = V_0^{(u)} + A_0^{(u)} z + \sum_{i=1}^{\infty} \mathcal{J}_0(k_i^{(u)}\rho)\left[A_i^{(u)} e^{-k_i^{(u)} z} + B_i^{(u)} e^{k_i^{(u)} z}\right] \tag{10.29}$$

where $\mathcal{J}_0$ is the Bessel function of the first kind of order 0 and $u = 1, 2, 3$ indicates quantities referring to the three homogeneous regions respectively. Substituting Eqn.(10.29) into Eqns.(10.26,10.28) we can obtain and

$$\begin{aligned}
j_z^{(u)}(\rho,z) &= a_0^{(u)} - \sum_{i=1}^{\infty} \mathcal{J}_0(k_i^{(u)}\rho)\left[a_i^{(u)} e^{-k_i^{(u)} z} - b_i^{(u)} e^{k_i^{(u)} z}\right] && (10.30)\\
j_\rho^{(u)}(\rho,z) &= \sum_{i=1}^{\infty} \mathcal{J}_1(k_i^{(u)}\rho)\left[a_i^{(u)} e^{-k_i^{(u)} z} + b_i^{(u)} e^{k_i^{(u)} z}\right] && (10.31)\\
j_\phi^{(u)}(\rho,z) &= 0 && (10.32)
\end{aligned}$$

and

$$E_\rho^{(u)}(\rho,z) = \frac{j_\rho^{(u)}(\rho,z)}{\sigma^{(u)}} \tag{10.33}$$

where $\mathcal{J}_1$ is the Bessel function of the first kind of order 1 and

$$\begin{aligned}
a_0^{(u)} &= -\sigma^{(u)} A_0^{(u)} && (10.34)\\
a_i^{(u)} &= \sigma^{(u)} A_i^{(u)} k_i^{(u)} && (10.35)\\
b_i^{(u)} &= \sigma^{(u)} B_i^{(u)} k_i^{(u)} && (10.36)
\end{aligned}$$

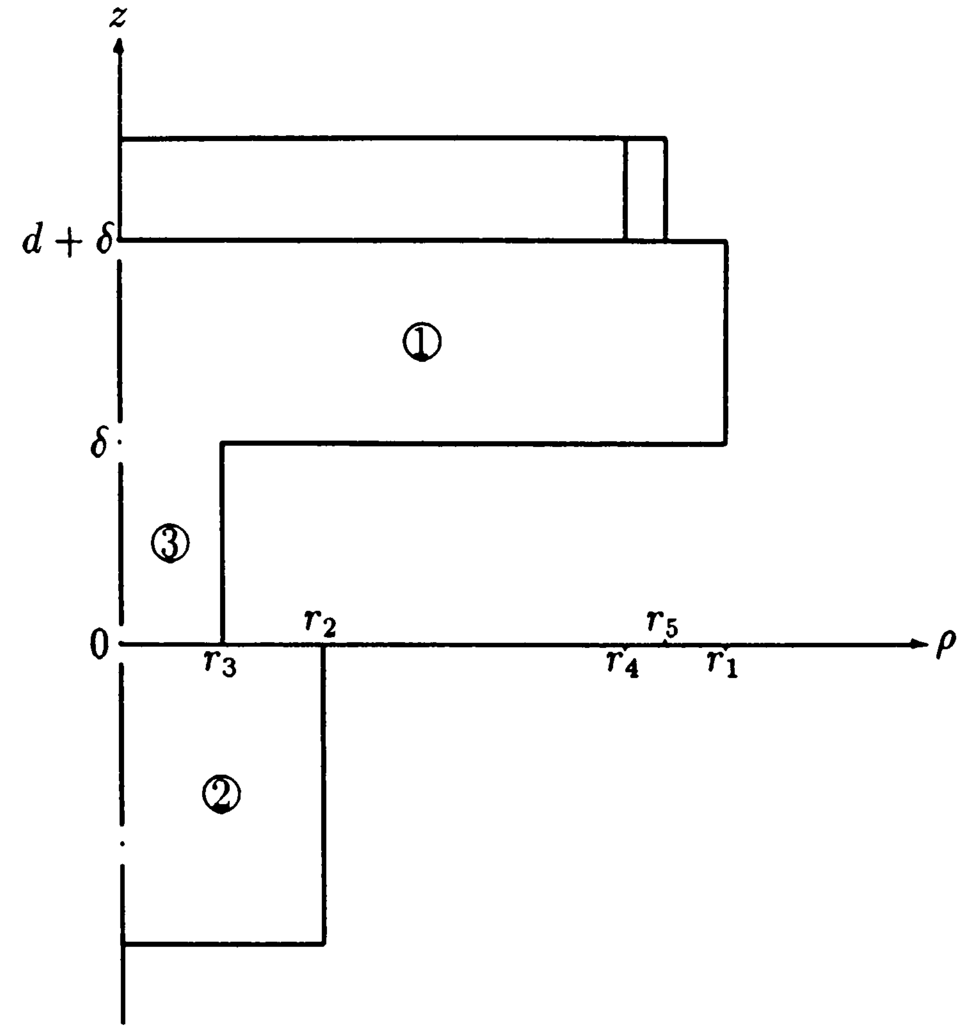

Figure 10.3 : The structure for EM formulation
r_1– radius of the water-cup; r_2– radius of the copper rod
r_3– radius of the liquid-rod interface; r_4– inner radius of the copper ring
r_5– outer radius of the copper ring; d– height of the water-cup; δ– auxilliary length

are still unknown coefficients.

Since the radial current densities must vanish at boundaries r_u for $u = 1,2,3$ respectively, we have, from Eqn.(10.31), the result

$$k_i^{(u)} = \frac{\alpha_i}{r_u} \tag{10.37}$$

in which α_i is the ith non-zero root of $\mathcal{J}_1(x) = 0$.[4]

If $z \longrightarrow -\infty$, $j_z^{(2)}$ should be finite and uniform. This leads to

$$a_i^{(2)} = 0 \tag{10.38}$$

$$a_0^{(2)} = \frac{I_0}{\pi r_2^2} \tag{10.39}$$

where I_0 is the total current.

In order to determine the unknowns in Eqns.(10.34,10.35,10.36), we apply the boundary conditions to the interfaces $z = 0$, $z = \delta$ and $z = d + \delta$ respectively, i.e.,

[4]Refer to Appendix 3.1

at $z = 0$:

$$j_z^{(2)} = \begin{cases} j_z^{(3)} & \text{for } 0 \le \rho < r_3 \\ 0 & \text{for } r_3 < \rho \le r_2 \end{cases} \tag{10.40}$$

$$E_\rho^{(3)} = E_\rho^{(2)} \quad \text{for } 0 \le \rho \le r_3 \tag{10.41}$$

at $z = \delta$:

$$j_z^{(1)} = \begin{cases} j_z^{(3)} & \text{for } 0 \le \rho < r_3 \\ 0 & \text{for } r_3 < \rho \le r_1 \end{cases} \tag{10.42}$$

$$E_\rho^{(3)} = E_\rho^{(1)} \quad \text{for } 0 \le \rho \le r_3 \tag{10.43}$$

at $z = d + \delta$:

$$j_z^{(1)} = \begin{cases} 0 & \text{for } 0 \le \rho < r_4 \\ \dfrac{I_0}{\pi(r_5^2 - r_4^2)} & \text{for } r_4 < \rho < r_5 \\ 0 & \text{for } r_5 < \rho \le r_1 \end{cases} \tag{10.44}$$

in which, for our purpose, we assume a uniform current in the copper ring on the grounds that according to experimental observation, the driving forces seem to come out from the rod-liquid interface so that the current density distribution on ring-liquid interface is expected not to be important in this case. For the same reason, the electric field matching equation at this interface is also omitted.

Substitution of the current densities and electric fields expanded in Eqns.(10.30) to (10.33) in association with Eqns.(10.38,10.39) into the above matching equations yields

$$a_0^{(2)} + \sum_{n=1}^{\infty} \mathcal{J}_0(k_n^{(2)}\rho) b_n^{(2)} = \begin{cases} a_0^{(3)} - \sum_{p=1}^{\infty} \mathcal{J}_0(k_p^{(3)}\rho)\left[a_p^{(3)} - b_p^{(3)}\right] & \text{for } 0 \le \rho < r_3 \\ 0 & \text{for } r_3 < \rho \le r_2 \end{cases} \tag{10.45}$$

$$\frac{1}{\sigma^{(3)}} \sum_{p=1}^{\infty} \mathcal{J}_1(k_p^{(3)}\rho)\left[a_p^{(3)} + b_p^{(3)}\right] = \frac{1}{\sigma^{(2)}} \sum_{n=1}^{\infty} \mathcal{J}_1(k_n^{(2)}\rho) b_n^{(2)} \quad \text{for } 0 \le \rho \le r_3 \tag{10.46}$$

$$\begin{aligned} &a_0^{(1)} - \sum_{m=1}^{\infty} \mathcal{J}_0(k_m^{(1)}\rho)\left[a_m^{(1)} e^{-k_m^{(1)}\delta} - b_m^{(1)} e^{k_m^{(1)}\delta}\right] \\ &= \begin{cases} a_0^{(3)} - \sum_{p=1}^{\infty} \mathcal{J}_0(k_p^{(3)}\rho)\left[a_p^{(3)} e^{-k_p^{(3)}\delta} - b_p^{(3)} e^{k_p^{(3)}\delta}\right] & \text{for } 0 \le \rho < r_3 \\ 0 & \text{for } r_3 < \rho \le r_1 \end{cases} \end{aligned} \tag{10.47}$$

$$\frac{1}{\sigma^{(3)}}\sum_{p=1}^{\infty}\mathcal{J}_1(k_p^{(3)}\rho)\left[a_p^{(3)}e^{-k_p^{(3)}\delta}+b_p^{(3)}e^{k_p^{(3)}\delta}\right]$$
$$=\frac{1}{\sigma^{(1)}}\sum_{m=1}^{\infty}\mathcal{J}_1(k_m^{(1)}\rho)\left[a_m^{(1)}e^{-k_m^{(1)}\delta}+b_m^{(1)}e^{k_m^{(1)}\delta}\right]\quad \text{for } 0\le\rho\le r_3 \tag{10.48}$$

$$a_0^{(1)}-\sum_{m=1}^{\infty}\mathcal{J}_0(k_m^{(1)}\rho)\left[a_m^{(1)}e^{-k_m^{(1)}(d+\delta)}-b_m^{(1)}e^{k_m^{(1)}(d+\delta)}\right]$$
$$=\begin{cases}0 & \text{for } 0\le\rho<r_4\\ \dfrac{I_0}{\pi(r_5^2-r_4^2)} & \text{for } r_4<\rho<r_5\\ 0 & \text{for } r_5<\rho\le r_1\end{cases} \tag{10.49}$$

Multiplying Eqn.(10.45) by $\rho\mathcal{J}_0(k_{n'}^{(2)}\rho)$, Eqn.(10.46) by $\rho\mathcal{J}_1(k_{p'}^{(3)}\rho)$, Eqn.(10.47) by $\rho\mathcal{J}_0(k_{m'}^{(1)}\rho)$, Eqn.(10.48) by $\rho\mathcal{J}_1(k_{p'}^{(3)}\rho)$ and Eqn.(10.49) by $\rho\mathcal{J}_0(k_{m'}^{(1)}\rho)$ respectively and then integrating with respect to ρ in the region defined for the L.H.S. of each equation, we arrive at

$$a_0^{(2)}\int_0^{r_2}\rho\mathcal{J}_0(k_{n'}^{(2)}\rho)d\rho+\sum_{n=1}^{\infty}\int_0^{r_2}\rho\mathcal{J}_0(k_{n'}^{(2)}\rho)\mathcal{J}_0(k_n^{(2)}\rho)d\rho b_n^{(2)}$$
$$=a_0^{(3)}\int_0^{r_3}\rho\mathcal{J}_0(k_{n'}^{(2)}\rho)d\rho-\sum_{p=1}^{\infty}\int_0^{r_3}\rho\mathcal{J}_0(k_{n'}^{(2)}\rho)\mathcal{J}_0(k_p^{(3)}\rho)d\rho\left[a_p^{(3)}-b_p^{(3)}\right]$$
$$\text{for } n'=0,1,2,\ldots \tag{10.50}$$

$$\frac{1}{\sigma^{(3)}}\sum_{p=1}^{\infty}\int_0^{r_3}\rho\mathcal{J}_1(k_{p'}^{(3)}\rho)\mathcal{J}_1(k_p^{(3)}\rho)d\rho\left[a_p^{(3)}+b_p^{(3)}\right]$$
$$=\frac{1}{\sigma^{(2)}}\sum_{n=1}^{\infty}\int_0^{r_3}\rho\mathcal{J}_1(k_{p'}^{(3)}\rho)\mathcal{J}_1(k_n^{(2)}\rho)d\rho b_n^{(2)}$$
$$\text{for } p'=1,2,3,\ldots \tag{10.51}$$

$$a_0^{(1)}\int_0^{r_1}\rho\mathcal{J}_0(k_{m'}^{(1)}\rho)d\rho-\sum_{m=1}^{\infty}\int_0^{r_1}\rho\mathcal{J}_0(k_{m'}^{(1)}\rho)\mathcal{J}_0(k_m^{(1)}\rho)d\rho\left[a_m^{(1)}-b_m^{(1)}\right]$$
$$=a_0^{(3)}\int_0^{r_3}\rho\mathcal{J}_0(k_{m'}^{(1)}\rho)d\rho-\sum_{p=1}^{\infty}\int_0^{r_3}\rho\mathcal{J}_0(k_{m'}^{(1)}\rho)\mathcal{J}_0(k_p^{(3)}\rho)d\rho\left[a_p^{(3)}-b_p^{(3)}\right]$$
$$\text{for } m'=0,1,2,\ldots \tag{10.52}$$

$$\frac{1}{\sigma^{(3)}}\sum_{p=1}^{\infty}\int_0^{r_3}\rho\mathcal{J}_1(k_{p'}^{(3)}\rho)\mathcal{J}_1(k_p^{(3)}\rho)d\rho\left[a_p^{(3)}+b_p^{(3)}\right]$$
$$=\frac{1}{\sigma^{(2)}}\sum_{m=1}^{\infty}\int_0^{r_3}\rho\mathcal{J}_1(k_{p'}^{(3)}\rho)\mathcal{J}_1(k_m^{(1)}\rho)d\rho\left[a_m^{(1)}+b_m^{(1)}\right]$$
$$\text{for } p'=1,2,3,\ldots \tag{10.53}$$

$$a_0^{(1)} \int_0^{r_1} \rho \mathcal{J}_0(k_{m'}^{(1)}\rho)d\rho - \sum_{m=1}^{\infty} \int_0^{r_1} \rho \mathcal{J}_0(k_{m'}^{(1)}\rho)\mathcal{J}_0(k_m^{(1)}\rho)d\rho \left[a_m^{(1)}e^{-k_m^{(1)}d} - b_m^{(1)}e^{k_m^{(1)}d}\right]$$
$$= \frac{I_0}{\pi(r_5^2 - r_4^2)} \int_{r_4}^{r_5} \rho \mathcal{J}_0(k_{m'}^{(1)}\rho)d\rho \qquad \text{for } m' = 0,1,2,... \qquad (10.54)$$

where we have imposed $\delta = 0$.

Applying the orthogonal properties of the Bessel function[5]

$$\int_0^R \rho \mathcal{J}_0(\lambda'\rho)\mathcal{J}_0(\lambda\rho)d\rho = \begin{cases} \frac{R^2}{2}[\mathcal{J}_0(\lambda R)]^2 & \text{for } \lambda = \lambda' \\ 0 & \text{for } \lambda \neq \lambda' \end{cases} \qquad (10.55)$$

if λR and $\lambda' R$ are the roots of $\mathcal{J}_0'(x) = -\mathcal{J}_1(x) = 0$, or

$$\int_0^R \rho \mathcal{J}_1(\lambda'\rho)\mathcal{J}_1(\lambda\rho)d\rho = \begin{cases} \frac{R^2}{2}[\mathcal{J}_0(\lambda R)]^2 & \text{for } \lambda = \lambda' \\ 0 & \text{for } \lambda \neq \lambda' \end{cases} \qquad (10.56)$$

if λR and $\lambda' R$ are the roots of $\mathcal{J}_1(x) = 0$, to Eqns.(10.50) to (10.54), and using the result of Eqn.(10.37), we finally obtain

$$a_0^{(1)} = \frac{I_0}{\pi r_1^2} \qquad (10.57)$$
$$a_0^{(3)} = \frac{I_0}{\pi r_3^2} \qquad (10.58)$$

and

$$b_n^{(2)}\frac{r_2^2}{2}\left[\mathcal{J}_0(k_n^{(2)}r_2)\right]^2$$
$$= a_0^{(3)} \int_0^{r_3} \rho \mathcal{J}_0(k_n^{(2)}\rho)d\rho - \sum_{p=1}^{\infty} \int_0^{r_3} \rho \mathcal{J}_0(k_n^{(2)}\rho)\mathcal{J}_0(k_p^{(3)}\rho)d\rho \left[a_p^{(3)} - b_p^{(3)}\right]$$
$$\text{for } n = 1,2,3,... \qquad (10.59)$$

$$\frac{1}{\sigma^{(3)}}\left[a_p^{(3)} + b_p^{(3)}\right]\frac{r_3^2}{2}\left[\mathcal{J}_0(k_p^{(3)}r_3)\right]^2$$
$$= \frac{1}{\sigma^{(2)}}\sum_{n=1}^{\infty} \int_0^{r_3} \rho \mathcal{J}_1(k_p^{(3)}\rho)\mathcal{J}_1(k_n^{(2)}\rho)d\rho b_n^{(2)}$$
$$\text{for } p = 1,2,3,... \qquad (10.60)$$

$$-\left[a_m^{(1)} - b_m^{(1)}\right]\frac{r_1^2}{2}\left[\mathcal{J}_0(k_m^{(1)}r_1)\right]^2$$
$$= a_0^{(3)} \int_0^{r_3} \rho \mathcal{J}_0(k_m^{(1)}\rho)d\rho - \sum_{p=1}^{\infty} \int_0^{r_3} \rho \mathcal{J}_0(k_m^{(1)}\rho)\mathcal{J}_0(k_p^{(3)}\rho)d\rho \left[a_p^{(3)} - b_p^{(3)}\right]$$
$$\text{for } m = 1,2,3,... \qquad (10.61)$$

[5]Refer to Gray and Mathews [54], pp.14–16 and 91.

$$\frac{1}{\sigma^{(3)}}\left[a_p^{(3)}+b_p^{(3)}\right]\frac{r_3^2}{2}\left[\mathcal{J}_0(k_p^{(3)}r_3)\right]^2$$
$$=\frac{1}{\sigma^{(2)}}\sum_{m=1}^{\infty}\int_0^{r_3}\rho\mathcal{J}_1(k_p^{(3)}\rho)\mathcal{J}_1(k_m^{(1)}\rho)d\rho\left[a_m^{(1)}+b_m^{(1)}\right]$$
$$\text{for } p=1,2,3,... \qquad (10.62)$$

$$\left[a_m^{(1)}e^{-k_m^{(1)}d}-b_m^{(1)}e^{k_m^{(1)}d}\right]\frac{r_1^2}{2}\left[\mathcal{J}_0(k_m^{(1)}r_1)\right]^2$$
$$=\frac{I_0}{\pi(r_5^2-r_4^2)}\int_{r_4}^{r_5}\rho\mathcal{J}_0(k_m^{(1)}\rho)d\rho$$
$$\text{for } m=1,2,3,... \qquad (10.63)$$

Equations (10.59) to (10.63) are sets of coupled linear equations which can be arranged into a linear equation system expressed by

$$\begin{pmatrix} [I] & -[I] & [0] & -[M_{13}] & [M_{13}] \\ [D_N] & -[D_P] & [0] & [0] & [0] \\ [0] & [0] & [I] & -[M_{23}] & [M_{23}] \\ [E_{31}] & [E_{31}] & [0] & -[I] & -[I] \\ [0] & [0] & [E_{32}] & -[I] & -[I] \end{pmatrix}\begin{pmatrix} [a^{(1)}] \\ [b^{(1)}] \\ [b^{(2)}] \\ [a^{(3)}] \\ [b^{(3)}] \end{pmatrix}=\begin{pmatrix} [C_1] \\ [C_2] \\ [C_3] \\ [0] \\ [0] \end{pmatrix} \qquad (10.64)$$

in which $[a^{(u)}]=[a_1^{(u)},a_2^{(u)},...]^T$ for $u=1$ and 3; and $[b^{(u)}]=[b_1^{(u)},b_2^{(u)},...]^T$ for $u=1,2,3$ are the unknown column matrices with T indicating a transposed matrix; $[I]$ and $[0]$ represent the unit and null matrices respectively; the other submatrices are derived from Eqns.(10.59) to (10.63) with the elements

$$\begin{aligned}
C_1(m,1) &= a_0^{(3)}\frac{\int_0^{r_3}\rho\mathcal{J}_0(k_m^{(1)}\rho)d\rho}{\frac{r_1^2}{2}\left[\mathcal{J}_0(k_m^{(1)}r_1)\right]^2} \\
C_2(n,1) &= -a_0^{(3)}\frac{\int_0^{r_3}\rho\mathcal{J}_0(k_n^{(2)}\rho)d\rho}{\frac{r_2^2}{2}\left[\mathcal{J}_0(k_n^{(2)}r_2)\right]^2} \\
C_3(m,1) &= \frac{I_0}{\pi(r_5^2-r_4^2)}\frac{\int_{r_4}^{r_5}\rho\mathcal{J}_0(k_m^{(1)}\rho)d\rho}{\frac{r_1^2}{2}\left[\mathcal{J}_0(k_m^{(1)}r_1)\right]^2} \\
M_{13}(m,p) &= \frac{\int_0^{r_3}\rho\mathcal{J}_0(k_m^{(1)}\rho)\mathcal{J}_0(k_p^{(3)}\rho)d\rho}{\frac{r_1^2}{2}\left[\mathcal{J}_0(k_m^{(1)}r_1)\right]^2}
\end{aligned}$$

$$
\begin{aligned}
M_{23}(n,p) &= -\frac{\int_0^{r_3} \rho \mathcal{J}_0(k_n^{(2)}\rho)\mathcal{J}_0(k_p^{(3)}\rho)d\rho}{\frac{r_2^2}{2}\left[\mathcal{J}_0(k_m^{(2)}r_2)\right]^2} \\
E_{31}(m,p) &= \frac{\sigma^{(3)}}{\sigma^{(1)}}\frac{\int_0^{r_3} \rho \mathcal{J}_1(k_m^{(1)}\rho)\mathcal{J}_1(k_p^{(3)}\rho)d\rho}{\frac{r_3^2}{2}\left[\mathcal{J}_0(k_p^{(3)}r_3)\right]^2} \\
E_{32}(p,n) &= \frac{\sigma^{(3)}}{\sigma^{(2)}}\frac{\int_0^{r_3} \rho \mathcal{J}_1(k_n^{(2)}\rho)\mathcal{J}_1(k_p^{(3)}\rho)d\rho}{\frac{r_3^2}{2}\left[\mathcal{J}_0(k_p^{(3)}r_3)\right]^2} \\
D_N(m,m) &= diagonal\ e^{-k_m^{(1)}d} \\
D_P(m,m) &= diagonal\ e^{k_m^{(1)}d}
\end{aligned}
$$

Obviously, all the unknowns can be determined by solving Eqn.(10.64) so as to find particular solutions of the current densities in regions 1 and 2 according to Eqns.(10.30,10.31).

Once the current densities are found, the magnetic induction at a space position is calculated by Eqn.(10.10) with the solution of vector potential

$$\mathbf{A}(\mathbf{r}) = \frac{\mu_0}{4\pi}\int_{\tau'}\frac{\mathbf{j}(\mathbf{r}')}{|\mathbf{r}-\mathbf{r}'|}d\tau' \tag{10.65}$$

where $\mathbf{r}$ and $\mathbf{r}'$ denote the position vectors of field and source respectively. In our case, because the current component $j_\phi = 0$ and the current distributions are independent of the ϕ coordinates, it can be shown[6] that

$$A_\phi = 0, \quad B_z = 0, \quad B_\rho = 0 \tag{10.66}$$

and

$$B_\phi(\rho,z) = \frac{\mu_0}{4\pi}\int_0^{2\pi}\int_{\rho_a}^{\rho_b}\int_{z_a}^{z_b}\rho'\frac{j_z(\rho',z')(\rho-\rho'\cos\phi') - j_\rho(\rho',z')(z-z')\cos\phi'}{[(z-z')^2+\rho^2+\rho'^2-2\rho\rho'\cos\phi']^{3/2}}d\phi' d\rho' dz' \tag{10.67}$$

Considering the axisymmetrical property of $\mathbf{j}$ and $\mathbf{B}$, we can, as a matter of fact, take the advantage of Ampère's circuital law

$$\oint_l \mathbf{B}\cdot d\mathbf{l} = \mu_0 \int\int_s \mathbf{j}\cdot d\mathbf{s} \tag{10.68}$$

to obtain a more elegant formula

$$B_\phi(\rho,z) = \frac{\mu_0}{\rho}\int_0^\rho j_z(\rho',z)\rho' d\rho' \tag{10.69}$$

[6]See Appendix 10.1 for details.

for calulation of the magnetic induction.

The determination of electrodynamic force distributions is rather straightforward

$$\mathbf{f}(\rho, z) = j_\rho(\rho, z)B_\phi(\rho, z)\mathbf{a}_z - j_z(\rho, z)B_\phi(\rho, z)\mathbf{a}_\rho \tag{10.70}$$

according to the Lorentz force law.

10.2.3 Numerical results and Discussion

A computer programme based on the above formulation was developed and run on VAX in the Oxford University Computer Centre. To make the linear equation system of Eqn.(10.64) solvable, we must define finite dimensions of the system by truncating the harmonics expanded, say the first m_1, m_2 and m_3 harmonics in regions 1,2 and 3 respectively. However, as it has been pointed out in Section 3.2 that the truncated solution suffers from the relative convergence problem, which can clearly be observed in Fig.10.4. By trial-and-error it was found that to obtain a stable numerical solution, the relation of $m_1 > (r_1/r_3)m_3$, $m_2 > (r_2/r_3)m_3$ and $m_1 > m_2$ must hold. In practice m_1, m_2 and m_3 must not be too large, for computational reasons. For the numerical results given following, unless otherwise noted, $m_1 = 250$, $m_2 = 100$ and $m_3 = 30$ were selected. Besides, $I_0 = 100\,A$, $\sigma^{(2)}/\sigma^{(1)} = 10^7$ with $\sigma^{(2)} = 5.8 \times 10^7\,(\Omega m)^{-1}$ were assumed.

Since the formulation is analysis-oriented, it can easily be seen that the numerical solutions of current densities not only satisfy the field equations at all interior points of regions 1 and 2, but also satisfy the boundary conditions at $\rho = r_1$ and $\rho = r_2$ by all means. Hence, as far as the accuracy of numerical results is concerned, we need only to check their boundary values at $z = 0$ and $z = d$ respectively, which are shown in Fig.10.5. This check confirms that the remainder boundary conditions are also satisfied. Thus the reliability of numerical solution is guaranteed according to the uniqueness of solution [135]. Figure 10.6 shows the current distributions in the salt-water region, where we can see that (i) the distributions are quite non-uniform in the vicinity of the rod-liquid interface as would be expected; (ii) the amplitude of the current density decays quickly away from the rod-liquid interface and at the ring-liquid interface it is

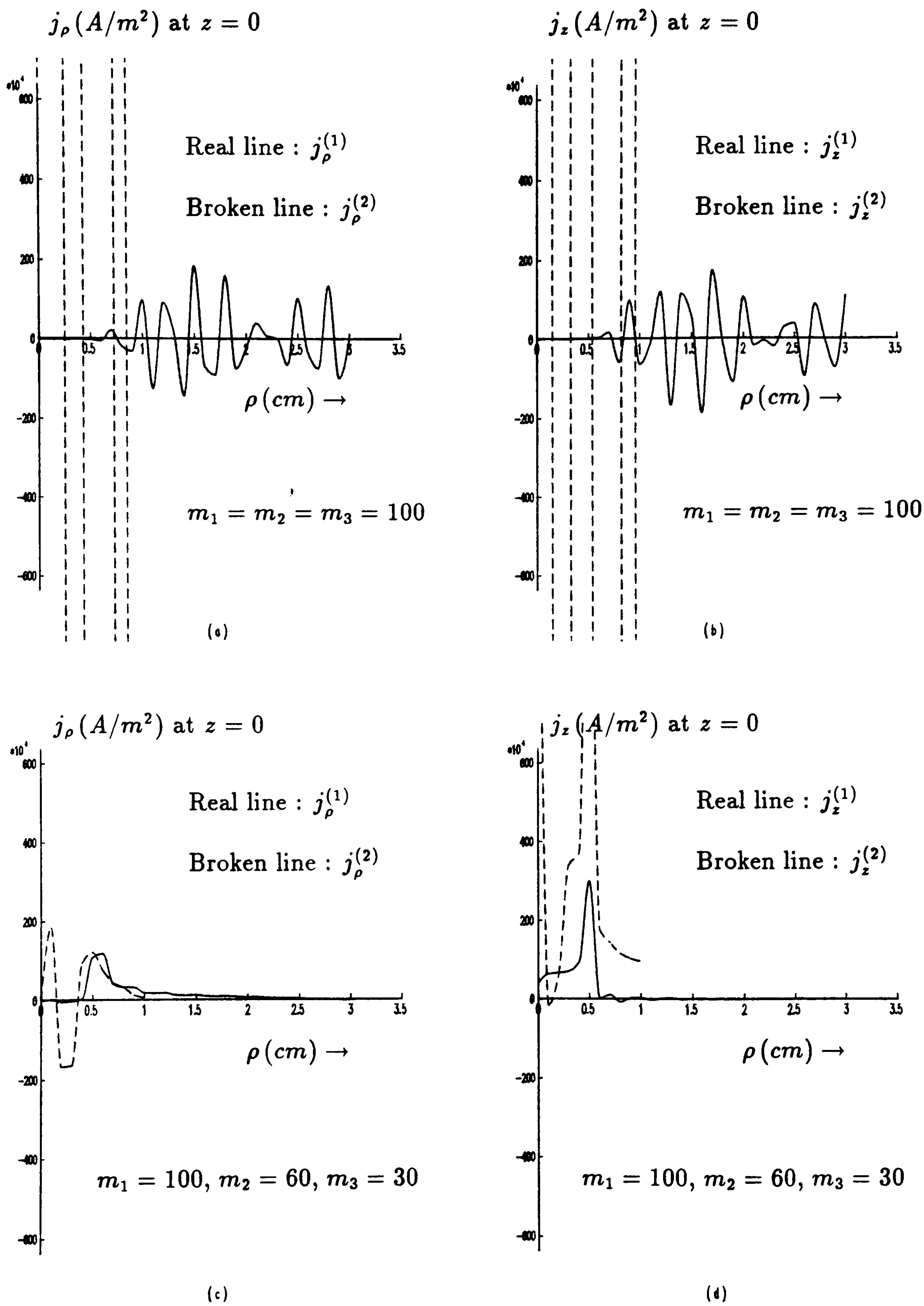

Figure 10.4: Demonstration of relative convergence problem

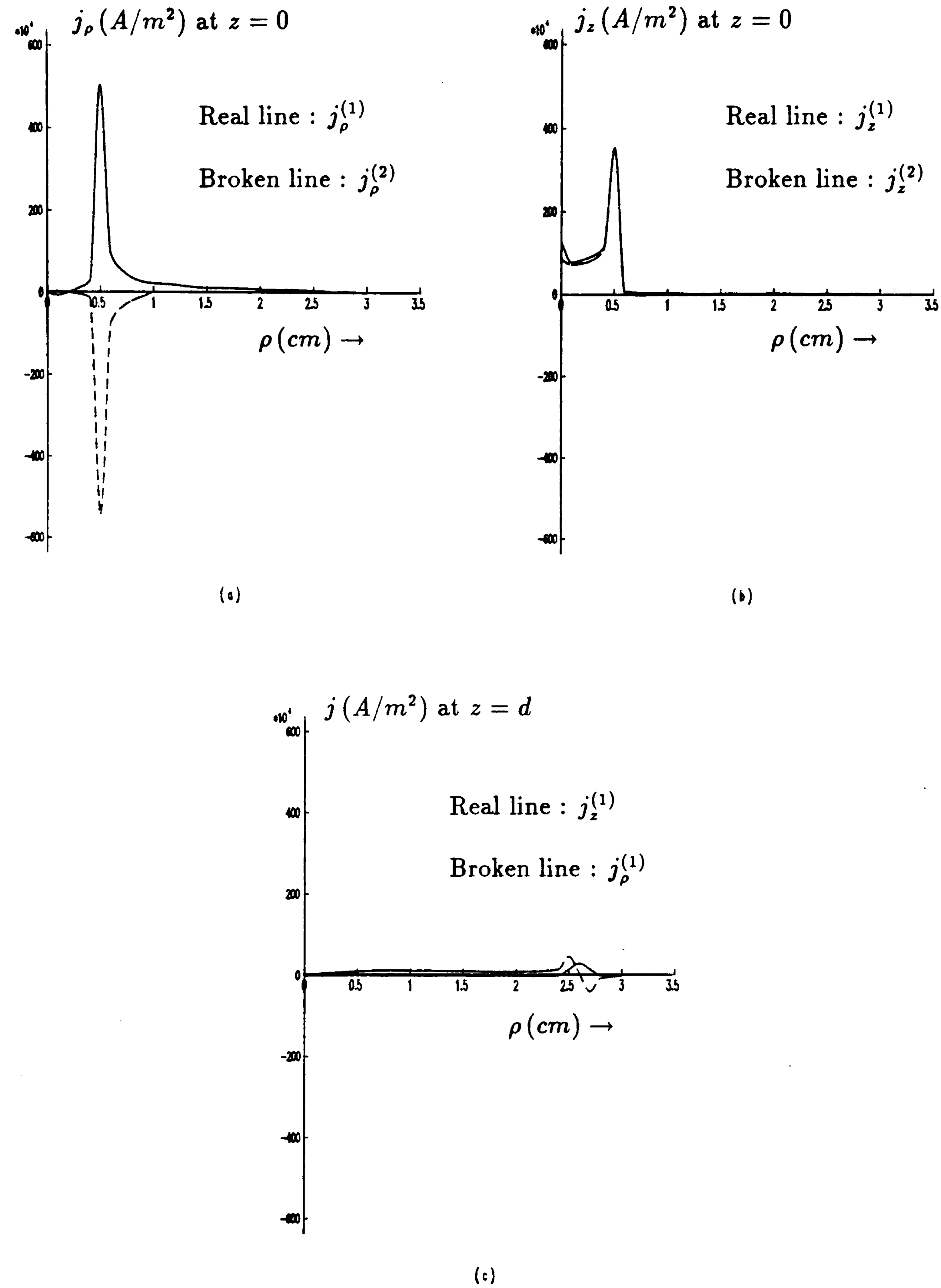

Figure 10.5: Current densities at boundaries

small and not important so that the assumption of uniform current distribution on that interface is not a critical one; (iii) the current not only has an axial component, but also has a radial component. The flow pattern of the current is displayed in Fig.10.7 which is mapped from

$$\rho B_{\phi}(\rho, z) = const. \tag{10.71}$$

The proof is given in Appendix 10.2.

The magnetic induction was first computed by two different numerical integration routines according to Eqn.(10.67) and Eqn.(10.69) to enable us to check the numerical results. It was found that both of the results were in agreement, but the routine based on Eqn.(10.69) was numerically more efficient since only 1D integration was involved. It should be mentioned that when the integration of Eqn.(10.67) was taken over region 2 (the copper rod), the integrating distance with respect to z-coordinate was cut up to $4\,cm$ because the result was almost invariable after that as shown in Fig.10.8. The computed distribution of the magnetic induction in the salt-water region is depicted in Fig.10.9. The magnetic induction reaches a maximum with a value of about $4 \times 10^{-3}\,Tesla$ at the point of $\rho = r_3$, $z = 0$. This is in good agreement with the theoretical prediction of Eqn.(10.22). Figure 10.10 shows the distributions of electrodynamic forces, which demonstrate that (i) the force distributions are very non-uniform; (ii) in the salt-water, the $\mathbf{j} \times \mathbf{B}$ force has not only a radial (or transverse) component, but also has an axial (or longitudinal) component; and (iii) around the edge of rod-liquid interface, there exist the peaks of two components with $f_{\rho,max} = 1.40 \times 10^4\,N/m^3$ and $f_{z,max} = 1.95 \times 10^4\,N/m^3$.

A first glance at the distributions of electrodynamic force may give an impression that the electrodynamic force does have a component in the axial direction which seems to try to push the salt water away from the copper rod and could be responsible for the experimental observation. However, if we take an integration of this force distribution over the salt-water, we can find that the resultant up-thrust force is much smaller than that exerted on the metal weight through the salt-water, that is about $21.6\,N$ according to the experiment report [132]. Therefore, we can certainly say that the electrodynamic model alone cannot explain the observed explosive phenomenon and another model must be sought. Considering the fluid properties of salt water, we will examine another model in combination of electrodynamics and hydrodynamics, that is the so-called magnetohydrodynamic (MHD) model.

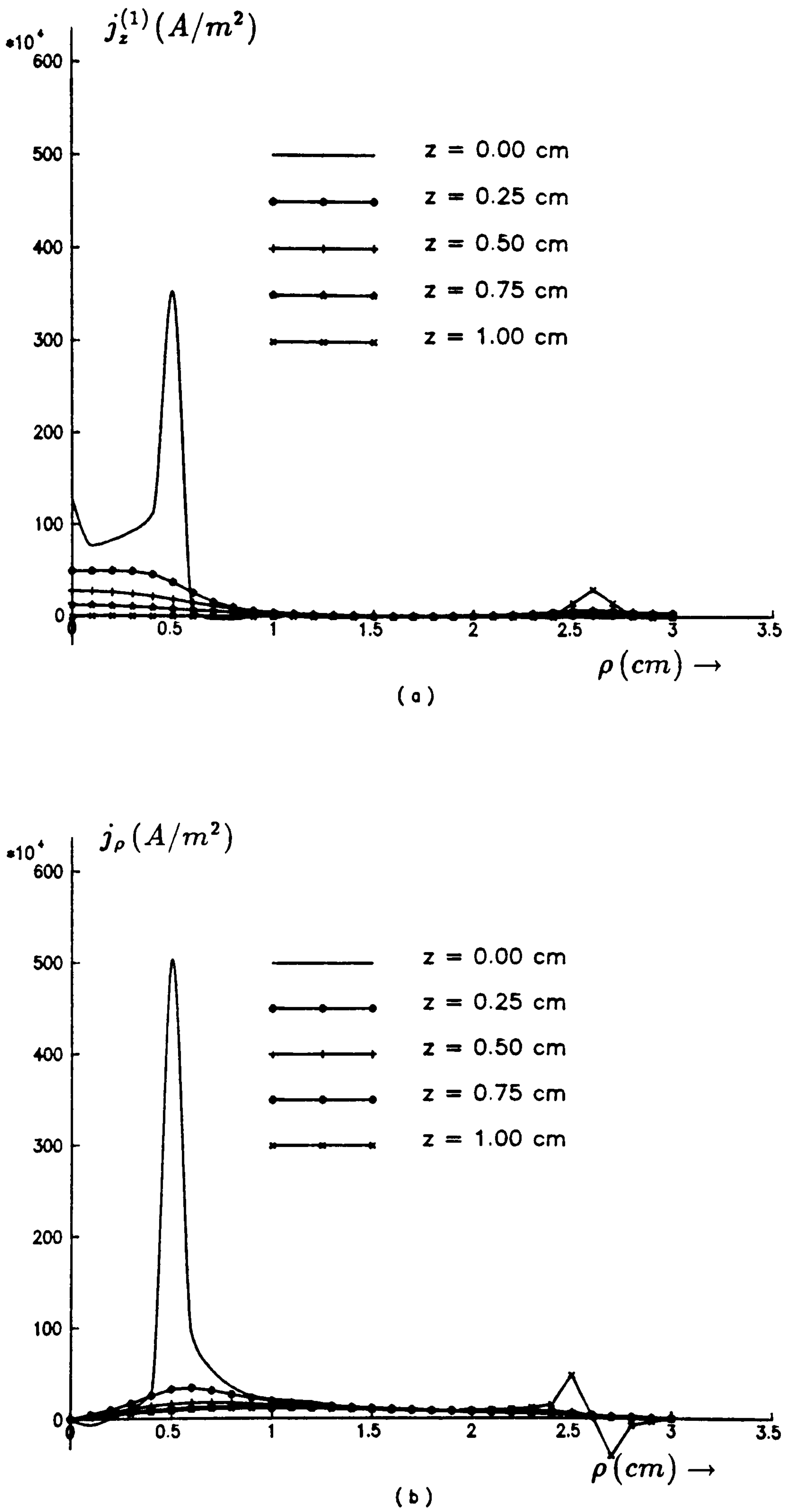

Figure 10.6: Current distributions in the salt-water

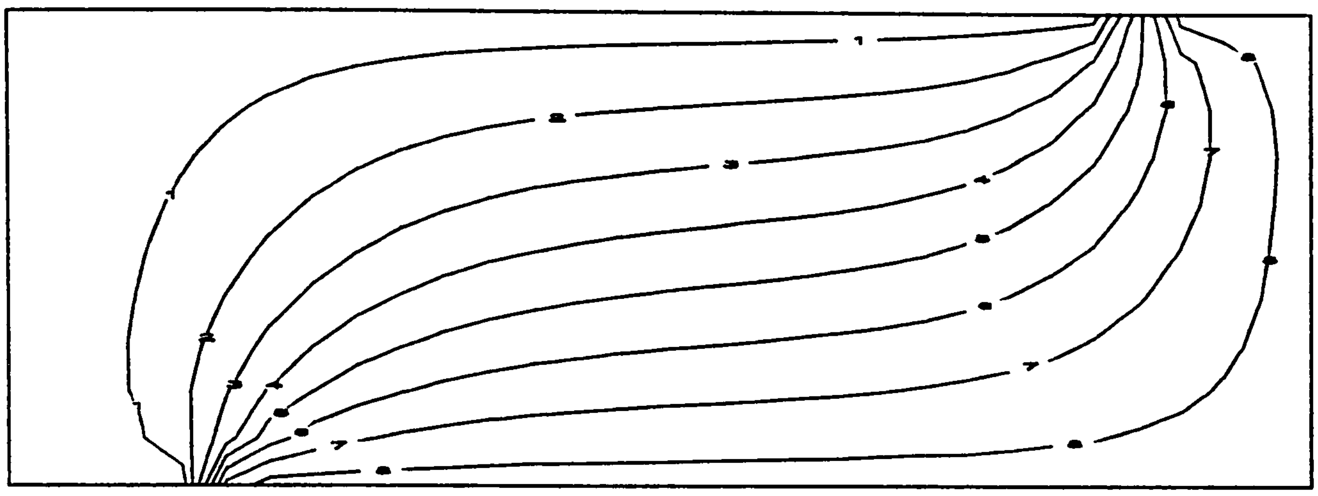

CONTOUR KEY	
1	0.0394
2	0.1185
3	0.1976
4	0.2768
5	0.3559
6	0.4350
7	0.5141
8	0.5932

Figure 10.7: Current flow pattern in the salt-water

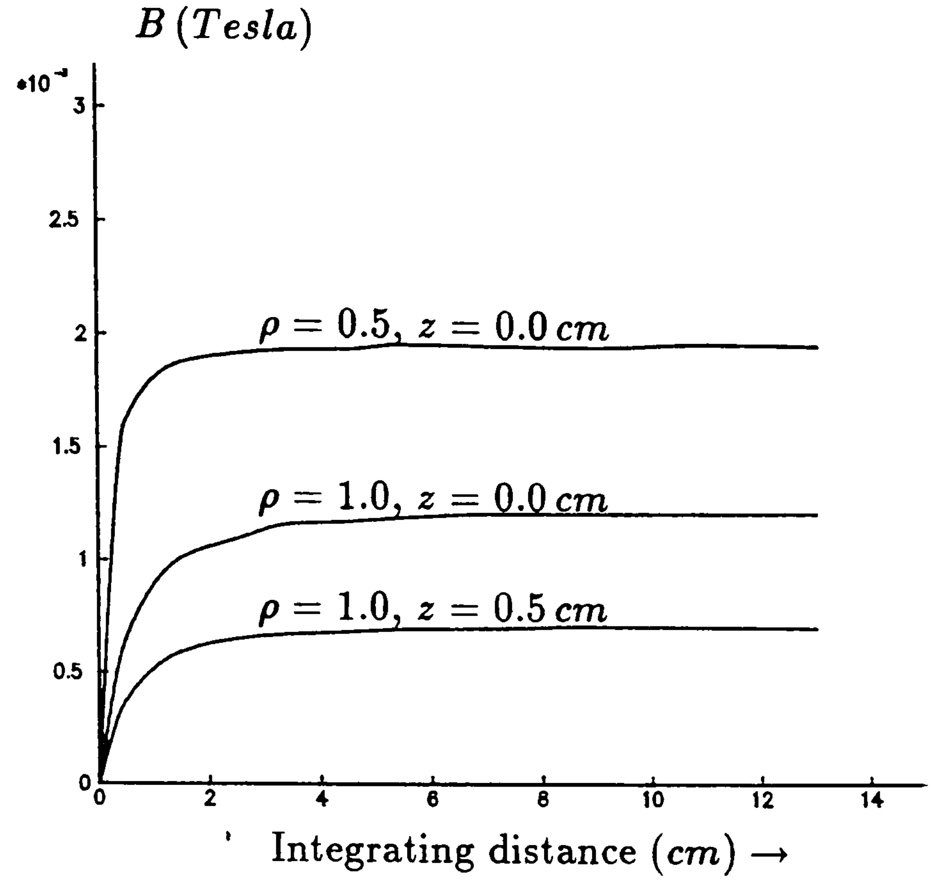

Figure 10.8: Magnetic induction due to current in region 2 as a function of integrating distance away from rod-liquid interface

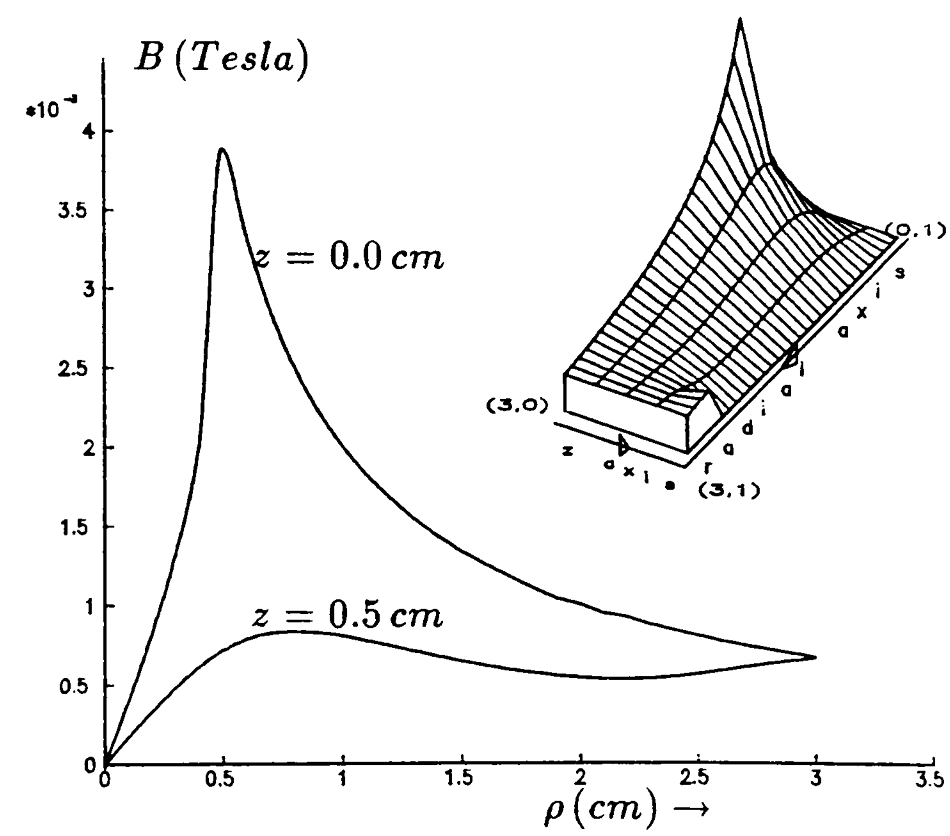

Figure 10.9: Magnetic induction in the salt-water

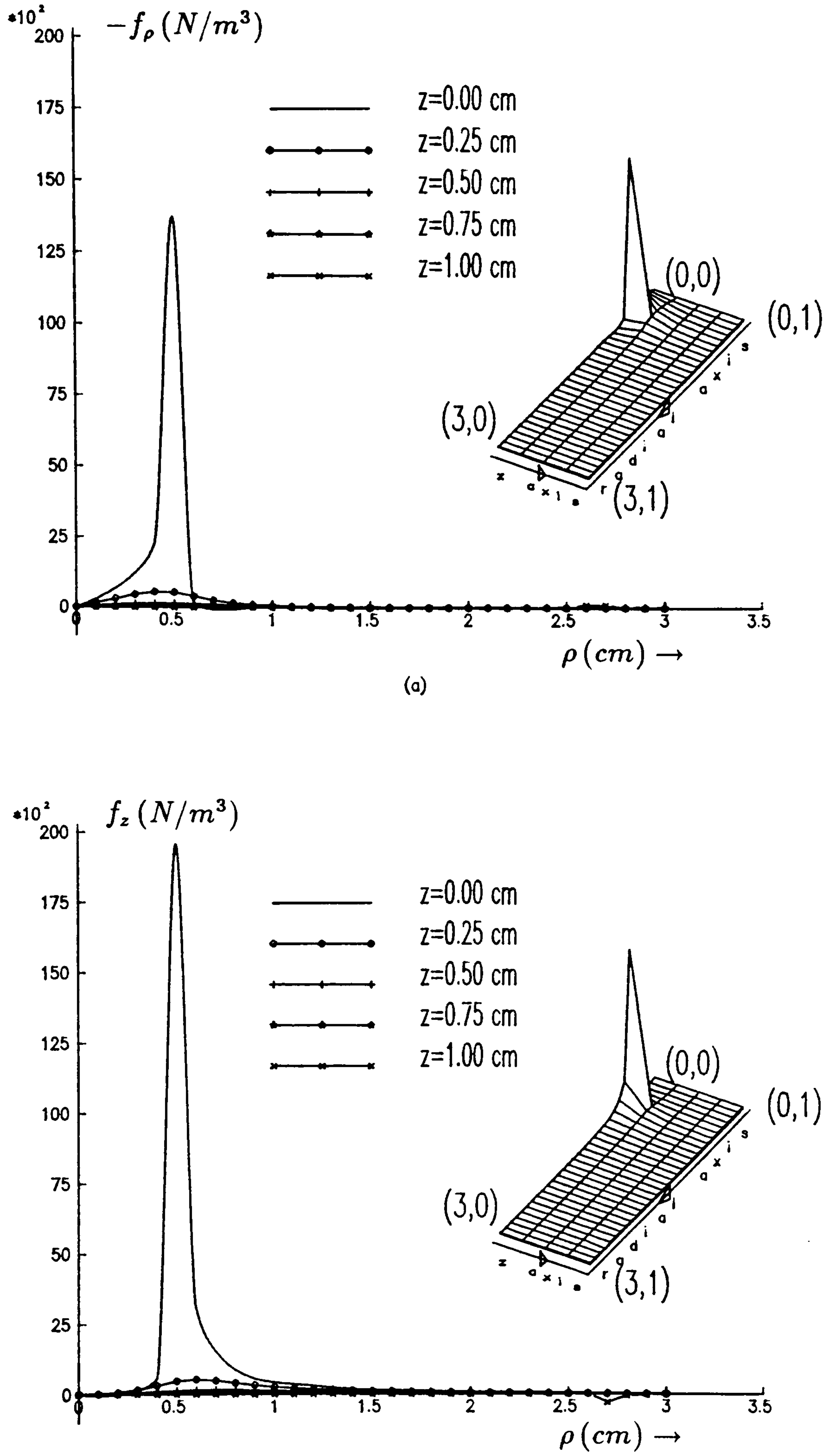

Figure 10.10: Electrodynamic force distributions in the salt-water

10.3 Magnetohydrodynamic Model

10.3.1 Formulation

Suppose the salt water is an incompressible conducting fluid. In general, the motion of an incompressible conducting fluid subjected to the electromagnetic force is governed by the non-linear Navier-Stokes equation [136]

$$\rho_m \frac{D\mathbf{v}}{Dt} + \nabla p = \mathbf{j} \times \mathbf{B} - \eta \nabla \times \mathbf{w} \tag{10.72}$$

where $D/Dt = \partial/\partial t + (\mathbf{v} \cdot \nabla)$,[7] ρ_m is the mass density, p is the pressure which includes the gravitational pressure and is sometime referred to as the piezometric pressure, $\mathbf{j} \times \mathbf{B}$ is the electrodynamic force density, η is the viscosity, $\mathbf{v}$ is the fluid velocity and $\mathbf{w} = \nabla \times \mathbf{v}$ is the fluid vorticity. In the case of an inviscid fluid, Equation (10.72) degenerates to

$$\rho_m \frac{D\mathbf{v}}{Dt} + \nabla p = \mathbf{j} \times \mathbf{B} \tag{10.73}$$

If the motion is steady, all the terms involving $\partial/\partial t$ are just left out in the above two equations.

From Eqn.(10.73) Maecker [137] has tried to estimate the maximum pressure based on a simplified electric arc model as shown in Fig.10.11. He first assumed $\mathbf{v} = 0$ and a uniform axial current density $j_z = I_0/(\pi r_a^2)$ at the cathode surface, then obtained

$$p(\rho) = \frac{\mu_0 I_0 j_z}{4\pi} \left(1 - \frac{\rho^2}{r_a^2}\right) \quad \text{for } \rho \leq r_a,\ z = 0 \tag{10.74}$$

which is the pressure due to the pinch force.

Secondly, he integrated Eqn.(10.73) along a streamline l in a steady fluid

$$\int_l (\mathbf{j} \times \mathbf{B}) \cdot d\mathbf{l} = \int_l \nabla p \cdot d\mathbf{l} + \bar{\rho}_m \int_l \left[\nabla v^2/2 - \mathbf{v} \times (\nabla \times \mathbf{v})\right] \cdot d\mathbf{l} \tag{10.75}$$

[7] In general, the motion of fluid can be described in two ways. One is the Eulerian representation giving the variation of fluid properties at a fixed point in space as a function of time. The other is the Lagrangian representation following the properties of a fluid element in the flow. Through this Chapter we adopt the Eulerian represention while the "substantive" or "material" derivative D/Dt which refers to a fluid element is only employed to simplify expressions.

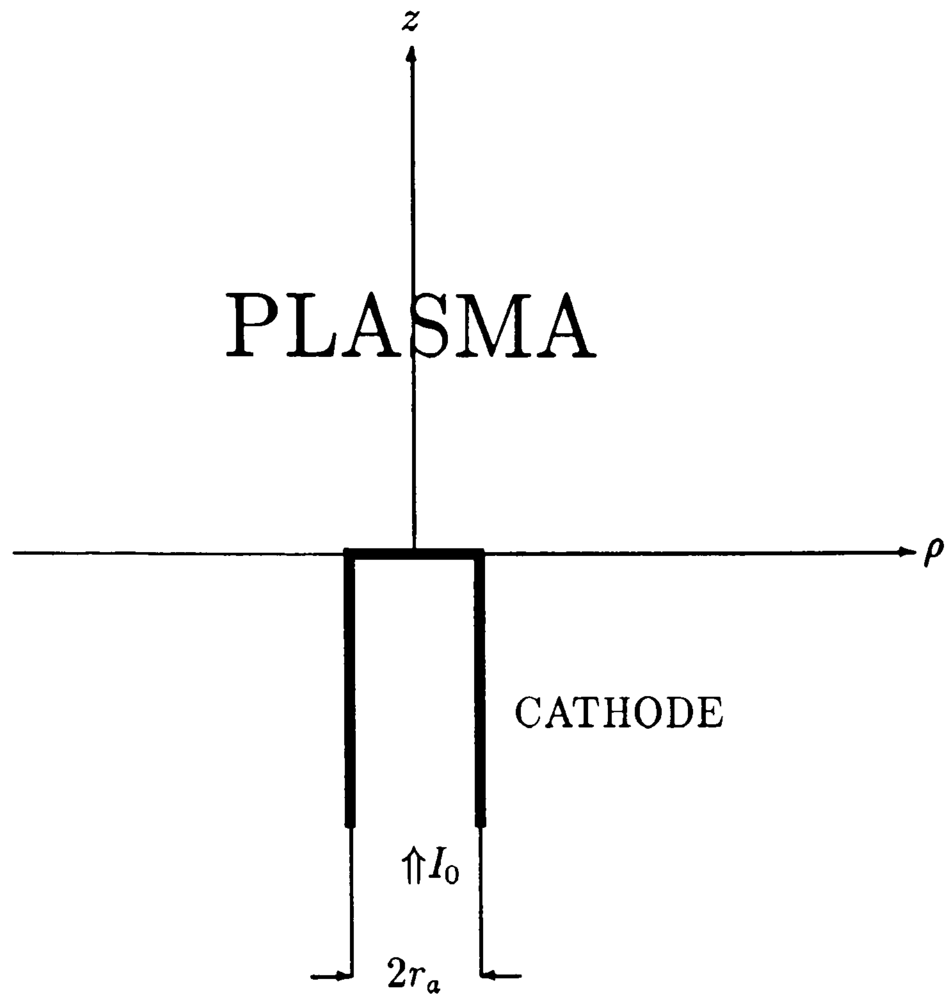

Figure 10.11 : The simplified electric arc model

where $\bar{\rho}_m$ is the average mass density and we note $\nabla v^2/2 - \mathbf{v} \times (\nabla \times \mathbf{v}) = (\mathbf{v} \cdot \nabla)\mathbf{v}$. According to the definition of streamline, $d\mathbf{l}$ is parallel to $\mathbf{v}$, thus

$$\mathbf{v} \times (\nabla \times \mathbf{v}) \cdot d\mathbf{l} = (d\mathbf{l} \times \mathbf{v}) \cdot (\nabla \times \mathbf{v}) = 0$$

and Eqn.(10.75) becomes

$$\begin{aligned} \int_l (\mathbf{j} \times \mathbf{B}) \cdot d\mathbf{l} &= \int_l (\nabla p + \bar{\rho}_m \nabla v^2/2) \cdot d\mathbf{l} \\ &= p + \bar{\rho}_m v^2/2 + C \end{aligned} \tag{10.76}$$

because ∇p and $\nabla v^2/2$ are conservative fields, where C is an arbitrary constant of reference. It is noticed that Eqn.(10.76) is analogous to the Bernoulli equation [137].

From Eqn.(10.76) Maecker gave the expression for estimating the maximum pressure

$$p_{max} = \frac{\mu_0 I_0 j_z}{4\pi} = \bar{\rho}_m \frac{v_{max}^2}{2} \tag{10.77}$$

Although this estimate may be plausible, the transition from Eqn.(10.76) to Eqn. (10.77) is still unclear for the reason given following.

Let us consider a conducting fluid element $\rho_m d\tau$ with $d\tau$ indicating an arbitrary volume. Suppose the element has a mass velocity $\mathbf{v}$ and experiences an electromagnetic force $\mathbf{f} = \rho\mathbf{E} + \mathbf{j} \times \mathbf{B}$, where ρ denotes the charge density. The density of work per unit time done by the electromagnetic force on the fluid element can be expressed as

$$\mathbf{v} \cdot \mathbf{f} = \mathbf{v} \cdot (\rho\mathbf{E} + \mathbf{j} \times \mathbf{B}) + \rho\mathbf{v} \cdot (\mathbf{v} \times \mathbf{B}) \tag{10.78}$$

because $\mathbf{v} \cdot (\mathbf{v} \times \mathbf{B}) = 0$. Thus

$$\begin{aligned} \mathbf{v} \cdot \mathbf{f} &= \rho\mathbf{v} \cdot \mathbf{E} - \mathbf{j} \cdot (\mathbf{v} \times \mathbf{B}) + \rho\mathbf{v} \cdot (\mathbf{v} \times \mathbf{B}) \\ &= \rho\mathbf{v} \cdot \mathbf{E} - (\mathbf{v} \times \mathbf{B}) \cdot (\mathbf{j} - \rho\mathbf{v}) \end{aligned} \tag{10.79}$$

Substracting both sides from $\mathbf{E} \cdot \mathbf{j}$ gives

$$\begin{aligned} \mathbf{E} \cdot \mathbf{j} - \mathbf{v} \cdot \mathbf{f} &= \mathbf{E} \cdot \mathbf{j} - \rho\mathbf{v} \cdot \mathbf{E} + (\mathbf{v} \times \mathbf{B}) \cdot (\mathbf{j} - \rho\mathbf{v}) \\ &= (\mathbf{E} + \mathbf{v} \times \mathbf{B}) \cdot (\mathbf{j} - \rho\mathbf{v}) \end{aligned} \tag{10.80}$$

which can be rewritten

$$\mathbf{E} \cdot \mathbf{j} = \mathbf{v} \cdot \mathbf{f} + (\mathbf{E} + \mathbf{v} \times \mathbf{B}) \cdot (\mathbf{j} - \rho\mathbf{v}) \tag{10.81}$$

On the other hand, we have

$$\mathbf{E} \cdot \mathbf{j} = -\left(\frac{\partial w_e}{\partial t} + \nabla \cdot \mathbf{P}\right) \tag{10.82}$$

according to the law of electromagnetic field energy [138], where for our notation, w_e denotes the density of electromagnetic field energy and $\mathbf{P}$ the Poynting vector. Replacing $\mathbf{E} \cdot \mathbf{j}$ in Eqn.(10.81) by Eqn.(10.82), we obtain

$$-\left(\frac{\partial w_e}{\partial t} + \nabla \cdot \mathbf{P}\right) = \mathbf{v} \cdot \mathbf{f} + (\mathbf{E} + \mathbf{v} \times \mathbf{B}) \cdot (\mathbf{j} - \rho\mathbf{v}) \tag{10.83}$$

where all quantities are observed at the laboratory frame. It is clear that the L.H.S. indicates the time rate of decrease in the density of electromagnetic energy while the R.H.S. represents the total density of electromagnetic power converted to some other forms of energy. We note that $\rho\mathbf{v}$ is identified with the convection current so that $(\mathbf{j} - \rho\mathbf{v})$ is the conduction current. If $|\mathbf{v}| \ll c$, where c is the light speed, it can be shown [139] that the net charge ρ arising from the motion can be ignored and

$$\mathbf{j} = \sigma(\mathbf{E} + \mathbf{v} \times \mathbf{B}) \tag{10.84}$$

On substituting Eqn.(10.83) for $(\mathbf{E} + \mathbf{v} \times \mathbf{B})$ and letting $\rho = 0$, we find

$$-\left(\frac{\partial w_e}{\partial t} + \nabla \cdot \mathbf{P}\right) = \mathbf{v} \cdot (\mathbf{j} \times \mathbf{B}) + \frac{j^2}{\sigma} \tag{10.85}$$

Now it is more apparent that the second term on the R.H.S. of Eqn.(10.85) represents ohmic dissipation, which is transformed into the Joule heat while the first term is the density of work per unit time done by the electrodynamic force on the moving fluid, which, if it does not vanish, is transformed into mechanical energy. If the motion of fluid does directly arise from the electrodynamic force,[8] the created kinetic energy of fluid must come from the electromagnetic energy. In other words, the equation

$$\mathbf{v} \cdot (\mathbf{j} \times \mathbf{B}) \neq 0 \tag{10.86}$$

or its equivalent

$$(\mathbf{v} \times \mathbf{j}) \cdot \mathbf{B} \neq 0 \tag{10.87}$$

should hold at least somewhere in the fluid. This means that $(\mathbf{j} \times \mathbf{B})$ is not perpendicular to $\mathbf{v}$ or $\mathbf{j}$ is not parallel to $\mathbf{v}$ in general.

Return to Maecker's equation (10.76). We note that $(\mathbf{j} \times \mathbf{B}) \cdot d\mathbf{l}$ does not always vanish according to the above argument so the result in Eqn.(10.77) could only be derived through special paths, presumably by taking the integration on the L.H.S. of Eqn.(10.76) along the line where $\mathbf{B} = 0$. Nevertheless, in order to determine whether Maecker's result can also be employed for estimating the maximum pressure as well as to see other MHD effects in our particular problem, we are going to solve the non-linear Navier-Stokes equation (10.72) numerically by means of the finite difference method (FDM).

[8]We will show in Appendix 10.3 that in our case the $(\mathbf{j} \times \mathbf{B})$ force does accelerate the fluid element.

10.3.2 Solution by Finite Difference Method

We note that owing to the axial symmetry of velocity field

$$\mathbf{v}(\rho, z) = v_\rho(\rho, z)\mathbf{a}_\rho + v_z(\rho, z)\mathbf{a}_z \tag{10.88}$$

and owing to the incompressibility and continuity

$$\nabla \cdot \mathbf{v} = 0 \tag{10.89}$$

it is therefore possible for us to introduce a scalar function, usually called the Stoke's stream function, ψ so that

$$v_\rho = -\frac{1}{\rho}\frac{\partial \psi}{\partial z} \tag{10.90}$$

$$v_z = \frac{1}{\rho}\frac{\partial \psi}{\partial \rho} \tag{10.91}$$

and then

$$\begin{aligned}\mathbf{w} = \nabla \times \mathbf{v} &= \left(\frac{\partial v_\rho}{\partial z} - \frac{\partial v_z}{\partial \rho}\right)\mathbf{a}_\phi \\ &= \frac{1}{\rho}\left(-\frac{\partial^2 \psi}{\partial z^2} + \frac{\partial^2 \psi}{\partial \rho^2} - \frac{1}{\rho}\frac{\partial \psi}{\partial \rho}\right)\mathbf{a}_\phi \\ &= w\mathbf{a}_\phi \end{aligned} \tag{10.92}$$

Taking the curl of Eqn.(10.72), we have

$$\rho_m \nabla \times \frac{D\mathbf{v}}{Dt} = \nabla \times (\mathbf{j} \times \mathbf{B}) - \eta \nabla \times \nabla \times \mathbf{w} \tag{10.93}$$

in which

$$\begin{aligned}\nabla \times \frac{D\mathbf{v}}{Dt} &= \nabla \times \left\{\frac{\partial \mathbf{v}}{\partial t} + (\mathbf{v} \cdot \nabla)\mathbf{v}\right\} \\ &= \frac{\partial \mathbf{w}}{\partial t} + \nabla \times \left\{\nabla(\frac{v^2}{2}) - \mathbf{v} \times (\nabla \times \mathbf{v})\right\} \\ &= \frac{\partial \mathbf{w}}{\partial t} - \nabla \times (\mathbf{v} \times \mathbf{w}) \end{aligned} \tag{10.94}$$

because $\nabla \times \nabla(v^2/2) = 0$. According to Eqns.(10.88,10.92), Eqn. (10.94) can further be written

$$\begin{aligned}\nabla \times \frac{D\mathbf{v}}{Dt} &= \frac{\partial w}{\partial t}\mathbf{a}_\phi - \nabla \times (v_\rho w \mathbf{a}_z - v_z w \mathbf{a}_\rho) \\ &= \frac{\partial w}{\partial t}\mathbf{a}_\phi + \left\{\frac{\partial (v_\rho w)}{\partial z} + \frac{\partial (v_z w)}{\partial \rho}\right\}\mathbf{a}_\phi \end{aligned} \tag{10.95}$$

Similarly, the term $\nabla \times \nabla \times \mathbf{w}$ on the R.H.S.of Eqn.(10.93) can be expanded into

$$\begin{aligned}\nabla \times \nabla \times \mathbf{w} &= \nabla \times \left\{-\frac{\partial w}{\partial z}\mathbf{a}_\rho + \left(\frac{w}{\rho} + \frac{\partial w}{\partial \rho}\right)\mathbf{a}_z\right\} \\ &= \left(-\frac{\partial^2 w}{\partial z^2} - \frac{1}{\rho}\frac{\partial w}{\partial \rho} + \frac{w}{\rho^2} - \frac{\partial^2 w}{\partial \rho^2}\right)\mathbf{a}_\phi \qquad (10.96)\end{aligned}$$

Since

$$\mathbf{B} = B_\phi(\rho, z)\mathbf{a}_\phi \qquad (10.97)$$

for an axisymmetrical magnetic field and

$$\mathbf{j} = \frac{1}{\mu_0}\nabla \times \mathbf{B} \qquad (10.98)$$

the first term on the R.H.S. of Eqn.(10.93) can also be expanded as

$$\begin{aligned}\nabla \times (\mathbf{j} \times \mathbf{B}) &= \frac{1}{\mu_0}\nabla \times [(\nabla \times \mathbf{B}) \times \mathbf{B}] \\ &= -2\frac{1}{\rho}\frac{B_\phi}{\mu_0}\frac{\partial B_\phi}{\partial z}\mathbf{a}_\phi \qquad (10.99)\end{aligned}$$

which is nothing else but $2f_z/\rho$ according to Appendix 10.3. As a consequence of these expansions, Eqn.(10.93) becomes

$$\frac{\partial w}{\partial t} + \left\{\frac{\partial(v_\rho w)}{\partial z} + \frac{\partial(v_z w)}{\partial \rho}\right\} = 2\frac{f_z}{\rho} - \eta\left(-\frac{\partial^2 w}{\partial z^2} - \frac{1}{\rho}\frac{\partial w}{\partial \rho} + \frac{w}{\rho^2} - \frac{\partial^2 w}{\partial \rho^2}\right) \qquad (10.100)$$

Next, by introducing the following nondimensional variables

$$\begin{aligned}&R = \frac{\rho}{z_0}, \qquad Z = \frac{z}{z_0}, \qquad T = \frac{t}{(z_0/v_0)}, \\ &U = \frac{v_z}{v_0}, \qquad V = \frac{v_\rho}{v_0}, \qquad W = -\frac{w}{(v_0/z_0)}, \\ &\Psi = \frac{\psi}{v_0 z_0^2}, \qquad F_z = \frac{f_z}{(v_0^2\rho_m/z_0)}, \quad F_\rho = \frac{f_\rho}{(v_0^2\rho_m/z_0)}, \qquad (10.101) \\ &Re = \frac{v_0 z_0 \rho_m}{\eta}\end{aligned}$$

where z_0 is an arbitrary length of reference and a convenient choice is $z_0 = d$, the height of salt-water in the water-cup; v_0 is an arbitrary velocity of reference; f_z and f_ρ

are the axial and radial components of ($\mathbf{j} \times \mathbf{B}$) force respectively; and R_e is the fluid Reynolds number, we can arrive at a system of coupled equations

$$V = -\frac{1}{R}\frac{\partial \Psi}{\partial Z} \tag{10.102}$$

$$U = \frac{1}{R}\frac{\partial \Psi}{\partial R} \tag{10.103}$$

$$W = \frac{1}{R}\left(\frac{\partial^2}{\partial R^2} - \frac{1}{R}\frac{\partial}{\partial R} + \frac{\partial^2}{\partial Z^2}\right)\Psi \tag{10.104}$$

$$\begin{aligned} \frac{\partial W}{\partial T} &= -\frac{\partial(UW)}{\partial Z} - \frac{\partial(VW)}{\partial R} - \frac{2F_z}{R} \\ &\quad + \frac{1}{R_e}\left(\frac{\partial^2}{\partial R^2} + \frac{1}{R}\frac{\partial}{\partial R} - \frac{1}{R^2} + \frac{\partial^2}{\partial Z^2}\right) W \end{aligned} \tag{10.105}$$

from Eqns.(10.90) to (10.92) and (10.100) respectively. We note that Eqn.(10.104) is the elliptic Poisson equation with the unknown Ψ while Eqn.(10.105) is the parabolic vorticity transport equation.

It is apparent that the problem described by this system of coupled equations is an initial-boundary problem so that the initial and boundary conditions must be prescribed to obtain an appropriate solution. In our case, the salt water was at rest before the discharge started. Thus the initial conditions are

$$\Psi = W = U = V = 0 \qquad \text{at } t = 0 \tag{10.106}$$

The boundary conditions, depending on the type of boundary, may be prescribed as

$$V = U = 0 \qquad \text{at no-slip boundary} \tag{10.107}$$

$$W = V = 0 \qquad \text{at axisymmetric flow boundary} \tag{10.108}$$

$$\frac{\partial V}{\partial Z} = \frac{\partial W}{\partial Z} = 0 \qquad \text{at outflow boundary} \tag{10.109}$$

where the outflow is assumed in the z direction. The conditions in the first two equations are apparent. The conditions in the last equation are not so obvious and were developed by Thoman and Szewczyk with the aim of allowing the most free-flow adjustment at the boundary which still gives a solution, and which have been used successfully by others in a variety of problems.[9]

The system of coupled equations, involving the nonlinear equation (10.105), cannot be solved analytically or rigorously. Hence an approximate solution will be given at

[9]See page 154 of the book by Roache [141].

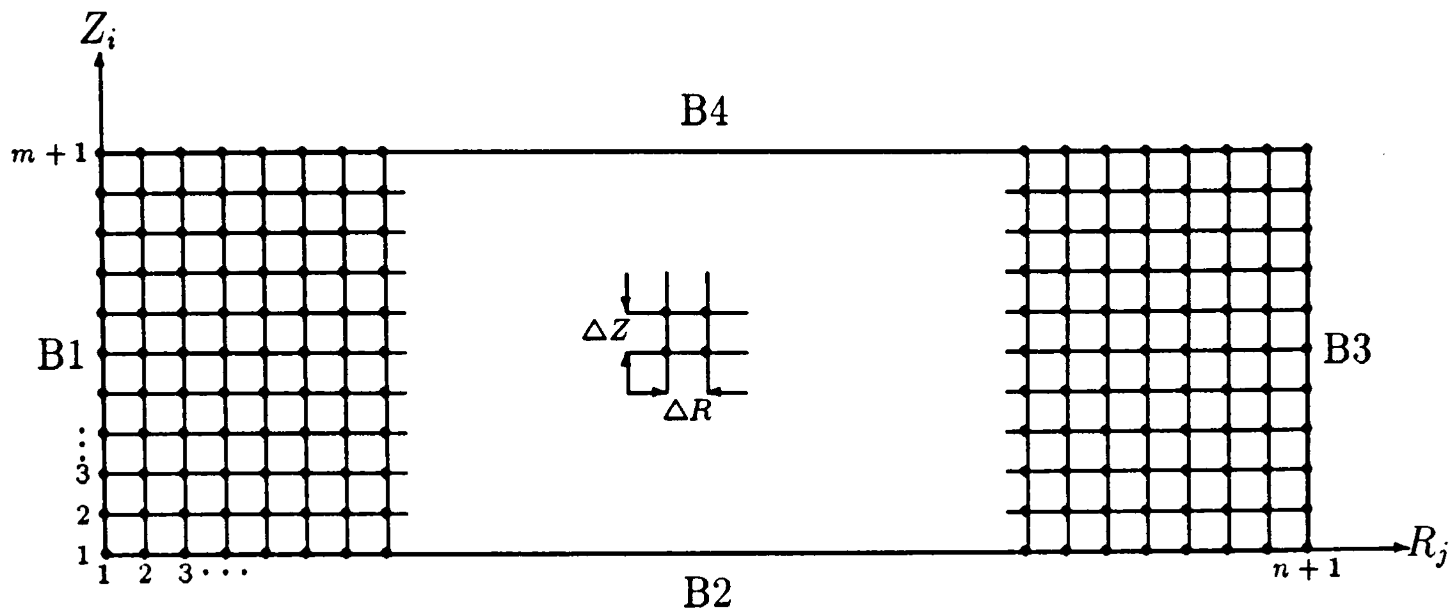

Figure 10.12 : The mesh coordinates for the finite-difference solution
B1– symmetric boundary; B2– no-slip boundary
B3– no-slip boundary; B4– no-slip/outflow boundary

$(m+1) \times (n+1)$ of mesh points having coordinates $Z_i = (i-1)\Delta Z$, $R_j = (j-1)\Delta R$ as shown in Fig.10.12 and at discrete time steps separated by ΔT. For simplicity ΔZ and ΔR are chosen to have the same value h, which is not, however, necessary in general. Since Eqns.(10.102) to (10.104) are linear, the associated finite–difference equations can be easily derived by approximating all linear spatial derivatives with three-point central differences,[10] i.e.,

$$V_{i,j} = -\frac{\Psi_{i+1,j} - \Psi_{i-1,j}}{2hR_j} \tag{10.110}$$

$$U_{i,j} = \frac{\Psi_{i,j+1} - \Psi_{i,j-1}}{2hR_j} \tag{10.111}$$

$$h^2 R_j W_{i,j} = -\Psi_{i,j} + \Psi_{i+1,j} + \Psi_{i-1,j} + \alpha_j \Psi_{i,j+1} + \beta_j \Psi_{i,j-1} \tag{10.112}$$

[10]The basic finite–difference forms for partial derivatives can be derived from partial Taylor series expansions. The centered difference approximation has a second order accuracy, that is a truncation error of order ΔR^2 or ΔZ^2.

with

$$\begin{aligned}\alpha_j &= 1-\frac{h}{2R_j}\\ \beta_j &= 1+\frac{h}{2R_j}\end{aligned}$$

The subscripts (i,j) denote quantities evaluated at the mesh point (Z_i, R_j).

The last term on the R.H.S. of Eqn.(10.105) is also linear and can be approximated in a similar way. However, care must be taken in approximating the first two nonlinear terms. An "upwind" difference scheme is used for the approximation in order to satisfy vorticity conservation and to preserve stability of the numerical solutions,[11] namely

$$\begin{aligned}\left(\frac{\partial(UW)}{\partial Z}\right)_{i,j} &= \frac{1}{2h}[(U_f-|U_f|)W_{i+1,j}-(U_b+|U_b|)W_{i-1,j}\\ &\quad +(U_f+|U_f|-U_b+|U_b|)W_{i,j}] \qquad (10.113)\\ \left(\frac{\partial(VW)}{\partial R}\right)_{i,j} &= \frac{1}{2h}[(V_f-|V_f|)W_{i,j+1}-(V_b+|V_b|)W_{i,j-1}\\ &\quad +(V_f+|V_f|-V_b+|V_b|)W_{i,j}] \qquad (10.114)\end{aligned}$$

with

$$\begin{aligned}U_f &= \frac{U_{i+1,j}+U_{i,j}}{2}\\ U_b &= \frac{U_{i,j}+U_{i-1,j}}{2}\\ V_f &= \frac{V_{i,j+1}+V_{i,j}}{2}\\ V_b &= \frac{V_{i,j}+V_{i,j-1}}{2}\end{aligned}$$

The time derivative in Eqn.(10.105) is approximated by a forward difference

$$\left(\frac{\partial W}{\partial T}\right)_{i,j} = \frac{W'_{i,j}-W_{i,j}}{\Delta T} \qquad (10.115)$$

in which the unprimed and primed quantities represent, respectively, the values at two consecutive time levels T and $T+\Delta T$. Now we are able to write the finite-difference equation of Eqn.(10.105) as

$$\begin{aligned}W'_{i,j} &= W_{i,j}+\Delta T\left(-\left(\frac{\partial(UW)}{\partial z}\right)_{i,j}-\left(\frac{\partial(VW)}{\partial R}\right)_{i,j}-\frac{F_{z,i,j}}{R_j}\right)\\ &\quad +\frac{\Delta T}{R_e}\left(\frac{W_{i,j+1}-W_{i,j-1}}{2R_jh}-\frac{W_{i,j}}{R_j^2}+\frac{W_{i,j+1}+W_{i,j-1}+W_{i+1,j}+W_{i-1,j}-4W_{i,j}}{h^2}\right)\end{aligned}$$
$$(10.116)$$

[11]See page 73 of the book by Roache [141].

So far we have derived the finite-difference expressions of Eqns.(10.102) to (10.105). Before we discuss their solutions, we should express the boundary conditions in discrete forms. It will be seen soon that the velocity is not directly solved as a boundary value problem so that the boundary conditions relative to the velocity should be also expressed in terms of the stream function. A comprehensive discussion about boundary conditions incorporated in the FDM has been given by Roache [141]. In our case, we have

$$\Psi_{1,j} = \Psi_{i,n+1} = 0 \tag{10.117}$$

$$W_{i,1} = \Psi_{i,1} = 0 \tag{10.118}$$

$$\Psi_{m+1,j} = \begin{cases} 2\Psi_{m,j} - \Psi_{m-1,j} & \text{if outflow boundary} \\ 0 & \text{if no-slip boundary} \end{cases} \tag{10.119}$$

$$W_{1,j} = 2\Psi_{2,j}/(R_j h^2) \tag{10.120}$$

$$W_{i,n+1} = 2\Psi_{i,n}/(R_j h^2) \tag{10.121}$$

$$W_{m+1,j} = \begin{cases} W_{m,j} & \text{if outflow boundary} \\ 2\Psi_{m,j}/(R_j h^2) & \text{if no-slip boundary} \end{cases} \tag{10.122}$$

$$U_{i,1} = 2\Psi_{i,2}/h^2 \tag{10.123}$$

The condition of Eqn.(10.117) is equivalent to that of Eqn.(10.107) because the line along boundaries B2 and B3 (referring to Fig.10.12) may be treated as a streamline with zero velocity and because any constant value of Ψ along the line may be selected and here the conventional choice is $\Psi = 0$. The condition of Eqn.(10.118) is identical with that of Eqn.(10.108). Some explanation may be necessary for $\Psi_{i,1} = 0$. Since $V = 0$ at boundary B1, thus $V_{i,1} = 0$ or $\Psi_{i+1,1} = \Psi_{i-1,1} = constant$ for $i = 2, 3, ...m$ according to Eqn.(10.110). But $\Psi_{1,1} = 0$ from Eqn.(10.117), and then the continuity of stream function at mesh point $i = 1$, $j = 1$ leads to $\Psi_{i,1} = 0$ for any i. For our purpose, we treat boundary B4 either as the outflow boundary or the non-slip boundary because the real boundary may be a combination of them. The condition in Eqn.(10.119) for the outflow approximates $\partial V/\partial Z = 0$. Since $V \propto \partial\Psi/\partial Z$, the condition $\partial V/\partial Z = 0$ implies $\partial^2\Psi/\partial Z^2 = 0$, which is approximated by linear extrapolation out to $i = m + 1$.

For constant $\triangle Z$,

$$\frac{\partial^2\Psi}{\partial Z^2}|_{i,j} \approx \frac{\Psi_{i+1,j} + \Psi_{i-1,j} - 2\Psi_{i,j}}{\triangle Z^2} \tag{10.124}$$

according to the centred difference form of $\partial^2\Psi/\partial Z^2$. Set $\partial^2\Psi/\partial Z^2|_{m,j} = 0$ and assume $\partial^2\Psi/\partial Z^2|_{m+1,j} \approx \partial^2\Psi/\partial Z^2|_{m,j}$ for a small $\triangle Z$ leads to the outflow condition in Eqn.(10.119).

At no-slip boundaries, vorticity can be produced so that the boundary values of W should be obtained from the no-slip conditions.[12] Using boundary B2 as an example, we expand $\Psi_{2,j}$ by a Taylor series out from the wall values, $\Psi_{1,j}$

$$\Psi_{2,j} = \Psi_{1,j} + \frac{\partial\Psi}{\partial Z}|_{1,j}\triangle Z + \frac{1}{2}\frac{\partial^2\Psi}{\partial Z^2}|_{1,j}\triangle Z^2 + 0(\triangle Z) \tag{10.125}$$

But $\partial\Psi/\partial Z|_{1,j} \propto V_{1,j} = 0$ by the no-slip condition. Now $W = \partial U/\partial R - \partial V/\partial Z$. Along the bottom wall, $\partial U/\partial R = 0$ because $U = constant$ (i.e. U=0 by the no-slip condition). Thus $W_{1,j} = -\partial V/\partial Z|_{1,j} = (1/R_j)\partial^2\Psi/\partial Z^2|_{1,j}$. Substituting this into Eqn.(10.125), noting $\Psi_{1,j} = 0$ and $\triangle Z = h$, and ignoring $0(\triangle Z)$ yields Eqn.(10.120). Similarly, we can determine the boundary values of vorticity which satisfy the no-slip conditions at boundaries B3 and B4 (if no-slip boundary is assumed) by Eqns.(10.121,10.122).

The relation in Eqn.(10.123) is derived from Eqn.(10.103) by assuming constant velocity within a small radial distance h from the symmetric axis and considering the streams to be convergent at this boundary [142].

Now we are going to discuss how to solve the discrete coupled equations. Firstly, we can clearly see from the discrete parabolic vorticity transport equation (10.116) that if all field quantities, namely, the velocity, the vorticity and the magnetic force at a previous time are known, then the vorticity field at the present time succeeding a $\triangle T$ can be updated immediately.

Secondly, let us look at the discrete Poisson equation (10.112). Suppose at interior mesh points the vorticities $W_{i,j}$ for $i = 2,3...m$ and $j = 2,3...n$ are known, and at boundary mesh points the boundary values of stream function $\Psi_{1,j}$, $\Psi_{m+1,j}$, $\Psi_{i,1}$ and $\Psi_{i,n+1}$ are prescribed. Expand Eqn.(10.112) into a set of linear algebraic equations

[12]See page 140 of the book [141].

such as

$$\begin{aligned}
-4\Psi_{2,2}+\Psi_{3,2}+\Psi_{1,2}+\alpha_2\Psi_{2,3}+\beta_2\Psi_{2,1} &= h^2R_2W_{2,2} && \text{for } i=2, j=2 \\
-4\Psi_{3,2}+\Psi_{4,2}+\Psi_{2,2}+\alpha_2\Psi_{3,3}+\beta_2\Psi_{3,1} &= h^2R_2W_{3,2} && \text{for } i=3, j=2 \\
\vdots &= \vdots && \\
-4\Psi_{m,2}+\Psi_{m+1,2}+\Psi_{m-1,2}+\alpha_2\Psi_{m,3}+\beta_2\Psi_{m,1} &= h^2R_2W_{m,2} && \text{for } i=m, j=2 \\
-4\Psi_{2,3}+\Psi_{3,3}+\Psi_{1,3}+\alpha_3\Psi_{2,4}+\beta_3\Psi_{2,2} &= h^2R_3W_{2,3} && \text{for } i=2, j=3 \\
\vdots &= \vdots && \\
-4\Psi_{2,n}+\Psi_{3,n}+\Psi_{1,n}+\alpha_n\Psi_{2,n+1}+\beta_n\Psi_{2,n-1} &= h^2R_nW_{2,n} && \text{for } i=2, j=n \\
\vdots &= \vdots && \\
-4\Psi_{m,n}+\Psi_{m+1,n}+\Psi_{m-1,n}+\alpha_n\Psi_{m,n+1}+\beta_n\Psi_{m,n-1} &= h^2R_nW_{m,n} && \text{for } i=m, j=n
\end{aligned}$$

which may be written in the form

$$[A][\Psi]=[C] \tag{10.126}$$

where the known matrix $[A]$, with real coefficients, is of size $(m-1)(n-1)$ by $(m-1)(n-1)$, the known right-hand vector [C] is of size $(m-1)(n-1)\times 1$, and the required solution vector $[\Psi]$ has $(m-1)(n-1)$ components indicating the values of stream function at the all interior mesh points. Although Eqn.(10.126) may be solved by any standard method, such as the Gaussian elimination method, it may require a lot of computer memory and CPU time when m and n are large. Alternatively, we adopt Liebman's iterative method[13] to solve directly Eqn.(10.112) instead of Eqn.(10.126). In this method, for the given vorticities $W_{i,j}$ and the boundary values of stream function, the remaining unknowns $\Psi_{i,j}$ for $i=2,3,...m$ and $j=2,3,...n$ are approximated by Liebman's iterative formula

$$\Psi_{i,j}^{(k+1)}=\frac{1}{4}\left(\Psi_{i+1,j}^{(k)}+\Psi_{i-1,j}^{(k+1)}+\alpha_j\Psi_{i,j+1}^{(k)}+\beta_j\Psi_{i,j-1}^{(k+1)}-h^2R_jW_{i,j}\right) \tag{10.127}$$

if we sweep in $i\uparrow$, $j\uparrow$, where k indicates the kth iteration. It has been shown elsewhere [141] that as $k\to\infty$, $\Psi^{(k)}$ will converge to the exact solution of Ψ. Hence to

[13] Refer to page 113 of the book by Roache [141].

arrive at a solution of the stream function, Eqn.(10.127) is repeatedly computed for all interior mesh points starting from a set of arbitrarily assumed values, for instance, $\Psi_{i,j} = 0$ for all interior values. After each computation, the difference of the updated and the previous values of $\Psi_{i,j}$ is recorded as a local error. The iterative procedure is terminated only when the sum of absolute errors at all interior points is less than a specified local criterion, and then the resultant $\Psi_{i,j}$ will be taken as the solution of stream field.

Once all $\Psi_{i,j}$ are found the velocities $V_{i,j}$ and $U_{i,j}$ can be determined by subsitutions according to Eqns.(10.110,10.111).

It becomes clearer that an overall procedure for solving the complete MHD problem by means of the finite difference method may be summarized as follows. Giving the prescribed boundary conditions, the solution starts with the establishment of initial values of Ψ, V, U, W and F_z at all mesh points at time $T = 0$. These initial conditions may correspond to some real initial situation for a transient problem of interest, or to a rough guess for the steady-state solution if only the steady state is of interest. Then the computational cycle begins as Eqn.(10.116) is used to calculate the new values of W at all interior points at a new time level, increased by an increment $\triangle T$. The next step in the computational cycle is to solve Eqn.(10.112) by means of Liebman's iterative formula of Eqn.(10.127) for new values of stream function Ψ, using the new values of W as the "source" term. After this, new velocity components are evaluated by Eqns.(10.110,10.111). The last step in the computational cycle is to update boundary values because they usually depend on the new values of Ψ and W (already calculated) at interior points near the boundary points as shown by Eqns.(10.119) to (10.123). Then the computational cycle is repeated until the desired time is reached, or until some convergence criterion for a steady state is satisfied. Schematically, the procedure for computation of a steady flow is illustrated in Fig.10.13.

After determining the velocity and vorticity fields of the fluid, the pressure, in which we are more interested, can be obtained from Eqn.(10.72). For a steady flow, Eqn.(10.72) may be written as

$$\nabla p^* = \mathbf{f}^* \tag{10.128}$$

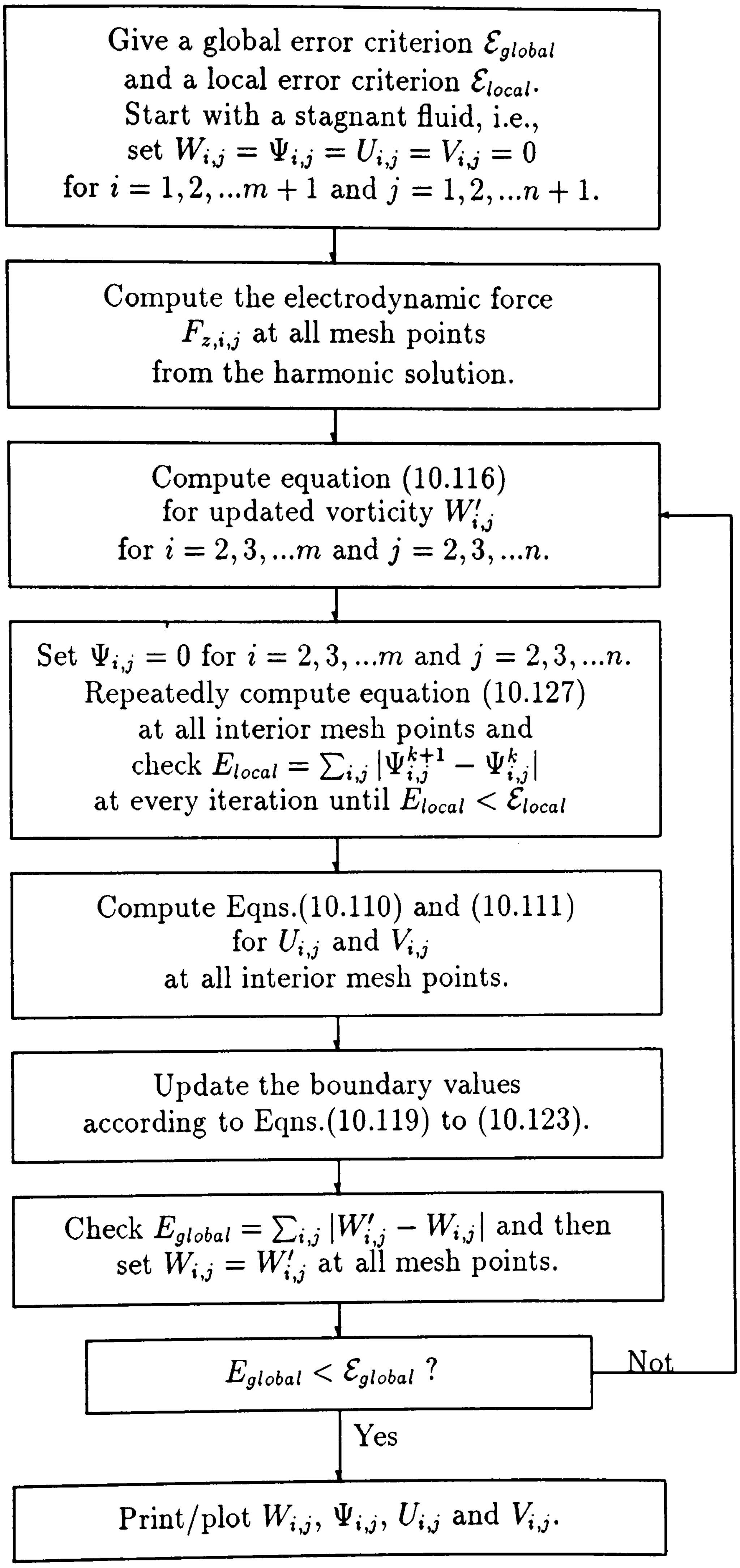

Figure 10.13 : The flow chart of the MHD computation

with

$$p^* = p + \rho_m \frac{v^2}{2} \tag{10.129}$$
$$f^* = \mathbf{j} \times \mathbf{B} - \eta \nabla \times \mathbf{w} + \rho_m \mathbf{v} \times \mathbf{w} \tag{10.130}$$

Equation (10.128) is equivalent to the associated partial differential equations

$$\frac{\partial p^*}{\partial \rho} = f^*_\rho \tag{10.131}$$
$$\frac{\partial p^*}{\partial z} = f^*_z \tag{10.132}$$

for the axisymmetrical fields, where

$$f^*_\rho = f_\rho - \rho_m v_z w + \eta \frac{\partial w}{\partial z} \tag{10.133}$$
$$f^*_z = f_z + \rho_m v_\rho w - \eta \left(\frac{w}{\rho} + \frac{\partial w}{\partial \rho} \right) \tag{10.134}$$

are the radial and axial components of $\mathbf{f}^*$ respectively. In general the solution of p^* is found by solving the Poisson equation [141]

$$\frac{\partial^2 p^*}{\partial \rho^2} + \frac{\partial^2 p^*}{\partial z^2} = \frac{\partial f^*_\rho}{\partial \rho} + \frac{\partial f^*_z}{\partial z} \tag{10.135}$$

However we note from Eqn.(10.128) that $\nabla \times \mathbf{f}^* = 0$. This means $\partial f^*_\rho / \partial z = \partial f^*_z / \partial \rho$ so that Eqns.(10.131) and (10.132) are consistent [143], and we may find p^* in the following way.

Integrating Eqn.(10.131) with respect to ρ yields

$$p^*(\rho, z) = \int_0^\rho f^*_\rho(\rho', z) d\rho' + c(z) + c_0 \tag{10.136}$$

in which $c(z)$ is a function of z and c_0 is a constant. Substituting this into Eqn.(10.132) gives

$$\frac{d}{dz} c(z) = f^*_z(\rho, z) - \frac{\partial}{\partial z} \int_0^\rho f^*_\rho(\rho' z) d\rho' \tag{10.137}$$

thus

$$\begin{aligned} c(z) &= \int_0^z f^*_z(\rho, z') dz' - \int_0^z \left(\frac{\partial}{\partial z'} \int_0^\rho f^*_\rho(\rho', z') d\rho' \right) dz' \\ &= \int_0^z f^*_z(\rho, z') dz' - \int_0^\rho f^*_\rho(\rho', z) d\rho' + \int_0^\rho f^*_\rho(\rho', 0) d\rho' \end{aligned} \tag{10.138}$$

for a fixed ρ. Replacing $c(z)$ in Eqn.(10.136) by Eqn.(10.138), we arrive at

$$p^*(\rho,z) = \int_0^{\rho} -f_\rho^*(\rho',0)d\rho' + \int_0^z f_z^*(\rho,z')dz' + c_0 \tag{10.139}$$

Since $v = 0$ at the no-slip boundary $\rho = r_1$ and if the piezometric pressure is assumed to be constant[14] at this boundary and taken to be zero as a reference level, the constant c_0 is determined and p^* is solely given by

$$p^*(\rho,z) = \int_\rho^{r_1} -f_\rho^*(\rho',0)d\rho' + \int_0^z f_z^*(\rho,z')dz' - \int_0^z f_z^*(r_1,z')dz' \tag{10.140}$$

By substitution of nondimensional variables in Eqn.(10.101) into the R.H.S. of Eqns.(10.133) and (10.134) yields

$$\begin{aligned} f_\rho^* &= \frac{v_0^2\rho_m}{z_0}\left(F_\rho + UW - \frac{1}{R_e}\frac{\partial W}{\partial Z}\right) && (10.141)\\ f_z^* &= \frac{v_0^2\rho_m}{z_0}\left(F_z - VW + \frac{1}{R_e}(\frac{W}{R} + \frac{\partial W}{\partial R})\right) && (10.142)\end{aligned}$$

Defining new nondimensional quantities

$$\begin{aligned} F_\rho^* &= \frac{f_\rho^*}{(v_0^2\rho_m/z_0)} && (10.143)\\ F_z^* &= \frac{f_z^*}{(v_0^2\rho_m/z_0)} && (10.144)\\ P^* &= \frac{p^*}{v_0^2\rho_m} && (10.145)\end{aligned}$$

Equation (10.140) can be written into a dimensionless form

$$P^*(R,Z) = \int_R^{R_1} -F_\rho^*(R',0)dR' + \int_0^Z F_z^*(R,Z')dZ' - \int_0^Z F_z^*(R_1,Z')dZ' \tag{10.146}$$

Since the values of integrands in Eqn.(10.146) have been known at the mesh points, the solution of P^* can be found by any standard numerical integration routine, and then the pressure is calculated by

$$p = v_0\rho_m(P^* - \frac{U^2+V^2}{2}) \tag{10.147}$$

according to Eqn.(10.129) because $v^2 = v_z^2 + v_\rho^2$.

[14]This assumption is verified *a posteriori* by the numerical results.

10.3.3 Numerical results and Discussion

A computer programme was developed on the basis of the above formulation and run on VAX in the Oxford University Computer Centre. For the computations, 341 mesh points with $m = 10$ and $n = 30$ are chosen by trial-and-error, which gives a dimensionless grid size $h = 0.1$. The local criterion for convergence of the solution of transport equation is chosen as $\varepsilon_{local} = 10^{-4}$. The reference constants for normalization are $z_0 = 1\,cm$ and $v_0 = 1\,cm/s$. Considering that at about a room temperature the mass density and viscosity of water are $\rho_m = 10^3\,kg/m^3$ and $\eta = 10^{-3}\,Ns/m^2$, this results in a Reynolds number $R_e = 100$.

For our purpose, we restrict ourselves to the steady state case. As numerical instability may occur in the process of approaching the steady state solution if the size of the time increment is not properly chosen. For a given grid size h, the constraint on $\triangle T$ is

$$\triangle T \leq \left[\frac{1}{2h}(U_f + |U_f| - U_b + |U_b| + V_f + |V_f| - V_b + |V_b|) + \frac{1}{R_e h^2}(4 + \frac{h^2}{R_j^2})\right]^{-1} \tag{10.148}$$

for a stable solution [142]. However $\triangle T$ cannot be calculated from this inequality at the beginning of a computation because velocity field is not known *a priori*. Nevertheless, we use a fixed $\triangle T = 0.01$ and then calculate the R.H.S. of the inequality at every time step in all computations to ensure the chosen $\triangle T$ always satisfies the inequality. The global criterion $\varepsilon_{global} = 10^{-2}$ is imposed to approximate a steady state solution.

The numerical results are shown in Fig.10.14 to Fig.10.17. From these figures we can see that (i) the fluid flow patterns (the contours of stream function) strongly depend on the boundary conditions applied to the top surface B4 and are quite different from the current flow pattern in Fig.10.7 ; (ii) the vorticity always spreads out from the edge of rod-liquid interface in all cases and it seems that the diffusion of this edge vorticity drives the problem; (iii) along the centre axis ($\rho = 0$) the quantity P^* is constant; (iv) the fluid velocity is only of the order of several centimetres per second; (v) the changes in the distribution and magnitude of the pressure are not significant from one case to the other. Similar features were observed from the numerical results computed for $R_e = 50$, and 500 respectively.

Vorticity $w(\rho, z)\, 1/s$

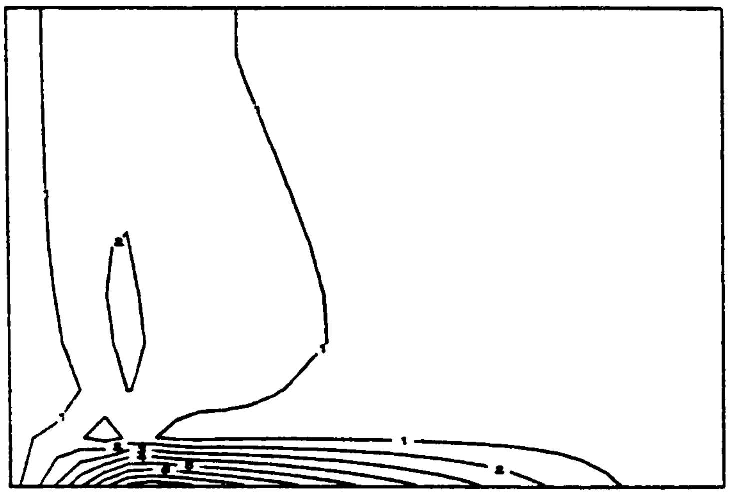

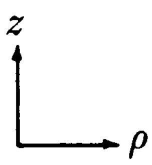

CONTOUR KEY	
1	4.6375
2	13.9125
3	23.1875
4	32.4625
5	41.7375
6	51.0125
7	60.2875
8	69.5625

Stream function $\psi(\rho, z)\, cm^3/s$

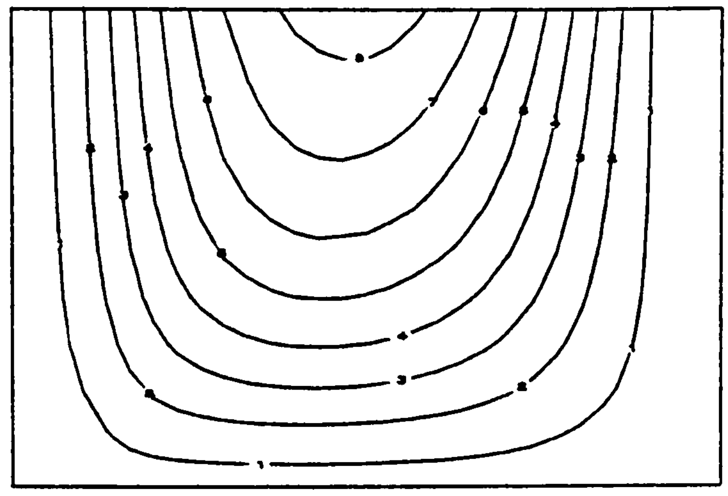

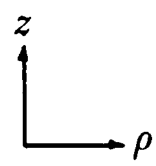

CONTOUR KEY	
1	0.1350
2	0.4050
3	0.6750
4	0.9450
5	1.2150
6	1.4850
7	1.7550
8	2.0250

Axial velocity $v_z(\rho, z)\, cm/s$

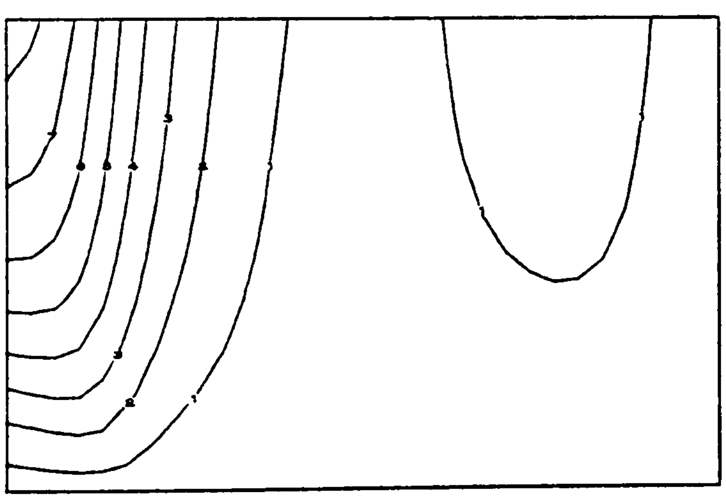

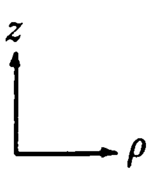

CONTOUR KEY	
1	0.5925
2	1.7775
3	2.9625
4	4.1475
5	5.3325
6	6.5175
7	7.7025
8	8.8875

Radial velocity $v_\rho(\rho, z)\, cm/s$

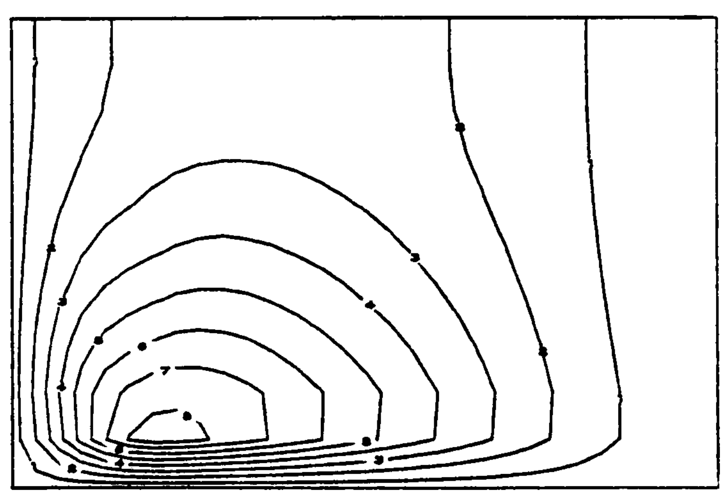

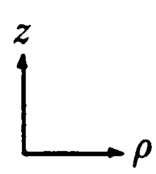

CONTOUR KEY	
1	0.2281
2	0.6844
3	1.1406
4	1.5969
5	2.0531
6	2.5094
7	2.9656
8	3.4219

Figure 10.14 : Vorticity, stream function and velocity
$R_e = 100$ with the outflow boundary on B4

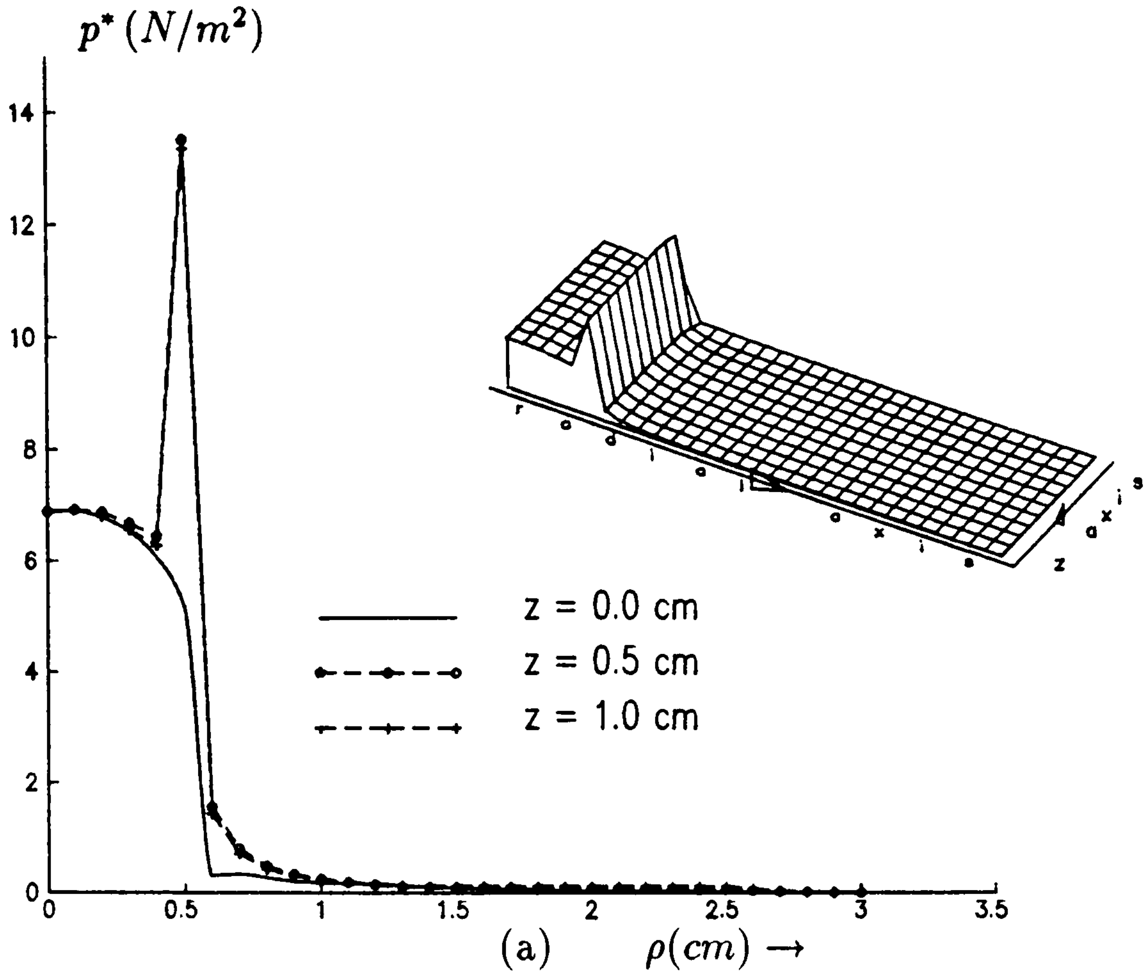

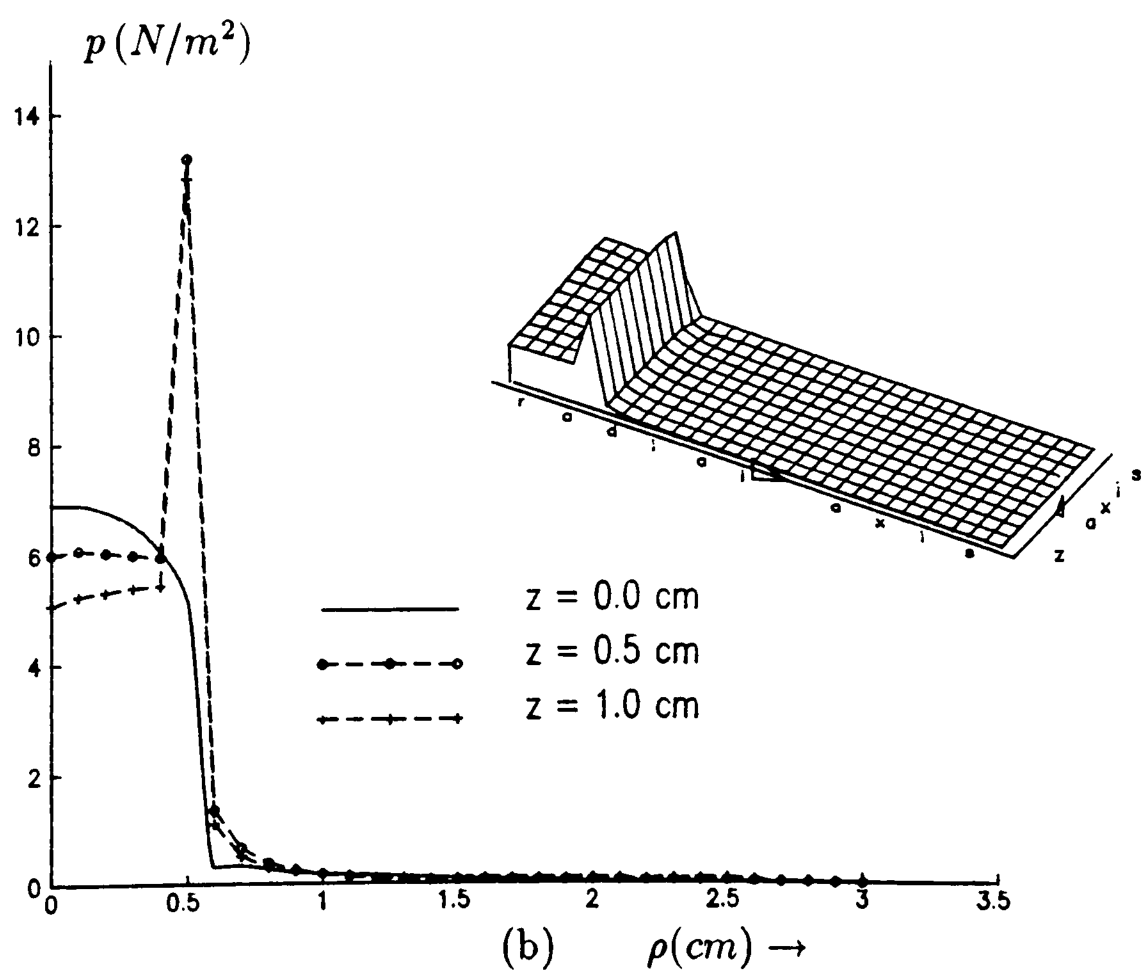

Figure 10.15 : Quantity $p^*(\rho, z)$ and pressure $p(\rho, z)$
$R_e = 100$ with the outflow boundary on B4

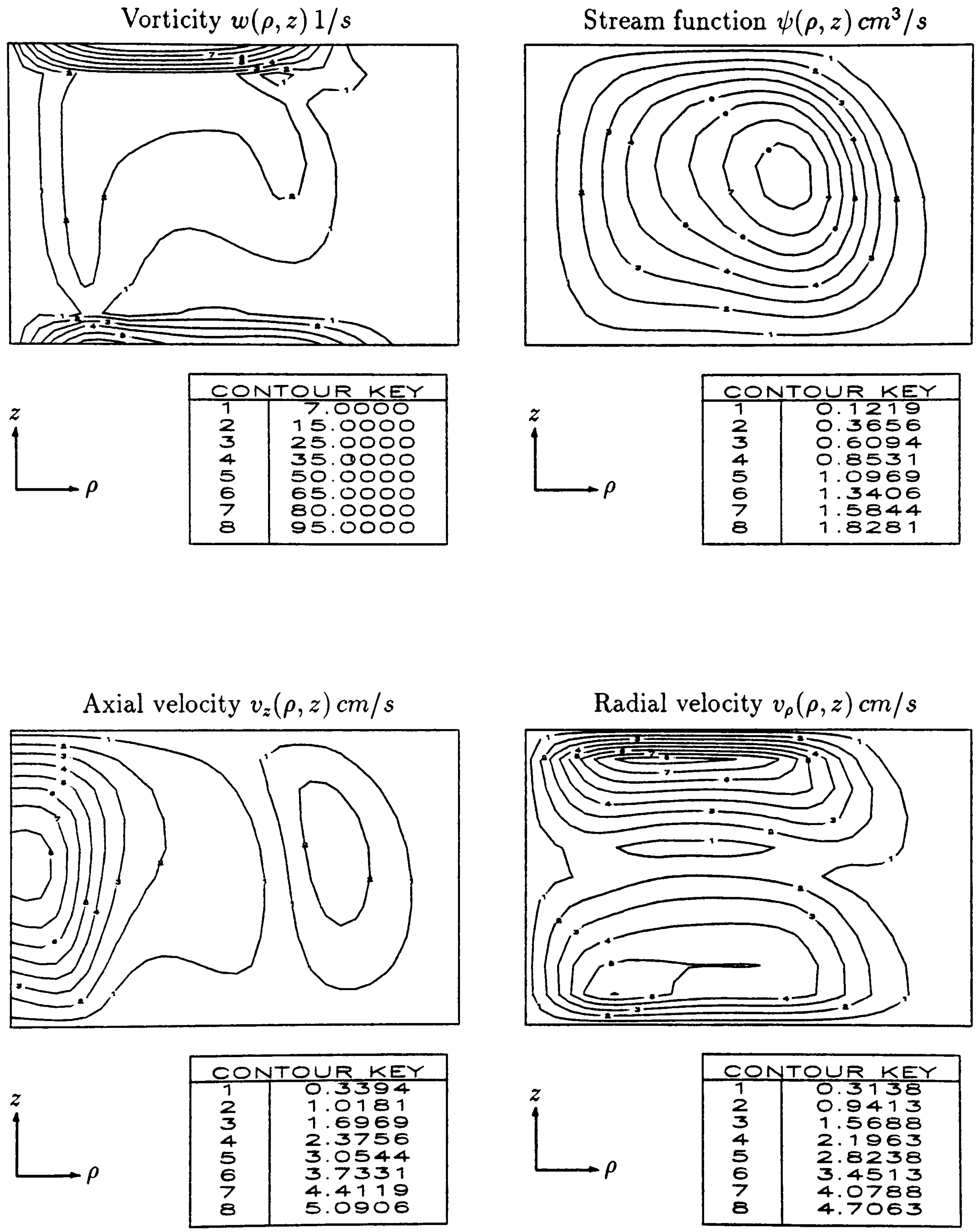

Vorticity $w(\rho, z)\, 1/s$ — CONTOUR KEY

1	7.0000
2	15.0000
3	25.0000
4	35.0000
5	50.0000
6	65.0000
7	80.0000
8	95.0000

Stream function $\psi(\rho, z)\, cm^3/s$ — CONTOUR KEY

1	0.1219
2	0.3656
3	0.6094
4	0.8531
5	1.0969
6	1.3406
7	1.5844
8	1.8281

Axial velocity $v_z(\rho, z)\, cm/s$ — CONTOUR KEY

1	0.3394
2	1.0181
3	1.6969
4	2.3756
5	3.0544
6	3.7331
7	4.4119
8	5.0906

Radial velocity $v_\rho(\rho, z)\, cm/s$ — CONTOUR KEY

1	0.3138
2	0.9413
3	1.5688
4	2.1963
5	2.8238
6	3.4513
7	4.0788
8	4.7063

Figure 10.16 : Vorticity, stream function and velocity
$R_e = 100$ with the no-slip boundary on B4

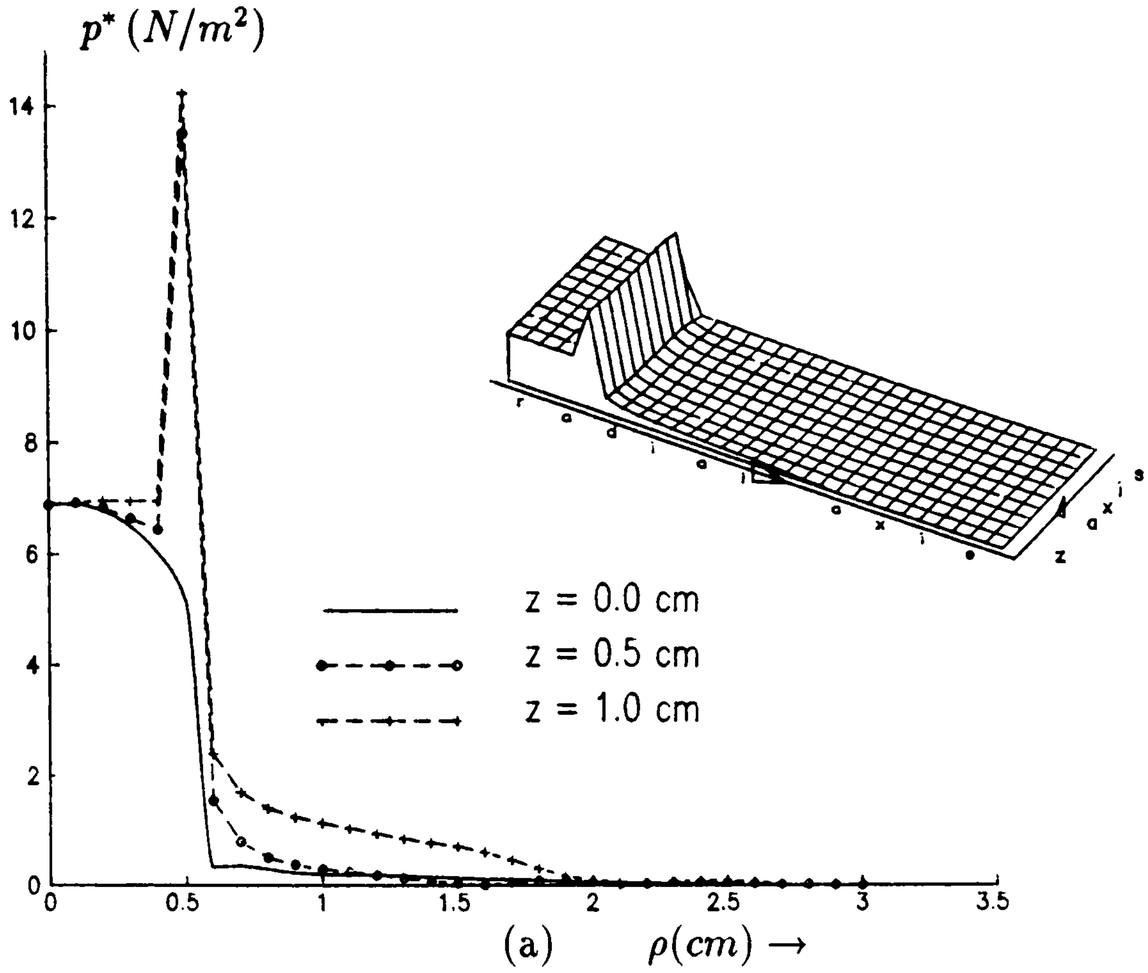

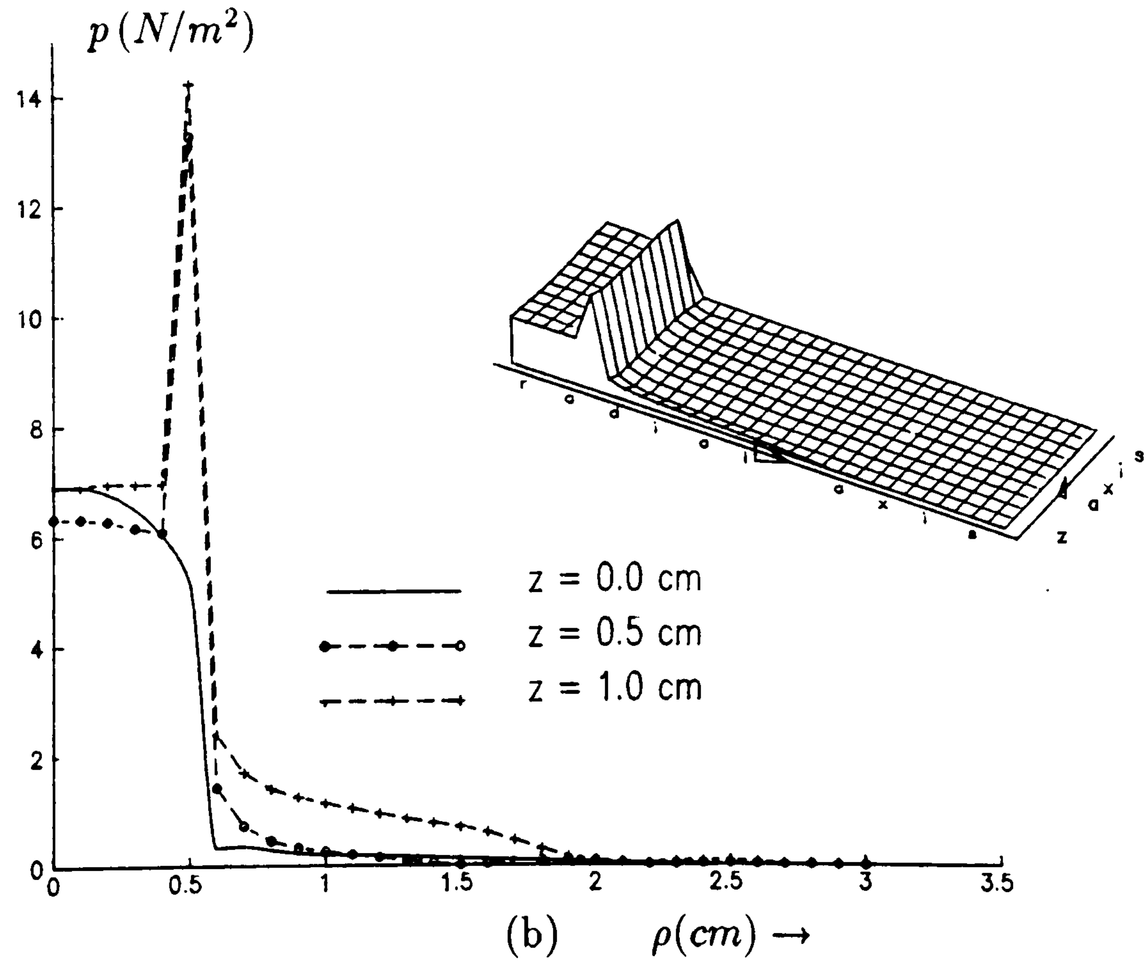

Figure 10.17 : Quantity $p^*(\rho, z)$ and pressure $p(\rho, z)$
$R_e = 100$ with the no-slip boundary on B4

The first point is apparent because both the velocity and the current density are the solutions of boundary-value problems. The second point is consistent with the result that $\nabla \times (\mathbf{j} \times \mathbf{B})$, which is proportional to f_z , is the strongest at the edge of the rod-liquid interface because if $\nabla \times (\mathbf{j} \times \mathbf{B}) = 0$ the $\mathbf{j} \times \mathbf{B}$ force is balanced by the pressure and it would not be possible to bring about any motion in the fluid which is initially stagnant. This may clearly be seen from the process of the solution of the MHD problem, that is f_z drives the vorticity in the transport equation while the vorticity plays a "source" role in the Poisson equation for the stream function. The third point is in agreement with Maecker's equation (10.76) because $\mathbf{B} = 0$ along the centre axis. The last two points strongly suggest that the motion of fluid has little effect on the resultant pressure. Hence we may ignore the hydrodynamic effect and work out the pressure by

$$\nabla p = \mathbf{j} \times \mathbf{B} \tag{10.149}$$

which can be expressed by an integration form obtained in an analogous way to that used to deal with Eqn.(10.128) previously, that is

$$p(\rho, z) = \int_{\rho}^{r_1} -f_\rho(\rho', 0)d\rho' + \int_0^z f_z(\rho, z')dz' - \int_0^z f_z(r_1, z')dz' \tag{10.150}$$

in which the first term on the R.H.S. is the pressure due to the familiar pinch effect. The computational results according to Eqn.(10.150) are shown in Fig.10.18 and are in close agreement to those previously obtained by taking the hydrodynamics into account.

It should be remarked that in the MHD approach we ignored the influence of fluid motion on the original electromagnetic fields, namely we ignored the induced current with a density $\mathbf{j}_{ind} = \sigma(\mathrm{v} \times \mathbf{B})$ because for $v \sim 10^{-2}\, m/s$, $B \sim 10^{-3}\, tesla$ and $\sigma \sim 10\,(\Omega m)^{-1}$, the induced current density is only of the order of $10^{-4}\, A/m^2$, which is much smaller than the conduction current density which amounted to 10^4 to $10^6\, A/m^2$, so is negligible.

So far we have shown by the magnetohydrodynamic model for the incompressible conducting fluid in the water-cup that the pressure at top liquid surface due to the electrodynamic forces is only the order of $10^1\, N/m^2$, which may result in an up-thrust

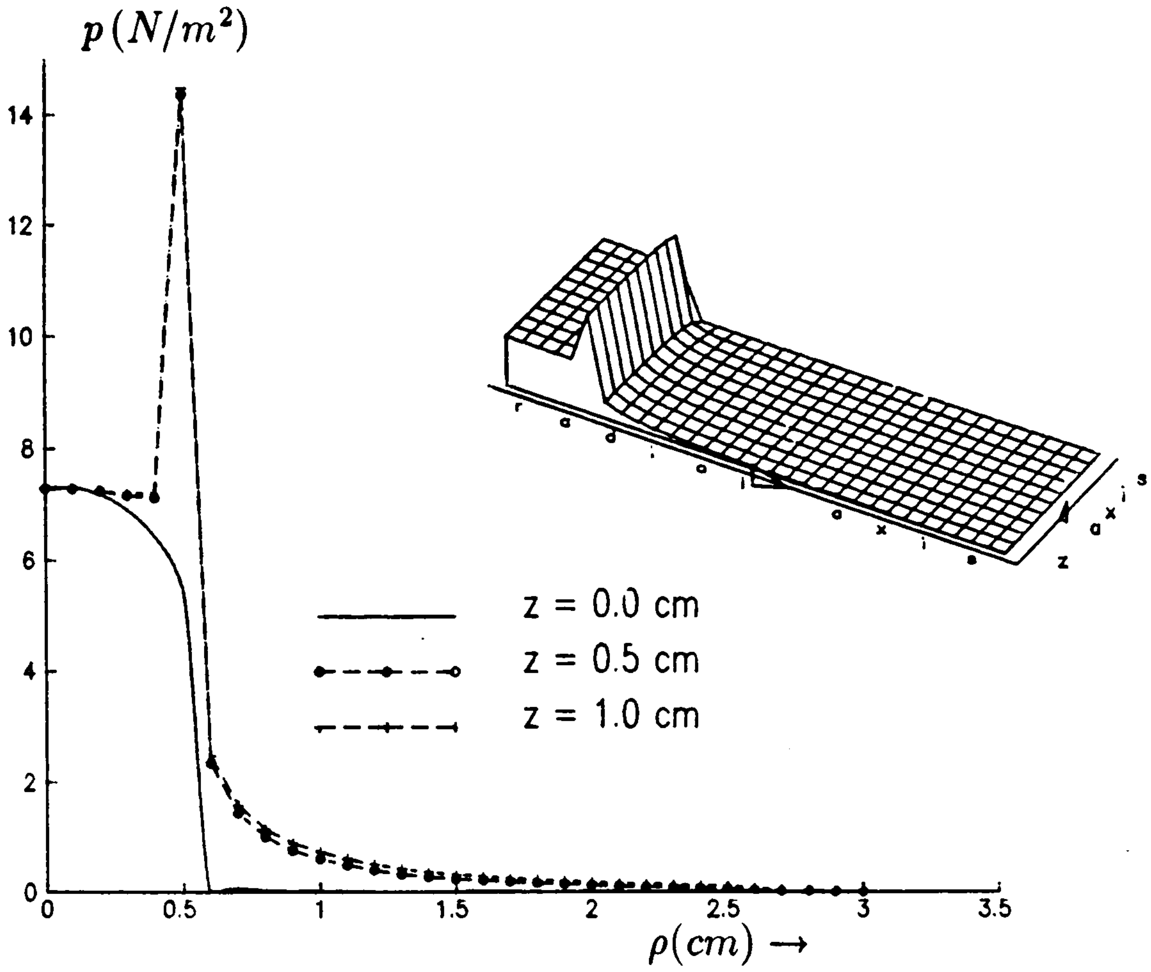

Figure 10.18 : Pressure $p(\rho, z)$ based on the magnetostatic computation

force of $10 \times (\pi r_3^2) = 7.85 \times 10^{-3} N$ for $r_3 = 0.5\,cm$. This order of magnitude is obviously much smaller than the $21.6\,N$ required for throwing the metal weight into the air. Therefore, it seems that the high pressure is unlikely to be a direct effect of electrodynamic forces, but more likely due to shock waves caused by under-water arcs. A support of the latter will be presented briefly in the next section.

Before going to the next section, a short explanation should be given of the case in which the discharge through salt-water is silent and leaves the water undisturbed. In this case, there is no under-water arc so neither spark nor shock wave occurs. Nevertheless, the electrodynamic forces do have some effect on the conducting liquid. We know from the experiments [132] that the discharging time is about $0.41\,ms$. Taking the maximum discharging current $100\,A$ through this period and making a transient analysis of the Navier-Stokes equation (10.72), we find that by the time $t = 0.5\,ms$, the velocity field of the fluid has almost not yet been established as indicated by Fig.10.19.

This means that the discharging time is too short for electrodynamic forces to bring about an observable motion of the conducting liquid. That is the reason why the salt water is undisturbed in this case.

10.4 Shock waves in liquid

As a matter of fact the water is not an ideal incompressible fluid and shock wave could exist. Some similar experiments of shock sound by under-water discharges were investigated [130] previous to Graneau's experiments [132], and it was believed that the high pressure in the liquid is due to the shock waves. According to shock wave theory [144], the fundamental equations which are necessary to define the physical properties of shock waves are the three equations of motion

$$\frac{\partial \rho_m}{\partial t} + \nabla \cdot (\rho_m \mathrm{v}) = 0 \tag{10.151}$$

$$\frac{\partial \mathrm{v}}{\partial t} + (\mathrm{v} \cdot \nabla)\mathrm{v} + \frac{\nabla p}{\rho_m} = 0 \tag{10.152}$$

$$\rho_m \left(\frac{\partial \mathcal{E}^*}{\partial t} + \mathrm{v} \cdot \nabla \mathcal{E}^* \right) + \nabla \cdot (p\mathrm{v}) = 0 \tag{10.153}$$

together with an appropriate equation of state

$$p = \mathcal{F}(\rho_m, \mathcal{S}) \tag{10.154}$$

where ρ_m is the mass density; v the fluid velocity; p the pressure; $\mathcal{E}^*$ the internal energy;[15] and $\mathcal{S}$ the entropy. Equation (10.151) represents the conservation of mass and is also referred to as the equation of continuity. Equation (10.152) indicates the conservation of momentum, which is identical with the Navier-Stokes equation in the absence of body forces for an inviscid fluid. Equation (10.153) denotes the conservation of energy given by the first law of thermodynamics on the assumption that the gain in total energy of the fluid is due solely to the work done by the pressure forces in compressing and accelerating the fluid.

[15]The internal energy is expressed by the symbol, $\mathcal{E}^*$ instead of $\mathcal{E}$, to show that it includes both the velocity and the internal, or temperature, energy.

Vorticity $w(\rho, z)\, 1/s$

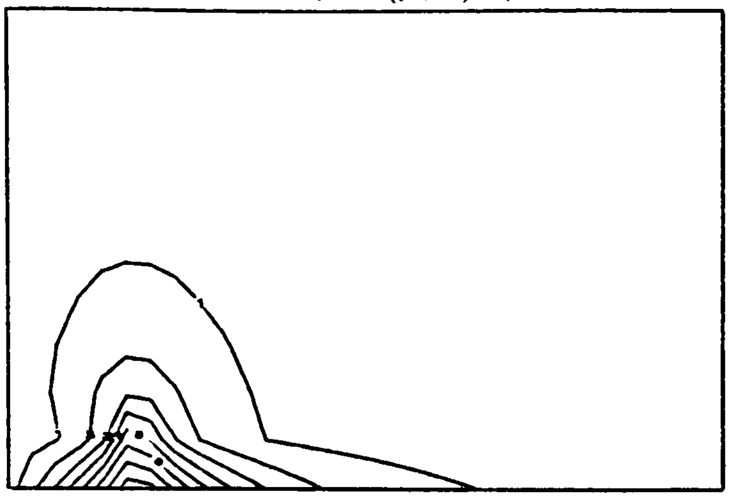

CONTOUR	KEY
1	0.0335
2	0.1005
3	0.1675
4	0.2345
5	0.3015
6	0.3685
7	0.4355
8	0.5025

Stream function $\psi(\rho, z)\, cm^3/s$

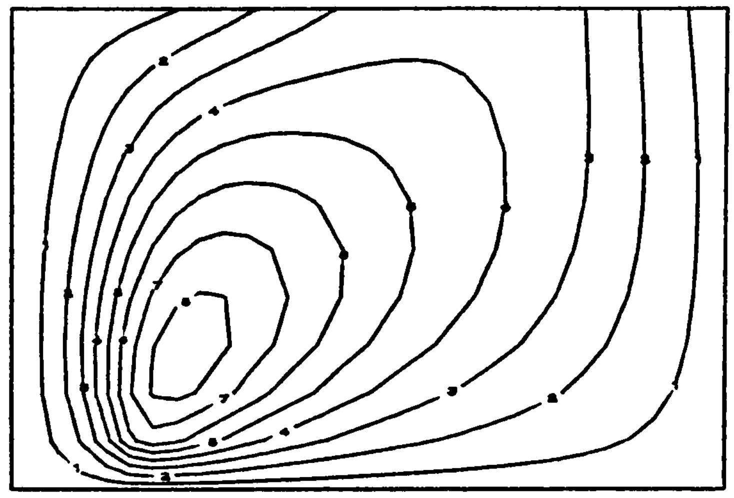

CONTOUR	KEY
1	0.0001
2	0.0004
3	0.0006
4	0.0009
5	0.0011
6	0.0014
7	0.0017
8	0.0019

Axial velocity $v_z(\rho, z)\, cm/s$

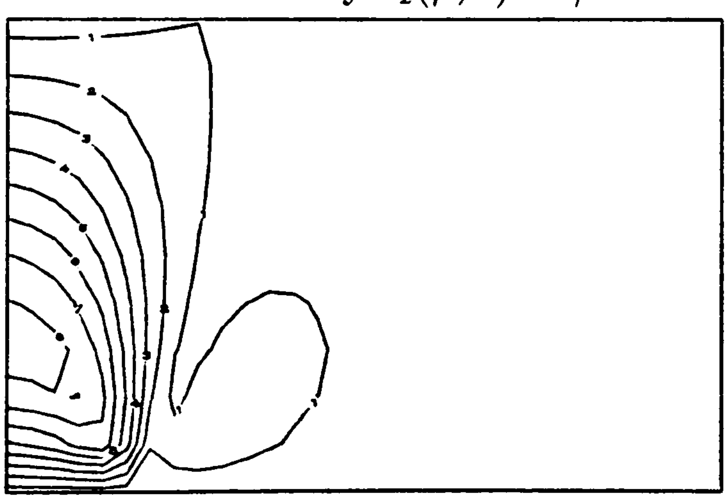

CONTOUR	KEY
1	0.0009
2	0.0028
3	0.0047
4	0.0065
5	0.0084
6	0.0102
7	0.0121
8	0.0140

Radial velocity $v_\rho(\rho, z)\, cm/s$

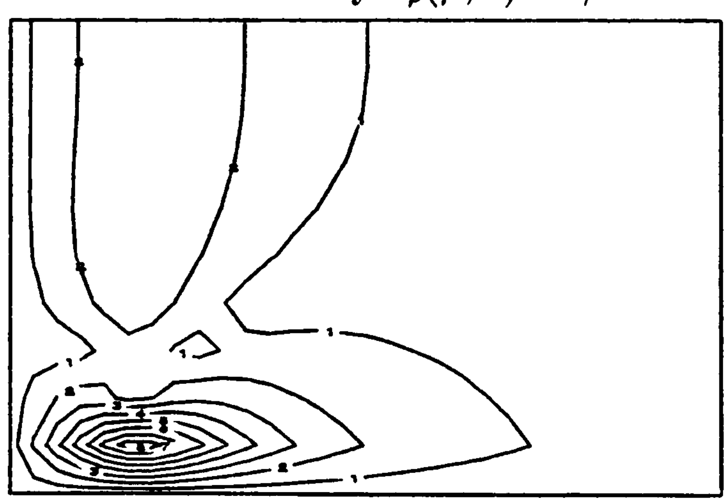

CONTOUR	KEY
1	0.0010
2	0.0031
3	0.0051
4	0.0071
5	0.0092
6	0.0112
7	0.0132
8	0.0153

Figure 10.19 : Vorticity, stream function and velocity by the time=0.5 ms based on the transient analysis
$R_e = 100$ with the outflow boundary on B4

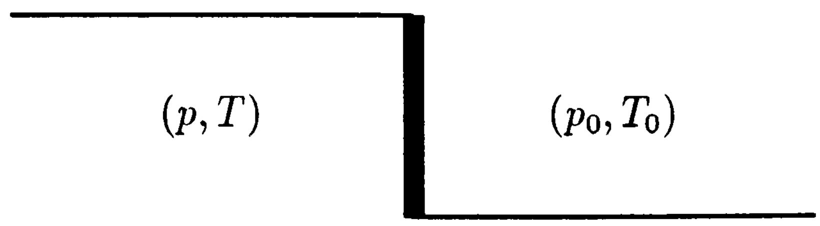

Figure 10.20 : The thermodynamic states of a shock wave front

On the other hand we know that when a mass element of fluid is traversed by a shock wave front, it suffers, an almost discontinuous change in its thermodynamic state as Fig.10.20 shown, where (p_0, T_0) and (p, T) are the state variables ahead of and behind the shock wave front respectively. Richardson, Arons and Halverson [145] described, qualitatively, the procedures of this change by the aid of a sketch drawing (Fig.10.21), in which a given mass element of fluid initially in the state (p_0, T_0) ahead of a shock front will attain a state (p, T) along a single curve labeled "Hugoniot" as the shock wave front is passing by and finally returns to a state (p_0, T_1) along the adiabatic. In general T_1 is larger than T_0 because of the dissipation occuring at the front. Richardson and his co-workers also gave the solution of shock wave for water based on the governing equations (10.151) to (10.154). With the help of their solution, Penney and Pike [146] were able to evaluate the shock wave properties in various fluids. For our purpose, some properties of interest are listed in Table 10.2. From this table, one can clearly see that a shock wave in a liquid medium is characterized by a small rise in temperature and an extremely large change in pressure. The reason is because water is much less compressible than air.

In the water-cup experiment, the pressure required to produce $21.6\,N$ up lift force on the metal weight is much smaller than 2000 atm[16] so that the rise in temperature due to the shock wave[17] can be expected from Table 10.2 to be too small to account

[16] $1\,atm = 10^5\,N/m^2$.

[17] The temperature may also rise due to the current heating the conducting liquid.

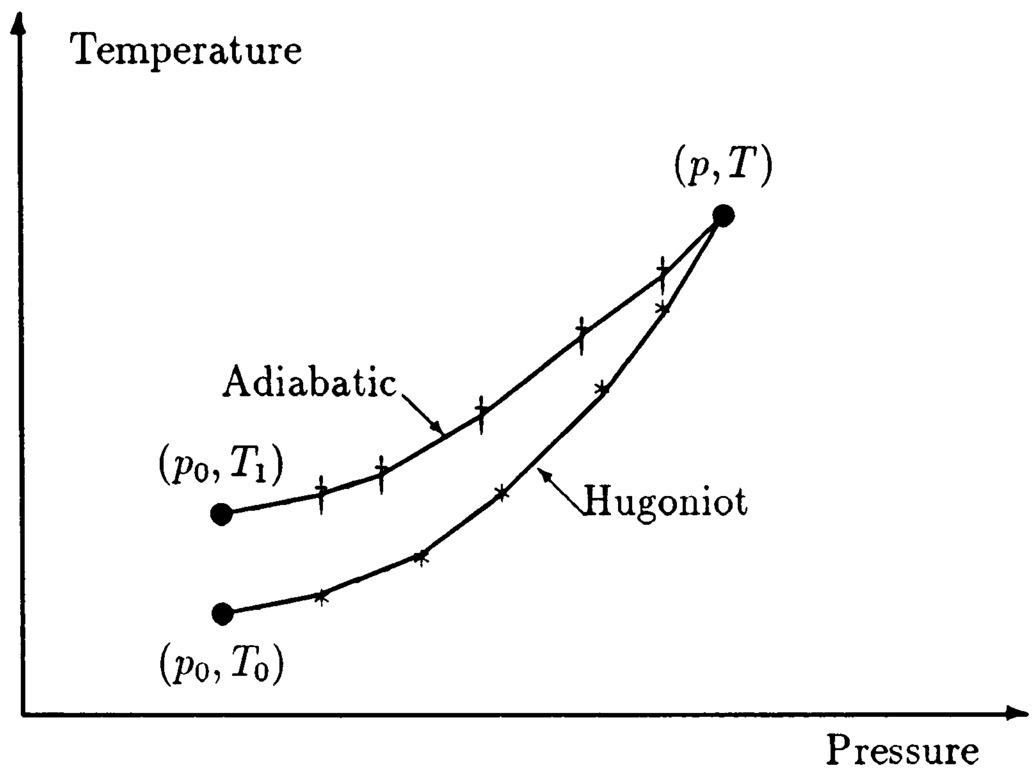

Figure 10.21 : The procedures of change in state due to a shock wave

Table 10.2: Shock wave properties in air and water after Penney and Pike

Fluid	p (atm)	$T - T_0$ (^0c)	$T_1 - T_0$ (^0c)
Air	20	900	250
	100	3440	1240
	200	5090	2350
	500	7940	3860
Water	2000	5	<0.02
	10000	36	5
	20000	70	18
	50000	152	52

$T_0 = 300\,K$ $p_0 = 1\,atm$

for. Thus the associated dissipated energy due to the shock is small too. This explains why the rise in temperature and the dissipation of energy in both experimental cases of (a) silent discharge and (b) arc discharge are not much different from one case to the other even with the same stored discharge energy.

However, it should be noted that the energy distribution and the way of dissipating energy in the both cases could be different. The shock wave could be created by rapidly releasing high energy locally as done in the under–water arc.

Appendix 10.1

For an axisymmetric current Eqn.(10.65) can be written in a cylindrical coordinate system as

$$\mathbf{A}(\mathbf{r}) = \frac{\mu_0}{4\pi}\int_{\tau'} \frac{j_z(\rho', z')}{|\mathbf{r}-\mathbf{r}'|}\rho' d\rho' d\phi' dz' \, \mathbf{a}_z + \frac{\mu_0}{4\pi}\int_{\tau'} \frac{j_\rho(\rho', z')}{|\mathbf{r}-\mathbf{r}'|}\mathbf{a}_\rho \rho' d\rho' d\phi' dz' \tag{10.155}$$

with

$$|\mathbf{r}-\mathbf{r}'| = [(z-z')^2 + \rho^2 + \rho'^2 - 2\rho\rho'\cos(\phi-\phi')]^{1/2} \tag{10.156}$$

In Eqn.(10.155) $\mathbf{a}_\rho$ cannot be taken out of the integral because it is a function of ϕ'

$$\mathbf{a}_\rho = \cos\phi' \, \mathbf{a}_x + \sin\phi' \, \mathbf{a}_y \tag{10.157}$$

where $\mathbf{a}_x$ and $\mathbf{a}_y$ are the unit vectors of x and y axes in a Cartesian coordinate system. Thus we may express Eqn.(10.155) by

$$\mathbf{A}(\mathbf{r}) = A_x\mathbf{a}_x + A_y\mathbf{a}_y + A_z\mathbf{a}_z \tag{10.158}$$

with

$$A_x = \frac{\mu_0}{4\pi}\int_{\tau'} \frac{j_\rho(\rho', z')}{|\mathbf{r}-\mathbf{r}'|}\cos\phi' \rho' d\rho' d\phi' dz' \tag{10.159}$$

$$A_y = \frac{\mu_0}{4\pi}\int_{\tau'} \frac{j_\rho(\rho', z')}{|\mathbf{r}-\mathbf{r}'|}\sin\phi' \rho' d\rho' d\phi' dz' \tag{10.160}$$

$$A_z = \frac{\mu_0}{4\pi}\int_{\tau'} \frac{j_z(\rho', z')}{|\mathbf{r}-\mathbf{r}'|}\rho' d\rho' d\phi' dz' \tag{10.161}$$

Since

$$\mathbf{a}_x = \cos\phi \, \mathbf{a}_\rho - \sin\phi \, \mathbf{a}_\phi \tag{10.162}$$

$$\mathbf{a}_y = \sin\phi \, \mathbf{a}_\rho + \cos\phi \, \mathbf{a}_\phi \tag{10.163}$$

according to the transformations of unit vectors in Cartesian and cylindrical coordinate systems. Substituting those into Eqn.(10.158) gives

$$\begin{aligned} \mathbf{A}(\mathbf{r}) &= (A_x\cos\phi + A_y\sin\phi)\mathbf{a}_\rho + (A_y\cos\phi - A_x\sin\phi)\mathbf{a}_\phi + A_z\mathbf{a}_z \\ &= A_\rho\mathbf{a}_\rho + A_\phi\mathbf{a}_\phi + A_z\mathbf{a}_z \end{aligned} \tag{10.164}$$

Let us firstly consider A_ϕ which may be written

$$A_\phi = \frac{\mu_0}{4\pi}\iint j_\rho(\rho',z')\left(\int_0^{2\pi}\frac{\sin(\phi'-\phi)}{[(z-z')^2+\rho^2+\rho'^2-2\rho\rho'\cos(\phi-\phi')]^{1/2}}d\phi'\right)\rho'd\rho'dz' \tag{10.165}$$

because the origin of coordinates is inside current region τ'. Expressing the integral with respect to ϕ' by

$$\int_0^{2\pi}\frac{\sin(\phi'-\phi)}{[(z-z')^2+\rho^2+\rho'^2-2\rho\rho'\cos(\phi-\phi')]^{1/2}}d\phi' = -\int_0^{2\pi}\frac{\sin(\phi-\phi')}{[a+b\cos(\phi-\phi')]^{1/2}}d\phi' \tag{10.166}$$

with

$$a = (z-z')^2+\rho^2+\rho'^2 \tag{10.167}$$

$$b = -2\rho\rho' \tag{10.168}$$

it is easily shown that the R.H.S.on Eqn.(10.166) equals zero, thus

$$A_\phi = 0 \tag{10.169}$$

as it is expected. Physically, one would also expect that both A_ρ and A_z are independent of ϕ for an axisymmetric current. However it can be seen that ϕ appears in the formulas of them, which may cause a confusion. This difficulty can be moved by checking $\partial A_\rho/\partial\phi$ and $\partial A_z/\partial\phi$. For example,

$$\frac{\partial A_z}{\partial\phi} = -\frac{\mu_0}{4\pi}\iint j_z(\rho',z')\left(\int_0^{2\pi}\frac{\sin(\phi-\phi')}{[a+b\cos(\phi-\phi')]^{3/2}}d\phi'\right)\rho\rho'^2d\rho'dz' \tag{10.170}$$

because

$$\frac{\partial}{\partial\phi}\frac{1}{|\mathbf{r}-\mathbf{r}'|} = \frac{-\rho\rho'\sin(\phi-\phi')}{[(a+b\cos(\phi-\phi')]^{3/2}} \tag{10.171}$$

where a and b are the same as those given in Eqn.(10.167) and Eqn.(10.168) respectively. We can find again that the integral with respect to ϕ' in Eqn.(10.170) vanshes so that

$$\frac{\partial A_z}{\partial\phi} = 0 \tag{10.172}$$

Similarly, we can prove that

$$\frac{\partial A_\rho}{\partial \phi} = 0 \tag{10.173}$$

Therefore, ϕ which appears in the formulas of A_ρ and A_z is a parameter of reference rather than a variable and may be assigned to any value. To be simplest, we let $\phi = 0$ which leads to

$$A_\rho = \frac{\mu_0}{4\pi} \iint j_\rho(\rho', z') \left(\int_0^{2\pi} \frac{\cos\phi'}{[(z-z')^2 + \rho^2 + \rho'^2 - 2\rho\rho'\cos\phi']^{1/2}} d\phi' \right) \rho' d\rho' dz' \tag{10.174}$$

$$A_z = \frac{\mu_0}{4\pi} \iint j_z(\rho', z') \left(\int_0^{2\pi} \frac{1}{[(z-z')^2 + \rho^2 + \rho'^2 - 2\rho\rho'\cos\phi']^{1/2}} d\phi' \right) \rho' d\rho' dz' \tag{10.175}$$

in the forms without involving ϕ. Hence for an axisymmetric current the vector potential in cylindrical coordinates is in general given by

$$\mathbf{A}(\mathbf{r}) = A_\rho(\rho, z)\, \mathbf{a}_\rho + A_z(\rho, z)\, \mathbf{a}_z \tag{10.176}$$

and the associated magnetic induction is

$$\mathbf{B}(\mathbf{r}) = \nabla \times \mathbf{A}(\mathbf{r}) = \left(\frac{\partial A_\rho}{\partial z} - \frac{\partial A_z}{\partial \rho} \right) \mathbf{a}_\phi \tag{10.177}$$

because the other partial derivatives are zero. By substitution of Eqns.(10.174,10.175) into Eqn.(10.177) yields

$$\begin{aligned} B_\phi = {} & \frac{\mu_0}{4\pi} \iint j_\rho(\rho', z') \left(\int_0^{2\pi} \frac{-(z-z')\cos\phi'}{[(z-z')^2 + \rho^2 + \rho'^2 - 2\rho\rho'\cos\phi']^{3/2}} d\phi' \right) \rho' d\rho' dz' \\ - {} & \frac{\mu_0}{4\pi} \iint j_z(\rho', z') \left(\int_0^{2\pi} \frac{-(\rho - \rho'\cos\phi')}{[(z-z')^2 + \rho^2 + \rho'^2 - 2\rho\rho'\cos\phi']^{3/2}} d\phi' \right) \rho' d\rho' dz' \end{aligned} \tag{10.178}$$

which is identical with Eqn.(10.67).

Appendix 10.2

Since the current density $\mathbf{j}$ in our case is a two-dimensional and solenoidal vector field, i.e.,

$$\mathbf{j} = j_\rho(\rho, z)\mathbf{a}_\rho + j_z(\rho, z)\mathbf{a}_z \tag{10.179}$$

$$\nabla \cdot \mathbf{j} = 0 \tag{10.180}$$

we can introduce a new scalar function ν such that

$$j_\rho = -\frac{1}{\rho}\frac{\partial \nu}{\partial z} \tag{10.181}$$

$$j_z = \frac{1}{\rho}\frac{\partial \nu}{\partial \rho} \tag{10.182}$$

to satisfy Eqn.(10.180). On the other hand we have

$$j_\rho = \frac{1}{\mu_0}\frac{\partial B_\phi}{\partial z} \tag{10.183}$$

$$j_z = \frac{1}{\mu_0}\left[\frac{B_\phi}{\rho} + \frac{\partial B_\phi}{\partial \rho}\right] \tag{10.184}$$

from $\nabla \times \mathbf{B} = \mu_0 \mathbf{j}$ for $\mathbf{B} = B_\phi(\rho, z)\mathbf{a}_\phi$. By comparison of these two sets of current density components, we get

$$\frac{\partial \nu}{\partial z} = \frac{\partial}{\partial z}\left(\frac{\rho B_\phi}{\mu_0}\right) \tag{10.185}$$

$$\frac{\partial \nu}{\partial \rho} = \frac{\partial}{\partial \rho}\left(\frac{\rho B_\phi}{\mu_0}\right) \tag{10.186}$$

It is easily to see that

$$\nu = \frac{\rho B_\phi}{\mu_0} + c_0 \tag{10.187}$$

where c_0 is an arbitray constant.

In the 2-D space, we have

$$d\mathbf{r} = d\rho \mathbf{a}_\rho + dz \mathbf{a}_z \tag{10.188}$$

where $\mathbf{r}$ is a position vector. Thus

$$\mathbf{j} \times d\mathbf{r} = (j_\rho dz - j_z d\rho)\mathbf{a}_\rho \times \mathbf{a}_z \tag{10.189}$$

Substituting Eqns.(10.181,10.182) into Eqn.(10.189) yields

$$\mathbf{j} \times d\mathbf{r} = -\frac{1}{\rho}\left(\frac{\partial \nu}{\partial z}dz + \frac{\partial \nu}{\partial \rho}d\rho\right)\mathbf{a}_\rho \times \mathbf{a}_z \tag{10.190}$$

In evidence, if

$$d\nu = \frac{\partial \nu}{\partial z}dz + \frac{\partial \nu}{\partial \rho}d\rho = 0 \tag{10.191}$$

$\mathbf{j}$ is parallel to $d\mathbf{r}$. In other words, along any $\nu = const.\,(d\nu = 0)$ curve, the current density has only a tangential component, which means that the current flows such curves. From Eqn.(10.187) we immediately find that such curves can be mapped by

$$\rho B_\phi = const. \tag{10.192}$$

In this case the scalar function ν may be identified as a current stream function.

Appendix 10.3

In the experiments, the salt water was stationary before discharges. If the electrodynamic force does not accelerate the liquid while discharging, the magnetic field in the liquid, $\rho_m = const.$, at rest must satisfy the equation[18]

$$\nabla \times (\nabla \times \mathbf{B} \times \mathbf{B}) = 0 \tag{10.193}$$

In fact, the equation can be obtained by letting $\mathbf{v} = 0$ in Eqn.(10.73) and taking the curl of the both sides if we note $\nabla \times \mathbf{B} = \mu_0 \mathbf{j}$. It follows that if Eqn.(10.193) is not held, the $(\mathbf{j} \times \mathbf{B})$ force not only cause pressure in the liquid, but also accelerate the liquid. Following we will show that in our case the condition for $\nabla \times (\mathbf{j} \times \mathbf{B}) = 0$ or Eqn.(10.193) is

$$(\mathbf{j} \times \mathbf{B}) \cdot \mathbf{a}_z = 0 \tag{10.194}$$

Since we just consider a DC discharge, the steady and axisymmetrical current density and magnetic field can be expressed in the general forms

$$\mathbf{j} = j_\rho(\rho, z)\mathbf{a}_\rho + j_z(\rho, z)\mathbf{a}_z \tag{10.195}$$

$$\mathbf{B} = B_\phi(\rho, z)\mathbf{a}_\phi \tag{10.196}$$

Take the curl of Eqn.(10.196)

$$\nabla \times \mathbf{B} = -\frac{\partial B_\phi(\rho, z)}{\partial z}\mathbf{a}_\rho + \frac{1}{\rho}\frac{\partial(\rho B_\phi(\rho, z))}{\partial \rho}\mathbf{a}_z \tag{10.197}$$

On substituting $\mu_0 \mathbf{j}$ for $\nabla \times \mathbf{B}$, we get

$$j_\rho(\rho, z) = -\frac{1}{\mu_0}\frac{\partial B_\phi(\rho, z)}{\partial z} \tag{10.198}$$

$$j_z(\rho, z) = \frac{1}{\mu_0}\left[\frac{B_\phi(\rho, z)}{\rho} + \frac{\partial B_\phi(\rho, z)}{\partial \rho}\right] \tag{10.199}$$

Hence the electrodynamic force is given by

$$\begin{aligned} \mathbf{j} \times \mathbf{B} &= j_\rho(\rho, z)B_\phi(\rho, z)\mathbf{a}_z - j_z(\rho, z)B_\phi(\rho, z)\mathbf{a}_\rho \\ &= f_z(\rho, z)\mathbf{a}_z + f_\rho(\rho, z)\mathbf{a}_\rho \end{aligned} \tag{10.200}$$

[18] Refer to page 37 of a book by Ferraro and Plumpton [140].

with

$$f_z(\rho,z) = -\frac{B_\phi(\rho,z)}{\mu_0}\frac{\partial B_\phi(\rho,z)}{\partial z} \quad (10.201)$$

$$f_\rho(\rho,z) = -\frac{B_\phi(\rho,z)}{\mu_0}\left[\frac{B_\phi(\rho,z)}{\rho} + \frac{\partial B_\phi(\rho,z)}{\partial \rho}\right] \quad (10.202)$$

Since

$$\nabla \times (\mathbf{j} \times \mathbf{B}) = \left[\frac{\partial f_\rho(\rho,z)}{\partial z} - \frac{\partial f_z(\rho,z)}{\partial \rho}\right]\mathbf{a}_\phi \quad (10.203)$$

obviously, $\nabla \times (\mathbf{j} \times \mathbf{B}) = 0$ is subject to

$$\frac{\partial f_\rho(\rho,z)}{\partial z} = \frac{\partial f_z(\rho,z)}{\partial \rho} \quad (10.204)$$

Substituting Eqns.(10.201,10.202) into Eqn.(10.204) yields

$$\frac{2B_\phi(\rho,z)}{\rho}\frac{\partial B_\phi(\rho,z)}{\partial z} = 0 \quad (10.205)$$

which leads to

$$\frac{\partial B_\phi(\rho,z)}{\partial z} = 0 \quad (10.206)$$

because B_ϕ does not vanish in general. Substitution of Eqn.(10.206) into Eqn.(10.201) gives

$$f_z(\rho,z) = 0 \quad (10.207)$$

which is nothing else but Eqn.(10.194).

It has been numerically shown previously that the longitudinal force component does not vanish so that Eqn.(10.194) or Eqn.(10.207) is not held at all in our case and consequently, the $(\mathbf{j} \times \mathbf{B})$ force does accelerate the fluid.

Conclusions

In the first part of this thesis, a 3D electrodynamic model has been proposed for the retrograde motion of the electric arc — an old mystery of physics. The model is studied in detail for the first time by means of electromagnetic field theory and computational techniques. Some salient results can be drawn from this study as follows :

- Because of the tiny size of the cathode spot the electrodynamic effects on the spot motion will be local rather than global. In other words, one only needs to consider the current path near the spot instead of the whole closed circuit.

- It is possible and reasonable to solve coupling boundary-value problems between cathode and plasma column by the decoupling approach if the conductivity at the interface is widely different.

- As the plasma column is bent in Lorentzian direction due to the applied magnetic field, the current distribution over the cathode spot is no longer uniform and becomes stronger on the Lorentzian side while weaker on the retrograde side. This point is very important but was overlooked by the previous investigators.

- To make the spot move in the retrograde direction a necessary condition is that that the self magnetic field induced by the arc current exceeds the applied magnetic field somewhere in the spot region. However, only the combination of the nonuniform current distribution in the spot together with this necessary condition could serve for a complete cause of the retrograde motion.

- The electrodynamic forces can indeed account for the retrograde motion if the average current density of the cathode spot is of the order of $10^8\ A/cm^2$, which is in agreement with the value suggested by recent studies of spot current density.

- The proposed model has been shown to be consistent with a number of well-known features of the retrograde motion, including the retrograde motion of multi-spots which is for the first time related to electrodynamics.

In the second half of this thesis, some recent issues in electrodynamics have been studied based on theoretical and computational approaches. Some conclusions can be summarized as below :

- The Lorentz and Ampère force laws are equivalent in magnetostatics regardless of where the target current element is located and whether it has finite physical size or not provided that Ampère force law is correctly used.

- Whenever the Ampère force law is used, the complete calculation, in which the integration is taken over whole current system, always gives the correct prediction of both net force and force distribution whereas the incomplete calculation, in which the integration is selectly performed on partial current system, predicts only the net force correctly.

- So far as the electromagnetic jet propulsion and the electromagnetic impulse pendulum are concerned, it has been theoretically demonstrated that the reaction of the Lorentz force on the moving conductor is carried by the remainder of the current system as observed in the experiments.

- To determine electrodynamic forces in continuous media, the field theory of classical relativistic electrodynamics not only gives the correct prediction, but is also self consistent even though there might be some difficulty in explaining the mechanism of force transmission .

- On the water-arc explosions, it has been shown that neither the pure EM model nor the MHD model for the incompressible conducting fluid could explain the explosive phenomenon; this strongly suggests that the shock wave produced by the under-water arc must account for the phenomenon.

Appendix A

On the pulsed wire fragmentation

A.1 Background

In 1964 when Nasilowski [147] was studying the rupture of fuse wires with the experimental set-up in Fig.A.1, he found that a large current pulse of several thousand amperes would shatter a 1-mm-diameter straight copper wire of 1.5 m length into about 100 pieces (Fig.A.2), varing in length from 0.3 to 3 cm, with unmistakable signs of tensile fracture in the solid state. Recently, Graneau [92] at M.I.T. reported similar experiments in modified form as shown in Fig.A.3. A 1.2-mm-diameter straight aluminium wire of one metre length or a 1.2-mm-diameter aluminium wire bent into the shape of a semicircle with a radius of 25 cm was subjected to current pulses of up to 7000 amperes. The current was derived from a capacitor bank and passed through an inductor to allow it to ring down at 2000 Hz over a period of 5-10 ms. Depending on the peak current reached, the wire broke into 10 to 50 pieces of irregular length. The fracture faces were examined with optical and electron scanning microscopes. This left little doubt that tensile fracture had taken place in the solid state. His experiments confirm the earlier findings of Nasilowski. The rapid tensile failures on straight wires using capacitor discharges have also been observed by Graneau [117], Robson and Sethian [110]. This phenomenon is then called wire fragmentation. In fact the phenomenon may be traced back as early as to 1939 when Foitzik carried out experiments with large pulse currents [148].

The experimental observation is well established. However the mechanism of the phenomenon remains still unclear[116, 149] because the phenomenon may involve elec-

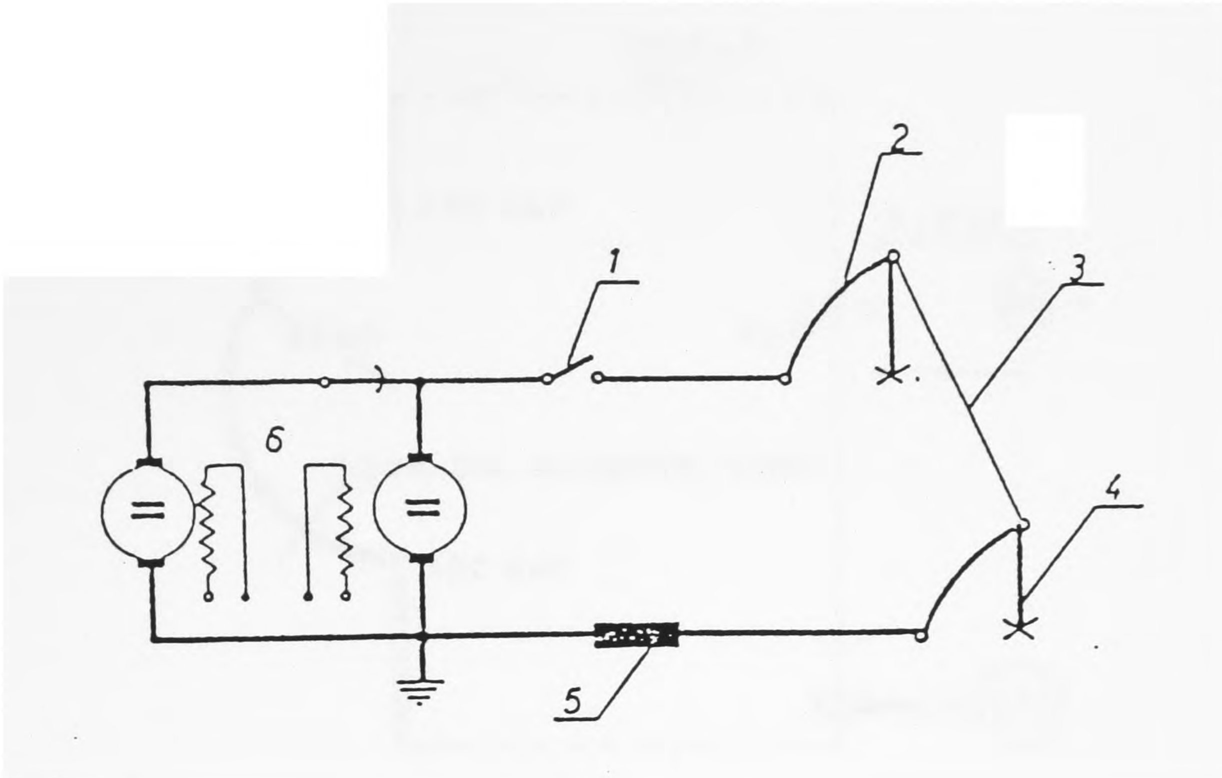

Figure A.1 : Nasilowski's experiment set-up
(1) contactor (2) flexible conductor (3) tested wire
(4) wooden stand (5) shunt (6) DC generators

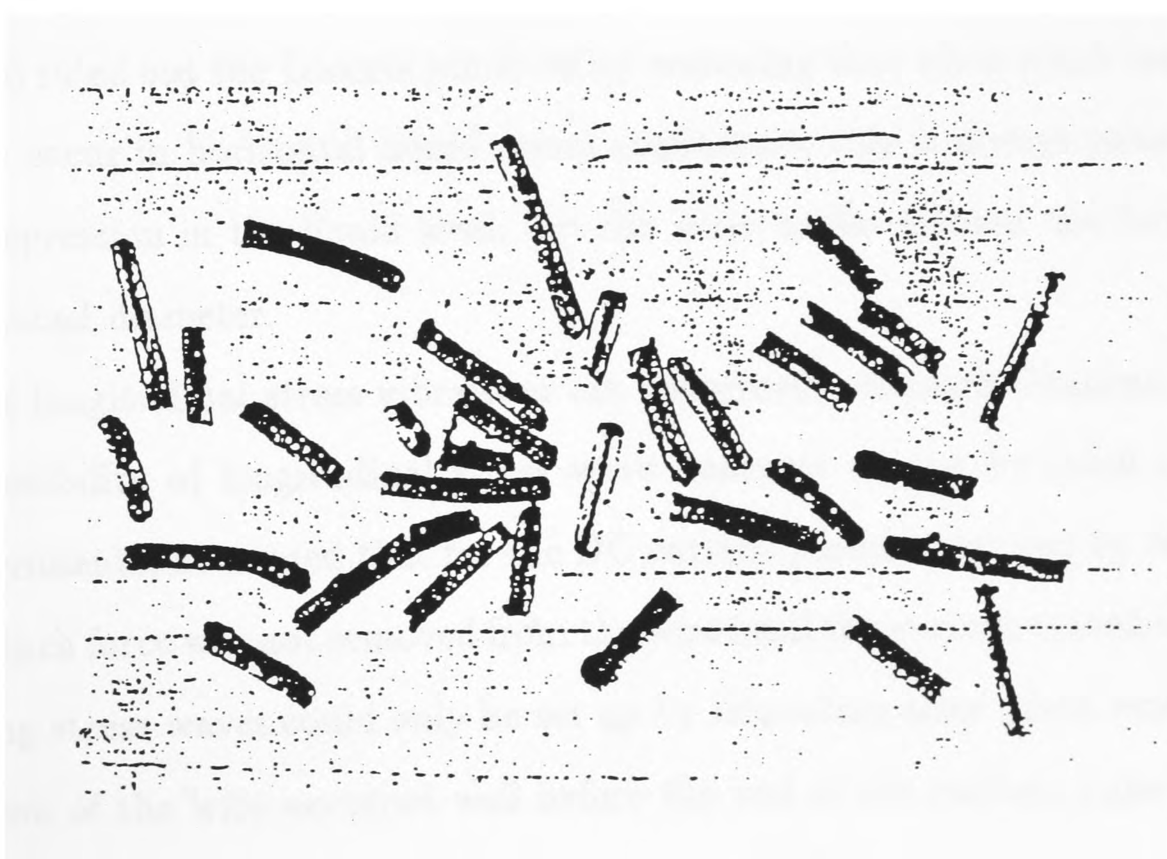

Figure A.2 : Fragments of the 1.0 mm diameter copper wires

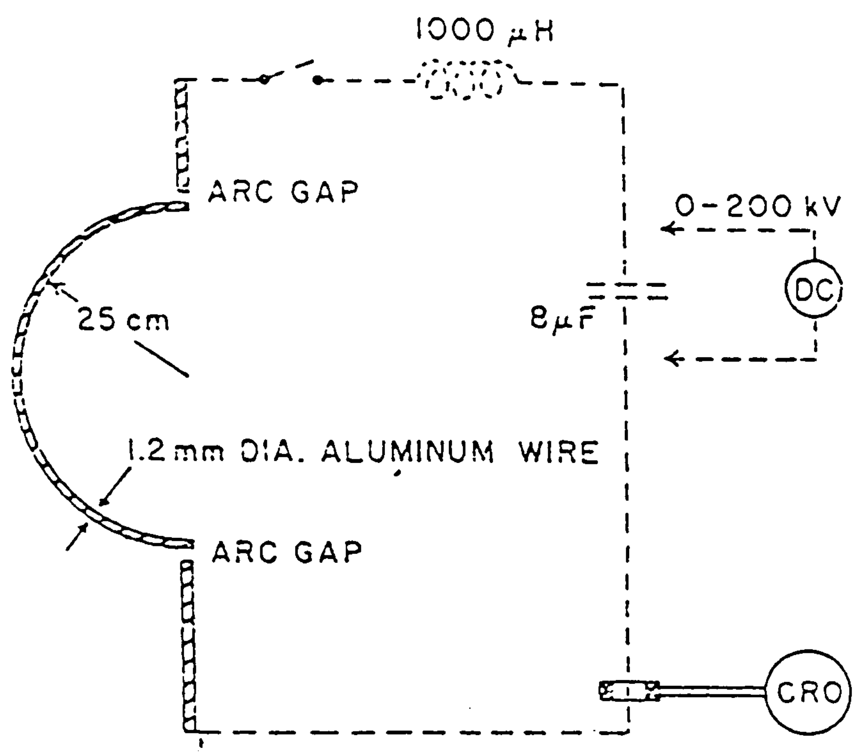

Figure A.3 : Graneau's wire fragmentation experiment

trodynamic, thermal, thermodynamic and mechanical effects. The thermal effect was ruled out by both Nasilowski and Graneau because no visible melting was observed. Graneau also ruled out the Lorentz pinch-off by reasoning that when pinch constriction and rupture occur in horizontal liquid metal conductors, this is always preceded by a V-shaped depression in the liquid level, but the wires broke without the formation of necks of reduced diameter.

As far as longitudinal stress vibrations are concerned, although Graneau admitted that the possibility of longitudinal stress wave fractures cannot be ruled out in the M.I.T. experiments, he argued that for the DC current pulses employed by Nasilowski, the radial pinch force was not removed from the wire until the current ceased to flow and the travelling stress waves could only be set up by relaxation after pinch removal. The fragmentation of the wire occurred well before the end of the current pulse, however, eliminating the possibility of fracture resulting from the longitudinal stress waves.

Graneau realized that the transverse forces can set up bending stresses which tend to straighten the wire and have a tensile component associated with them. But he stated even if large bending deformations did occur, it would still seem unlikely that the highly ductile, 99%-pure aluminium wire could be shattered in many pieces.

Material defects, as for example radial cracks and inclusions of foreign matter, could be the cause of local overheating and premature fracture in bending or tension. Graneau points out that no defects of this kind have been found in the series of wire samples subjected to fragmentation and none of the microscopic examinations of fracture faces revealed the presence of prior material defects so that any explanation of wire fragmentation that invokes material defects is very doubtful.

Graneau then offers a theoretical explanation based on Ampère's force law for this hitherto unexplained phenomenon as a piece of evidence to prove that the traditional Lorentz force law is incorrect in metallic conductors. This is one of the recent controversial issues in electrodynamics. Graneau is not alone in his ideas concerning the Ampère's tension predicted by his use of Ampère's force law, as this theory has been expounded by others [103, 108, 126, 150].

Graneau might be correct as far as the material defects and the bending stresses caused by the transverse forces are concerned. However, we do not agree with his explanation based on the Ampère's force law because his theoretical calculation is incomplete as we have discussed in Chapter 7.

Considering that the Lorentz pinch forces can excite longitudinal stress waves during the current rise-time, we suggest that the phenomenon might be understood by classical relativistic electrodynamics in association with the theory of stress waves in elastic solids.

A.2 Stress wave model

The governing equations of the problem are Maxwell's equations together with Ohm's and Lorentz force laws which are coupled to the stress wave equation[1] in isotropic solids, that is

$$\rho_m \frac{\partial^2 \mathbf{s}}{\partial t^2} = (\lambda + \mu)\mathrm{grad}\,\mathrm{div}\mathbf{s} + \mu \nabla^2 \mathbf{s} + \mathbf{f} \tag{A1}$$

[1]Refer to Kolsky [151], page 198 .

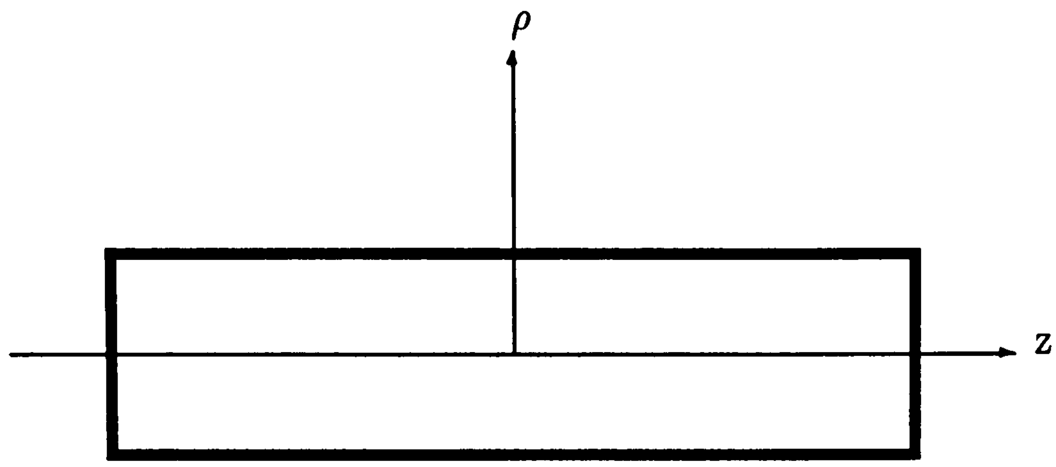

Figure A.4 : A straight wire in cylindrical coordinate system

where s is the displacement vector, ρ_m is the mass density, λ and μ are Lamé's constants[2] (μ is also known as the shear or rigidity modulus) and $\mathbf{f}$ is the body force density. In this problem we are only interested in electromagnetically driving forces, i.e., $\mathbf{f} = \mathbf{j} \times \mathbf{B}$. Therefore we have the problem of electromagnetically driven stress waves.

For our purpose, let us consider a straight wire in a cylindrical coordinate system (Fig.A.4) and suppose s is independent of ϕ. Thus Eqn.(A1) can be expressed as

$$-\frac{f_\phi}{\rho_m} + \frac{\partial^2 s_\phi}{\partial t^2} = c_T^2 \left(\frac{\partial^2 s_\phi}{\partial z^2} - \frac{\partial^2 s_\phi}{\partial \rho^2} + \frac{1}{\rho}\frac{\partial s_\phi}{\partial \rho} - \frac{\partial s_\phi}{\rho^2} \right) \tag{A2}$$

$$-\frac{f_\rho}{\rho_m} + \frac{\partial^2 s_\rho}{\partial t^2} = c_T^2 \left(\frac{\partial^2 s_\rho}{\partial z^2} - \frac{\partial^2 s_z}{\partial z \partial \rho} \right) + c_L^2 \left(\frac{\partial^2 s_\rho}{\partial \rho^2} + \frac{\partial^2 s_z}{\partial z \partial \rho} + \frac{1}{\rho}\frac{\partial s_\rho}{\partial \rho} - \frac{s_\rho}{\rho^2} \right) \tag{A3}$$

$$-\frac{f_z}{\rho_m} + \frac{\partial^2 s_z}{\partial t^2} = c_T^2 \left(\frac{\partial^2 s_z}{\partial z^2} - \frac{\partial^2 s_\rho}{\partial z \partial \rho} + \frac{1}{\rho}\frac{\partial s_z}{\partial \rho} - \frac{1}{\rho}\frac{\partial s_\rho}{\partial z} \right) + c_L^2 \left(\frac{\partial^2 s_z}{\partial z^2} + \frac{\partial^2 s_\rho}{\partial z \partial \rho} + \frac{1}{\rho}\frac{\partial s_\rho}{\partial z} \right) \tag{A4}$$

where s_ρ, s_z and s_ϕ are the components of displacment vector s; f_ρ, f_z and f_ϕ are the components of Lorentz force density; and

$$c_T = \left(\frac{\mu}{\rho_m} \right)^{1/2} \tag{A5}$$

[2]Young's modulus $= \frac{\mu(3\lambda+2\mu)}{\lambda+\mu}$; Poisson's ratio $= \frac{\lambda}{2(\lambda+\mu)}$.

$$c_L = \left(\frac{\lambda + 2\mu}{\rho_m}\right)^{1/2} \tag{A6}$$

are the transverse wave velocity and longitudinal wave velocity in an unbounded medium,[3] respectively.

Now we are able to see that Eqn.(A2) is decoupled from Eqns.(A3) and (A4). Furthermore, we may justifiably assume that $\mathbf{s} = 0$ at $t = 0$ and $f_\phi = 0$ so that Eqn.(A2) is omitted. We also note that if the wire were infinitely long, $\mathbf{s}$ would be independent of z, and Eqns.(A3) and (A4) would be decoupled from one to the other. However this is not the case because all tested wires in the experiments have finite length of about 1 meter. Thus Eqns.(A3) and (A4) are coupled to each other. In this case we would expect that the impact transverse force alone could excite the longitudinal stress wave even without the longitudinal force.

If the displacements are found from Eqns.(A3,A4) the strains of interest can be determined by the strain–displacement relations[4]

$$\epsilon_\rho = \frac{\partial s_\rho}{\partial \rho} \tag{A7}$$

$$\epsilon_z = \frac{\partial s_z}{\partial z} \tag{A8}$$

$$\epsilon_\phi = \frac{s_\rho}{\rho} \tag{A9}$$

$$2\epsilon_{zr} = 2\epsilon_{rz} = \frac{\partial s_\rho}{\partial z} + \frac{\partial s_z}{\partial \rho} \tag{A10}$$

The stresses of interest are then calculated according to the stress–strain relations

$$\tau_z = \lambda(\epsilon_\rho + \epsilon_\phi + \epsilon_z) + 2\mu\epsilon_z \tag{A11}$$

$$\tau_\rho = \lambda(\epsilon_\rho + \epsilon_\phi + \epsilon_z) + 2\mu\epsilon_\rho \tag{A12}$$

$$\tau_\phi = \lambda(\epsilon_\rho + \epsilon_\phi + \epsilon_z) + 2\mu\epsilon_\phi \tag{A13}$$

$$\tau_{zr} = \tau_{rz} = 2\mu\epsilon_{zr} \tag{A14}$$

[3] Refer to Achenbach [152], Chapter 4.

[4] Refer to Achenbach [152], page 74.

A.3 Further work

At first a simple model without considering the body forces may be investigated. The electrodynamic forces are then assumed to act on the wire surface in terms of the magnetic pressure $B^2/2\mu_0$. It would be expected that the results of studying this model could indicate the excitation of stress waves probably due to pinch forces and the successive reflections of waves which might give amplification.

The second model may take the body forces ($\mathbf{j} \times \mathbf{B}$) into account while keeping the wire surface free from stress. This model is more accurate but more complicated.

When studying these two models, following the experiments reported in the literature, two types of mechanical boundary conditions at both ends of the wire, namely either no stress or no displacement, may be considered. The geometry of the wire may also be considered as straight or semicircular. The latter may be studied first to see whether the transverse forces are important for this particular geometry.

Appendix B

Useful Vector Relations

A summary of the more useful formulas from vector analysis is given as follows.[1] Note that $\mathbf{A}$, $\mathbf{B}$, $\mathbf{C}$, $\mathbf{D}$ are arbitrary vector fields, ϕ and ψ arbitrary scalar fields.

B.1 Vector Formulas

General relations :

1. $\mathbf{A}\cdot\mathbf{B}\times\mathbf{C} = \mathbf{A}\times\mathbf{B}\cdot\mathbf{C} \equiv (\mathbf{A},\mathbf{B},\mathbf{C}) = (\mathbf{B},\mathbf{C},\mathbf{A}) = (\mathbf{C},\mathbf{A},\mathbf{B})$

2. $\mathbf{A}\times(\mathbf{B}\times\mathbf{C}) = (\mathbf{A}\cdot\mathbf{C})\mathbf{B} - (\mathbf{A}\cdot\mathbf{B})\mathbf{C}$

3. $\mathbf{A}\times(\mathbf{B}\times\mathbf{C}) + \mathbf{B}\times(\mathbf{C}\times\mathbf{A}) + \mathbf{C}\times(\mathbf{A}\times\mathbf{B}) = 0$

4. $(\mathbf{A}\times\mathbf{B})\cdot(\mathbf{C}\times\mathbf{D}) = \mathbf{A}\cdot[\mathbf{B}\times(\mathbf{C}\times\mathbf{D})] = (\mathbf{A}\cdot\mathbf{C})(\mathbf{B}\cdot\mathbf{D}) - (\mathbf{A}\cdot\mathbf{D})(\mathbf{B}\cdot\mathbf{C})$

5. $(\mathbf{A}\times\mathbf{B})\times(\mathbf{C}\times\mathbf{D}) = (\mathbf{A}\times\mathbf{B}\cdot\mathbf{D})\mathbf{C} - (\mathbf{A}\times\mathbf{B}\cdot\mathbf{C})\mathbf{D}$

6. $grad(\phi\psi) \equiv \nabla(\phi\psi) = \phi\nabla\psi + \psi\nabla\phi$

7. $div(\phi\mathbf{A}) \equiv \nabla\cdot(\phi\mathbf{A}) = \mathbf{A}\cdot\nabla\phi + \phi\nabla\cdot\mathbf{A}$

8. $curl(\phi\mathbf{A}) \equiv \nabla\times(\phi\mathbf{A}) = \phi\nabla\times\mathbf{A} - \mathbf{A}\times\nabla\phi$

9. $div(\mathbf{A}\times\mathbf{B}) \equiv \nabla\cdot(\mathbf{A}\times\mathbf{B}) = \mathbf{B}\cdot(\nabla\times\mathbf{A}) - \mathbf{A}\cdot(\nabla\times\mathbf{B})$

10. $curl(\mathbf{A}\times\mathbf{B}) \equiv \nabla\times(\mathbf{A}\times\mathbf{B}) = \mathbf{A}(\nabla\cdot\mathbf{B}) - \mathbf{B}(\nabla\cdot\mathbf{A}) + (\mathbf{B}\cdot\nabla)\mathbf{A} - (\mathbf{A}\cdot\nabla)\mathbf{B}$

11. $grad(\mathbf{A}\cdot\mathbf{B}) \equiv \nabla(\mathbf{A}\cdot\mathbf{B}) = \mathbf{A}\times(\nabla\times\mathbf{B}) + \mathbf{B}\times(\nabla\times\mathbf{A}) + (\mathbf{B}\cdot\nabla)\mathbf{A} + (\mathbf{A}\cdot\nabla)\mathbf{B}$

[1] Refer to Panofsky and Phillips [50], Moon and Spencer [153], Durney and Johnson [154].

12. $\nabla^2\phi = \nabla \cdot \nabla\phi$

13. $\nabla^2\mathbf{A} = \nabla(\nabla \cdot \mathbf{A}) - \nabla \times (\nabla \times \mathbf{A})$

14. $\nabla \times \nabla\phi = 0$

15. $\nabla \cdot (\nabla \times \mathbf{A}) = 0$

<u>Special relations</u> :

Let $\mathbf{r}$ be the radius vector, of magnitude r, from the origin to the point x, y, z, and let $\mathbf{J}$ be any constant vector. Then

16. $\nabla \cdot \mathbf{r} = 3$

17. $\nabla \times \mathbf{r} = 0$

18. $\nabla r = \mathbf{r}/r$

19. $\nabla(1/r) = -\mathbf{r}/r^3$

20. $\nabla \cdot (\mathbf{r}/r^3) = -\nabla^2(1/r) = 0$ if $r \neq 0$

21. $\nabla \cdot (\mathbf{J}/r) = \mathbf{J} \cdot [\nabla(1/r)] = -(\mathbf{J} \cdot \mathbf{r})/r^3$

22. $\nabla \times [\mathbf{J} \times (\mathbf{r}/r^3)] = -\nabla[(\mathbf{J} \cdot \mathbf{r})/r^3]$ if $r \neq 0$

23. $\nabla^2(\mathbf{J}/r) = \mathbf{J}\nabla^2(1/r) = 0$ if $r \neq 0$

24. $\nabla \times (\mathbf{J} \times \mathbf{B}) = \mathbf{J}(\nabla \cdot \mathbf{B}) + \mathbf{J} \times (\nabla \times \mathbf{B}) - \nabla(\mathbf{J} \cdot \mathbf{B})$

<u>Integral relations</u> :

If τ is a volume bounded by a closed surface s, with $d\mathbf{s}$ positive outward from the enclosed volume,

25. $\int_s \mathbf{A} \cdot d\mathbf{s} = \int_\tau (\nabla \cdot \mathbf{A}) d\tau$ – Gauss's theorem

26. $\int_s \phi d\mathbf{s} = \int_\tau (\nabla\phi) d\tau$

27. $\int_s \mathbf{A} \times d\mathbf{s} = -\int_\tau (\nabla \times \mathbf{A}) d\tau$

If s is an open surface bounded by the contour l, of which the line element is $d\mathbf{l}$,

28. $\oint_l \mathbf{A} \cdot d\mathbf{l} = \int_s (\nabla \times \mathbf{A}) \cdot d\mathbf{s}$ – Stokes's theorem

29. $\oint_l \phi d\mathbf{l} = -\int_s (\nabla \phi) \times d\mathbf{s}$

B.2 Vector Relations in Curvilinear coordinates

Cartesian coordinates :

Orthogonal line elements are dx, dy, dz.

Derivatives of all unit vectors are zero.

30. $\nabla \psi = \frac{\partial \psi}{\partial x}\mathbf{a}_x + \frac{\partial \psi}{\partial y}\mathbf{a}_y + \frac{\partial \psi}{\partial z}\mathbf{a}_z$

31. $\nabla \cdot \mathbf{A} = \frac{\partial A_x}{\partial x} + \frac{\partial A_y}{\partial y} + \frac{\partial A_z}{\partial z}$

32. $\nabla \times \mathbf{A} = \left(\frac{\partial A_z}{\partial y} - \frac{\partial A_y}{\partial z}\right)\mathbf{a}_x + \left(\frac{\partial A_x}{\partial z} - \frac{\partial A_z}{\partial x}\right)\mathbf{a}_y + \left(\frac{\partial A_y}{\partial x} - \frac{\partial A_x}{\partial y}\right)\mathbf{a}_z$

33. $\nabla^2 \psi = \frac{\partial^2 \psi}{\partial x^2} + \frac{\partial^2 \psi}{\partial y^2} + \frac{\partial^2 \psi}{\partial z^2}$

34. $$\nabla^2 \mathbf{A} = \left(\frac{\partial^2 A_x}{\partial x^2} + \frac{\partial^2 A_x}{\partial y^2} + \frac{\partial^2 A_x}{\partial z^2}\right)\mathbf{a}_x$$
$$+ \left(\frac{\partial^2 A_y}{\partial x^2} + \frac{\partial^2 A_y}{\partial y^2} + \frac{\partial^2 A_y}{\partial z^2}\right)\mathbf{a}_y$$
$$+ \left(\frac{\partial^2 A_z}{\partial x^2} + \frac{\partial^2 A_z}{\partial y^2} + \frac{\partial^2 A_z}{\partial z^2}\right)\mathbf{a}_z$$

Cylindrical coordinates :

Orthogonal line elements are $d\rho$, $\rho d\phi$, dz.

$\mathbf{a}_\rho = \cos\phi \mathbf{a}_x + \sin\phi \mathbf{a}_y$

$\mathbf{a}_\phi = -\sin\phi \mathbf{a}_x + \cos\phi \mathbf{a}_y$

$\mathbf{a}_z = \mathbf{a}_z$

$\frac{\partial \mathbf{a}_\rho}{\partial \phi} = \mathbf{a}_\phi, \qquad \frac{\partial \mathbf{a}_\phi}{\partial \phi} = -\mathbf{a}_\rho.$

All other partial derivatives of unit vectors are zero.

35. $\nabla\psi = \frac{\partial\psi}{\partial\rho}\mathbf{a}_\rho + \frac{1}{\rho}\frac{\partial\psi}{\partial\phi}\mathbf{a}_\phi + \frac{\partial\psi}{\partial z}\mathbf{a}_z$

36. $\nabla\cdot\mathbf{A} = \frac{1}{\rho}\frac{\partial(\rho A_\rho)}{\partial\rho} + \frac{1}{\rho}\frac{\partial A_\phi}{\partial\phi} + \frac{\partial A_z}{\partial z}$

37. $\nabla\times\mathbf{A} = \left(\frac{1}{\rho}\frac{\partial A_z}{\partial\phi} - \frac{\partial A_\phi}{\partial z}\right)\mathbf{a}_\rho + \left(\frac{\partial A_\rho}{\partial z} - \frac{\partial A_z}{\partial\rho}\right)\mathbf{a}_\phi + \frac{1}{\rho}\left(\frac{\partial(\rho A_\phi)}{\partial\rho} - \frac{\partial A_\rho}{\partial\phi}\right)\mathbf{a}_z$

38. $\nabla^2\psi = \frac{1}{\rho}\frac{\partial}{\partial\rho}\left(\rho\frac{\partial\psi}{\partial\rho}\right) + \frac{1}{\rho^2}\frac{\partial^2\psi}{\partial\phi^2} + \frac{\partial^2\psi}{\partial z^2}$

39. $$\nabla^2\mathbf{A} = \left(\frac{\partial^2 A_\rho}{\partial\rho^2} + \frac{1}{\rho}\frac{\partial A_\rho}{\partial\rho} - \frac{A_\rho}{\rho^2} + \frac{1}{\rho^2}\frac{\partial^2 A_\rho}{\partial\phi^2} - \frac{2}{\rho^2}\frac{\partial A_\phi}{\partial\phi} + \frac{\partial^2 A_\rho}{\partial z^2}\right)\mathbf{a}_\rho$$
$$+ \left(\frac{\partial^2 A_\phi}{\partial\rho^2} + \frac{1}{\rho}\frac{\partial A_\phi}{\partial\rho} - \frac{A_\phi}{\rho^2} + \frac{1}{\rho^2}\frac{\partial^2 A_\phi}{\partial\phi^2} + \frac{2}{\rho^2}\frac{\partial A_\rho}{\partial\phi} + \frac{\partial^2 A_\phi}{\partial z^2}\right)\mathbf{a}_\phi$$
$$+ \left(\frac{\partial^2 A_z}{\partial\rho^2} + \frac{1}{\rho}\frac{\partial A_z}{\partial\rho} + \frac{1}{\rho^2}\frac{\partial^2 A_z}{\partial\phi^2} + \frac{\partial^2 A_z}{\partial z^2}\right)\mathbf{a}_z$$

Spherical coordinates :

Orthogonal line elements are dr, $rd\theta$, $r\sin\theta d\phi$.

$\mathbf{a}_r = \sin\theta\cos\phi\mathbf{a}_x + \sin\theta\sin\phi\mathbf{a}_y + \cos\theta\mathbf{a}_z$

$\mathbf{a}_\theta = \cos\theta\cos\phi\mathbf{a}_x + \cos\theta\sin\phi\mathbf{a}_y - \sin\theta\mathbf{a}_z$

$\mathbf{a}_\phi = -\sin\phi\mathbf{a}_x + \cos\phi\mathbf{a}_y$

$\frac{\partial\mathbf{a}_r}{\partial\theta} = \mathbf{a}_\theta, \qquad \frac{\partial\mathbf{a}_\theta}{\partial\theta} = -\mathbf{a}_r, \qquad \frac{\partial\mathbf{a}_\phi}{\partial\phi} = -\mathbf{a}_\rho$

$\frac{\partial\mathbf{a}_r}{\partial\phi} = \sin\theta\mathbf{a}_\phi, \qquad \frac{\partial\mathbf{a}_\theta}{\partial\phi} = \cos\theta\mathbf{a}_\phi$

All other partial derivatives of unit vectors are zero.

40. $\nabla\psi = \frac{\partial\psi}{\partial r}\mathbf{a}_r + \frac{1}{r}\frac{\partial\psi}{\partial\theta}\mathbf{a}_\theta + \frac{1}{r\sin\theta}\frac{\partial\psi}{\partial\phi}\mathbf{a}_\phi$

41. $\nabla\cdot\mathbf{A} = \frac{1}{r^2}\frac{\partial(r^2 A_r)}{\partial r} + \frac{1}{r\sin\theta}\frac{\partial(\sin\theta A_\theta)}{\partial\theta} + \frac{1}{r\sin\theta}\frac{\partial A_\phi}{\partial\phi}$

42. $$\nabla\times\mathbf{A} = \frac{1}{r\sin\theta}\left(\frac{\partial(\sin\theta A_\phi)}{\partial\theta} - \frac{\partial A_\theta}{\partial\phi}\right)\mathbf{a}_r + \left(\frac{1}{r\sin\theta}\frac{\partial A_r}{\partial\phi} - \frac{1}{r}\frac{\partial(rA_\phi)}{\partial r}\right)\mathbf{a}_\theta$$
$$+ \frac{1}{r}\left(\frac{\partial(rA_\theta)}{\partial r} - \frac{\partial A_r}{\partial\theta}\right)\mathbf{a}_\phi$$

43. $\nabla^2\psi = \frac{1}{r^2}\frac{\partial}{\partial r}\left(r^2\frac{\partial\psi}{\partial r}\right) + \frac{1}{r^2\sin\theta}\frac{\partial}{\partial\theta}\left(\sin\theta\frac{\partial\psi}{\partial\theta}\right) + \frac{1}{r^2\sin^2\theta}\frac{\partial^2\psi}{\partial\phi^2}$

44. $$\nabla^2 \mathbf{A} = \left(\frac{\partial^2 A_r}{\partial r^2} + \frac{2}{r}\frac{\partial A_r}{\partial r} - \frac{2}{r^2}A_r + \frac{1}{r^2}\frac{\partial^2 A_r}{\partial \theta^2} + \frac{\cot\theta}{r^2}\frac{\partial A_r}{\partial \theta} \right.$$
$$\left. + \frac{1}{r^2 \sin^2\theta}\frac{\partial^2 A_r}{\partial \phi^2} - \frac{2}{r^2}\frac{\partial A_\theta}{\partial \theta} - \frac{2\cot\theta}{r^2}A_\theta - \frac{2}{r^2 \sin\theta}\frac{\partial A_\phi}{\partial \phi} \right) \mathbf{a}_r$$
$$+ \left(\frac{\partial^2 A_\theta}{\partial r^2} + \frac{2}{r}\frac{\partial A_\theta}{\partial r} - \frac{A_\theta}{r^2 \sin^2\theta} + \frac{1}{r^2}\frac{\partial^2 A_\theta}{\partial \theta^2} + \frac{\cot\theta}{r^2}\frac{\partial A_\theta}{\partial \theta} \right.$$
$$\left. + \frac{1}{r^2 \sin^2\theta}\frac{\partial^2 A_\theta}{\partial \phi^2} + \frac{2}{r^2}\frac{\partial A_r}{\partial \theta} - \frac{2\cot\theta}{r^2 \sin\theta}\frac{\partial A_\phi}{\partial \phi} \right) \mathbf{a}_\theta$$
$$+ \left(\frac{\partial^2 A_\phi}{\partial r^2} + \frac{2}{r}\frac{\partial A_\phi}{\partial r} - \frac{A_\phi}{r^2 \sin^2\theta} + \frac{1}{r^2}\frac{\partial^2 A_\phi}{\partial \theta^2} + \frac{\cot\theta}{r^2}\frac{\partial A_\phi}{\partial \theta} \right.$$
$$\left. + \frac{1}{r^2 \sin^2\theta}\frac{\partial^2 A_\phi}{\partial \phi^2} + \frac{2}{r^2 \sin\theta}\frac{\partial A_r}{\partial \phi} + \frac{2\cot\theta}{r^2 \sin\theta}\frac{\partial A_\theta}{\partial \phi} \right) \mathbf{a}_\phi$$

B.3 The Corollaries of Gauss's Theorem

The 1st Green's theorem :

45. $$\int_s (\phi \nabla \psi) \cdot d\mathbf{s} \equiv \int_s \phi \frac{\partial \psi}{\partial n} ds = \int_\tau \left(\phi \nabla^2 \psi + \nabla \phi \cdot \nabla \psi \right) d\tau$$

The 2nd Green's theorem :

46. $$\int_s \left(\psi \frac{\partial \phi}{\partial n} - \phi \frac{\partial \psi}{\partial n} \right) ds = \int_\tau \left(\psi \nabla^2 \phi - \phi \nabla^2 \psi \right) d\tau$$

Appendix C

Useful Constants and Conversions

Speed of light in vacuum	$c = 2.99792458 \times 10^{8}\, m/s$
Permittivity of vacuum	$\epsilon_0 = 8.85418782 \times 10^{-12}\, F/m$
Permeability of vacuum	$\mu_0 = 4\pi \times 10^{-7}\, H/m$
Elementary charge	$e = 1.602177 \times 10^{-19}\, C$
Electron rest mass	$m = 9.10938 \times 10^{-31}\, kg$
Boltzmann constant	$\kappa = 1.3806 \times 10^{-23}\, J/K$
Conductivity of copper	$5.80 \times 10^{7}\, (\Omega m)^{-1}$
Conductivity of aluminium	$3.54 \times 10^{7}\, (\Omega m)^{-1}$
Conductivity of seawater	$\sim 5\, (\Omega m)^{-1}$
$1\, Tesla = 10^{4}\, Gauss$	
$1\, atm = 760\, Torr = 1.013 \times 10^{5}\, Pa$	
$1\, atm = 1.013\, bar$	
$1\, Torr = 1\, mmHg$	
$1\, Pa = 1\, Newton/m^{2}$	
$1\, Newton = 10^{5}\, Dyne$	

Bibliography

[1] Somerville J M, *The Electric Arc, John Wiley and Sons INC., London, 1959*

[2] Kesaev I G, *Cathode Processes in the Mercury Arc, Consultants Burean, New York, 1964*

[3] Hoyaux M F, *Arc Physics, Spring-Verlag, New York, 1968*

[4] Lafferty J M, Ed. *Vacuum Arcs – Theory and Application, John Wiley and Sons INC., New York, 1980*

[5] Raizer Y P, *Gas Discharge Physics, Ed. Allen J E, Spring-Verlag, Berlin, 1991*

[6] Stark J, *Phys.Zeit. 4 (1903)440*

[7] Minorsky N, *J.Phys.Radium, 9 (1928) 127*

[8] Tanberg R, *Nature, 124 (1929) 371*

[9] Smith C G, *Phys. Rev. 63 (1943) 217*

[10] Smith C G, *Phys. Rev. 69 (1946) 96*

[11] Smith C G, *Phys. Rev. 73 (1948) 543*

[12] Smith C G, *J.Appl. Phys. 28 (1957) 1328*

[13] Gallagher C J and Cobine J D, *Phys. Rev. 71 (1947) 481*

[14] Gallagher C J, *J.Appl.Phys. 21 (1950) 768*

[15] Longini R L, *Phys. Rev. 71 (1947) 642*

[16] Rothstein J, *Phys. Rev. 78 (1950) 331*

[17] Yamamura J, *J.Appl.Phys. 21 (1950) 193*

[18] St. John R M and Winans J G, *Phys. Rev. 94 (1954) 1097*

[19] Ware A A, *Proc.Phys.Soc. A 67 (1954) 869*

[20] Robson A E and von Engel A, *Phys. Rev. 93 (1954) 653*

[21] Robson A E and von Engel A, *Phys. Rev. 104 (1956) 15*

[22] Robson A E, *Proc. 4th Int. Conf. on Ionization Phenomena in Gases, Uppsala, vol.1 (1959) 346*

[23] Robson A E, *J. Phys.D: Appl. Phys.11 (1978) 1917*

[24] Ecker G and Müller K G, *J. Appl.Phys. 29 (1958) 1606*

[25] Guile A E and Secker RE, *J.Appl. Phys. 29 (1958) 1662*

[26] Hull A W, *Phys. Rev. 126 (1962) 1603*

[27] Roman W C, *Proc. 6th Int. Conf. Ion. Gases, 2 (1963) 287*

[28] Fursei G N and Vorontsov-vel'iaminov, *Sov.Phys.-Tech.phys. 12 (1968) 1377*

[29] Sena L A, *Sov.Phys.-Tech.phys. 13 (1969) 1601*

[30] Hermoch V, *IEEE Trans. PS-1 (1973) 62*

[31] Carter R P and Murphrce D L, *J.Appl. Phys. 44 (1973) 5190*

[32] Pimley K, *The retrograde motion of electric arc cathode spots, M.Sc.Thesis : The University of Oxford (1973)*

[33] Alferov V I, Vitkovskaka O N and Shchrbakov G I, *Sov.Phys.-Tech.phys. 22 (1977) 57*

[34] Fang D Y, *J.Phys.D: Appl.Phys. 15 (1982) 833*

[35] Fang D Y, *IEEE Trans. PS-11 (1983) 110*

[36] Harris L P, *IEEE Trans. PS-11 (1983) 94*

[37] Drouet M G, *IEEE Trans. PS-13 (1985) 235*

[38] Molzhes B Y and Nemchinskii V A, *Sov.Phys.-Tech.Phys. 30 (1985) 136*

[39] Schrade H O, *IEEE Trans. PS-17 (1989) 635*

[40] Schrade H O, Auweter-kurtz M and Kurtz H L, *IEEE Trans. PS-11 (1983) 103*

[41] Swift P D, McKenzie D R and Falconer I S, *J.Appl.Phys. 66 (1989) 505*

[42] Swift P D, *J.Appl.Phys. 67 (1990) 1720*

[43] Moizhes B Y and Nemchinsky V A *J.Phys. D: Appl.Phys. 24 (1991) 2014*

[44] Rakhovskii V I, *IEEE Trans. PS-4 (1976) 81*

[45] Hower G W O, *Wireless Engineer, Vol.XXII (1945) 469*

[46] Hammond P, *Energy methods in electromagnetism, Clarendon Press, Oxford, (1981)*

[47] Jüttner B, *IEEE Trans. PS-15 (1987) 474*

[48] Daalder J E, *IEEE Trans. PAS-93 (1974) 1747*

[49] Daalder J E, *Ph.D. Thesis, Eindhoven University of Technology (1978)*

[50] Panofsky W K H and Phillips M, *Classical electricity and magnetism, 2nd Ed. Addison-Wesley, Reading, (1962)*

[51] Brown S C (Ed.), *Fundamentals of plasma physics, John Wiley & Sons, New york, (1980)*

[52] Miyamoto K, *Plasma physics for nuclear fusion, The MIT Press, Massachusetts, (1980)*

[53] Smythe W R, *Static and dynamic electricity, McGRAW-Hill, London, (1950)*

[54] Gray A and Matheas G B , *A treaties on Bessel functions and their application to physics, Dover, New York, (1966) 91*

[55] NAG, *Fortran Library Introduction Guide, Mark 14, The Numerical Algorithms Group Limited, (1990)*

[56] Barton G , *Elements of Green's functions and propagation, Clarendon Press, Oxford, (1989)*

[57] Sokolnikoff I S and Redheffer K M, *Mathematics of physics and modern engineering, McGRAW-Hill Book Company, 2nd Edition, New York, (1966)*

[58] Brebbia C A and Domingnez J , *Boundary elements - An introductory course, McGraw-Hill Book Company, New York, (1989)*

[59] Hammer P C and Strond A H, *Math.Tables and Other Aids to Computation, 12 (1958) 272*

[60] Cowper G R, *Int.J.Num.Meth.Eng., 7 (1973) 405*

[61] Hayami K and Brebbia C A, *Boundary Elements IX, Vol.1 (1987) 375*

[62] Telles J C F, *Int.J.Num.Meth.Eng., 24 (1987) 959*

[63] Jun L et.al., *Engineering Analysis, 2 (1985) 118*

[64] Brebbia C A, Telles J C F and Wrobel L C , *Boundary element techniques - Theory and applications in engineering, Springer-Verlag, Berlin, (1984)*

[65] Nielsen K L, *Methods in numerical analysis, The Macmillan Company, New York, (1956)*

[66] Stroud A H and Secrest D, *Gaussian quadrature formulas, Prentice Hall, (1966)*

[67] Cohen H D, *Int.J.Num.Meth.Eng. 1 (1980) 470*

[68] Zienkiewicz O C, et.al., *J.Num.Meth.Engng. 3 (1971) 519*

[69] Hong JS and Allen JE, *'On the electrodynamic explanation of the retrograde motion of the electric arc', The Int.Conf.on Plasma Physics (1992)*

[70] Smeets P, *Ph.D. Thesis, Eindhoven University of Technology (1987)*

[71] Himler G J and Cohn G I, *Electl Engng 67 (1948) 1148*

[72] Mitterauer J and Till P, *IEEE Trans. PS-15 (1987) 488*

[73] Hantzche E and Jüttner B, *IEEE Trans. PS-13 (1985) 230*

[74] Robertson R M, *Phys. Rev. 53 (1938) 578*

[75] Kimblin C W , *J. Appl. Phys. 44 (1973) 3074*

[76] Kimblin C W , *IEEE Trans. PS-10 (1982) 322*

[77] Von Engel A, *Ionized Gases, 2nd Ed. Oxford (1965), Chapter 4*

[78] Miller H C, *J.Appl.Phys. 52 (1981) 4523*

[79] Papoular R, *Electrical Phenomena in Gases, Iliffe Books Ltd., London (1965) 21*

[80] Reece M P, *Proc.IEE, 110 (1963) 793*

[81] Rakhovskii V I, *IEEE Trans. PS-4 (1976) 81*

[82] Djakov B E and Holmes R, *1970 IEE Int. Gas Discharge Conf. London (London) 468*

[83] Gundlach H C W , *1972 Proc. 5th Int. Symp. on Discharges and Electrical Insulation in Vacuum (Poznan) 249*

[84] Sherman J C, Webster R, Jenkins J E and Holmes R, *J. Phys. D: Appl. Phys.8 (1975) 696*

[85] Agarwal M S and Holmes R, *J. Phys.D: Appl. Phys.17 (1984) 743*

[86] Schellekens H, *Physica, 104C (1981) 130*

[87] Schellekens H and Schram D C, *IEEE Trans. PS-13 (1985) 261*

[88] Miller H C, *1982 Proc. 10th Int. Symp. on Discharges and Electrical Insulation in Vacuum (Colombia)*

[89] Sherman J C, et al, *J. Phys.D: Appl. Phys.11 (1978) 379*

[90] Boxman R L, Goldsmith S, Izraeli I and Shalev S, *IEEE Trans. PS-11 (1983) 138*

[91] Izraeli I, Goldsmith S and Boxman R L, *IEEE Trans. PS-11 (1983) 160*

[92] Graneau P , *IEEE Trans. Mag. 20 (1984), 444*

[93] Ternan JG , *J. Appl. Phys. 57 (1985), 1743*

[94] Jolly DC, *Phys. Lett. A, 107 (1985), 231*

[95] Graneau P , *J. Appl. Phys. 58 (1985), 3638*

[96] Ternan JG , *J. Appl. Phys. 58 (1985), 3639*

[97] Aspden H, *Phys. Lett. A, 111 (1985), 22*

[98] Moyssides PG, *J. Appl. Phys. 59 (1986), 19*

[99] Garretson CM, *Am.J. Phys. 54 (1986), 253*

[100] Christodoulides C, *J. Phys. A: Math. Gen. 20 (1987), 2037*

[101] Christodoulides C, *Phys. Lett. A, 120 (1987), 129*

[102] Christodoulides C, *Am.J. Phys. 56 (1988), 357*

[103] Whitney CK, *Am.J. Phys. 56 (1988), 871*

[104] Whitney CK, *Phys. Lett. A, 128 (1988),232*

[105] Strnad J, *Phys. Lett. A, 137 (1989),11*

[106] Graneau P, *Phys. Lett. A, 137 (1989), 87*

[107] Christodoulides C, *Phys. Lett. A, 141 (1989), 383*

[108] Cornille P, *J. Phys. A: Math. Gen. 22 (1989), 4075*

[109] Graneau P N, *Phys. Lett. A, 147 (1990), 92*

[110] Robson A E and Sethian J D, *Am. J. Phys., 60 (1992), 1111*

[111] Maxwell JC, *A Treatise on Electricity and Magnetism , vol.2 (Clarendon, Oxford, 1873)*

[112] Whittaker ET, *A History of the Theories of Aether and Electricity, (Tomash Publishers, 1951)*

[113] Graneau P, *J.Appl.Phys., 53 (1982), 6648*

[114] Graneau P, *Fortschr. Phys., 34 (1986), 457*

[115] Graneau P, *Ampere-Neumann Electrodynamics of Metals, (Hadronic Press, 1985)*

[116] Graneau P and Graneau P N *Phys. Lett. A, 165 (1992), 1*

[117] Graneau P, *Phys. Lett. A, 97 (1983), 253*

[118] Graneau P, *Nature, 295 (1982) 311*

[119] Hillas A M, *Nature, 302 (1983) 271*

[120] Graneau P, *Nature, 302 (1983) 271*

[121] Jackson J D, *Classical electrodynamics, John Wiley & Sons, London (1962)*

[122] French A P, *Special relativity, Van Nostrand Reinhold, England (1984)*

[123] Maxwell C, *Clerk Maxwell "Scientific Papers", Vol.2, Cambridge University Press, (1890) 311*

[124] Smithells C J, *Metals Reference Book, Butterworths, London (1976) 940*

[125] Rosser W G V, *Classical electromagnetism via relativity, Butterworths, London (1968)*

[126] Pappas P T, *Nuovo Cimento, 76 (B) (1983) 189*

[127] Graneau P and Graneau P N, *Nuovo Cimento, Vol.7 D, N.1 (1986) 31*

[128] Fano, Chu and Adler, *Electromagnetic fields, energy, and forces, John Wiley & Sons, INC., London (1960) 428*

[129] Allen J E and Jones T V, *J.Appl.Phys. 67 (1990) 18*

[130] Früngel F B, *High speed pulse technology, Academic, New York, Vol.1 (1965)*

[131] Gilchrist I and Crossland B, *The forming of sheet metal using an underwater electrical discharge, IEE Conference Publication, No.38 (1967) 92*

[132] Graneau P and Graneau P N, *Appl. Phys. Lett. 46 (1985) 468*

[133] Aspden H, *IEEE Trans., PS-14 (1986) 282*

[134] Dragone L, *J. Appl. Phys. 62 (1987) 3477*

[135] Stratton J A, *Electromagnetic theory, McGRAW-Hill, London, (1941)*

[136] Shercliff J A, *Magnetohydrodynamics, Pergamon press, Oxford, (1965)*

[137] Maecker H, *Z.Phys., 14 (1955) 198*

[138] Abraham M and Becker R, *The classical theory of electricity and magnetism, Blackie & Son, London (1937)*

[139] Rosser W G V, *Classical eletromagnetism via relativity, Butterworths, London (1968)*

[140] Ferraro V C A and Plumpton C, *Magneto-fluid mechanics, 2nd Edition, Clarendon Press, Oxford (1966)*

[141] Roache P J, *Computational fluid dynamics, Hermosa Publishers, Albuquerque, N.M. (1972)*

[142] Uberoi M S and Chow C Y, *The Physics of Fluids, 20 (1977) 1815*

[143] Rektorys K, *Survey of applicable mathematics, Iliffe Books LTD, London (1969) 911*

144] Bradley J N, *Shock waves in chemistry and physics, John Wiley & Sons INC., London (1962) 13*

145] Richardson A B, Arons A B and Halverson R R, *J Chem. Phys., 15 (1947) 785*

146] Penney W G and Pike H H M, *Reports on Progress in Physics, 13 (1950) 46*

147] Nasilowski J, *Exploding wires, vol.3, Eds. Chase W G and Moore H K, Plenum, New york (1964) 295*

[148] Foitzik R, *Elektrotechnische Zeitschrift, 60 (1939) 89*

[149] Aspden H, *Phys. Lett. A 107 (1985) 238*

[150] Rambaut M, *Phys. Lett. A 154 (1991) 210*

[151] Kolsky H, *Stress waves in solids, Dover Publications, INC., New York (1963)*

[152] Achenbach I D, *Wave propagation in elastic solids, North-Holland Publishing Company, Amsterdam (1973)*

[153] Moon P and Spencer D E, *Foundations of electrodynamics, D.VAN NOSTRAND COMPANY, INC., Princeton (1960) 300*

[154] Durney C H and Johnson C C, *Introduction to modern electromagnetics, McGraw-Hill Book Company, New York (1969)*